Università degli Studi dell'Aquila

Dipartimento di Ingegneria Industriale e dell'Informazione e di Economia

Dottorato di Ricerca in Ingegneria Industriale
e dell'Informazione e di Economia
Curriculum in Ingegneria Elettrica, Elettronica e dell'Informazione
XXXVI Ciclo

Advanced Methods for the Transient Analysis of Linear Electrical Systems

S.S.D. ING-IND/31

Dottorando:
Fabrizio Loreto

Coordinatore del corso:
Prof.ssa Katia Gallucci

Tutor:
Prof. Giulio Antonini

Anno Accademico 2022-2023

Table of Contents

Abstract

The efficiency of the devices is an increasingly central aspect in the design process. Therefore, nowadays high-fidelity modeling of systems is a strongly necessary requirement in the engineering reality. For this purpose, simulation has become a central tool, taking on an indispensable role as an aid to planning. Through simulation it is possible to analyze, in relatively short times, the performances of different project alternatives, avoiding investing time and money, which would otherwise be required, in order to build physical prototypes. Hence, the trend is more and more oriented to virtual prototyping.

In particular, in the context of the design of electrical and electronic devices, electromagnetic simulation is a popular tool. In fact, the use of a tool of this kind allows to verify compliance with the provided apparatus specifications and, above all, to conceptually optimize the performance characteristics. To do this, relevant informations about complex phenomena affecting electronic systems such as crosstalk, signal dispersion, reflections, radiation, conductors and dielectric losses should be extracted. Moreover, these phenomena are increasingly evident as the value of the operating frequencies increases, since the parasitic elements play a crucial role on the interconnections behavior. Unfortunately, the high frequency behavior of such passive structures can alter the global performances of a system degrading significantly its efficiency, if adequate countermeasures are not taken.

For example, in digital electronic data transmission systems, in order to produces

increasingly faster and more performing calculators, speed processing is exponentially growing from year to year, leading to an increase in the drive clock frequency. As the capacitive and inductive couplings along the interconnections become important, and the losses due to the skin effect continue to grow, undesired couplings and losses are the primary cause of signal distortion and attenuation, undermining the integrity of the digital system. Only in-depth studies, with consequent optimization, in the simulation phase is able to guarantee this integrity.

Another current example concerns power converters such as: rectifiers, choppers for direct current electric drives and inverters for alternating current electric drives. Indeed, in power electronics, in order to improve electromechanical performance of the drive, increasing switching frequencies are used to drive semiconductor elements. Hence, in converters, it is usual to deal with conducted and radiated electromagnetic emissions issues, with consequent decrease in efficiency. The emission spectrum of disturbances in converters can even reach hundreds of MHz. As already mentioned for digital devices, at these frequencies, the skin effect causes large losses, resulting in overheating of the components. For this reason, even in this area, it is necessary to resort to electromagnetic simulation tools, able to predict and optimize the overall efficiency of the drive.

Several suitable numerical techniques able to perform full-wave analyses can be found in literature. Among them, the most employed fall in the categories of differential or integral methods. The former are based on the discretization of Maxwell equations over the volume computational domain and on the enforcing of appropriate boundary conditions at the interface between different materials and over virtual surfaces delimiting the domain for ensuring the radiation condition. The discretization is performed both in time/frequency and space and the field computation is carried out for each time/frequency sample and for each point of the resulting space grid (mesh), including air-filled zones. The most known differential methods are the Finite-Element Method (FEM) and the Finite-Differences method (FD).

On the other hand, volume Integral Equations (IE) methods are built around the definition of the Electric Field Integral Equation (EFIE) or the Magnetic Field Integral Equation (MFIE) in conjunction with the application of the Volume Equiv-

alence Principle for Maxwell Equations. The EFIE and MFIE are formulated and discretized in space and time only in the volume portions occupied by material bodies (e.g. metals and dielectrics), being not necessary to carry out the computations in vacuum portions and to enforce boundary conditions on virtual surfaces surrounding the computational domain, since the radiation condition is an intrinsic feature of the IE formulation. Throughout the years, volumetric IE methods have proved to be robust tools for full-wave simulation of scattering EM problems for electronics applications.

Another classification of numerical methods concerns their subdivision in frequency-domain (FD) and time-domain (TD) methods. The latter, although more challenging, are often preferred to the former in their capability to produce broadband data from a single simulation. Moreover, in electric and electronic applications a growing number of non-linear devices of the semiconductor type is observed. This obviously complicates FD-based analyses, rendering more feasible TD-based analyses. In this context, Time Domain Integral Equations (TDIE) methods have gained a rising interest for scattering problems, since they do not require approximate boundary conditions and the time-step is not related to the mesh size by stability conditions like the Courant-Friedrichs-Levy (CFL) one. Moreover, TDIE methods do not suffer from numerical phase dispersion, one of the main causes of inaccuracy in differential methods.

However, full-wave TDIE methods are often based on the approximation of the model propagation delays, which can be the source of late-time instabilities showing up in the TD solutions obtained with standard time-stepping solvers. Precise measures for their prediction and management have not yet been investigated and the finding of a systematic relation between the instabilities and the approximation degrees employed in the propagation delays representation is still an open issue.

The Partial Elements Equivalent Circuit (PEEC) is an integral-equations method that has gained particular attention in the last years, due to its peculiarity of translating a scattering EM problem into a circuit SPICE-like representation. This representation has been demonstrated to be very useful since the connection of the EM model to common devices represented by lumped elements is straightforward.

In the standard volume PEEC (VPEEC), this is achieved by resorting to the volume equivalence principle applied to the volumes occupied by the scatterers. It is then possible to obtain a volumetric Electric Field Integral Equation (EFIE), where the currents flowing in the scatterer in the original problem represent at the same time the unknowns and the sources of the scattered field. The discretization of the problem is obtained by expanding the electric currents into constant basis functions all over the computational domain and adopting Galerkin testing procedure, giving rise to a volume mesh. The problem is then completed by applying the continuity equation for the electric current over the scatterer surface, again assuming constant basis functions, and using Galerkin testing process as well, giving rise to a surface mesh. Finally, a global discretized dual-mesh EM model is achieved, where currents flowing in the elementary volumes and charges residing over the elementary surfaces are supposed to radiate in a free-space environment. The magnetic coupling between the mesh volumes is described by the so-called partial inductances, while the electric coupling between the mesh surfaces is described by coefficients of potential, two circuit-like quantities. In the circuit context, the full-wave mutual magnetic and electric interactions are described by interaction integrals containing the free-space Green function as a kernel.

Description of the Thesis

The purpose of this doctoral work is to explore alternative TD simulation techniques in the context of the PEEC method. The key motivation arises from the necessity of stable full-wave models, able to include propagation delays in the PEEC formulation. Quasi-Static (QS) PEEC models have been widely employed in the past decades as efficient and reliable tools for the analysis and verification of the EM behavior of common structures typically employed in the electronic industry. Such models have demonstrated to be robust and, above all, always stable.

In the last three decades, the technological evolution in electronics and the growing necessity of small and compact devices has led to an increase of the geometrical complexity of signal interconnecting structures. Moreover, for efficiency and functional purposes, an impressive increase of the working frequencies has been observed throughout the years, especially in the signal electronics and microwave areas. Such context has brought to the necessity of analyzing complex electrically long structures in the simulation stage. This has required the development of full-wave solvers, able to catch correctly the propagation delays and to represent more accurately all the non-ideal loss mechanisms affecting such devices.

In the PEEC method, such delays are buried in the partial elements, complicating the circuit representation and giving rise to computationally demanding models, inevitably lengthening the simulation times. In order to keep the computational burden within an acceptable level, several approximations have been introduced for

the representation of delayed partial elements. Unfortunately, those approximations, can lead to unpredictable instabilities showing up in the TD final results.

For the reasons already explained, two different approaches for obtaining stable TD PEEC models have been investigated in this work.

A possibility is to resort to Inverse Laplace Transform (ILT) techniques, naturally grounded in the frequency domain, collecting and combining the results obtained through the evaluation of the Laplace-domain PEEC model over specified points of the complex plane. Such a technique is relatively simple in its implementation, being necessary few changes to standard FD PEEC solvers.

Another investigated option is the rigorous TD representation of partial elements through the Cagniard deHoop (CdH) technique, giving rise to direct TD convolution-based PEEC models.

In what follows, both these macro-techniques are deeply investigated, highlighting rigorously all the advantages and disadvantages involved in their employment. Where possible, several methods to overcome the limits of such techniques are proposed, always paying particular attention to not excessively increase the computational burden.

1 The PEEC method

Over the past 50 years many different numerical technique for the modeling of electromagnetic phenomena have been developed. Among such techniques the Partial Element Equivalent Circuit (PEEC) method has proved to be particularly well suited for the representation of parasitic effect rising in interconnects modeling. In its early age the PEEC method was used for the modeling of inductive effects of multiconductor systems in free space [1]. Immediately after also capacitive effects [2] were included in the model through the general integral-equation-based approach and then the method was expanded to full-wave conditions [3]. After about two decades the modeling of dielectrics materials was included in the picture [4], exploiting the volume equivalence principle and the introduction of an equivalent current including part of the displacement component. In recent years many other materials with different properties have been gradually included [5–13].

The main difference among the PEEC method and other integral equation based techniques, such as the Method of Moments (MoM) [14], resides in the fact that it provides a circuit interpretation of the Mixed Potential Integral Equation (MPIE) [15] in terms of partial elements, namely resistances, partial inductances and coefficients of potential. This makes the PEEC method particularly well suited for its integration within design process where electronic engineers work, because the resulting equivalent circuit can be studied by means of SPICE-like circuit solvers [16] in both the time and frequency domains.

Over the years, several improvements of the PEEC method have been performed

thus allowing it to handle complex problems involving both circuits and electromagnetic fields

To speed-up the equivalent circuit analysis, fast multipole based techniques [17] as well as the adaptive cross approximation (ACA) [18–23] have been used. Moreover effective model-order reduction techniques can be adopted leading to compact models preserving the accuracy at the ports and the physical properties of the original system.

In the standard approach, volumes and surfaces are discretized into elementary regions, hexahedra and quadrilateral patches respectively [24] over which the current and charge densities are expanded into a series of basis functions. Pulse basis functions are usually adopted as expansion and weight functions. Such choice of pulse basis functions corresponds to assume constant current density and charge density over the elementary volume (inductive) and surface (capacitive) cells, respectively. Following the standard Galërkin's testing procedure nodes and branches are generated and electrical lumped elements are identified modeling both the magnetic and electric field coupling. Conductors are modeled by their ohmic resistance, while dielectrics requires modeling the excess charge due to the dielectric polarization [4]. Magnetic and electric field coupling are modeled by partial inductances and coefficients of potential, respectively.

The aim of this chapter is to describe the entire PEEC method by starting from Maxwell's Equations.

1.1 Integral Formulation of Maxwell's Equations

Maxwell differential equation in time domain are [15]

$$\nabla \times \boldsymbol{H}(\boldsymbol{r},t) = \frac{\partial \boldsymbol{D}(\boldsymbol{r},t)}{\partial t} + \boldsymbol{J}(\boldsymbol{r},t) \tag{1.1}$$

$$\nabla \times \boldsymbol{E}(\boldsymbol{r},t) = -\frac{\partial \boldsymbol{B}(\boldsymbol{r},t)}{\partial t} \tag{1.2}$$

$$\nabla \cdot \boldsymbol{B}(\boldsymbol{r},t) = 0 \tag{1.3}$$

$$\nabla \cdot \boldsymbol{D}(\boldsymbol{r},t) = q(\boldsymbol{r},t) \tag{1.4}$$

where $\boldsymbol{H}(\boldsymbol{r},t)$ is the magnetizing field, $\boldsymbol{D}(\boldsymbol{r},t)$ is the displacement field, $\boldsymbol{E}(\boldsymbol{r},t)$ is the electric field, $\boldsymbol{B}(\boldsymbol{r},t)$ is the magnetic field, $q(\boldsymbol{r},t)$ is the charge density and $\boldsymbol{J}(\boldsymbol{r},t)$ is the current density. For linear isotropic medium, the fields $\boldsymbol{H},\boldsymbol{B},\boldsymbol{E}$ and $\boldsymbol{D}$ satisfy the following constitutive relations

$$\boldsymbol{B}(\boldsymbol{r},t) = \mu_0\mu_r\boldsymbol{H}(\boldsymbol{r},t) \tag{1.5}$$

$$\boldsymbol{D}(\boldsymbol{r},t) = \varepsilon_0\varepsilon_r\boldsymbol{E}(\boldsymbol{r},t) \tag{1.6}$$

where μ_r and ε_r are the relative permeability and permittivity, respectively. It is useful to express fields in terms of potentials. Because of the solenoidality of $\boldsymbol{B}$, (1.3), a magnetic vector potential can be defined as

$$\boldsymbol{B}(\boldsymbol{r},t) = \nabla\times\boldsymbol{A}(\boldsymbol{r},t). \tag{1.7}$$

Substituting (1.7) into (1.2) it follows that

$$\nabla\times\left(\boldsymbol{E}(\boldsymbol{r},t)+\frac{\partial\boldsymbol{A}(\boldsymbol{r},t)}{\partial t}\right)=\boldsymbol{0}. \tag{1.8}$$

The previous equation allows to define the electric scalar potential $\boldsymbol{\Phi}(\boldsymbol{r},t)$ such that

$$\boldsymbol{E}(\boldsymbol{r},t)+\frac{\partial\boldsymbol{A}(\boldsymbol{r},t)}{\partial t}=-\nabla\Phi(\boldsymbol{r},t). \tag{1.9}$$

Such equation relates the electric field $\boldsymbol{E}$ with the potentials $\boldsymbol{A}$ and Φ. The next step is to express such potentials $\boldsymbol{A}$ and Φ in terms of the sources $\boldsymbol{J}$ and q, respectively. To this aim, by substituting (1.7) and (1.9) into (1.1), it follows that

$$\nabla\times\nabla\times\boldsymbol{A}(\boldsymbol{r},t)=\mu_0\varepsilon_0\frac{\partial}{\partial t}\left(-\frac{\partial\boldsymbol{A}(\boldsymbol{r},t)}{\partial t}-\nabla\Phi(\boldsymbol{r},t)\right)-\mu_0\boldsymbol{J}(\boldsymbol{r},t). \tag{1.10}$$

Using the Laplacian identity

$$\nabla\times\nabla\times\boldsymbol{A}(\boldsymbol{r},t)=\nabla(\nabla\cdot\boldsymbol{A}(\boldsymbol{r},t))-\nabla^2\boldsymbol{A}(\boldsymbol{r},t) \tag{1.11}$$

and enforcing the Lorenz gauge

$$\nabla\cdot\boldsymbol{A}(\boldsymbol{r},t)=-\mu_0\varepsilon_0\frac{\partial\Phi(\boldsymbol{r},t)}{\partial t} \tag{1.12}$$

the Helmholtz equation for the magnetic vector potential is obtained

$$\nabla^2 \boldsymbol{A}(\boldsymbol{r},t) - \mu_0\varepsilon_0 \frac{\partial \boldsymbol{A}(\boldsymbol{r},t)}{\partial t^2} = -\mu_0 \boldsymbol{J}(\boldsymbol{r},t). \tag{1.13}$$

If we replace (1.9) in (1.4) in free space we have

$$\nabla \cdot \left[-\frac{\partial \boldsymbol{A}(\boldsymbol{r},t)}{\partial t} - \nabla\Phi(\boldsymbol{r},t) \right] = \frac{q(\boldsymbol{r},t)}{\varepsilon_0} \tag{1.14}$$

and from (1.12) also the Helmholtz equation for the electric scalar potential can be obtained

$$\nabla^2 \Phi(\boldsymbol{r},t) - \mu_0\varepsilon_0 \frac{\partial \Phi(\boldsymbol{r},t)}{\partial t^2} = -\frac{q(\boldsymbol{r},t)}{\varepsilon_0}. \tag{1.15}$$

In homogenous medium both equations (1.13) and (1.15) have a closed-form solution for:

- the magnetic vector potential $\boldsymbol{A}(\boldsymbol{r},t)$ due to a current $\boldsymbol{J}(\boldsymbol{r},t)$ in the volume V'
- the electric scalar potential $\Phi(\boldsymbol{r},t)$ due to the charge distribution $q(\boldsymbol{r}',t)$ over the surface S'.

They are

$$\boldsymbol{A}(\boldsymbol{r},t) = \frac{\mu_0}{4\pi} \int_{V'} G(\boldsymbol{r},\boldsymbol{r}')\, \boldsymbol{J}(\boldsymbol{r}',t')\, dV' \tag{1.16}$$

and

$$\Phi(\boldsymbol{r},t) = \frac{1}{4\pi\varepsilon_0} \int_{S'} G(\boldsymbol{r},\boldsymbol{r}')\, q(\boldsymbol{r}',t') dS' \tag{1.17}$$

where $G(\boldsymbol{r},\boldsymbol{r}')$ is the homogeneous Green's function

$$G(\boldsymbol{r},\boldsymbol{r}') = \frac{e^{-jk|\boldsymbol{r}-\boldsymbol{r}'|}}{|\boldsymbol{r}-\boldsymbol{r}'|} \tag{1.18}$$

being

$$k = \omega\sqrt{\varepsilon_0\mu_0}. \tag{1.19}$$

In equations (1.16) and (1.17) t' denotes the time at which the current and charge distributions, $\boldsymbol{J}$ and q, act as sources of $\boldsymbol{A}$ and Φ respectively; it is different from

t because of the finite value of the speed of light in the homogenous medium, $c = 1/\sqrt{\mu\varepsilon}$. It means that they can be related by

$$t' = t - \frac{|\boldsymbol{r} - \boldsymbol{r}'|}{c}. \tag{1.20}$$

For electrically small problems, the quasi-static approximation can be used. In such condition (1.16) and (1.17) are simplified as

$$\boldsymbol{A}(\boldsymbol{r}, t) = \frac{\mu_0}{4\pi} \int_{V'} \frac{\boldsymbol{J}(\boldsymbol{r}', t')}{|\boldsymbol{r} - \boldsymbol{r}'|} dV' \tag{1.21}$$

and

$$\Phi(\boldsymbol{r}, t) = \frac{1}{4\pi\varepsilon_0} \int_{S'} \frac{q(\boldsymbol{r}', t')}{|\boldsymbol{r} - \boldsymbol{r}'|} dS'. \tag{1.22}$$

In deriving relations (1.21) and (1.22) all the Maxwell's equations (1.1)–(1.4) have been used along with the Lorenz gauge (1.12). So far equation (1.9) for the electric field has not been used yet.

In conductors the relation between current density and electric field is expressed by the constitutive relation

$$\boldsymbol{E}(\boldsymbol{r}, t) = \frac{\boldsymbol{J}(\boldsymbol{r}, t)}{\sigma} \tag{1.23}$$

where σ is the conductor conductivity. Substituting equation (1.23) into the electric field equation (1.9) and taking into account that an external electric field $\boldsymbol{E}_0(\boldsymbol{r}, t)$ can be impressed at point $\boldsymbol{r}$ at time t, the Electric Field Integral Equation (EFIE) is obtained as

$$\boldsymbol{E}_0(\boldsymbol{r}, t) = \frac{\boldsymbol{J}(\boldsymbol{r}, t)}{\sigma} + \frac{\partial}{\partial t} \frac{\mu_0}{4\pi} \int_{V'} \frac{\boldsymbol{J}(\boldsymbol{r}', t')}{|\boldsymbol{r} - \boldsymbol{r}'|} dV' + \nabla\Phi(\boldsymbol{r}, t) \tag{1.24}$$

which holds at any point in a conductor and where the electric scalar potential is related to the charge distribution by equation (1.22). The continuity equation must be enforced in order to ensure charge conservation

$$\nabla \cdot \boldsymbol{J}(\boldsymbol{r}, t) = -\frac{\partial q(\boldsymbol{r}, t)}{\partial t}. \tag{1.25}$$

Assuming that the charge is located only on the surface of conductors, for any point $\boldsymbol{r}$ located inside the conductors equation (1.25) becomes

$$\nabla \cdot \boldsymbol{J}(\boldsymbol{r}, t) = 0 \tag{1.26}$$

while on their surfaces, using the divergence theorem, it follows that

$$\hat{\boldsymbol{n}} \cdot \boldsymbol{J}(\boldsymbol{r}, t) = \frac{\partial q(\boldsymbol{r}, t)}{\partial t} \tag{1.27}$$

where $\hat{\boldsymbol{n}}$ is the outward normal to the surface S'. If we put everything together, the set of equations to be solved is

$$\begin{aligned}
\boldsymbol{E}_0(\boldsymbol{r}, t) &= \frac{\boldsymbol{J}(\boldsymbol{r}, t)}{\sigma} + \frac{\partial}{\partial t}\frac{\mu_0}{4\pi}\int_{V'}\frac{\boldsymbol{J}(\boldsymbol{r}', t')}{|\boldsymbol{r}-\boldsymbol{r}'|}dV' + \nabla\Phi(\boldsymbol{r}, t) && (1.28)\\
\Phi(\boldsymbol{r}, t) &= \frac{1}{4\pi\varepsilon_0}\int_{S'}\frac{q(\boldsymbol{r}', t')}{|\boldsymbol{r}-\boldsymbol{r}'|}dS' \qquad \boldsymbol{r} \in S' && (1.29)\\
\nabla \cdot \boldsymbol{J}(\boldsymbol{r}, t) &= 0 \qquad \boldsymbol{r} \in V' && (1.30)\\
\hat{\boldsymbol{n}} \cdot \boldsymbol{J}(\boldsymbol{r}, t) &= \frac{\partial q(\boldsymbol{r}, t)}{\partial t} \qquad \boldsymbol{r} \in S'. && (1.31)
\end{aligned}$$

The unknowns of this problem are represented by the current density $\boldsymbol{J}(\boldsymbol{r}, t)$, the charge density $q(\boldsymbol{r}, t)$ on the surface of the conductors and the electric scalar potential distribution $\Phi(\boldsymbol{r}, t)$ of conductors which can be directly expressed as a function of the charge density for $\boldsymbol{r} \in S'$.
In the Laplace domain equations (1.28)–(1.31) can be rewritten, including the propagation, as:

$$\begin{aligned}
\boldsymbol{E}_0(\boldsymbol{r}, s) &= \frac{\boldsymbol{J}(\boldsymbol{r}, s)}{\sigma} + \frac{s\mu_0}{4\pi}\int_{V'}\frac{\boldsymbol{J}(\boldsymbol{r}', s)\, e^{-s\tau}}{|\boldsymbol{r}-\boldsymbol{r}'|}dV' + \nabla\Phi(\boldsymbol{r}, s) && (1.32)\\
\Phi(\boldsymbol{r}, s) &= \frac{1}{4\pi\varepsilon_0}\int_{S'}\frac{q(\boldsymbol{r}', s)\, e^{-s\tau}}{|\boldsymbol{r}-\boldsymbol{r}'|}dS' \qquad \boldsymbol{r} \in S' && (1.33)\\
\nabla \cdot \boldsymbol{J}(\boldsymbol{r}, s) &= 0 \qquad \boldsymbol{r} \in V' && (1.34)\\
\hat{\boldsymbol{n}} \cdot \boldsymbol{J}(\boldsymbol{r}, s) &= sq(\boldsymbol{r}, s) \qquad \boldsymbol{r} \in S' && (1.35)
\end{aligned}$$

where $\tau = |\boldsymbol{r}-\boldsymbol{r}'|/c$ and s is the Laplace variable.

The most popular method for the discretization of integral equations was called by Harrington the *Method of Moments* (MoM) [14], such method has been used in many different implementation [25–29]. Usually the solution is found in the frequency domain, assuming $s = j\omega$. As a first step the unknown quantities $\boldsymbol{J}(\boldsymbol{r}, s)$ and $\boldsymbol{q}(\boldsymbol{r}, s)$ are approximated by a weighted sum of finite set of basis functions

$\boldsymbol{b} \in \mathbb{R}^3$ and $p \in \mathbb{R}$

$$\boldsymbol{J}(\boldsymbol{r}, s) \cong \sum_{n=1}^{N_v} \boldsymbol{b}_n(\boldsymbol{r}) I_n(s) \tag{1.36}$$

$$q(\boldsymbol{r}, s) \cong \sum_{m=1}^{N_s} p_m(\boldsymbol{r}) Q_m(s) \tag{1.37}$$

where $I_n(s)$ and $Q_m(s)$ are the basis function weights which must be determined at each angular frequency s, N_v and N_s represent the number of volume and surface basis functions and the corresponding elementary volume and surface sub-regions, respectively. Expansion (1.36)–(1.37) are substituted into (1.32)–(1.33), evaluated for $s = j\omega$, yielding

$$\begin{aligned} \boldsymbol{E}_0(\boldsymbol{r}, s) &= \sum_{n=1}^{N_v} \frac{\boldsymbol{b}_n(\boldsymbol{r}) I_n(s)}{\sigma} + \frac{s\mu_0}{4\pi} \sum_{n=1}^{N_v} \int_{V_n} \boldsymbol{b}_n(\boldsymbol{r}_n) I_n(s) \frac{e^{-s\tau}}{|\boldsymbol{r} - \boldsymbol{r}_n|} dV_n + \\ &\quad + \nabla\Phi(\boldsymbol{r}, s) \end{aligned} \tag{1.38}$$

$$\Phi(\boldsymbol{r}, s) = \frac{1}{4\pi\varepsilon_0} \sum_{m=1}^{N_s} \int_{S_m} p_m(\boldsymbol{r}_m) Q_m(s) \frac{e^{-s\tau}}{|\boldsymbol{r} - \boldsymbol{r}_m|} dS_m. \tag{1.39}$$

Next, the Galërkin's testing or weighting process [28] is used to generate a system of equations for the unknowns weights $I_n(s), n = 1, \ldots, N_v$ and $Q_m(s), m = 1, \ldots, N_s$ by enforcing the residuals of equations (1.32)–(1.33) to be orthogonal to a set of weighting functions which are chosen to be coincident with the basis functions

$$\begin{aligned} \Bigg\langle & -\boldsymbol{E}_0(\boldsymbol{r}, s) + \frac{\sum_{n=1}^{N_v} \boldsymbol{b}_n(\boldsymbol{r}) I_n(s)}{\sigma} + \\ & + \frac{s\mu_0}{4\pi} \left(\sum_{n=1}^{N_v} \int_{V_n} \boldsymbol{b}_n(\boldsymbol{r}_n) I_n(s) \frac{e^{-s\tau}}{|\boldsymbol{r} - \boldsymbol{r}_n|} \right) dV_n + \nabla\Phi(\boldsymbol{r}, s), \boldsymbol{b}_i(\boldsymbol{r}) \Bigg\rangle = 0 \end{aligned} \tag{1.40}$$

$$\left\langle \Phi(\boldsymbol{r}, s) - \frac{1}{4\pi\varepsilon_0} \sum_{m=1}^{N_s} \int_{S_m} p_m(\boldsymbol{r}_m) Q_m(s) \frac{e^{-s\tau}}{|\boldsymbol{r} - \boldsymbol{r}_m|} dS_m, p_j(\boldsymbol{r}) \right\rangle = 0 \tag{1.41}$$

where the inner products are defined as

$$\langle \boldsymbol{f}(\boldsymbol{r}), \boldsymbol{b}_i(\boldsymbol{r}) \rangle = \int_{V_i} \boldsymbol{f}(\boldsymbol{r}) \cdot \boldsymbol{b}_i(\boldsymbol{r}) dV_i \qquad \text{for } i = 1, \ldots, N_v \tag{1.42}$$

$$\langle g(\boldsymbol{r}), p_j(\boldsymbol{r}) \rangle = \int_{S_j} g(\boldsymbol{r}) \cdot p_j(\boldsymbol{r}) dS_j \qquad \text{for } j = 1, \ldots, N_s. \tag{1.43}$$

1.1.1 Basis and weighting functions for conductor surfaces

A number of different typologies of basis and weighting functions can be chosen to set equations (1.40) and (1.41). The most popular are the piecewise constant, piecewise linear, RWG [26] set of basis and/or weighting functions. In the following it will be assumed the piecewise constant set of functions which are more suited to model Manhattan type structures. Thus, by assuming to deal with orthogonal conductors whose surface is discretized into N_s elementary rectangular patches which are electrically small compared with the wavelength of the highest frequency of interest. More specifically, the unknown electrical current and charge densities are taken to have constant values over each cell in the discrete model.
Under these assumption the basis functions used to expand the charge density are chosen as

$$p_m(\boldsymbol{r}) = \begin{cases} \frac{1}{S_m} & \text{if } \boldsymbol{r} \in S_m \\ 0 & \text{otherwise.} \end{cases} \tag{1.44}$$

With the basis function in (1.44) the corresponding weight Q_m represents the charge on patch m. Finally, equation (1.39) can be rewritten as

$$\Phi(\boldsymbol{r}, s) = \sum_{m=1}^{N_s} \left[\frac{1}{4\pi\varepsilon_0} \frac{1}{S_m} \int_{S_m} \frac{e^{-s\tau}}{|\boldsymbol{r} - \boldsymbol{r}_m|} dS_m \right] Q_m(s) \tag{1.45}$$

which allows to evaluate the potential at point $\boldsymbol{r}$, at frequency s, due to the charge on the N_s patches covering the conductors. In a way equation (1.45) models the electric field coupling in the background medium with permittivity ε_0.

The Galërkin procedure results in the evaluation of the average value of scalar potential $\Phi(\boldsymbol{r}, s)$ over the surface of each patch. The potential term is

$$\langle \Phi(\boldsymbol{r}, s), p_\ell(\boldsymbol{r}) \rangle = \frac{1}{S_\ell} \int_{S_\ell} \Phi(\boldsymbol{r}_\ell, s)\, dS_\ell = \Phi_\ell \quad \text{for } \ell = 1, \ldots, N_s \tag{1.46}$$

being Φ_ℓ the potential of the surface ℓ, that of course is assumed constant over all the surface. The charge term, instead, becomes

$$\begin{aligned} &\left\langle \sum_{m=1}^{N_s} \left[\frac{Q_m(s)}{4\pi\varepsilon_0 S_m} \int_{S_m} \frac{e^{-s\tau}}{|\boldsymbol{r} - \boldsymbol{r}_m|} dS_m \right], p_\ell(\boldsymbol{r}) \right\rangle = \\ &\qquad = \sum_{m=1}^{N_s} \frac{Q_m(s)}{4\pi\varepsilon_0 S_m S_\ell} \int_{S_\ell} \int_{S_m} \frac{e^{-s\tau}}{|\boldsymbol{r} - \boldsymbol{r}_m|} dS_m dS_\ell \quad \text{for } \ell = 1, \ldots, N_s. \end{aligned} \tag{1.47}$$

Hence, equation (1.45) becomes

$$\Phi_\ell = \sum_{m=1}^{N_s} \left[P_{\ell,m}(s)\, Q_m(s) \right] \qquad \text{for } \ell = 1, \ldots, N_s \tag{1.48}$$

where the coefficient of potential $P_{\ell,m}(s)$, defined in (1.48), is

$$P_{\ell,m}(s) = \frac{1}{4\pi\varepsilon_0 S_\ell S_m} \int_{S_\ell} \int_{S_m} \frac{e^{-s\tau}}{|\boldsymbol{r}_\ell - \boldsymbol{r}_m|} dS_m dS_\ell. \tag{1.49}$$

Hence, the relation between the scalar potential, $\mathbf{\Phi}(s) \in \mathbb{C}^{N_s}$, of the N_s patches and the charges, $Q(s) \in \mathbb{C}^{N_s}$, located on the same patches set is

$$\mathbf{\Phi}(s) = \mathbf{P}(s)\, \mathbf{Q}(s) \tag{1.50}$$

where matrix $\mathbf{P}$ entries are the coefficients of potential in (1.49) and are, in general, frequency dependent. In quasi static regime, since $e^{-s\tau} \to 1$, the frequency dependence can be suppressed and they can be expressed as

$$P_{\ell,m} = \frac{1}{4\pi\varepsilon_0} \frac{1}{S_\ell S_m} \int_{S_\ell} \int_{S_m} \frac{1}{|\boldsymbol{r}_\ell - \boldsymbol{r}_m|} dS_m dS_\ell. \tag{1.51}$$

The displacement currents in the background medium, $\mathbf{I}_c$, can be computed as

$$\mathbf{I}_c(s) = s\mathbf{Q}(s) = s\mathbf{P}(s)^{-1}\, \mathbf{\Phi}(s). \tag{1.52}$$

1.1.2 Basis and weighting functions for conductor volumes

Conductor volumes are discretized into N_v elementary orthogonal hexahedra (parallelepipeds) being, as before, electrically small compared with the wavelength of the highest frequency of interest. Let ℓ_n and a_n the length and the cross section of volume V_n, respectively.

The basis functions used to expand the current density are chosen as

$$\boldsymbol{b}_n(\boldsymbol{r}) = \begin{cases} \frac{\hat{\boldsymbol{u}}_n}{a_n} & \text{if } \boldsymbol{r} \in V_n \\ \mathbf{0} & \text{otherwise} \end{cases} \tag{1.53}$$

where $\hat{\boldsymbol{u}}_n$ is the unit vector indicating the current orientation in volume V_n. With such a choice of the basis function the corresponding weight represents the current

flowing in the volume V_n with orientation $\hat{\boldsymbol{u}}_n$. When the Galërkin scheme is applied, the terms in equation (1.38) rewrite as

$$\begin{aligned}\left\langle \boldsymbol{E}_0\left(\boldsymbol{r},s\right),\boldsymbol{b}_i\left(\boldsymbol{r}\right)\right\rangle &= \frac{1}{a_i}\int_{a_i}\int_{\ell_i}\boldsymbol{E}_0\left(\boldsymbol{r}_i,s\right)\cdot\hat{\boldsymbol{u}}_i\;d\ell_i\;da_i \\ &= \int_{\ell_i}E_0\left(\boldsymbol{r}_i,s\right)d\ell_i \\ &= \ell_i E_0\left(\boldsymbol{r}_i,s\right) \qquad \text{for } i=1,\ldots,N_v\end{aligned} \tag{1.54}$$

where $E_0\left(\boldsymbol{r}_i,s\right)=\boldsymbol{E}_0\left(\boldsymbol{r}_i,s\right)\cdot\hat{\boldsymbol{u}}_i$ is the component of $\boldsymbol{E}_0\left(\boldsymbol{r}_i,s\right)$ directed as $\hat{\boldsymbol{u}}_i$. It can be noticed that in 1.54 the component of the extern electric field has been assumed constant in the section of the volume. The conductivity term result in

$$\begin{aligned}\left\langle\frac{\sum_{n=1}^{N_v}\boldsymbol{b}_n\left(\boldsymbol{r}\right)I_n\left(s\right)}{\sigma},\boldsymbol{b}_i\left(\boldsymbol{r}\right)\right\rangle &= \sum_{n=1}^{N_v}\frac{I_n\left(s\right)}{\sigma}\int_{a_i}\int_{\ell_i}\boldsymbol{b}_n\left(\boldsymbol{r}\right)\cdot\boldsymbol{b}_i\left(\boldsymbol{r}\right)\;d\ell_i\;da_i \\ &= \frac{I_n\left(s\right)}{\sigma}\int_{a_i}\int_{\ell_i}\frac{1}{a_i^2}d\ell_i\;da_i \\ &= \frac{I_n\left(s\right)}{\sigma}\frac{\ell_i}{a_i} \qquad \text{for } i=1,\ldots,N_v\end{aligned} \tag{1.55}$$

since by definition

$$\boldsymbol{b}_n\left(\boldsymbol{r}\right)\cdot\boldsymbol{b}_i\left(\boldsymbol{r}\right)=\begin{cases}\frac{1}{a_n^2} & \text{if } i=n \\ \boldsymbol{0} & \text{otherwise.}\end{cases} \tag{1.56}$$

The Green's function term

$$\begin{aligned}&\left\langle\frac{s\mu_0}{4\pi}\left(\sum_{n=1}^{N_v}\int_{V_n}\boldsymbol{b}_n\left(\boldsymbol{r}_n\right)I_n\left(s\right)\frac{e^{-s\tau}}{\left|\boldsymbol{r}-\boldsymbol{r}_n\right|}\right)dV_n,\boldsymbol{b}_i\left(\boldsymbol{r}\right)\right\rangle = \\ &\qquad= \frac{s\mu_0}{4\pi}\sum_{n=1}^{N_v}\int_V\int_{V_n}I_n\left(s\right)\frac{e^{-s\tau}}{\left|\boldsymbol{r}-\boldsymbol{r}_n\right|}\boldsymbol{b}_n\left(\boldsymbol{r}_n\right)\cdot\boldsymbol{b}_i\left(\boldsymbol{r}\right)dV_n\;dV \\ &\qquad= \frac{s\mu_0}{4\pi}\sum_{n=1}^{N_v}\frac{I_n\left(s\right)}{a_i a_n}\int_{V_i}\int_{V_n}\frac{e^{-s\tau}}{\left|\boldsymbol{r}_i-\boldsymbol{r}_n\right|}\hat{\boldsymbol{u}}_n\cdot\hat{\boldsymbol{u}}_i\;dV_n\;dV_i \\ &\qquad\qquad\qquad\qquad\qquad\qquad\qquad\qquad\qquad\qquad\qquad\qquad \text{for } i=1,\ldots,N_v\end{aligned} \tag{1.57}$$

and finally

$$\begin{aligned}\left\langle \nabla\Phi\left(\boldsymbol{r},s\right),\boldsymbol{b}_i\left(\boldsymbol{r}\right)\right\rangle &= \frac{1}{a_i}\int_{a_i}\int_{\ell_i}\nabla\Phi\left(\boldsymbol{r},s\right)\cdot\hat{\boldsymbol{u}}_i d\ell_i\, da_i \\ &= \int_{\ell_i}\frac{\partial\Phi\left(\boldsymbol{r}_i,s\right)}{d\ell_i}d\ell_i \\ &= \Phi_{i_2}\left(s\right)-\Phi_{i_1}\left(s\right) \qquad \text{for } i=1,\ldots,N_v\end{aligned} \tag{1.58}$$

where $\Phi_{i_1}\left(s\right)$ and $\Phi_{i_2}\left(s\right)$ represent the potential at the extremes of the volume V_i along the $\hat{\boldsymbol{u}}_i$ direction. Hence equation (1.38) becomes

$$\begin{aligned}E_0\left(\boldsymbol{r}_i,s\right)\ell_i &= \frac{\ell_i I_i\left(s\right)}{\sigma a_i}+\frac{s\mu_0}{4\pi}\sum_{n=1}^{N_v}\frac{1}{a_i}\frac{1}{a_n}\int_{V_i}\int_{V_n}I_n\left(s\right)\frac{e^{-s\tau}}{\left|\boldsymbol{r}_i-\boldsymbol{r}_n\right|}\hat{\boldsymbol{u}}_i\cdot\hat{\boldsymbol{u}}_n dV_n dV_i + \\ &+ \Phi_{2i}\left(s\right)-\Phi_{1i}\left(s\right) \qquad \text{for } i=1,\ldots,N_v.\end{aligned} \tag{1.59}$$

Each term of equation (1.59) represents a voltage drop across volume V_i along the $\hat{\boldsymbol{u}}_i$ direction and, thus, it can be rewritten as

$$\Phi_{i_1}\left(s\right)-\Phi_{i_2}\left(s\right) = V_{0_i}\left(s\right)+R_i I_i+s\sum_{n=1}^{N_v}L_{p_{i,n}}I_n\left(s\right) \tag{1.60}$$

where the following definitions have been made

$$V_{0_i}\left(s\right) = -E_0\left(\boldsymbol{r}_i,s\right)\ell_i \tag{1.61}$$

$$R_i = \frac{\ell_i}{\sigma a_i} \tag{1.62}$$

$$L_{p_{i,n}}\left(s\right) = \frac{\mu_0}{4\pi}\frac{1}{a_i a_n}\int_{V_i}\int_{V_n}\frac{e^{-s\tau}}{\left|\boldsymbol{r}_i-\boldsymbol{r}_n\right|}\hat{\boldsymbol{u}}_i\cdot\hat{\boldsymbol{u}}_n dV_n dV_i. \tag{1.63}$$

V_{0_i} represents the voltage source due to external fields, R_i is the resistance of the $i-$th cell, where current flows along in the direction identified by ℓ_i, and $L_{p_{i,n}}$ is the partial inductance [1] between the $i-$th and the $n-$th volume cells .
The set of equation like (1.60), that are generated after the Galërkin procedure, can be expressed in matrix form as

$$-\mathbf{A}\boldsymbol{\Phi}\left(s\right)-\mathbf{R}\mathbf{I}\left(s\right)-s\mathbf{L}_p\left(s\right)\mathbf{I}\left(s\right)-\mathbf{V}_0\left(s\right)=\mathbf{0} \tag{1.64}$$

where $\boldsymbol{\Phi}\in\mathbb{C}^N$ is the set of potentials to infinity and $\mathbf{I}\in\mathbb{C}^{N_v}$ are all the currents flowing through the longitudinal branches. It is worth noticing that $N\geq N_s$, this

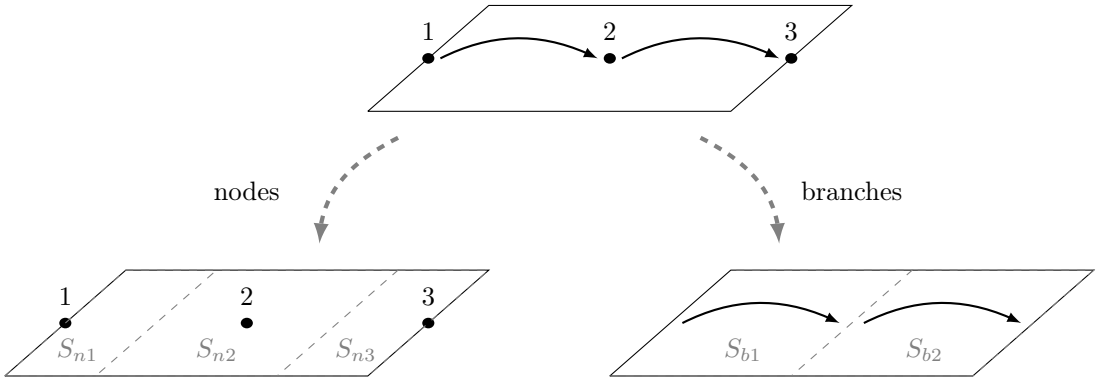

Figure 1.1: Strip of conductor and its discretization with 3 nodes and 2 branches and associated surfaces.

happens because in the most general case of 3D structures, nodes interior to the conductors may occur. **A** is the connectivity matrix whose entries are

$$a_{n,k} = \begin{cases} +1 & \text{if current } I_n \text{ enters node } k \\ -1 & \text{if current } I_n \text{ leaves node } k \\ 0 & \text{otherwise.} \end{cases} \tag{1.65}$$

The discretization process described above has allowed to achieve topological circuit elements such as branches and nodes. **A** is the matrix describing such graph.

Once the elements in (1.64) are known, the generation of the equivalent circuit is straightforward.

1.2 Equivalent Circuit Models from EM structures

In previous section we saw as circuit-like equation can be used to achieved from Maxwell equation to describe an electromagnetic problem. For sake of clarity we will apply the procedure in simplified conditions. Let us consider a strip of conductor, and let us assume that we are discretizing such strip along one direction as shown in Fig. 1.1. Such process yields a graph with three nodes, 1,2 and 3, and two branches, connecting them. The corresponding unknowns are the potential to infinity of the nodes, Φ_1,Φ_2 and Φ_3, and the currents I_1 and I_2 flowing through the branches. For each node there is a surface cell, S_{ni}, in which the potential is assumed to be

constant. For each branch there is a surface cell, S_{bi}, where the current is assumed to be constant. After the discretization process it is possible to define the matrix A by (1.65) leading, for the example in Fig. 1.1, to

$$\mathbf{A} = \begin{bmatrix} -1 & 1 & 0 \\ 0 & -1 & 1 \end{bmatrix}. \tag{1.66}$$

1.2.1 Model for electric field coupling

The electric field coupling is derived from equation (1.50) which in this example writes as

$$\Phi_1 = P_{1,1}Q_1 + P_{1,2}Q_2 + P_{1,3}Q_3 \tag{1.67}$$

$$\Phi_2 = P_{2,1}Q_1 + P_{2,2}Q_2 + P_{2,3}Q_3 \tag{1.68}$$

$$\Phi_3 = P_{3,1}Q_1 + P_{3,2}Q_2 + P_{3,3}Q_3 \tag{1.69}$$

where Q_i is the charge on the surface S_{ni} for $i = 1, 2, 3$ and $P_{i,j}$ is the coefficient of potential computed by (1.49). I we divide each of the (1.67)–(1.69) for the self coefficient $P_{i,i}$ we have

$$\frac{\Phi_1}{P_{1,1}} = Q_1 + \frac{P_{1,2}}{P_{1,1}}Q_2 + \frac{P_{1,3}}{P_{1,1}}Q_3 \tag{1.70}$$

$$\frac{\Phi_2}{P_{2,2}} = \frac{P_{2,1}}{P_{2,2}}Q_1 + Q_2 + \frac{P_{2,3}}{P_{2,2}}Q_3 \tag{1.71}$$

$$\frac{\Phi_3}{P_{3,3}} = \frac{P_{3,1}}{P_{3,3}}Q_1 + \frac{P_{3,2}}{P_{3,3}}Q_2 + Q_3 \tag{1.72}$$

now we can derive the total currents (towards the infinity node) from the charges as

$$I_{t_k} = sQ_k \qquad \text{for } k = 1, \ldots, 3 \tag{1.73}$$

if we move the currents to the left hand side we get

$$I_{t_1} = s\frac{\Phi_1}{P_{1,1}} - s\frac{P_{1,2}}{P_{1,1}}Q_2 - s\frac{P_{1,3}}{P_{1,1}}Q_3 \tag{1.74}$$

$$I_{t_2} = s\frac{\Phi_2}{P_{2,2}} - s\frac{P_{2,1}}{P_{2,2}}Q_1 - s\frac{P_{2,3}}{P_{2,2}}Q_3 \tag{1.75}$$

$$I_{t_3} = s\frac{\Phi_3}{P_{3,3}} - s\frac{P_{3,1}}{P_{3,3}}Q_1 - s\frac{P_{3,2}}{P_{3,3}}Q_2. \tag{1.76}$$

Last equations allow the identification of two contributions: the self terms, which can be modeled as currents flowing in capacitors with values

$$C_1 = \frac{1}{P_{1,1}} \tag{1.77}$$

$$C_2 = \frac{1}{P_{2,2}} \tag{1.78}$$

$$C_3 = \frac{1}{P_{3,3}} \tag{1.79}$$

and the mutual coupling, that can be modeled by current controlled current sources (CCCSs) as

$$I_{f_1} = s\frac{P_{1,2}}{P_{1,1}}Q_2 + s\frac{P_{1,3}}{P_{1,1}}Q_3 \tag{1.80}$$

$$I_{f_2} = s\frac{P_{2,1}}{P_{2,2}}Q_1 + s\frac{P_{2,3}}{P_{2,2}}Q_3 \tag{1.81}$$

$$I_{f_3} = s\frac{P_{3,1}}{P_{3,3}}Q_1 + s\frac{P_{3,2}}{P_{3,3}}Q_2. \tag{1.82}$$

With the last definitions (1.74)–(1.76) can be rewritten as

$$I_{t_1} = sC_1\Phi_1 - I_{f_1} \tag{1.83}$$

$$I_{t_2} = sC_2\Phi_2 - I_{f_2} \tag{1.84}$$

$$I_{t_3} = sC_3\Phi_3 - I_{f_3}. \tag{1.85}$$

It can be seen that the three KCL (1.83)–(1.85) lead to the circuit in Fig. 1.2 where the ground is the infinity node.

When the graph has more than three nodes, the $k-$th CCCS can be defined as

$$I_{f_k} = \sum_{\substack{m=1 \\ m\neq k}}^{N_s} \frac{P_{k,m}}{P_{k,k}} sQ_m = \sum_{\substack{m=1 \\ m\neq k}}^{N_s} \frac{P_{k,m}}{P_{k,k}} I_{t_m}. \tag{1.86}$$

The relation between mutual coupling currents, $\mathbf{I}_f$, and total currents, $\mathbf{I}_t$, can be expressed in matrix form as

$$\mathbf{I}_f = \mathbf{K}\mathbf{I}_t \tag{1.87}$$

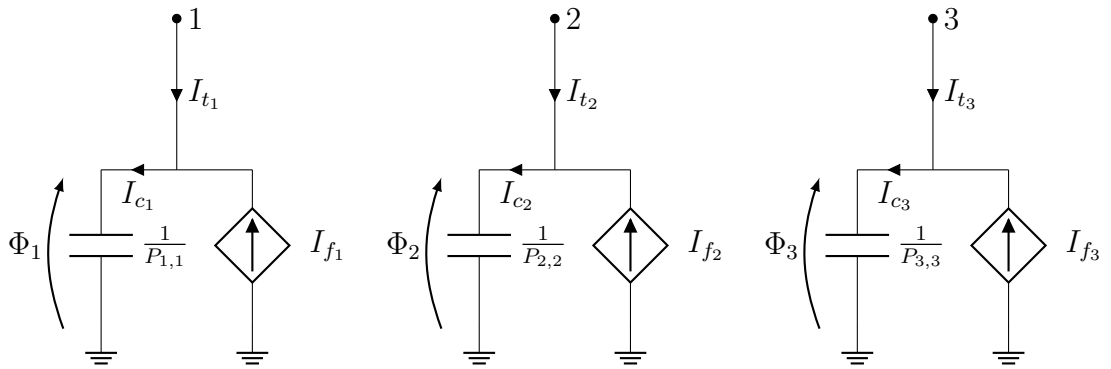

Figure 1.2: Equivalent circuit model for electric field coupling.

where

$$\mathbf{K} = \begin{bmatrix} 0 & \frac{P_{1,2}}{P_{1,1}} & \cdots & \frac{P_{1,N_s}}{P_{1,1}} \\ \frac{P_{2,1}}{P_{2,2}} & 0 & \cdots & \frac{P_{2,N_s}}{P_{2,2}} \\ \vdots & \vdots & \ddots & \vdots \\ \frac{P_{N_s,1}}{P_{N_s,N_s}} & \frac{P_{N_s,2}}{P_{N_s,N_s}} & \cdots & 0 \end{bmatrix}. \tag{1.88}$$

In the same way we can express the relation between the potentials $\mathbf{\Phi}$ and the self induced effects $\mathbf{I}_c$ as

$$\mathbf{I}_c = s\mathbf{\Lambda}\mathbf{\Phi} \tag{1.89}$$

where

$$\mathbf{\Lambda} = \begin{bmatrix} \frac{1}{P_{1,1}} & 0 & \cdots & 0 \\ 0 & \frac{1}{P_{2,2}} & \cdots & 0 \\ \vdots & \vdots & \vdots & \vdots \\ 0 & 0 & \cdots & \frac{1}{P_{N_s,N_s}} \end{bmatrix}. \tag{1.90}$$

1.2.2 Model for magnetic field coupling

The circuit model for the magnetic field coupling is obtained working on the branches of Fig. 1.1. It is derived form equation (1.59) and after the Galërkin procedure is expressed in matrix form from (1.64). For the considered example it writes as

$$\Phi_1 - \Phi_2 = R_1 + sL_{p_{1,1}}I_1 + sL_{p_{1,2}}I_2 + V_{0_1} \tag{1.91}$$

$$\Phi_2 - \Phi_3 = R_2 + sL_{p_{2,2}}I_2 + sL_{p_{2,1}}I_1 + V_{0_2}. \tag{1.92}$$

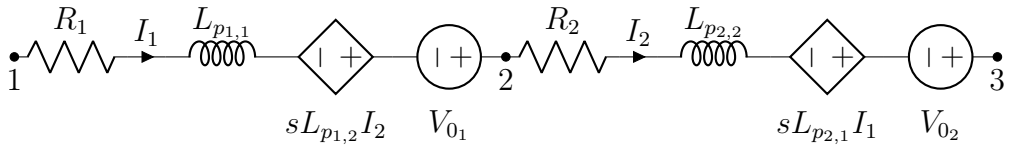

Figure 1.3: Equivalent circuit model for magnetic field coupling.

where $L_{p_{2,1}} = L_{p_{1,2}}$. It can be noticed that the two KVL (1.91)–(1.92) describe the circuit in Fig. 1.3.

1.2.3 PEEC equivalent circuit

At this stage the equivalent circuits for the electric and magnetic field coupling have been drawn, the next process is to connect the equivalent circuits shown in Figs. 1.2 and 1.3. This is accomplished connecting the three pieces in Fig. 1.2 to the three nodes 1,2 and 3 in Fig. 1.3. When the connection is performed the circuit in Fig. 1.4 is achieved.

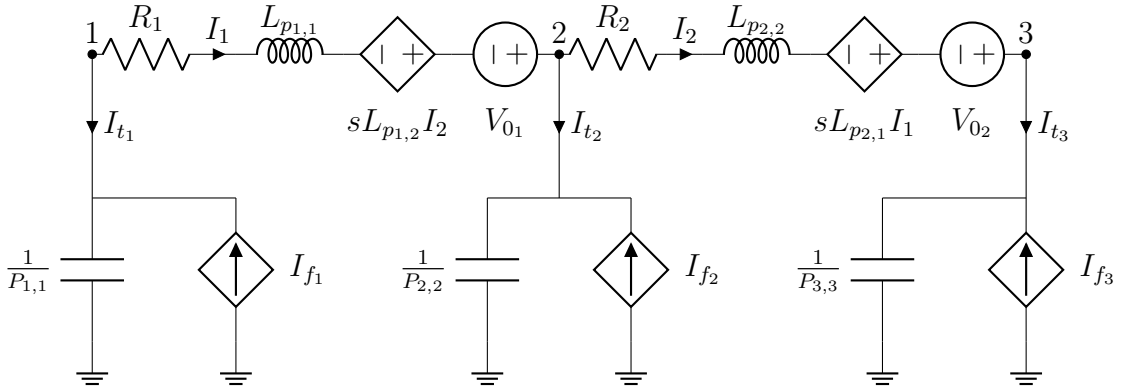

Figure 1.4: Equivalent circuit model for the simple example in Fig. 1.1.

1.2.4 Kirchhoff's current and voltage laws in the equivalent circuit

Once the equivalent circuit is generated, Kirchhoff's current and voltage laws can be enforced. As stated above the first set of equation comes from the KVL (1.64)

applied to a mesh constituted by the resistive-inductive branch connecting each couple of nodes and the capacitive branch connecting each node to infinity. For practical reason, equation (1.64) is repeated here

$$-\mathbf{A}\mathbf{\Phi}\left(s\right)-\mathbf{R}\mathbf{I}\left(s\right)-s\mathbf{L}_{p}\left(s\right)\mathbf{I}\left(s\right)-\mathbf{V}_{0}\left(s\right)=\mathbf{0}. \tag{1.93}$$

The Kirchhoff's current law (KCL) is enforced as a continuity equation. If we name the set of branches currents $\mathbf{I}$ and that external current sources set $\mathbf{I}_s$, the KCL can be written as

$$\mathbf{I}_{t}\left(s\right)-\mathbf{A}^{T}\mathbf{I}\left(s\right)=\mathbf{I}_{s}\left(s\right) \tag{1.94}$$

where $\mathbf{I}_t$ is the set of currents defined in (1.73) and $\mathbf{A}^T$ denotes the transpose matrix $\mathbf{A}$. Considering that the displacement currents $\mathbf{I}_t$ can be expressed as a function of the potentials $\mathbf{\Phi}$ as

$$\mathbf{\Phi}=\mathbf{P}\mathbf{Q}\quad\Rightarrow\quad\mathbf{I}_{t}=s\mathbf{Q}=\mathbf{P}^{-1}\mathbf{\Phi} \tag{1.95}$$

it is possible to write

$$s\mathbf{P}\left(s\right)^{-1}\mathbf{\Phi}\left(s\right)+\mathbf{Y}_{le}\mathbf{\Phi}\left(s\right)-\mathbf{A}^{T}\mathbf{I}\left(s\right)=\mathbf{I}_{s}\left(s\right) \tag{1.96}$$

where $\mathbf{Y}_{le}$ is the admittance matrix used to include lumped elements which might eventually connect nodes (*i.e.* port admittances).

From the implementation point of view it may be desirable to avoid the matrix inversion $\mathbf{P}\left(s\right)^{-1}$ because of its complexity ($O(n^3)$). A possible solution is achieved by premultiplying (1.96) with $\mathbf{P}\left(s\right)$, allowing to re-write the previous equation as

$$s\mathbf{\Phi}\left(s\right)+\mathbf{P}\mathbf{Y}_{le}\mathbf{\Phi}\left(s\right)-\mathbf{P}\left(s\right)\mathbf{A}^{T}\mathbf{I}\left(s\right)=\mathbf{P}\left(s\right)\mathbf{I}_{s}\left(s\right). \tag{1.97}$$

1.3 The partial elements

In section 1.2 we saw as the equivalent circuit can be built, by Galërkin procedure, from the Maxwell equations (1.1)–(1.4). In this section we show how the values of the partial elements (partial inductance, coefficients of potential and resistances), which constitute the equivalent circuit, can be computed.

1.3.1 Partial inductances

In the most general condition, the evaluation of partial inductance between two cells i and j requires the computation of double folded volume integral

$$L_{p_{i,j}}(s) = \frac{\mu_0}{4\pi a_i a_j} \int_{V_i} \int_{V_j} \frac{e^{-s\tau}}{|\boldsymbol{r}_i - \boldsymbol{r}_j|} \hat{\boldsymbol{u}}_i \cdot \hat{\boldsymbol{u}}_j \, dV_j dV_i. \tag{1.98}$$

The integral in (1.98) can be computed by numerical integration techniques, but the time needed for performing accurately such integration makes this road impractical sometimes. In many conditions, good results can be achieved assuming electrically small objects, since the geometrical sizes are much smaller than the wavelength. In such condition the exponential $e^{-s\tau} \to 1$ and the quasi-static approximation can be used

$$L_{p_{i,j}}(s) \approx L^{(qs)}_{p_{i,j}} = \frac{\mu_0}{4\pi a_i a_j} \int_{V_i} \int_{V_j} \frac{1}{|\boldsymbol{r}_i - \boldsymbol{r}_j|} \hat{\boldsymbol{u}}_i \cdot \hat{\boldsymbol{u}}_j \, dV_j dV_i \tag{1.99}$$

The analytical solutions of (1.99) for orthogonal geometries are available.

If the discretization matches the $\lambda_{min}/20$ rule: $max(dim) < \lambda_{min}/20$, being max(dim) the maximum dimension of cells and λ_{min} the minimum wavelength of interest, a center to center approximation can be assumed and the partial inductance can be computed as:

$$L_{p_{i,j}}(s) \approx \frac{\mu_0 e^{-s\tau^{cc}_{i,j}}}{4\pi a_i a_j} \int_{V_i} \int_{V_j} \frac{1}{|\boldsymbol{r}_i - \boldsymbol{r}_j|} \hat{\boldsymbol{u}}_i \cdot \hat{\boldsymbol{u}}_j \, dV_j dV_i = L^{(qs)}_{p_{i,j}} e^{-s\tau^{cc}_{i,j}} \tag{1.100}$$

where $\tau^{cc}_{i,j}$ is the center to center time delay between volume cells i and j. Such approximation is accurate for sufficiently far apart domains, while it is poor for near and adjacent domains.

It has been recently considered in [30] the evaluation of partial elements, for rectangular coordinates, using special Taylor series expansions of Green's function. The results exhibit superior accuracy and speed compared to the conventional numerical integration. To simplify the notation, we use

$$R = |\mathbf{r}_i - \mathbf{r}_j| = \sqrt{(x_i - x_j)^2 + (y_i - y_j)^2 + (z_i - z_j)^2} \tag{1.101}$$

This leads to the simpler notation of the partial inductance as:

$$L_{p_{i,j}}(s) = \frac{\mu_0}{4\pi a_i a_j} \int_{V_i} \int_{V_j} \frac{e^{-s\tau}}{R} \hat{\boldsymbol{u}}_i \cdot \hat{\boldsymbol{u}}_j dV_j \; dV_i. \tag{1.102}$$

The Taylor series of the exponential term around zero is

$$e^{-s\tau} = \sum_{l=0}^{\infty} \frac{(-\frac{s}{c})^l}{l!} R^l \approx 1 - \frac{s}{c}R + \frac{s^2}{2c^2}R^2 - \frac{s^3}{6c^3}R^3 + \dots. \tag{1.103}$$

This leads to the expanded version of (1.102) to be

$$\overline{L}p_{i,j}(s) = \frac{\mu_0}{4\pi a_i a_j} \sum_{l=0}^{N} \left[\frac{(-\frac{s}{c})^l}{l!} \int_{V_i} \int_{V_j} R^{l-1} \hat{\boldsymbol{u}}_i \cdot \hat{\boldsymbol{u}}_j dV_j \; dV_i \right] \tag{1.104}$$

Assuming a $\lambda/30$ mesh, a preliminary analysis of the Taylor's based expansions described in this section compared to the numerical computation of the full wave partial elements, has proven that the relative error remains smaller than 10^{-3} when at least four coefficients are considered in the expansion. Hence, in the following only four terms will be considered and partial inductance (1.104) reads

$$L_{p_{i,j}}(s) \approx Lp_{i,j}^{(qs)} \; + \; Lp_{i,j}^{(1)}(s) \; + \; Lp_{i,j}^{(2)}(s) \; + \; Lp_{i,j}^{(3)}(s) \tag{1.105}$$

where the first term

$$Lp_{i,j}^{(qs)} = \frac{\mu_0}{4\pi a_i a_j} \int_{V_i} \int_{V_j} \frac{1}{R} \hat{\boldsymbol{u}}_i \cdot \hat{\boldsymbol{u}}_j dV_j \; dV_i \tag{1.106}$$

is the conventional quasi-static partial inductance, and the remaining three terms are

$$Lp_{i,j}^{(1)}(s) = -\frac{s}{c} \frac{\mu_0}{4\pi a_i a_j} \int_{V_i} \int_{V_j} \hat{\boldsymbol{u}}_i \cdot \hat{\boldsymbol{u}}_j dV_j \; dV_i, \tag{1.107}$$

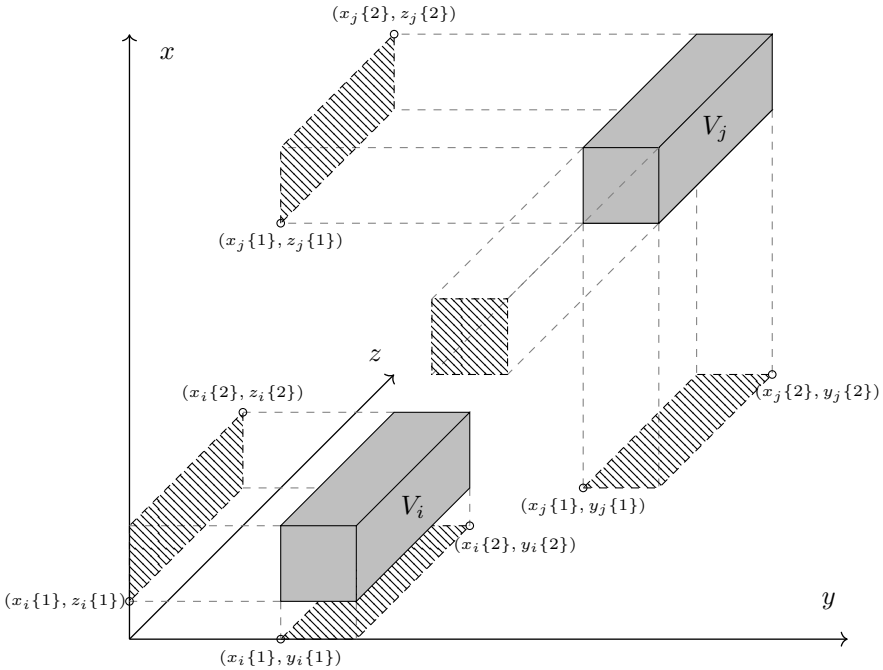

Figure 1.5: Partial inductance geometry for a pair of volume cells.

$$Lp_{i,j}^{(2)}(s) = \frac{s^2}{c^2}\frac{\mu_0}{8\pi a_i a_j}\int_{V_i}\int_{V_j} R\hat{\boldsymbol{u}}_i \cdot \hat{\boldsymbol{u}}_j \; dV_j \; dV_i, \tag{1.108}$$

$$Lp_{i,j}^{(3)}(s) = -\frac{s^3}{c^3}\frac{\mu_0}{24\pi a_i a_j}\int_{V_i}\int_{V_j} R^2\hat{\boldsymbol{u}}_i \cdot \hat{\boldsymbol{u}}_j \; dV_j \; dV_i. \tag{1.109}$$

In what follows a brief review of partial inductances computations is presented. A more detailed description of closed formula for partial inductances evaluation for standard configurations can be found in [1, 31, 32].

Mutual partial Inductances for orthogonal volume cells :

First of all, in order to avoid misunderstanding, we need to clarify what we mean with orthogonal volume cells. For orthogonal volume cells we mean parallel parallelepipeds, as the one shown in Fig. 1.5. The name orthogonal comes from the fact that all the faces of the cells are orthogonal to one of the cartesian axis. As it can be noticed from (1.99), because of the scalar product for orthogonal geometries the partial inductances are $\neq 0$ only when the two versors associated with the cells are

parallel to each other, or $\hat{\boldsymbol{u}}_i = \hat{\boldsymbol{u}}_j$. In such configuration the solution of (1.99) is

$$L_{p_{i,j}}^{(qs)} = \frac{\mu_0}{4\pi a_i a_n} \sum_{c_1=1}^{4} \sum_{c_2=1}^{4} \sum_{c_3=1}^{4} \sum_{h=1}^{7} (-1)^{c_1+c_2+c_3} \gamma_h (c_1, c_2, c_3) \tag{1.110}$$

where

$$\begin{aligned}
\gamma_1 (c_1, c_2, c_3) &= \frac{1}{60} \left(x_{c_1}^4 + y_{c_2}^4 + z_{c_3}^4 - 3x_{c_1}^2 y_{c_2}^2 - 3y_{c_2}^2 z_{c_3}^2 - 3x_{c_1}^2 z_{c_3}^2 \right) R (c_1, c_2, c_3) ; \\
\gamma_2 (c_1, c_2, c_3) &= \left(\frac{y_{c_2}^2 z_{c_3}^2}{4} - \frac{y_{c_2}^4}{24} - \frac{z_{c_3}^4}{24} \right) x_{c_1} \log \left(x_{c_1} + R (c_1, c_2, c_3) \right) \\
\gamma_3 (c_1, c_2, c_3) &= \left(\frac{y_{c_2}^2 x_{c_1}^2}{4} - \frac{y_{c_2}^4}{24} - \frac{x_{c_1}^4}{24} \right) z_{c_3} \log \left(z_{c_3} + R (c_1, c_2, c_3) \right) \\
\gamma_4 (c_1, c_2, c_3) &= \left(\frac{z_{c_3}^2 x_{c_1}^2}{4} - \frac{z_{c_3}^4}{24} - \frac{x_{c_1}^4}{24} \right) y_{c_2} \log \left(y_{c_2} + R (c_1, c_2, c_3) \right) \\
\gamma_5 (c_1, c_2, c_3) &= -\frac{1}{6} x_{c_1}^3 y_{c_2} z_{c_3} \tan^{-1} \left(\frac{y_{c_2} z_{c_3}}{x_{c_1} R (c_1, c_2, c_3)} \right) \\
\gamma_6 (c_1, c_2, c_3) &= -\frac{1}{6} x_{c_1} y_{c_2}^3 z_{c_3} \tan^{-1} \left(\frac{x_{c_1} z_{c_3}}{y_{c_2} R (c_1, c_2, c_3)} \right) \\
\gamma_7 (c_1, c_2, c_3) &= -\frac{1}{6} x_{c_1} y_{c_3} z_{c_5}^3 \tan^{-1} \left(\frac{x_{c_1} y_{c_2}}{z_{c_3} R (c_1, c_2, c_3)} \right)
\end{aligned} \tag{1.111}$$

being

$$R (c_1, c_2, c_3) = \sqrt{x_{c_1}^2 + y_{c_2}^2 + z_{c_3}^2} \tag{1.112}$$

and

$$\begin{aligned}
&x_1 = x_i\{2\} - x_j\{2\} \quad x_2 = x_i\{2\} - x_j\{1\} \quad x_3 = x_i\{1\} - x_j\{1\} \quad x_4 = x_i\{1\} - x_j\{2\} \\
&y_1 = y_i\{2\} - y_j\{2\} \quad y_2 = y_i\{2\} - y_j\{1\} \quad y_3 = y_i\{1\} - y_j\{1\} \quad y_4 = y_i\{1\} - y_j\{2\} \\
&z_1 = z_i\{2\} - z_j\{2\} \quad z_2 = z_i\{2\} - z_j\{1\} \quad z_3 = z_i\{1\} - z_j\{1\} \quad z_4 = z_i\{1\} - z_j\{2\}.
\end{aligned} \tag{1.113}$$

In equation (1.110) a_i and a_j are the surfaces orthogonal to the versors, $\hat{\boldsymbol{u}}_i$ and $\hat{\boldsymbol{u}}_n$, associated with the cells i and n respectively. Hence they depend on the direction in space of the branches. If, for instance, we are computing the partial inductance

for branches parallel to the x axis

$$\begin{aligned} a_i &= (y_i\{2\} - y_i\{1\})\,(z_i\{2\} - z_i\{1\}) \\ a_j &= (y_j\{2\} - y_j\{1\})\,(z_j\{2\} - z_j\{1\}) \end{aligned} \tag{1.114}$$

Self Partial Inductance of orthogonal volume cells :
When the cell is like one of those depicted in Fig. 1.5, the solution above holds even for the self term using the same cell for twice. In order to achieve better accuracy when the aspect ratios of the cell are high the self term can be computed as

$$\begin{aligned} \frac{L_{p_{i,i}}}{L} &= \frac{2\mu_0}{\pi}\{\frac{\omega^2}{24u}\left[\log\left(\frac{1+A_2}{\omega}\right) - A_5\right] + \frac{1}{24u\omega}\left[\log\left(\omega + A_2\right) - A_6\right] + \\ &+ \frac{\omega^2}{60u}(A_4 - A_3) + \frac{\omega^2}{24}[\log\left(\frac{u+A_3}{\omega}\right) - A_7] + \frac{\omega^2}{60u}(\omega - A_2) + \frac{1}{20u}(A_2 - A_4) + \\ &+ \frac{u}{4}A_5 - \frac{u^2}{6\omega}\arctan\left(\frac{\omega}{uA_4}\right) + \frac{u}{4\omega}A_6 - \frac{\omega}{6}\arctan\left(\frac{u}{\omega A_4}\right) + \frac{A_7}{4} + \\ &- \frac{1}{6\omega}\arctan\left(\frac{u\omega}{A_4}\right) + \frac{1}{24\omega^2}\left[\log(u + A_1) - A_7\right] + \frac{u}{20\omega^2}(A_1 - A_4) + \\ &+ \frac{1}{60\omega^2 u}(1 - A_2) + \frac{1}{60u\omega^2}(A_4 - A_1) + \frac{u}{20}(A_3 - A_4) + \\ &+ \frac{u^3}{24\omega^2}\left[\log\left(\frac{1+A_1}{u}\right) - A_5\right] + \frac{u^3}{24\omega}\left[\log\left(\frac{\omega + A_3}{u}\right) - A_6\right] + \\ &+ \frac{u^3}{60\omega^2}\left[(A_4 - A_1) + (u - A_3)\right]\} \end{aligned} \tag{1.115}$$

where

$$\begin{aligned} &u = L/W, && \omega = T/W, \\ &A_1 = \sqrt{1+u^2}, && A_2 = \sqrt{1+\omega^2} \\ &A_3 = \sqrt{\omega^2+u^2}, && A_4 = \sqrt{1+\omega^2+u^2} \\ &A_5 = \log\left(\tfrac{1+A_4}{A_3}\right), && A_6 = \log\left(\tfrac{\omega+A_4}{A_1}\right) \\ &A_7 = \log\left(\tfrac{u+A_4}{A_2}\right) \end{aligned} \tag{1.116}$$

and L, T and W are length, thickness and width of the cell respectively.

Partial inductances for 2D rectangular cells :
When the structure is like the one in the example in Fig. 1.1 in Section 1.2, the partial inductances can be computed as

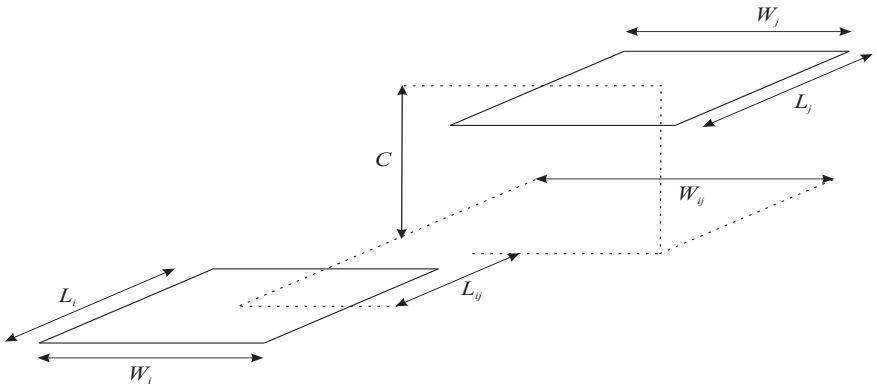

Figure 1.6: Partial inductance cells for 2 D structures.

$$L_{p_{i,j}}^{(qs)} = \frac{\mu_0}{4\pi}\frac{1}{W_i W_j}\sum_{k=1}^{4}\sum_{m=1}^{4}(-1)^{m+k}\sum_{h=1}^{4}\gamma_h \tag{1.117}$$

where

$$\begin{aligned}
\gamma_1 &= -\frac{1}{6}(y_m^2 - 2C^2 + x_k^2)R_{k,m} \\
\gamma_2 &= \frac{x_k^2 - C^2}{2} y_m \log\left(y_m + R_{k,m}\right) \\
\gamma_3 &= \frac{y_m^2 - C^2}{2} x_k \log\left(x_k + R_{k,m}\right) \\
\gamma_4 &= -y_m\, C\, x_k \arctan\left(\frac{x_k\, b_m}{R_{k,m}\, C}\right)
\end{aligned} \tag{1.118}$$

being

$$\begin{aligned}
&R_{k,m} = \sqrt{a_k^2 + b_m^2 + C^2}, \\
&x_1 = W_{ij} - \tfrac{W_i}{2} - \tfrac{W_j}{2}, \qquad x_2 = W_{ij} + \tfrac{W_i}{2} - \tfrac{W_j}{2} \\
&x_3 = W_{ij} + \tfrac{W_i}{2} + \tfrac{W_j}{2}, \qquad x_4 = W_{ij} - \tfrac{W_i}{2} + \tfrac{W_j}{2} \\
&y_1 = L_{ij} - \tfrac{L_i}{2} - \tfrac{L_j}{2}, \qquad y_2 = L_{ij} + \tfrac{L_i}{2} - \tfrac{L_j}{2} \\
&y_3 = L_{ij} + \tfrac{L_i}{2} + \tfrac{L_j}{2}, \qquad y_4 = L_{ij} - \tfrac{L_i}{2} + \tfrac{L_j}{2}.
\end{aligned} \tag{1.119}$$

The geometrical meanings of all the lengths are shown in Fig. 1.6. Because of how (1.117) has been written all the "L"s are parallel to the branches of the cells i and j, while the "W"s are orthogonal to them.

Partial inductances of wires :

When two dimensions are much smaller than the third one (*i.e.* wires), 3D cells can

be approximated as lines. In such hypothesis a closed formula for the mutual partial inductance between parallel filaments with equal length exists.

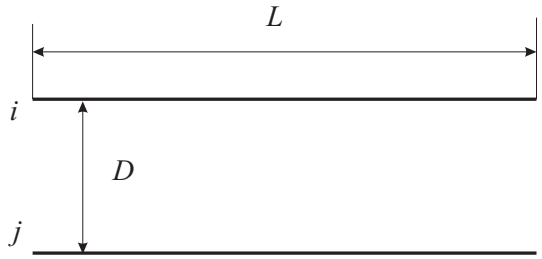

Figure 1.7: Two parallel filaments.

$$L_{p_{i,j}}^{(qs)} = \frac{\mu_0}{2\pi} L \left[\log \left(\frac{L}{D} + \sqrt{\left(\frac{L}{D}\right)^2 + 1} \right) + \frac{D}{L} - \sqrt{\left(\frac{D}{L}\right)^2 + 1} \right]. \tag{1.120}$$

A good approximation of the self partial inductance can be obtained by substituting d with the radius r of conductors

$$L_{p_{i,i}}^{(qs)} = \frac{\mu_0}{2\pi} L \left[\log \left(\frac{L}{r} + \sqrt{\left(\frac{L}{r}\right)^2 + 1} \right) + \frac{r}{L} - \sqrt{\left(\frac{r}{L}\right)^2 + 1} \right]. \tag{1.121}$$

1.3.2 Coefficients of potential

The evaluation of coefficients of potential requires the computation of double folded surface integrals as (1.49)

$$P_{\ell,m}(s) = \frac{1}{4\pi\varepsilon_0 S_\ell S_m} \int_{S_\ell} \int_{S_m} \frac{e^{-s\tau}}{|\boldsymbol{r}_\ell - \boldsymbol{r}_m|} dS_m dS_\ell. \tag{1.122}$$

As for partial inductances, the integral in (1.122) can be computed by numerical integration techniques, and though the time needed for performing accurately such integration is usually smaller than the one for partial inductances (since integrating over surfaces is usually lighter than over volumes) this road can be impractical sometimes. As for partial inductances, in many condition good results can be achieved

if assume to work with electrically small objects. In such condition the exponential $e^{-s\tau} \to 1$ and the quasi-static approximation can be used

$$P_{\ell,m}(s) \approx P_{\ell,m}^{(qs)} = \frac{1}{4\pi\varepsilon_0 S_\ell S_m} \int_{S_\ell}\int_{S_m} \frac{1}{|\boldsymbol{r}_\ell - \boldsymbol{r}_m|} dS_m dS_\ell \tag{1.123}$$

For selected geometry closed-form solution equation (1.123) are available. This allows to achieve good accuracy and fast evaluation for the coefficients of potential of basic geometries, which can be used as building blocks of the model.

As before, if the discretization matches the $\lambda_{min}/20$ rule, a center to center approximation can be assumed and the coefficient of potential can be computed as:

$$P_{\ell,m}(s) \approx \frac{e^{-s\tau_{\ell,m}^{cc}}}{4\pi\varepsilon_0 S_\ell S_m} \int_{S_\ell}\int_{S_m} \frac{1}{|\boldsymbol{r}_\ell - \boldsymbol{r}_m|} dS_m dS_\ell = P_{\ell,m}^{(qs)} e^{-s\tau_{\ell,m}^{cc}} \tag{1.124}$$

where $\tau_{\ell,m}^{cc}$ is the center to center distance between volume cells ℓ and m.

Also the coefficients of potential can be approximated through a Taylor's expansion of the exponential term inside the integral (1.122). Similarly to the partial inductances, we simplify the notation using:

$$R = |\mathbf{r}_\ell - \mathbf{r}_m| = \sqrt{(x_\ell - x_m)^2 + (y_\ell - y_m)^2 + (z_\ell - z_m)^2} \tag{1.125}$$

leading to:

$$P_{\ell,m}(s) = \frac{1}{4\pi\varepsilon_0} \frac{1}{S_\ell S_m} \int_{S_\ell}\int_{S_m} \frac{e^{-s\tau}}{R} dS_m dS_\ell \tag{1.126}$$

Applying the Taylor series expansion leads to

$$\overline{P}_{\ell,m}(s) = \frac{1}{4\pi\varepsilon_0 S_\ell S_m} \sum_{l=0}^{\infty} \left[\frac{(-\frac{s}{c})^l}{l!} \int_{S_\ell}\int_{S_m} R^{l-1} dS_m \, dS_\ell \right]. \tag{1.127}$$

Similar to the partial inductance, a four term expansion results in

$$P_{\ell,m}(s) \approx P_{\ell,m}^{(qs)} + P_{\ell,m}^{(1)}(s) + P_{\ell,m}^{(2)}(s) + P_{\ell,m}^{(3)}(s) \tag{1.128}$$

The first term of (1.127) is the usual quasi-static term:

$$P_{\ell,m}^{(qs)} = \frac{1}{4\pi\varepsilon_0 S_\ell S_m} \int_{S_\ell}\int_{S_m} \frac{1}{R} dS_m \, dS_\ell \tag{1.129}$$

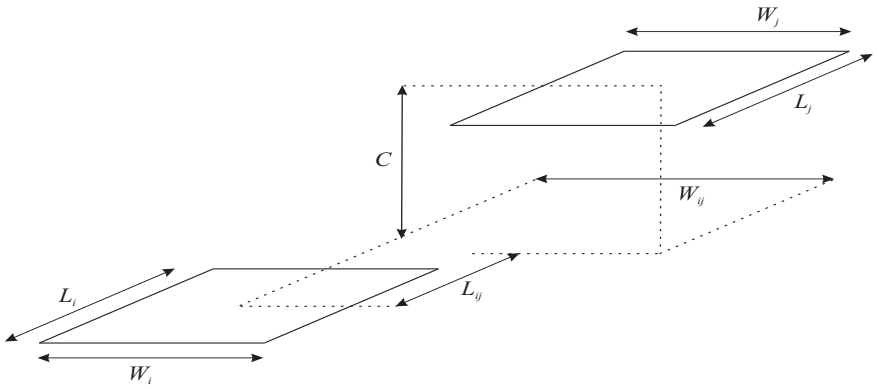

Figure 1.8: Geometry for the evaluation of coefficient of potential for parallel surface cells.

The other three elements are

$$P^{(1)}_{\ell,m}(s) = -\frac{s}{c}\frac{1}{4\pi\varepsilon_0 S_\ell S_m}\int_{S_\ell}\int_{S_m} dS_m\ dS_\ell, \tag{1.130}$$

$$P^{(2)}_{\ell,m}(s) = \frac{s^2}{c^2}\frac{1}{8\pi\varepsilon_0 S_\ell S_m}\int_{S_\ell}\int_{S_m} R\ dS_m\ dS_\ell, \tag{1.131}$$

$$P^{(3)}_{\ell,m}(s) = -\frac{s^3}{c^3}\frac{1}{24\pi\varepsilon_0 S_\ell S_m}\int_{S_\ell}\int_{S_m} R^2\ dS_m\ dS_\ell. \tag{1.132}$$

For each basic geometry a formulation for the evaluation of the partial coefficient of potential is given. The interested reader may refer to [2,33] for a complete overview of coefficients of potential computation. The two most basic configuration for the surface cells involved in the computation of coefficients of potential can have two different configurations, parallel and orthogonal.

Coefficients of Potential for parallel surface cells :

The graphical representation of two parallel surface cells is shown in Fig. 1.8. The solution of (1.123) for such configuration is given by

$$P^{(qs)}_{i,j} = \frac{1}{4\pi\varepsilon_0 S_i S_j}\sum_{k=1}^{4}\sum_{m=1}^{4}(-1)^{m+k}\sum_{h=1}^{4}\gamma_h \tag{1.133}$$

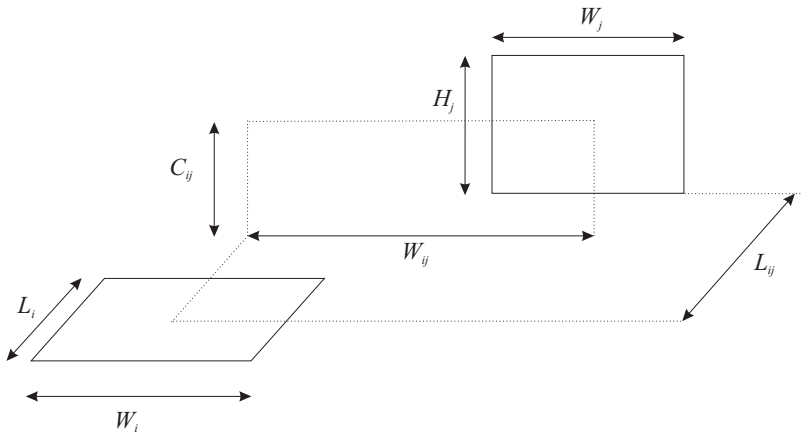

Figure 1.9: Geometry for the evaluation of coefficient of potential for orthogonal surface cells.

where

$$\begin{aligned}
\gamma_1 &= -\frac{1}{6}(y_m^2 - 2C^2 + x_k^2)R_{k,m} \\
\gamma_2 &= \frac{x_k^2 - C^2}{2} y_m \log\left(y_m + R_{k,m}\right) \\
\gamma_3 &= \frac{y_m^2 - C^2}{2} x_k \log\left(x_k + R_{k,m}\right) \\
\gamma_4 &= -y_m\, C\, x_k \arctan\left(\frac{x_k\, b_m}{R_{k,m}\, C}\right)
\end{aligned} \tag{1.134}$$

being

$$\begin{aligned}
&R_{k,m} = \sqrt{a_k^2 + b_m^2 + C^2}, \\
&x_1 = W_{ij} - \tfrac{W_i}{2} - \tfrac{W_j}{2}, \qquad x_2 = W_{ij} + \tfrac{W_i}{2} - \tfrac{W_j}{2} \\
&x_3 = W_{ij} + \tfrac{W_i}{2} + \tfrac{W_j}{2}, \qquad x_4 = W_{ij} - \tfrac{W_i}{2} + \tfrac{W_j}{2} \\
&y_1 = L_{ij} - \tfrac{L_i}{2} - \tfrac{L_j}{2}, \qquad y_2 = L_{ij} + \tfrac{L_i}{2} - \tfrac{L_j}{2} \\
&y_3 = L_{ij} + \tfrac{L_i}{2} + \tfrac{L_j}{2}, \qquad y_4 = L_{ij} - \tfrac{L_i}{2} + \tfrac{L_j}{2} \\
&S_i = W_i L_i \qquad\qquad S_j = W_j L_j.
\end{aligned} \tag{1.135}$$

The geometrical meanings of all the lengths are shown in Fig. 1.6.

Coefficients of Potential for orthogonal surface cells :

The second basic geometry made by two cells oriented perpendicularly to each other is depicted in Fig. 1.9. The evaluation of the coefficient of potential in such

configuration can be carried out with

$$P_{i,j}^{(qs)} = \frac{1}{4\pi\varepsilon_0 S_i S_j} \sum_{c_1=1}^{4} \sum_{c_2=1}^{2} \sum_{c_3=1}^{2} (-1)^{c_1+c_2+c_3} \sum_{h=1}^{7} \gamma_h(c_1, c_2, c_3) \tag{1.136}$$

where

$$\begin{aligned}
\gamma_1(c_1, c_2, c_3) &= -\frac{y_{c_2} z_{c_3}}{3} R(c_1, c_2, c_3) \\
\gamma_2(c_1, c_2, c_3) &= -\left(\frac{x_{c_1}^2}{2} - \frac{z_{c_3}^2}{6}\right) z_{c_3} \log\left(y_{c_2} + R(c_1, c_2, c_3)\right) \\
\gamma_3(c_1, c_2, c_3) &= -\left(\frac{x_{c_1}^2}{2} - \frac{y_{c_2}^2}{6}\right) y_{c_2} \log\left(c_{c_3} + R(c_1, c_2, c_3)\right) \\
\gamma_4(c_1, c_2, c_3) &= -x_{c_1} y_{c_2} z_{c_3} \log\left(x_{c_1} + R(c_1, c_2, c_3)\right) \\
\gamma_5(c_1, c_2, c_3) &= \frac{x_{c_1}^3}{6} \arctan\left(\frac{y_{c_2} z_{c_3}}{x_{c_1} R(c_1, c_2, c_3)}\right) \\
\gamma_6(c_1, c_2, c_3) &= \frac{y_{c_2}^2 x_{c_1}}{6} \arctan\left(\frac{x_{c_1} z_{c_3}}{y_{c_2} R(c_1, c_2, c_3)}\right) \\
\gamma_7(c_1, c_2, c_3) &= \frac{x_{c_1} z_{c_3}^2}{2} \arctan\left(\frac{x_{c_1} y_{c_2}}{z_{c_3} R(c_1, c_2, c_3)}\right)
\end{aligned} \tag{1.137}$$

being

$$\begin{aligned}
&R(c_1, c_2, c_3) = \sqrt{a_{c_1}^2 + b_{c_2}^2 + z_{c_3}^2}, \\
&x_1 = W_{ij} - \tfrac{W_i}{2} - \tfrac{W_j}{2}, && x_2 = W_{ij} + \tfrac{W_i}{2} - \tfrac{W_j}{2} \\
&x_3 = W_{ij} + \tfrac{W_i}{2} + \tfrac{W_j}{2}, && x_4 = W_{ij} - \tfrac{W_i}{2} + \tfrac{W_j}{2} \\
&y_1 = L_{ij} + \tfrac{L_i}{2}, && y_2 = L_{ij} - \tfrac{L_i}{2} \\
&z_1 = C_{ij} + \tfrac{H_j}{2}, && z_2 = C_{ij} - \tfrac{H_j}{2} \\
&S_i = W_i L_i && S_j = W_j H_j.
\end{aligned} \tag{1.138}$$

The geometrical meaning of the lengths is shown in Fig. 1.9.

Self Coefficient of Potential The evaluation of the partial self coefficient of potential can be performed by a modified version of (1.115), which is used for the evaluation of the partial self inductance for thin conductors, and it is

$$\begin{aligned}
P_{i,i} \;=\; & \frac{1}{4\pi\varepsilon_0 L} \frac{2}{3} \Bigg\{ 3 \log\left[u + (u^2+1)^{\frac{1}{2}}\right] + u^2 + \frac{1}{u} + \\
& + 3\, u \log\left[\frac{1}{u} + (\frac{1}{u^2} + 1)^{\frac{1}{2}}\right] - \left[u^{\frac{4}{3}} + (\frac{1}{u})^{\frac{2}{3}}\right]^{\frac{3}{2}} \Bigg\}
\end{aligned} \tag{1.139}$$

where $u = L/W$ using the and L and W are as in Fig. 1.10.

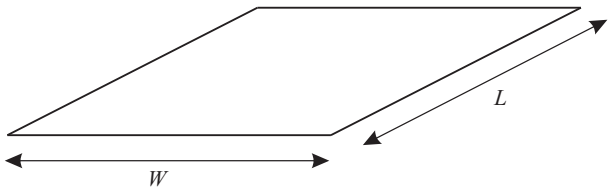

Figure 1.10: Rectangular conductor geometry for the evaluation of the self coefficient of potential.

1.3.3 Partial Resistances

The partial resistances in the PEEC models account for the losses in the conductors. They are evaluated by applying the second Ohm's Law at the volume cells representing the branches of the equivalent circuit. For the i branch it yields

$$R_i = \frac{\ell_i}{a_i \sigma_i} \tag{1.140}$$

where ℓ_i is the length of the volume cell in the current direction, a_i is the cross section normal to the current direction, and σ_i is the conductivity of the volume cell material.

A more general approach to the computation of partial elements for non-orthogonal geometries can be found in [24, 34].

1.4 Dielectrics Modeling in PEEC

The key idea for modeling dielectrics is to represent the displacement current due to the bound charges for dielectrics with $\varepsilon_r > 1$ separately from the conducting currents due to the free charges. Maxwell's equation for the displacement current is written as

$$\nabla \cdot \boldsymbol{E} = \frac{\boldsymbol{q}^F + \boldsymbol{q}^B}{\varepsilon_0} \tag{1.141}$$

where $\boldsymbol{q}^F$ is the free charge and $\boldsymbol{q}^B$ is the bound charge due to the dielectric regions. Thus, the global charge is $\boldsymbol{q}^T = \boldsymbol{q}^F + \boldsymbol{q}^B$.

The dielectric volumes can be taken into account in terms of the polarization current density associated with their presence. This can be accomplished by adding and subtracting the displacement current in the background medium

$$\varepsilon_0 \frac{\partial \boldsymbol{E}(\boldsymbol{r},t)}{\partial t} \tag{1.142}$$

in the right hand side of the Maxwell equation for the rotor of $\boldsymbol{H}$ [35] as

$$\begin{aligned} \nabla \times \boldsymbol{H}(\boldsymbol{r},t) &= \boldsymbol{J}^C(\boldsymbol{r},t) + \varepsilon_0\varepsilon_r \frac{\partial \boldsymbol{E}(\boldsymbol{r},t)}{\partial t} = \\ &= \boldsymbol{J}^C(\boldsymbol{r},t) + \varepsilon_0(\varepsilon_r - 1)\frac{\partial \boldsymbol{E}(\boldsymbol{r},t)}{\partial t} + \varepsilon_0 \frac{\partial \boldsymbol{E}(\boldsymbol{r},t)}{\partial t}. \end{aligned} \tag{1.143}$$

In the last equation it is possible to notice that we have 3 different current contribution, the first is the conductivity current $\boldsymbol{J}^C$, the last is the background medium displacement current and the second is the excess displacement current because of the dielectric medium. We can define a total current in the equation (1.143) which takes into account both the electric current related to the conductivity of the medium and the polarization current due to the dielectrics

$$\boldsymbol{J}^T(\boldsymbol{r},t) = \boldsymbol{J}^C(\boldsymbol{r},t) + \varepsilon_0(\varepsilon_r - 1)\frac{\partial \boldsymbol{E}(\boldsymbol{r},t)}{\partial t} = \boldsymbol{J}^C(\boldsymbol{r},t) + \boldsymbol{J}^D(\boldsymbol{r},t). \tag{1.144}$$

The magnetic vector potential at point $\boldsymbol{r}$, given in (1.21) writes as

$$\boldsymbol{A}(\boldsymbol{r},t) = \frac{\mu_0}{4\pi}\int_{V'} \frac{\boldsymbol{J}^T(\boldsymbol{r}',t')}{|\boldsymbol{r}-\boldsymbol{r}'|} dV'. \tag{1.145}$$

For points located inside conductors (1.28) reads

$$\begin{aligned} \boldsymbol{E}_0(\boldsymbol{r},t) &= \frac{\boldsymbol{J}^C(\boldsymbol{r},t)}{\sigma} + \frac{\partial}{\partial t}\frac{\mu_0}{4\pi}\int_{V'}\frac{\boldsymbol{J}^C(\boldsymbol{r}',t')}{|\boldsymbol{r}-\boldsymbol{r}'|}dV' + \\ &\quad +\varepsilon_0(\varepsilon_r-1)\frac{\mu_0}{4\pi}\int_{V'}\frac{1}{|\boldsymbol{r}-\boldsymbol{r}'|}\frac{\partial^2\boldsymbol{E}(\boldsymbol{r}',t')}{\partial t^2}dV' + \nabla\Phi(\boldsymbol{r},t) \end{aligned} \tag{1.146}$$

it can be noticed that when $\varepsilon_r = 1$ (1.146) is as in the regular case of conductors seen before. At a point $\boldsymbol{r}$ inside a dielectric region with relative permittivity ε_r (1.28) becomes

$$\begin{aligned} \boldsymbol{E}_0(\boldsymbol{r},t) &= \boldsymbol{E}(\boldsymbol{r},t) + \frac{\partial}{\partial t}\frac{\mu_0}{4\pi}\int_{V'}\frac{\boldsymbol{J}^C(\boldsymbol{r}',t')}{|\boldsymbol{r}-\boldsymbol{r}'|}dV' + \\ &+ \varepsilon_0(\varepsilon_r-1)\frac{\mu_0}{4\pi}\int_{V'}\frac{1}{|\boldsymbol{r}-\boldsymbol{r}'|}\frac{\partial^2\boldsymbol{E}(\boldsymbol{r}',t')}{\partial t^2}dV' + \nabla\Phi(\boldsymbol{r},t) \end{aligned} \tag{1.147}$$

where $\Phi(\boldsymbol{r},t)$ is

$$\Phi(\boldsymbol{r},t) = \frac{1}{4\pi\varepsilon_0}\int_{S'}\frac{\boldsymbol{q}^T(\boldsymbol{r}',t')}{|\boldsymbol{r}-\boldsymbol{r}'|}dS' \qquad \boldsymbol{r}\in S'. \tag{1.148}$$

It can be observed that the electric field at a point $\boldsymbol{r}$, $\boldsymbol{E}(\boldsymbol{r})$, is determined by the first time derivative of the current density distribution $\boldsymbol{J}^T(\boldsymbol{r},t)$, the gradient of the electric scalar potential $\nabla\Phi(\boldsymbol{r},t)$ but also by the second derivative of the electric field itself $\partial^2\boldsymbol{E}(\boldsymbol{r}',t')/\partial t^2$.

As stated before, the charges $\boldsymbol{q}^F$, $\boldsymbol{q}^B$ and $\boldsymbol{q}^T$ are on the surface of the conductors and dielectrics while the currents flow through volumes. The continuity equation cannot be enforced as in the conventional moment type solutions [14]

$$\nabla\cdot\boldsymbol{J}^T + \frac{\partial\boldsymbol{q}^T}{\partial t} = 0 \tag{1.149}$$

but it will be implemented in the form of Kirchhoff's current law enforced to each node. Thus, within each conductor and each homogeneous block of dielectric it follows that

$$\nabla\cdot\boldsymbol{J}^C(\boldsymbol{r}) = 0 \tag{1.150}$$

$$\nabla\cdot\boldsymbol{J}^D(\boldsymbol{r}) = 0. \tag{1.151}$$

Furthermore, on each conductor and dielectric the current normal to the surface causes accumulation of surface charge

$$\hat{\boldsymbol{n}} \cdot \boldsymbol{J}^C(\boldsymbol{r}) = \frac{\partial \boldsymbol{q}^F}{\partial t} \tag{1.152}$$

$$\hat{\boldsymbol{n}} \cdot \boldsymbol{J}^D(\boldsymbol{r}) = \frac{\partial \boldsymbol{q}^B}{\partial t}. \tag{1.153}$$

On the surface between touching conductor and dielectric blocks, equation (1.152) becomes

$$\hat{\boldsymbol{n}} \cdot \boldsymbol{J}^T(\boldsymbol{r}) = \frac{\partial \boldsymbol{q}^T}{\partial t}. \tag{1.154}$$

Let's refer to Fig. 1.11. It is possible to divide the conductors and dielectrics into blocks for which the conduction or displacement currents are assumed to be uniform. Further, the surfaces of conductors and dielectrics are completely laid out with panels to represent free and bound charges, respectively.

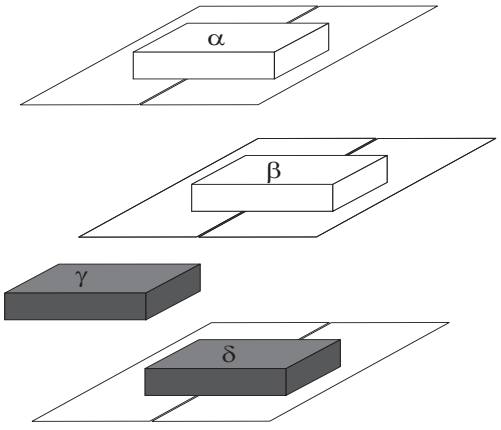

Figure 1.11: Cell structure for finite conductors and dielectrics.

Cells α and β represent conductors and free charge $\boldsymbol{q}^F$ is located on their surfaces. Dielectric cell γ is an internal cell and has no outside surface; there is no charge on its surface; finally, dielectric cell δ is on the surface of the dielectric body and presents bound charge $\boldsymbol{q}^B$ on its surface. In the following it will be referred to the total charge $\boldsymbol{q}^T$ to be general.

The vector quantities can be represented in terms of the Cartesian coordinates. For this case the vector quantities are $\boldsymbol{J} = J_x\hat{\boldsymbol{x}} + J_y\hat{\boldsymbol{y}} + J_z\hat{\boldsymbol{z}}$ and $\boldsymbol{E} = E_x\hat{\boldsymbol{x}} +$

$E_y\hat{\boldsymbol{y}} + E_z\hat{\boldsymbol{z}}$. The three integral equations are identical in form with the exception of the space directions x, y and z. It is possible to consider cells in the y-direction only, without loss of generality Equations (1.146) and (1.147) become three coupled integral equations. Vectors $\boldsymbol{r}$ and $\boldsymbol{r}'$ indicate the point where the electric field is evaluated and where the source, current or charge, is located, respectively.
Two different cases must be considered depending on the location of the field point $\boldsymbol{r}$. In the first case the field point $\boldsymbol{r}$ is located in a conductor, in the second one it is within a dielectric block.
Let's assume first that $\boldsymbol{r}$ is located inside a conductive cell and no external field $\boldsymbol{E}_0$ exists: equation (1.146) applied to the conductor cell α is

$$\begin{aligned} & \frac{J_y^C(\boldsymbol{r},t)}{\sigma_\alpha} + \frac{\partial}{\partial t}\frac{\mu_0}{4\pi}\int_{V_{\alpha'}} \frac{J^C(\boldsymbol{r}',t')}{|\boldsymbol{r}-\boldsymbol{r}'|}dV'_\alpha + \frac{\partial}{\partial t}\frac{\mu_0}{4\pi}\int_{V'_\beta} \frac{J^C(\boldsymbol{r}',t')}{|\boldsymbol{r}-\boldsymbol{r}'|}dV'_\beta + \\ + \;& \varepsilon_0(\varepsilon_\gamma - 1)\frac{\mu_0}{4\pi}\int_{V'_\gamma} \frac{1}{|\boldsymbol{r}-\boldsymbol{r}'|}\frac{\partial^2 E_y(\boldsymbol{r}',t')}{\partial t^2}dV'_\gamma + \\ + \;& \varepsilon_0(\varepsilon_\delta - 1)\frac{\mu_0}{4\pi}\int_{V'_\delta} \frac{1}{|\boldsymbol{r}-\boldsymbol{r}'|}\frac{\partial^2 E_y(\boldsymbol{r}',t')}{\partial t^2}dV'_\delta + \frac{1}{4\pi\epsilon_0}\int_{S'_\alpha}\frac{\partial}{\partial y}\frac{1}{|\boldsymbol{r}-\boldsymbol{r}'|}\boldsymbol{q}^T(\boldsymbol{r}',t')dS'_\alpha + \\ + \;& \frac{1}{4\pi\epsilon_0}\int_{S'_\beta}\frac{\partial}{\partial y}\frac{1}{|\boldsymbol{r}-\boldsymbol{r}'|}\boldsymbol{q}^T(\boldsymbol{r}',t')dS'_\beta + \frac{1}{4\pi\epsilon_0}\int_{S'_\delta}\frac{\partial}{\partial y}\frac{1}{|\boldsymbol{r}-\boldsymbol{r}'|}\boldsymbol{q}^T(\boldsymbol{r}',t')dS'_\delta = 0 \end{aligned} \tag{1.155}$$

where σ_α represents the electrical conductivity of cell α.
Applying the Galerkin solution each single term of (1.155) has a circuit interpretation. In the following it is assumed that density current J_y^C is uniform across the cross section a_α of cell α. Further, for the sake of simplicity, the quasi-static assumption will be used, e.g. $t = t'$, thus neglecting the delay due to the speed of light in the background medium. The first term of (1.155) represents the voltage drop across the resistance of the cell α

$$\frac{1}{a_\alpha}\int_{V_\alpha}\frac{J_y^C(\boldsymbol{r}_\alpha,t)}{\sigma_\alpha}dV_\alpha = \frac{1}{a_\alpha}\int_{a_\alpha}\int_{l_\alpha}\frac{J_y^C(\boldsymbol{r}_\alpha,t)}{\sigma_\alpha}da_\alpha dl_\alpha = \rho_\alpha\frac{l_\alpha}{a_\alpha}(a_\alpha J_y^C) = R_\alpha I_y^C. \tag{1.156}$$

The second term is the voltage drop across the self inductance of the cell α

$$\left(\frac{\mu_0}{4\pi a_\alpha a_\alpha}\int_{V'_\alpha}\int_{V_\alpha}\frac{1}{|\boldsymbol{r}_\alpha - \boldsymbol{r}'_\alpha|}dV'_\alpha dV_\alpha\right)\frac{d}{dt}(a_\alpha J_y^C) = L_{p_{\alpha,\alpha}}\frac{dI_y^C}{dt}. \tag{1.157}$$

This allows to identify the self partial inductance of cell α as

$$L_{p_{\alpha,\alpha}} = \frac{\mu_0}{4\pi a_\alpha a_\alpha} \int_{V'_\alpha} \int_{V_\alpha} \frac{1}{|\boldsymbol{r}_\alpha - \boldsymbol{r}'_\alpha|} dV'_\alpha dV_\alpha. \tag{1.158}$$

Following the same procedure it is possible to recognize in the third term of (1.155) the mutual partial inductance between the conductor cells α and β

$$L_{p_{\alpha,\beta}} = \frac{\mu_0}{4\pi a_\alpha a_\beta} \int_{V_\alpha} \int_{V_\beta} \frac{1}{|\boldsymbol{r}_\alpha - \boldsymbol{r}_\beta|} dV_\alpha dV_\beta. \tag{1.159}$$

The fourth and fifth terms model the coupling among the conductor cell α and dielectric cells γ and δ: as clearly seen, although the different nature of materials, such term still represents an inductive coupling

$$\varepsilon_0(\varepsilon_\gamma - 1)\frac{\mu_0}{4\pi a_\alpha} \int_{V_\alpha} \int_{V'_\gamma} \frac{1}{|\boldsymbol{r}_\alpha - \boldsymbol{r}'_\gamma|} \frac{\partial^2 E_y(\boldsymbol{r}'_\gamma, t_d)}{\partial t^2} dV'_\gamma dV_\alpha = \tag{1.160}$$

$$= \left(\frac{\mu_0}{4\pi a_\alpha} \int_{V_\alpha} \int_{V_\gamma} \frac{1}{|\boldsymbol{r}_\alpha - \boldsymbol{r}'_\gamma|} dV'_\gamma dV_\alpha \right) \frac{d}{dt} \left(a_\gamma \varepsilon_0 (\varepsilon_\gamma - 1) \frac{dE_y}{dt} \right) = L_{p_{\alpha,\gamma}} \frac{dI_y^P}{dt}$$

where the polarization current I_y^P appears. Again, the mutual partial inductance between cells α and γ can be evaluated by means of the same formula (1.159). The same consideration apply to the fifth term.

The last three terms of (1.155) describe the electric field produced in cell α by the charge located on the surface of cells α, β and δ. It is worth pointing out that the coefficients of potential describing such couplings are the same as in the free space. Let's consider what happens when the point $\boldsymbol{r}$ is located inside a dielectric cell γ; equation (1.147) becomes

$$\begin{aligned}
E_y(\boldsymbol{r}, t) \;+\; & \frac{\mu_0}{4\pi} \int_{V'_\alpha} K(\boldsymbol{r}, \boldsymbol{r}') \frac{\partial J_y^C(\boldsymbol{r}', t_d)}{\partial t} dV'_\alpha + \frac{\mu_0}{4\pi} \int_{V'_\beta} K(\boldsymbol{r}, \boldsymbol{r}') \frac{\partial J_y^C(\boldsymbol{r}', t_d)}{\partial t} dV'_\beta \\
+\; & \varepsilon_0(\varepsilon_\gamma - 1)\frac{\mu_0}{4\pi} \int_{V'_\gamma} K(\boldsymbol{r}, \boldsymbol{r}') \frac{\partial^2 E_y(\boldsymbol{r}', t_d)}{\partial t^2} dV'_\gamma + \\
+\; & \varepsilon_0(\varepsilon_\delta - 1)\frac{\mu_0}{4\pi} \int_{V'_\delta} K(\boldsymbol{r}, \boldsymbol{r}') \frac{\partial^2 E_y(\boldsymbol{r}', t_d)}{\partial t^2} dV'_\delta + \\
+\; & \frac{1}{4\pi\varepsilon_0} \int_{S'_\alpha} \frac{\partial K(\boldsymbol{r}, \boldsymbol{r}')}{\partial y} q^T(\boldsymbol{r}', t) dS'_\alpha + \frac{1}{4\pi\varepsilon_0} \int_{S'_\beta} \frac{\partial K(\boldsymbol{r}, \boldsymbol{r}')}{\partial y} q^T(\boldsymbol{r}', t) dS'_\beta + \\
+\; & \frac{1}{4\pi\varepsilon_0} \int_{S'_\delta} \frac{\partial K(\boldsymbol{r}, \boldsymbol{r}')}{\partial y} q^T(\boldsymbol{r}', t) dS'_\delta = 0.
\end{aligned} \tag{1.161}$$

The Galerkin's testing procedure is applied leading to find the corresponding equivalent circuits. The integration of the first term in (1.161) allows to define a voltage drop across a volume dielectric cell

$$\frac{1}{a_\gamma}\int_{a_\gamma}\int_{\ell_\gamma} E_y(\boldsymbol{r},t)d\ell_\gamma da_\gamma = \frac{1}{a_\gamma}a_\gamma\ell_\gamma E_y(t) = v_{c_\gamma}. \tag{1.162}$$

A polarization current flows through the dielectric cell γ

$$\begin{aligned} I_y^{POL} &= J_y^{POL}a_\gamma = \left(\varepsilon_0(\varepsilon_\gamma-1)\frac{dE_\gamma}{dt}\right)a_\gamma = \left(\varepsilon_0(\varepsilon_\gamma-1)\frac{dE_\gamma}{dt}\right)\frac{\ell_\gamma}{\ell_\gamma}a_\gamma = \\ &= \frac{d}{dt}\left[\left(\frac{\varepsilon_0(\varepsilon_\gamma-1)a_\gamma}{\ell_\gamma}\right)(\ell_\gamma E_y)\right] = C_e\frac{dv_{c_\gamma}}{dt} \end{aligned} \tag{1.163}$$

where the capacitance C_e, named *excess capacitance*, is defined as

$$C_e = \frac{\varepsilon_0(\varepsilon_\gamma-1)a_\gamma}{\ell_\gamma}. \tag{1.164}$$

The second and third terms in (1.161) describe an inductive coupling. The fourth term allows to define the partial self inductance of dielectric cell γ

$$\varepsilon_0(\varepsilon_\gamma-1)\frac{\mu_0}{4\pi}\frac{1}{a_\gamma}\int_{V_\gamma}\int_{V'_\gamma} K(\boldsymbol{r}_\gamma,\boldsymbol{r}'_\gamma)\frac{\partial^2 E_y(\boldsymbol{r}_\gamma,t_d)}{\partial t^2}dV'_\gamma dV_\gamma = \tag{1.165}$$

$$= \left(\frac{\mu_0}{4\pi}\frac{1}{a_\gamma a_\gamma}\int_{V_\gamma}\int_{V'_\gamma} K(\boldsymbol{r}_\gamma,\boldsymbol{r}'_\gamma)dV'_\gamma dV_\gamma\right)\frac{d}{dt}\left(a_\gamma\varepsilon_0(\varepsilon_\gamma-1)\frac{dE_y}{dt}\right) = L_{p_{\gamma,\gamma}}\frac{dI_y^{POL}}{dt}.$$

The last term allows to evaluate the mutual partial inductance between dielectric cells γ and δ

$$L_{p_{\gamma,\delta}} = \frac{\mu_0}{4\pi a_\gamma a_\delta}\int_{V_\gamma}\int_{V'_\delta}\frac{1}{\boldsymbol{r}_\gamma-\boldsymbol{r}'_\delta}dV'_\delta dV_\gamma. \tag{1.166}$$

Again, the last three terms are analogous to those evaluated in the free space. To summarize, ideal (lossless) dielectrics are modeled by volume cells characterized by the excess capacitance in series to the equivalent circuit for the inductive coupling described in terms of self and partial inductances, computed in free space. Fig. 1.12 shows the PEEC equivalent circuit of a dielectric bar assuming $N_v = 2$, $N_s = N = 3$.

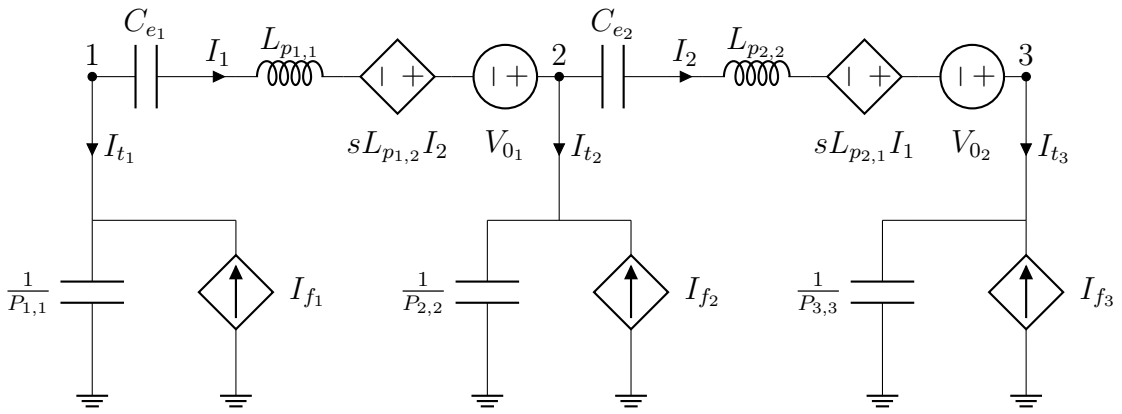

Figure 1.12: PEEC equivalent circuit for dielectrics.

More recent PEEC models of dispersive and lossy dielectrics have been proposed in [11, 36–38].

1.4.1 External incident Electric Fields

In the analysis of EMC problems the excitation can be represented by current, voltage-sources and external electric fields as well. The incorporation of incident fields in the PEEC method is explained in detail in [39] where a source equivalence, V_0, is derived from the left hand side in (1.28). The equivalent voltage source, V_0, is placed in series with each inductive volume cell equivalent circuit and calculated for a volume cell m using

$$V_{0_m}(t) = \frac{1}{a_m} \int_{a_m} \int_{\ell_m} \boldsymbol{E}^i(\boldsymbol{r}, t) da\, dl \tag{1.167}$$

where

$$\boldsymbol{E}^i(\boldsymbol{r}, t) = E_x^i(\boldsymbol{r}, t)\hat{x} + E_y^i(\boldsymbol{r}, t)\hat{y} + E_z^i(\boldsymbol{r}, t)\hat{z}. \tag{1.168}$$

1.5 Solution of PEEC models

PEEC models, as circuit problems, can be solved in both frequency and time domain. One of the advantages of such method is that most of the numerical techniques developed for circuits problem can be efficiently used. Moreover, as stated previously, because of the circuital interpretation the PEEC models can be easily solved by SPICE-like softwares.

1.5.1 Frequency domain

A PEEC frequency domain solver can be obtained just collecting equations (1.93) and (1.94). Omitting for simplicity the presence of dielectric materials (dielectric branches), we have:

$$\begin{bmatrix} -\mathbf{A} & -(\mathbf{R}+s\mathbf{L}_p(s)) \\ \mathbf{Y}_{le}+s\mathbf{P}^{-1}(s) & -\mathbf{A}^T \end{bmatrix} \cdot \begin{bmatrix} \mathbf{\Phi}(s) \\ \mathbf{I}(s) \end{bmatrix} = \begin{bmatrix} \mathbf{V}_0(s) \\ \mathbf{I}_s(s) \end{bmatrix}. \tag{1.169}$$

Solution of dense linear systems

An efficient and accurate solution of the linear system (1.169) is extremely important for the performance of the PEEC solver. The most common technique to solve linear systems is the LU decomposition [40]. Although elegant such method is not practical for solving large and dense linear systems as its complexity is $O(n^3)$, being n the number of the unknowns. It is much more convenient to use Krylov subspace iterative methods [40]. Many different implementation variants are available; the most popular is GMRES [41] whose complexity is $O(n^2)$ as requires matrix-vector products and converges in a very small number of iterations if an efficient *pre-conditioner* is used. Furthermore, the matrix-vector product can be accelerated by using fast-multipole techniques [42–45] or precorrected-FFT methods [46] which may reduce the complexity to $O(n\log(n))$.

1.5.2 Time domain

The development of time domain PEEC solver needs to consider the delay in the coupling terms. In order to keep things easy let us assume that partial inductances and coefficients of potential are evaluated as static coefficients, by (1.99) and (1.123). If such assumption is not made, the mutual coefficients lead to the Delay Differential Equation of the Neutral Type (NDDE) because of the finite propagation time in the physical spacing between the cells. From (1.169), the time domain form for quasi static condition can be achieved as

$$\begin{bmatrix} -\mathbf{A} & -\left(\mathbf{R}+\mathbf{L}_p\frac{d}{dt}\right) \\ \mathbf{Y}_{le}+\mathbf{P}^{-1}\frac{d}{dt} & -\mathbf{A}^T \end{bmatrix} \cdot \begin{bmatrix} \mathbf{\Phi}(t) \\ \mathbf{i}(t) \end{bmatrix} = \begin{bmatrix} \mathbf{v}_0(t) \\ \mathbf{i}_s(t) \end{bmatrix}. \tag{1.170}$$

The same system can be expressed in descriptor state-space form as:

$$\begin{bmatrix} \mathbf{0} & -\mathbf{L}_p \\ \mathbf{P}^{-1} & \mathbf{0} \end{bmatrix} \begin{bmatrix} \dot{\mathbf{\Phi}}(t) \\ \dot{\mathbf{i}}(t) \end{bmatrix} + \begin{bmatrix} -\mathbf{A} & -\mathbf{R} \\ \mathbf{Y}_{le} & -\mathbf{A}^T \end{bmatrix} \begin{bmatrix} \mathbf{\Phi}(t) \\ \mathbf{i}(t) \end{bmatrix} = \begin{bmatrix} \mathbf{v}_0(t) \\ \mathbf{i}_s(t) \end{bmatrix} \tag{1.171}$$

or more compactly

$$\mathbf{C}\,\dot{\mathbf{x}}(t) + \mathbf{G}\mathbf{x}(t) = \mathbf{B}\mathbf{u}(t). \tag{1.172}$$

When the delays are included using the center to center approximation introduced in (1.100) and (1.124) the propagation time between the cells m and n as given by

$$t'_{m,n} = t - \frac{|\boldsymbol{r}_m - \boldsymbol{r}_n|}{c} = t - \tau. \tag{1.173}$$

The mutual inductive coupling between those cells takes the form

$$v_{m,n} = L_{p_{m,n}} \frac{di_n(t'_{m,n})}{dt} \tag{1.174}$$

being $L_{p_{m,n}}$ the mutual partial inductance. The capacitive coupling, whose general form is $\mathbf{\Phi}(s) = \mathbf{PQ}(s)$ where $\mathbf{P}(s)$ is the coefficient of potential matrix, is affected in the exact same way. The equation describing the total current flowing from the node k to the infinity node changes as

$$i_{t_k}(t) = \frac{1}{P_{k,k}} \frac{\partial \Phi_k}{\partial t} - \sum_{\substack{m=1 \\ m\neq k}}^{N_s} \frac{P_{k,m}}{P_{k,k}} i_{c_m}(t'_{k,m}) \tag{1.175}$$

where i_{c_k} is the total capacitive current for cell k. It is possible to assign more than one delay for each cell pair leading to potentially multiple distances $R_{k,m}$ between points on two cells k and m.

The above formulation for a linear PEEC circuit consisting of PEEC models, using the Modified Nodal Analysis (MNA) technique [47], can be written as the following NDDE

$$\mathbf{C_0}\,\dot{\mathbf{x}} + \mathbf{G_0}\mathbf{x} = \sum_i \mathbf{G_i}\,\mathbf{x}(t-\tau_i) + \sum_i \boldsymbol{C_i}\,\dot{\mathbf{x}}(t-\tau_i) + \mathbf{B}\mathbf{u}(t) \tag{1.176}$$

where $\mathbf{C_0}$ and $\mathbf{G_0}$ represent non-delayed part of the system, while $\mathbf{C_i}$ and $\mathbf{G_i}$ are the elements having delay equals to τ_i. Finally, $\mathbf{B}$ is the input selector matrix and $\mathbf{u}$ are the inputs or forcing voltages and currents. The resulting electromagnetic and circuit (EM/Ckt) problem can be extremely large where the $\mathbf{L}_p$ and $\mathbf{P}$ coupling coefficients matrices are dense and very large. However the solution of the left hand part is importantly very sparse since it contains only the non-retarded part or the slightly retarded part of the matrix, depending on the time step h. In a time domain solver, the couplings have to be computed by picking up values in the past, delayed by the appropriate τ for the time domain from stored waveforms. Hence, the couplings are already known and the values are stamped into the known right hand side of the system rather than the MNA circuit coefficient matrix. The basic solution complexity is $O(n^2)$ where n is the system size.

One of the most important aspects which at present reduces the generality of the time domain approach is the long time stability of the solution. Improvements to the stability have been made over thirty years by numerous researchers. In [48], the general stability issue with full-wave time domain integral equation solution is described. Since then, much more progress has been made on the stability issue. For example. the impact of the delay points on the conductors was studied in [49] and the introduction of further delay points or cell subdivisions of the conductors on the stability issue was considered for PEEC models in [50]. A refinement strategy for the delay assignment is presented in [51]. More recently the stability of quasi-static PEEC models has been investigated [52].

The choice of the numerical integration method is very important for several

aspects of the solution. Early work on the solution of time domain electromagnetic integral equation solvers used explicit methods [48]. However, it became clear that explicit forward Euler type methods could only lead to stable solutions for very special cases and for extremely small time steps. For this reason, several researchers started to employ implicit methods for the time domain PEEC methods which are especially suited for this type of problem, *e.g.*, [53, 54]. One of the key considerations for the choice of the method is the behavior of the stability function $R(z)$ where $z = \lambda h$, λ is the eigenvalue and h is the time step [55]. It is clearly required that the stability functions which decay with $z \to \infty$. This is evident from the last section since there are several mechanisms in the model to dampen the amplitude above f_M such that a strong feedback reduction occurs without impacting the solution behavior below f_M. Three methods which are well suited for the task are the backward Euler method, the θ method for $\theta > 0.5$, and the Lobatto III-C method. In fact, the Lobatto III-C method decays as $1/(z^2)$, which is very desirable. However, as shown below, the size of the system matrix is a factor 2 larger than for the θ or the BE methods. The frequently used trapezoidal rule was shown to be one of the worst methods for these systems [54]. The stability function of the BE formula decays asymptotically as $1/(z)$, which is also very desirable. NDDE equations can be solved by an adaptation of the RK methods for ODEs, *e.g.*, [56]. Finally, it is also to be pointed out that the solution of (1.176) can be accelerated by means of the fast multipole method and multi-function techniques [17, 45, 57].

2

Inverse Laplace Transform techniques

In the last decades, time domain (TD) methods have found an increasing employment in electromagnetic (EM) simulations. The reasons for that are various and very different from each other. The most practical of them is connected to the computational efficiency: standard TD differential equations based simulations are able to produce broadband data in the frequency domain (FD) from a single run in the TD. Essentially, for implicit time marching methods, this fact is due to the structure of the system of equations that has to be solved, being necessary to perform the inversion of the system only one time. The corresponding frequency response can then be easily obtained through the Fourier Transform applied to the TD data. The same is not valid for FD solvers, since the inversion is necessarily repeated for each frequency sample in the band of evaluation. For this reason, using direct FD solvers, the computational complexity is highly connected to the number of frequency samples of interest within the selected band. The employment of TD analysis methods is also dictated by the increase of semiconductor elements in electronic circuits. The non-linear behavior of such elements makes it not possible a FD analysis, only applicable to linear models. On the other hand, TD resolution methods permit to directly incorporate those elements in the analysis, leading to global, complete TD models.

Nowadays, a growing complexity in integrated circuit technology is observed, due to the need of smaller structures, higher density of components and higher operating frequencies, leading to strongly coupled electrically long structures. For this reason,

the modeling and simulation of modern devices has become a critical stage in the design process. In this framework, it is clear that full-wave simulation tools are more and more required. In the PEEC method, the full-wave nature of the model is embedded in the partial elements, since they express the electric and magnetic couplings involved in the EM behavior of the structure. In this sense, a quasi-full-wave model can be reached introducing the center to center propagation delays in partial elements described in (1.100) and (1.124), obtaining the NDDE-TD formulation described in (1.176). Such kind of differential equations can be numerically solved using standard discretization techniques like the Gear's method, the trapezoidal rule (TR) and the backward Euler (BE) [58], in conjunction with an appropriate strategy able to manage the propagation delays [59]. However, the approximation of the model propagation delays is often the source of late-time instabilities showing up in the TD solutions obtained with standard time-stepping solvers [60]. Precise measures for their prediction and management have not yet been investigated and the finding of a systematic relation between the instabilities and the approximation degrees employed in the propagation delays representation is still an open issue. Effectively, the exact prediction of the instability behavior of a given PEEC model can be reasonably performed only when dealing with small problems, since a study of the poles of the MNA matrix has to be implemented [61]. In this framework, to circumvent the problem, several studies have been conducted about the employment of Inverse Laplace Transform (ILT) techniques in IE solvers. For the already cited reasons, in the context of this doctoral project, ILT techniques have been applied for the first time to PEEC retarded models.

Technically, all the ILT techniques are based on the approximation of the well known inverse Laplace integral expressed as:

$$x(t) = \frac{1}{j2\pi} \int_{\gamma - j\infty}^{\gamma + j\infty} X(s) e^{st} ds \tag{2.1}$$

Where $\gamma > \mathrm{Re}(p_k) \forall p_k$, where p_k are the poles of $X(s)$, being $x(t)$ a time dependent function and $X(s)$ its Laplace transform, and the complex exponential e^{st} is the kernel of the inverse transformation. The analytical solution is possible only for a limited set of cases. In general, the integral in (2.1) has to be performed in the

complex plane and this requires considerable analytical efforts that could lead to closed-form solutions only for a restricted class of functions. Fortunately, many approximation algorithms widely used in engineering modeling applications have been proposed in the last century. Among them, we remind the Weeks method (1966) [62], the Dubner-Abate method (1968) [63], the Stehfest method (1970) [64] (widely used in groundwater flow and petroleum reservoir applications) and the Durbin method (1974) [65]. A detailed comparison and description of all the approximate Laplace inverse transform methods was provided by B. Davies and B. Martin in [66] (1979). As pointed out in [67], it is difficult to recommend just one inversion method, since the performance is strictly dependent on the function type and, hence, on the application.

In the field of TD EM modeling and circuit simulation, there are two methods that have shown the best compromise between computational efficiency and accuracy:

- the Numerical Inversion of the Laplace Transform method (NILT) was proposed by M. Nakhla, K. Singhal and J. Vlach in 1973 [68] and is based on the Padé approximation of the kernel in (2.1);

- the method proposed by Hosono in 1981 [69], more recently referred to as the Fast Inverse Laplace Transform (FILT) method, is based on the approximation of the kernel in (2.1) by a trigonometric hyperbolic function.

Although these two methods are suitable for both EM and circuit modeling areas, the former has become more popular in TD circuit analysis and the latter in the transient EM modeling of antennas and microwave devices. Moreover, the NILT/-FILT techniques represent a valid alternative to the well-established Inverse Fast Fourier Transform (IFFT) method. Indeed, in order to restore aberrations-free TD results starting from an FD ($s = j\omega$) discrete representation of a given system, it is required to compute the system response solution over a pertinent frequency range using an appropriate number of frequency samples on the imaginary axis of the complex plane. These requirements often lead to significant computational efforts. On the contrary, NILT/FILT techniques return the TD response by taking advantage

of Cauchy's theorem that requires computing the response only on the singularities of the kernel. This implies that a reduced number of computations need to be performed in the complex plane.

This chapter is devoted to the presentation of the main results obtained through the employment of the two mentioned ILT techniques (NILT and FILT) to PEEC models. The main features of the NILT technique and its application to PEEC models are presented in Sec. 2.1 and 2.2, respectively. Subsequently, the computational advantages brought by the improvement of NILT, called NILTn, are discussed in Sec. 2.3. Finally, the description and the application of FILT to PEEC models are widely described in Sections 2.4 and 2.5 .

2.1 The Numerical Inversion of the Laplace Transform for circuit transient analysis

As mentioned before, the NILT technique is based on the approximation of the exponential kernel in (2.1) through its Padé approximant [70], leading to:

$$x_{N,M}(t) = \frac{1}{j2\pi t}\int_{\gamma-j\infty}^{\gamma+j\infty} X\left(\frac{z}{t}\right) E_{N,M}(z)dz \tag{2.2}$$

where the change of variable $z = st$ is assumed, being $x_{N,M}(t)$ the approximated TD circuit output of interest. The exponential function e^z in NILT is approximately evaluated using Padé functions of the usual form

$$\begin{aligned} e^z \approx E_{N,M}(z) = \frac{P_N(z)}{Q_M(z)} = \\ \frac{\sum_{i=0}^{N}(M+N-i)!(\binom{N}{i})z^i}{\sum_{i=0}^{M}(-1)^i(M+N-i)!(\binom{M}{i})z^i} = \sum_{i=1}^{M}\frac{K_i}{z-z_i} \end{aligned} \tag{2.3}$$

where $P_N(z)$ and $Q_M(z)$ are polynomials of order N and $M \geq N+2$, respectively; z_i and K_i denote the poles and residues of the rational function $\frac{P_N(z)}{Q_M(z)}$, respectively. It is possible to demonstrate that the Padé approximant $E_{N,M}(z)$ has the first $M+N+1$ terms of its Taylor's expansion exactly equal to the Taylor's expansion of e^z [71]. The choice $M = N+2$ has been shown to guarantee the solution stability [72]. By enclosing the integral along on the infinite arc in the right-half plane, we avoid the need to know the specific locations of the poles of the circuit. Only the poles of the Padé approximation of $e(z)$ contribute to the value of the integral. A sufficient condition for the integral along the semicircle infinite arc in the right-half plane to vanish is that $M >= N+2$. As far as this condition is satisfied, the integral on the arc has no effect on the accuracy of NILT. It is important to mention that the Padé approximation has to be programmed only once with high accuracy for variable degrees. Hence, the same formulation can be used for different problems. Finally, the integral (2.2) is evaluated using closed path Cauchy integration around the poles of $E_{N,M}(z)$ in the right half plane and $x_{N,M}(t)$ can be evaluated as

$$x_{N,M}(t) = -\frac{1}{t}\sum_{i=1}^{W}\mathrm{Re}\{K_i X\left(\frac{z_i}{t}\right)\} \tag{2.4}$$

where

$$W = \begin{cases} M/2, & \text{if } M \text{ is even} \\ (M+1)/2 & \text{if } M \text{ os odd.} \end{cases} \tag{2.5}$$

When M is odd eq. (2.4) can also be expressed as:

$$x_{N,M}(t) = -\frac{1}{t}\sum_{i=1}^{\frac{M-1}{2}} 2\mathrm{Re}\{K_i X\left(\frac{z_i}{t}\right)\} - \frac{1}{t}K_0 X\left(\frac{z_0}{t}\right) \tag{2.6}$$

because the residue-pole duo (K_0, z_0) is real, while the others couples are complex-conjugate [72]; In the Padé approximation, $M = 3$ to 8 poles are usually sufficient to accurately estimate a time response. In what follows, M will be taken as even assuming that odd values can be treated in a similar manner. Since, the Padé approximation of the exponential function in terms of rational function of order N/M matches the first $(N + M + 1)$ terms of the Taylor series expansion, higher values of M and N lead to better accuracy on the TD. However, this comes at the expense of increasing the computational cost. As can be seen from Eq. (2.4), evaluation of the response at a given time point requires computing the frequency response at $M/2$ complex frequencies. Those $M/2$ points are pre-specified, problem-independent points in the complex-domain, namely, points that coincide with the poles of the rational function of $E_{N,M}(z)$. It is also to be noticed that the evaluation at a specific time does not depend on the response at previous time points. This is fundamentally different for time-stepping algorithms where the evaluation of previous time points are used to evaluate the next time-point. Of course, time-stepping results in an accumulation of errors with time.

For illustrative purposes, in Fig. 2.1 are reported two different sets of poles of the kind z_i/t: s_6 and s_{12}, corresponding respectively to the choices: $M = 6$ and $M = 12$, with $N = M - 2$. The two sets are computed over the same generic time interval: $[1 - 5]$ ns. It is clear that, fixing a time sample, the higher is the integer M, the wider is the bandwidth covered by the set of poles. Moreover, it is to be noticed that going forward with the evaluation time, the bandwidth covered by each set tends to shrink around the origin of the complex plane.

The main drawback of the technique is that the achieved inversion formula (2.4) is very accurate for small values of time, but errors grow with time. This advantage

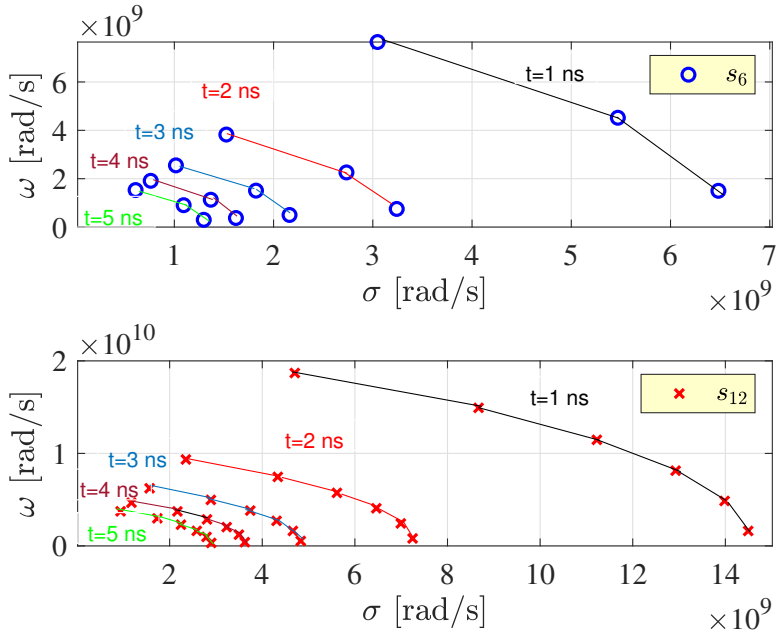

Figure 2.1: Two Padé poles sets moving in the complex plane as the evaluation time increases.

is shown by the error formula [72]

$$x(t) - x_{N,M}(t) = \Psi_{N,M} \frac{d^{N+M+1}}{dt^{N+M+1}} x(t)\Big|_{t=0} t^{N+M+1} + \mathcal{O}(t^{N+M+2}) \tag{2.7}$$

where:

$$\Psi_{N,M} = \frac{(-1)^M M! N!}{(M+N)! \cdot (M+N+1)!} \tag{2.8}$$

Moreover, by the inspection of (2.7) it is clear that the error is related to the shape of the function that has to be inverse-transformed, being more severe when dealing with functions with small rising times or exhibiting a marked impulsive nature. As discussed earlier, the higher the parameter M (and hence N) is chosen, the smaller the error will be, and this is clearly reflected also in (2.7). Unfortunately, it is not feasible to employ arbitrarily large values of M without that rounding errors in the residues K_i affect significantly the solution. This issue is easily explained through a simple example regarding the NILT-based computation of the function $f(t) = \sin(\omega t)$, with $\omega = 6.28 \cdot 10^9$ rad/s. In Fig. 2.2 it is shown that employing

$M = 24$ for the inverse transform guarantees a good accuracy until to 6 ns but is not enough for larger times. In order to preserve the accuracy over the entire time

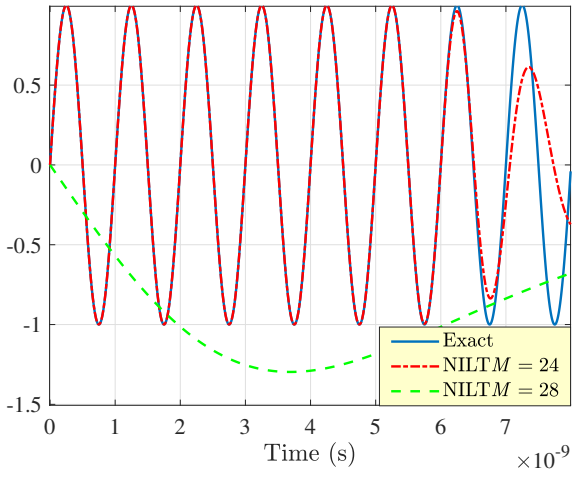

Figure 2.2: NILT-based computation of the sin function.

window, an option is to increase further the number of terms in the summation (2.4) choosing $M = 28$, but round errors in the high Padé residues blow up the solution (in this case the NILT results are scaled by a 10^{-11} factor). Hence, for this example, the choice is limited to values $M < 28$. Obviously, this is valid for general inverse Laplace transforms: every inversion has its expansion limit when approached through the Padé method.

2.2 The Numerical Inversion of the Laplace Transform applied to PEEC models

In the previous chapter it has been shown that collecting the PEEC circuit equations, written in the Laplace domain assuming zero initial conditions, it is possible to obtain the following compact matrix MNA representation:

$$\begin{bmatrix} -\mathbf{A} & -(\mathbf{Z}(s) + s\mathbf{L}_p(s)) \\ \mathbf{Y}_{le} + s\mathbf{P}^{-1}(s) & -\mathbf{A}^T \end{bmatrix} \cdot \begin{bmatrix} \mathbf{\Phi}(s) \\ \mathbf{I}(s) \end{bmatrix} = \begin{bmatrix} \mathbf{V}_0(s) \\ \mathbf{I}_s(s) \end{bmatrix}. \tag{2.9}$$

It is to be remarked that $\mathbf{Z}(s)$ is the generalized impedance diagonal matrix accounting for the self impedance of the volume branches both of the conductor and the dielectric type. Therefore, depending on the nature of the branch i, the ith diagonal entry $Z_i(s)$ will be described by a resistive or a capacitive impedance. Hence, decomposing the matrix, we can write:

$$\mathbf{Z}(s) = \mathbf{R} + \frac{1}{s}\mathbf{C}_d^{-1} \tag{2.10}$$

being $\mathbf{R}$ the resistances matrix and $\mathbf{C}_d$ the excess capacitances matrix.

Such kind of representation results in an algebraic system of equations that can be schematized as:

$$\mathbf{A}(s)\mathbf{X}(s) = \mathbf{U}(s) \tag{2.11}$$

being $\mathbf{A}(s)$ the characteristic matrix of the system, $\mathbf{X}(s)$ the unknowns vector and $\mathbf{U}(s)$ the vector containing the sources acting on the system.

As long as it is desired to obtain the TD vector $\mathbf{x}(t)$ associated to its Laplace counterpart $\mathbf{X}(s)$ in an assigned time window of evaluation, it is clear that, according to (2.4), for each time sample t it is required a number of $M/2$ evaluations of the system (2.11) on the complex plane, over known points defined by the Padé poles. Hence, the computational complexity appears to be strictly connected to the number of time samples employed. On the other hand, we have seen that, unlike time-stepping solvers, using NILT the number of samples involved in the computation (and hence the time-step) does not affect the accuracy of the obtained solution.

In operational terms, the inversion algorithm can be built on a digital computer by a slight modification of a yet existing program for frequency domain analysis of linear networks, without disposing particular structural changes. Moreover, since each complex plane evaluation is entirely independent from the others, the process is "embarassingly parallel", that is it is possible to resort to the parallel calculus subdividing the entire computation in work packages and delivering each work package to a "worker". The maximum number of workers that work in parallel on each work package depends on the number of cores of the digital computer.

For analysis purposes, it is useful to arrange the system (2.9) in the standard descriptor form. This can be accomplished introducing a new variable vector $\mathbf{V}_d(s)$ containing the capacitive voltage drops across the volume dielectric cells and noting that $\frac{1}{s}\mathbf{C}_d^{-1}\mathbf{I}(s) = \mathbf{\Gamma}^T\mathbf{V}_d(s)$, being $\mathbf{\Gamma}$ a matrix introduced to select the dielectric branches from the entire set of branches. Following this procedure and assuming zero initial conditions it is immediate to obtain from (2.9):

$$\begin{aligned} & s\underbrace{\begin{bmatrix} \mathbf{0} & -\mathbf{L}_p(s) & \mathbf{0} \\ \mathbf{P}^{-1}(s) & \mathbf{0} & \mathbf{0} \\ \mathbf{0} & \mathbf{0} & \mathbf{C}_d \end{bmatrix}}_{\mathbf{C}_{(s)}} \cdot \underbrace{\begin{bmatrix} \mathbf{\Phi}(s) \\ \mathbf{I}(s) \\ \mathbf{V}_d(s) \end{bmatrix}}_{\mathcal{X}_{(s)}} \\ = & -\underbrace{\begin{bmatrix} -\mathbf{A} & -\mathbf{R} & -\mathbf{\Gamma} \\ \mathbf{Y}_{le} & -\mathbf{A}^T & \mathbf{0} \\ \mathbf{0} & -\mathbf{\Gamma}^T & \mathbf{0} \end{bmatrix}}_{\mathbf{G}} \cdot \underbrace{\begin{bmatrix} \mathbf{\Phi}(s) \\ \mathbf{I}(s) \\ \mathbf{V}_d(s) \end{bmatrix}}_{\mathcal{X}_{(s)}} \\ & + \underbrace{\begin{bmatrix} \mathbb{I}_{n_n} & \mathbf{0} & \mathbf{0} \\ \mathbf{0} & \mathbb{I}_{n_b} & \mathbf{0} \\ \mathbf{0} & \mathbf{0} & \mathbf{0} \end{bmatrix}}_{\mathbf{B}} \cdot \underbrace{\begin{bmatrix} \mathbf{V}_0(s) \\ \mathbf{I}_s(s) \\ \mathbf{0} \end{bmatrix}}_{\mathbf{U}_{(s)}} \end{aligned} \tag{2.12}$$

which can be formalized in a more compact form as:

$$s\mathbf{C}(s) \cdot \mathcal{X}(s) = -\mathbf{G} \cdot \mathcal{X}(s) + \mathbf{B} \cdot \mathbf{U}(s) \tag{2.13}$$

where $\mathbf{C}(s)$ is generally a complex frequency dependent matrix including the potential coefficients $\mathbf{P}(s)$, the partial inductances $\mathbf{L}_p(s)$ and the excess capacitances $\mathbf{C}_d$.

Also, the matrix $\mathbf{G}$ contains the connectivity matrix $\mathbf{A}$ and matrices $\mathbf{R}$ and $\mathbf{Y}_{le}$ represent distributed and lumped losses. The matrices $\mathbb{I}_{n_n}$ and $\mathbb{I}_{n_b}$ are identity matrices of size equal to the number of nodes n_n and branches n_b, respectively. Lumped and distributed input sources are represented by vector $\mathbf{U}(s)$. Finally, $\mathcal{X}(s)$ is the new augmented variables vector (the state vector of the descriptor model).

2.2.1 Quasi-static PEEC models

As argued in the previous chapter, when dealing with electrically small objects the quasi-static assumption is suitable for partial elements, which results in the very simple formulas (1.99) and (1.123). Such assumptions leads the dependence on s to disappear in the matrix $\mathbf{C}(s)$ of the descriptor model (2.12). Hence, it is immediate to verify that the TD counterpart of the system (2.12) is a standard state-space representation:

$$\begin{aligned} & \frac{d}{dt}\underbrace{\begin{bmatrix} \mathbf{0} & -\mathbf{L}_p & \mathbf{0} \\ \mathbf{P}^{-1} & \mathbf{0} & \mathbf{0} \\ \mathbf{0} & \mathbf{0} & \mathbf{C}_d \end{bmatrix}}_{\mathbf{C}} \cdot \underbrace{\begin{bmatrix} \phi(t) \\ \mathbf{i}(t) \\ \mathbf{v}_d(t) \end{bmatrix}}_{\mathbf{x}(t)} \\ = & -\underbrace{\begin{bmatrix} -\mathbf{A} & -\mathbf{R} & -\mathbf{\Gamma} \\ \mathbf{Y}_{le} & -\mathbf{A}^T & \mathbf{0} \\ \mathbf{0} & -\mathbf{\Gamma}^T & \mathbf{0} \end{bmatrix}}_{\mathbf{G}} \cdot \underbrace{\begin{bmatrix} \phi(t) \\ \mathbf{i}(t) \\ \mathbf{v}_d(t) \end{bmatrix}}_{\mathbf{x}(t)} \\ + & \underbrace{\begin{bmatrix} \mathbb{I}_{n_n} & \mathbf{0} & \mathbf{0} \\ \mathbf{0} & \mathbb{I}_{n_b} & \mathbf{0} \\ \mathbf{0} & \mathbf{0} & \mathbf{0} \end{bmatrix}}_{\mathbf{B}} \cdot \underbrace{\begin{bmatrix} \mathbf{v}_0(t) \\ \mathbf{i}_s(t) \\ \mathbf{0} \end{bmatrix}}_{\mathbf{u}(t)} \end{aligned} \tag{2.14}$$

in compact form:

$$\mathbf{C} \cdot \frac{d}{dt}\mathbf{x}(t) = -\mathbf{G} \cdot \mathbf{x}(t) + \mathbf{B} \cdot \mathbf{u}(t) \tag{2.15}$$

being the vector $\mathbf{x}(t)$ the TD counterpart of the Laplace domain unknowns vector $\mathcal{X}(s)$. The Laplace domain version of (2.15), assuming non-zero initial conditions is:

$$(s\mathbf{C} + \mathbf{G})\,\mathcal{X}(s) = \mathbf{B} \cdot \mathbf{U}(s) + \mathbf{C}\mathbf{x}(0) \tag{2.16}$$

and the TD state vector can be recovered from the NILT formula:

$$\boldsymbol{x}_{N,M}(t) = -\frac{1}{t}\sum_{i=1}^{W} \mathrm{Re}\{K_i \mathcal{X}\left(\frac{z_i}{t}\right)\} \tag{2.17}$$

Numerical examples

With the aim of providing an application of the NILT technique a numerical example of NILT applied to a quasi-static PEEC model is presented.

The loaded microstrip

The structure under examination is a 20 cm long stubs loaded microstrip, illustrated in Fig. 2.3. The copper structure, placed over a lossless dielectric substrate with $\varepsilon_r = 4.4$ and thickness 1.6 mm, is composed by a microstrip which is periodically loaded by four microstrip stubs of length 38.5 mm, that are left open at the end of the dielectric. All the signal conductors have a width of 3 mm and a thickness of 35 μm. The distance between the microstrip line and the free edge of the dielectric is 8 mm. The device has two 50 Ω ports placed between the two ends of the main microstrip and the ground plane.

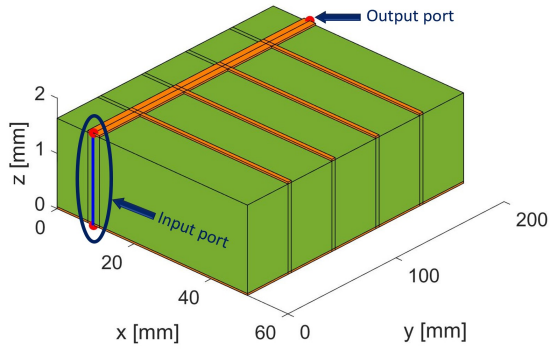

Figure 2.3: Loaded microstrip geometry.

For example purposes the PEEC 3D mesh is selected to satisfy the $\lambda_{min}/30$ condition in the three cartesian directions, being λ_{min} the free-space wavelength at $f_{max} = 500$ MHz. The PEEC model built exhibits 1128 inductive branches, among them 432 are dielectric branches, and 188 potential nodes. The model is excited with a step waveform at one of the two highlighted ports and both the port step responses are then observed. The transient is evaluated in the time window $[0 - 20]$ ns calculating the system (2.16) with zero initial conditions for each t over a set of points of the complex plane dictated by the Padé poles. The input port

step response is obtained via NILT using $M = 6$ and $M = 24$ and compared to a reference solution computed through a time-stepping solver. The results for the input port step response are collected and shown In Fig. 2.4. Considering (2.4),

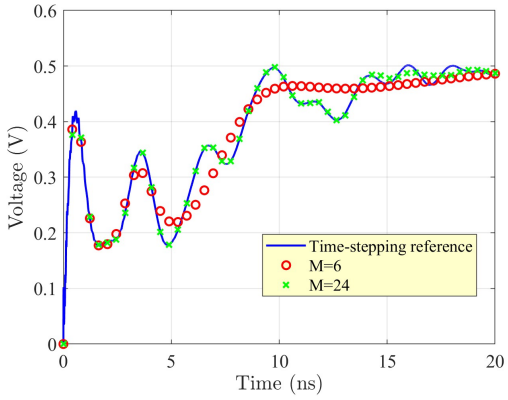

Figure 2.4: Input port step response of the loaded microstrip using two different NILT expansion orders.

using NILT with $M = 6$ means the resolution of the system (2.16), for each fixed time sample, for three different values of the complex variable s. It is evident from Fig. 2.4 that this choice is not adequate to provide a satisfactory accuracy in the time window of evaluation. Therefore, in order to obtain a more accurate step transient, the NILT results are recomputed employing an expansion order $M = 24$ (twelve evaluation per time-sample). This last choice certainly improve the accuracy of the results, but at the cost of increasing four times the computational burden. Analogous considerations are valid for the results of the output non-fed port, depicted in Fig. 2.5.

For completeness, the Padé poles and the corresponding residues for $M = 6$ and $M = 24$ are reported in Tabs. 2.1 and 2.2, respectively.

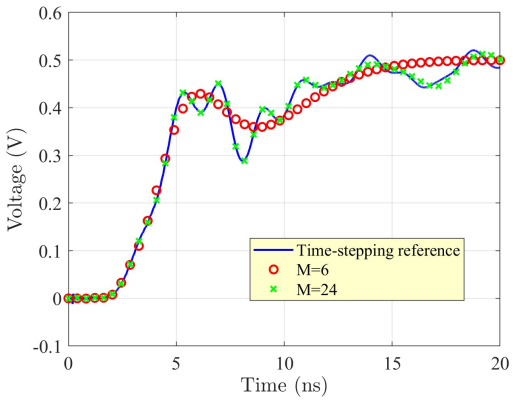

Figure 2.5: Output port step response of the loaded microstrip using two different NILT expansion orders.

Table 2.1: Padé poles and residues for the choice $M = 6$.

Poles	**Value**	**Residues**	**Value**
p_1	$3.048 + 7.65i$	R_1	$9.31 - 13.11i$
p_2	$5.47 + 4.52i$	R_2	$-37.16 + 124.63i$
p_3	$6.48 + 1.50i$	R_3	$27.84 - 315.06i$

The resetting procedure

The NILT method is extremely simple to apply, but, as explained, has the disadvantage that accuracy decreases as time increases. Consequently, to overcome this limitation, it has been found to be very useful to use the method with small time intervals and reset the problem so that in the next evaluation the previous result is considered as the initial point for the new step. Indeed, in lumped network theory, any time can be selected as zero time by taking into account the charges on the capacitors and the currents through the inductors. Those initial conditions are sufficient to reset the problem and move forward to the next computational step without any reference to the previous history of the transient. Practically speaking, given a fixed time-step h and being k the grid index corresponding to a given computation point $t = kh$, it is possible to compute the TD NILT state vector $\boldsymbol{x}_{N,M}(t)$ by evaluating the system (2.16) accounting for the state vector computed at the

Table 2.2: Padé poles and residues for the choice $M = 24$.

Poles	**Value**	**Residues**	**Value**
p_1	$6.73 + 41.54i$	R_1	$-95.77 + 1151.76i$
p_2	$12.44 + 37.01i$	R_2	$-252730.37 - 41804.24i$
p_3	$16.59 + 33.01i$	R_3	$9.5e^6 - 9.7e^6i$
p_4	$19.85 + 29.24i$	R_4	$-2e^7 - 3.12e^8i$
p_5	$22.48 + 25.61i$	R_5	$-1.92e^9 - 3.48e^9i$
p_6	$24.63 + 22.08i$	R_6	$2.64e^{10} + 1.77e^{10}i$
p_7	$26.38 + 18.60i$	R_7	$-1.69e^{11} - 3.07e^{10}i$
p_8	$27.77 + 15.17i$	R_8	$6.55e^{11} - 1.25e^{11}i$
p_9	$28.86 + 11.77i$	R_9	$-1.65e^{12} + 9.54e^{11}i$
p_{10}	$29.65 + 8.39i$	R_{10}	$2.76e^{12} - 3.06e^{12}i$
p_{11}	$30.17 + 5.03i$	R_{11}	$-2.87e^{12} + 6.19e^{12}i$
p_{12}	$30.43 + 1.68i$	R_{12}	$1.26e^{12} - 8.68e^{12}i$

previous step $\boldsymbol{x}_{N,M}[(k-1)h]$. Hence for the computation in t, the Laplace system to be inverted is:

$$(s\mathbf{C} + \mathbf{G})\,\mathcal{X}\,(s) = \mathbf{B} \cdot \mathbf{U}\,(s) + \mathbf{C}\mathbf{x}\,[(k-1)h] \tag{2.18}$$

and the unknowns vector can be expressed as:

$$\mathcal{X}\,(s) = (s\mathbf{C} + \mathbf{G})^{-1}\,\mathbf{B} \cdot \mathbf{U}\,(s) + \mathbf{C}\mathbf{x}\,[(k-1)h] \tag{2.19}$$

to which it is applied the following modified NILT formula:

$$\boldsymbol{x}_{N,M}(t = kh) = -\frac{1}{h}\sum_{i=1}^{W} \mathrm{Re}\{K_i \mathcal{X}\left(\frac{z_i}{h}\right)\} \tag{2.20}$$

The procedure can be repeated for each time-step. Otherwise, it is possible to perform a single reset at a chosen time point t_0, applying the standard NILT procedure to the system with zero initial conditions in the range $t = [t_{in}, t_0]$, saving the state vector $\boldsymbol{x}_{N,M}(t_0)$ and using it to re-initialize the procedure for the all computations in the range $t = [t_0, t_{end}]$. Obviously, the number of reset points can be arbitrarily

chosen. It is important to highlight that in case of continuous resetting, the system has to be evaluated only once over the set of poles z_i/h and each computational step consists on an update of the RHS products in (2.18).

In order to explore the efficiency of the resetting procedure, the step response of the loaded microstrip structure illustrated in Fig. 2.3 is reconsidered. The same PEEC model is generated and NILT with $M = 6$ is applied in conjunction with the continuous resetting procedure already explained. It is evident from Figs. 2.6 and 2.7 that there is a perfect superposition of the NILT and the reference results using $M = 6$. Hence, using the resetting it is not required to increase the computational complexity to obtain an accurate transient in the overall time window.

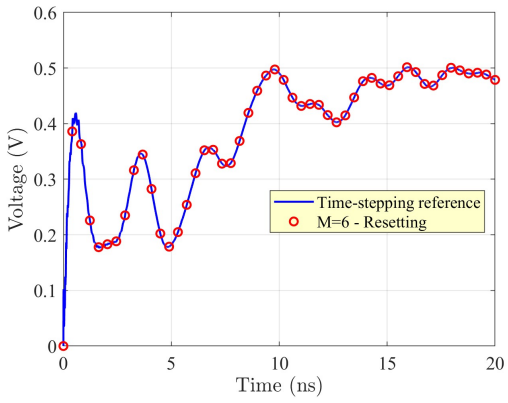

Figure 2.6: Input port step response of the loaded microstrip using NILT assisted by the resetting procedure.

2.2.2 Retarded PEEC models

When dealing with electrically long structures (or high frequency excitations) the quasi-static assumption on partial elements does not hold anymore. For this reason, a full-wave representation is needed, which means that the model mutual couplings expressed by the partial inductances and the coefficients of potential are those described in (1.98),(1.122) containing the free-space Green's function. At a system level, this is reflected by the s-dependence of the matrix $\mathbf{C}(s)$ in (2.12). Therefore, the standard state-space model (2.14) is not a valid TD represenation in such case.

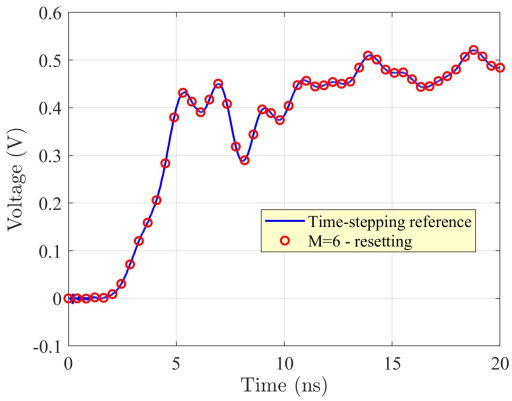

Figure 2.7: Output port step response of the loaded microstrip using NILT assisted by the resetting procedure.

The full-wave representation requires the computation of the integrals appearing in (1.98),(1.122) for each frequency sample for FD models, and for each point of the complex plane in case of NILT computations. With the aim of lighten the computational efforts in building PEEC models in the complex frequency domain, some approximation are usually employed. As shown in the previous chapter, the center to center approximation expressed in (1.100),(1.124) concentrate the distributed retardation effects in one single retardation related to the center to center distance between the two domains, while the Taylor's approximation (1.104), (1.127) is based on the Taylor's series expansion of the Green's function exponential inside the interaction integrals. Such kind of approximations permit avoiding the evaluation of the integrals for each complex frequency sample.

Stability considerations

As argued in the introduction of this chapter, the various approximations involving the exponential terms in the Green's functions can be the cause of instability issues rising in the direct TD resolution of the retarded PEEC system. Indeed, unstable oscillations are often observed in the TD responses of approximated retarded models. Such unstable responses are caused by the fact that might exist model's poles exhibiting a positive real part, leading to unstable system modes that evolve with

continuously growing up oscillations. The residues for such poles are very small since they are artificial and are not part of the actual problem solution. For this reason, we speak more properly of the so called "late-time instability", because the unstable oscillations usually become large enough only later in time.

In order to illustrate this issues, a small problem consisting in the PEEC EM model of a thin metal sheet of width 2 cm and length 10 cm is proposed. The simplest mesh related to this structure consists in two inductive branches that connect three potential surfaces, giving rise to the equivalent circuit illustrated in Fig. 2.8. The circuit is terminated through a resistor R_L.

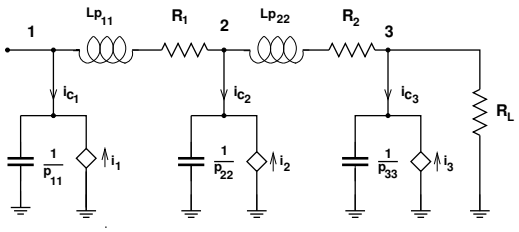

Figure 2.8: Simple example PEEC circuit for high frequency poles testing.

After several passages, for this specific problem, the characteristic matrix can be rearranged as:

$$\mathbf{A}(s) = \begin{bmatrix} \frac{s}{P_{11}} & 0 & \frac{P_{13}(s)}{P_{11}R_L} & 1 - \frac{P_{12}(s)}{P_{11}} & \frac{P_{12}(s)}{P_{11}} - \frac{P_{13}(s)}{P_{11}} \\ 0 & \frac{s}{p_{22}} & \frac{P_{23}(s)}{P_{22}R_L} & -1 + \frac{P_{21}(s)}{P_{22}} & 1 - \frac{P_{23}(s)}{P_{22}} \\ 0 & 0 & \frac{s}{P_{33}} + \frac{1}{R_L} & \frac{P_{13}(s)}{P_{33}} - \frac{P_{23}(s)}{P_{33}} & -1 + \frac{P_{23}(s)}{P_{33}} \\ 1 & -1 & 0 & -(R_1 + sL_{p_{11}}) & -sL_{p_{12}}(s) \\ 0 & 1 & -1 & -sL_{p_{21}}(s) & -(R_2 + sL_{p_{22}}) \end{bmatrix} \tag{2.21}$$

while the known term reads as:

$$\mathbf{U}(s) = \begin{bmatrix} I_i & \frac{P_{21}(s)}{P_{22}} I_i & \frac{P_{31}(s)}{P_{33}} I_i & 0 & 0 \end{bmatrix}^T \tag{2.22}$$

The partial mutual elements, $L_{p_{12}}(s)$, $P_{12}(s) = P_{21}(s), P_{13}(s) = P_{31}(s)$ and $P_{23}(s) = P_{32}(s)$ are assumed dependent on the s Laplace variable, while the s-dependence is neglected for self partial elements. A self resistance $R_1 = R_2 = 10$

mΩ has been assumed for each of the two cells. The poles of the circuit can be computed as the zeros of the determinant of matrix $\mathbf{A}(s)$. Figure 2.9 shows the poles in the complex plane using a first-order Taylor series expansion of the exponential term in the Green's function presented in (1.104) along with the poles obtained using the quasi-static assumption. It is evident that even for this small example, unstable poles appear when the exponential retardation term is considered and, in this case, approximated by a first-order Taylor series expansion.

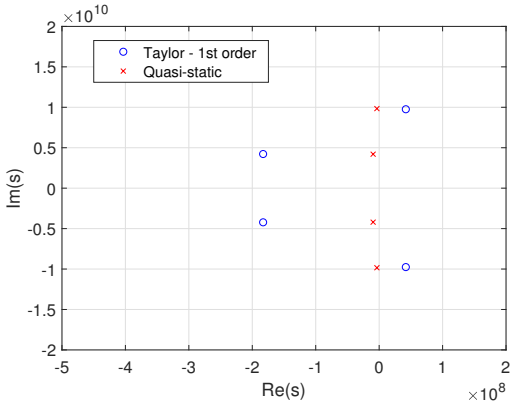

Figure 2.9: Poles in the complex plane using a first order Taylor series expansion of the exponential term in the Green's function.

When the direct TD simulation of a PEEC model exhibiting poles with positive real parts is run through conventional time marching algorithms, it is very likely, depending on the size of the time-step, that the unstable behavior will manifest itself in the solution. On the other hand, the NILT technique is based on the evaluation of the system in the complex plane only over the Padé poles, i.e. the TD waveforms are totally independent on the various poles of the model. Consequently, as it is often said, the NILT technique is able to filter the unstable poles, always providing aberrations-free and bounded responses, preserving their physical meaning.

Numerical examples

With the aim of underlying the advantages offered by the NILT method with respect standard time-stepping solvers in the TD resolution of retarded PEEC models, two

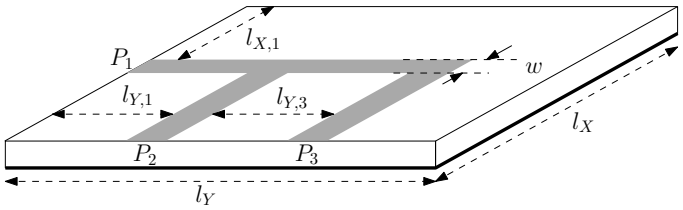

Figure 2.10: Structure of the three-port micro-strip power divider circuit.

numerical examples are presented. In the following examples, the retarded PEEC models are all obtained through the center to center approximation.

Three-port microstrip power divider

The three-port micro-strip power-divider circuit shown in Fig. 2.10 is considered in this paragraph. It is assumed that the input at P_1 is excited using a 50 Ω impedance source with a trapezoidal pulse. The other ports P_2 and P_3 are also terminated with 50 Ω. The dimensions of the circuit are [20, 20, 0.5] mm in the $[x, y, z]$ directions. The width of the micro-strips is 0.8 mm and the dielectric is lossless exhibiting a relative dielectric constant $\varepsilon_r = 2.2$. In this example, the Port 1 is excited by a trapezoidal pulse of width 4 ns, rise/fall times 0.2 ns. The equivalent circuit consists of 4216 branches and 1092 nodes.

The NILT algorithm has been run setting the order of the Padé approximation as $M = 16$ (8 poles) at the largest time point. The time window [0-6] ns has been sampled with 120 time samples for visualization purposes. The same problem has been analyzed by a frequency-domain PEEC solver and the time-domain results have been obtained by using the IFFT. For the comparison, further results have been obtained by using a BD2 time-stepping scheme applied to the center to center NDDE PEEC model. Figure 2.11 shows the waveform at the input P_1. Since the results at the ports P_2 and P_3 are very similar, we only show the result for port P_3 in Fig. 2.12.

We observe that all three methods agree well for this example problem. Not surprising, the late time instability dominates the solution for the time-stepping solution. The late-time instability shows up in the solution after about 1 ns in time.

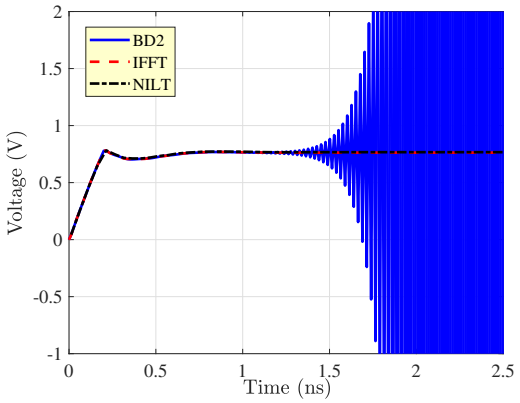

Figure 2.11: Port 1 voltage - power divider.

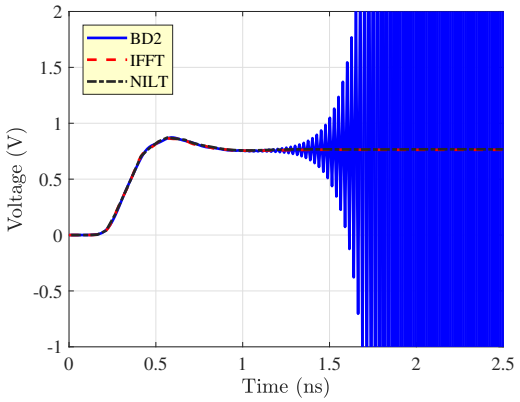

Figure 2.12: Port 3 voltage - power divider.

It is also worth mentioning that it is necessary to use a number of times/frequency samples quite high to get a reasonable accuracy of the IFFT results compared to the NILT ones. Figure 2.13 shows the error of the IFFT-based results compared to NILT for an increasing number of time samples. It is clearly seen that increasing the time samples from 115 to 800 allows to reduce the difference with respect to NILT.

As an additional test for this problem, we apply an approximated unit step response to Port 1 and the output waveform is observed at Port 2. In NILT, the first time point determines how steep the step is. The same signal is applied again for the three methods and the resultant waveforms at Port 2 are shown in Fig.

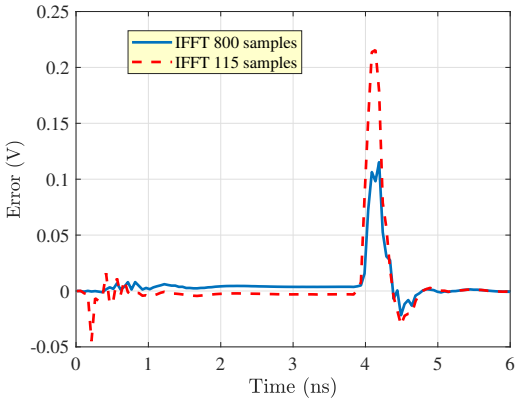

Figure 2.13: Port 3 voltage error of IFFT compared to NILT - power divider.

2.14. As expected, the result from the time-stepping method results in an unstable solution at an earlier time. Further, the inverse fast Fourier transform (IFFT) of port 2 voltage and the NILT approach result in reasonable waveforms. Both NILT and IFFT are stable and in a good agreement and are stable in spite of the fast input waveform result. As a further accuracy test, an approximate impulse response

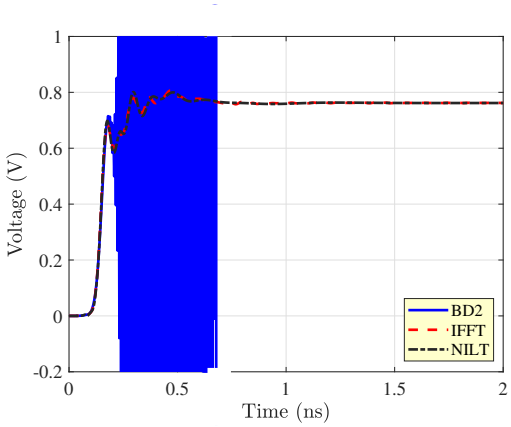

Figure 2.14: Port 2 step response with a higher bandwidth step - power divider.

which is the derivative of the step response has been computed. The good accuracy at the output port P_2 is shown in Fig. 2.15, confirming a good agreement of NILT with the IFFT. We see a slightly earlier time where the time-stepping is observed.

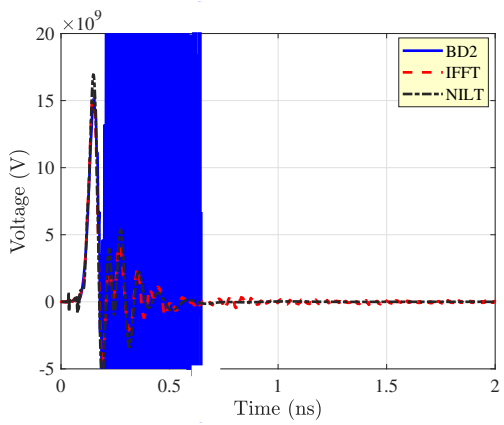

Figure 2.15: Port 2 impulse response with a higher bandwidth step - power divider.

Four-layer board

In this example, a four-layer 10 cm by 16 cm board structure shown in Fig. 2.16 is modeled. The $h = 700$ μm black layers are dielectrics with $\varepsilon_r = 4.1$. The conductors are $t = 50$ μm metal layers. Each of the numbered vertical lines in the side views in Fig. 2.16 represents a 100 mΩ connection port between a pair of metallic planes. In a somewhat arbitrary way, a voltage trapezoidal pulse is applied to port 1 while the voltage at the different ports is observed. The resulting equivalent circuit comprises 4480 branches and 616 nodes. We again applied the three different solver techniques to study the coupling results.

In the test, Port 1 is driven by a voltage trapezoidal pulse with rise time 3 ns and width 20 ns in series to the resistor.

Figures 2.17-2.18 show the first two port voltages comparing the results obtained using the time-stepping method through the BD2 scheme, the inverse fast Fourier transform (IFFT) and the NILT approach (NILT) of order $M = 16$ (8 poles). The time-stepping method becomes unstable after about 5 ns. At the first three ports which are located between the driven planes (Figs. 2.17-2.18), the IFFT and NILT are in a good agreement. The voltages obtained through IFFT at the ports 4-6 between the non-driven planes are affected by numerical oscillations around the NILT voltages. Figure 2.19 shows the voltage at port 6. Hence, it is clearly seen that the NILT approach results to be the most reliable method unlike the time-

stepping approach which is affected by instability and the IFFT-based approach which suffers from poor accuracy unless small time steps are adopted, resulting in a wideband frequency analysis, and large time windows are used leading to small frequency steps and, as a consequence, to many frequency samples.

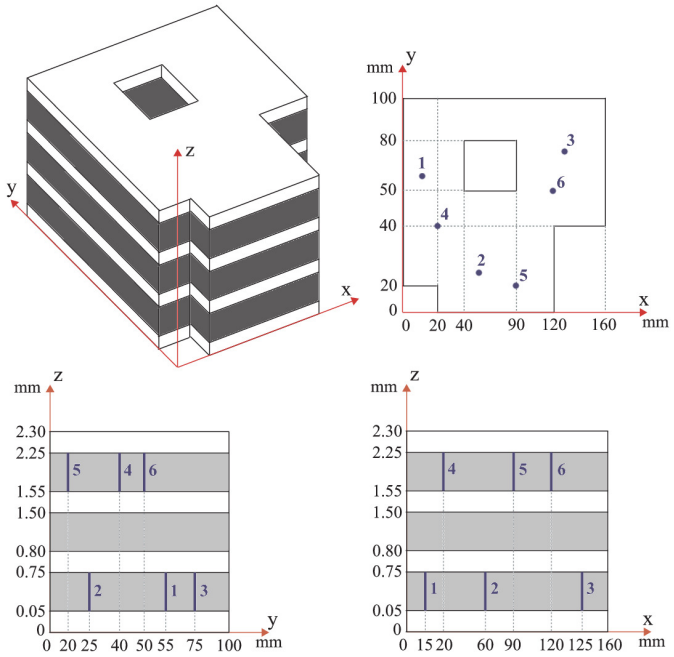

Figure 2.16: Geometry of the four-layer power bus.

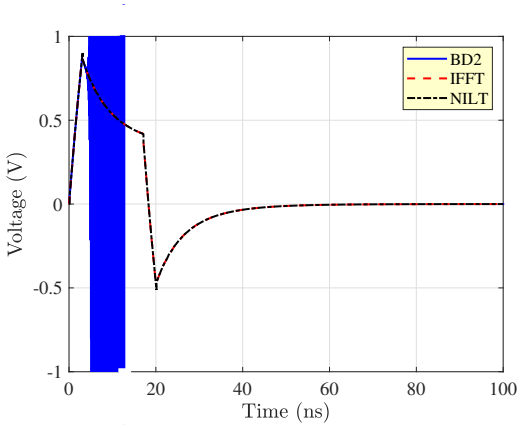

Figure 2.17: Port 1 voltage - four-layer power bus.

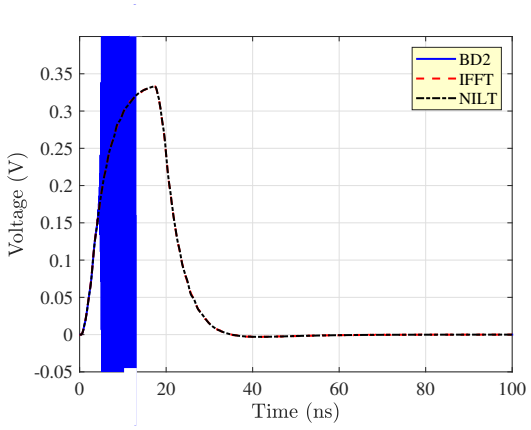

Figure 2.18: Port 2 voltage - four-layer power bus.

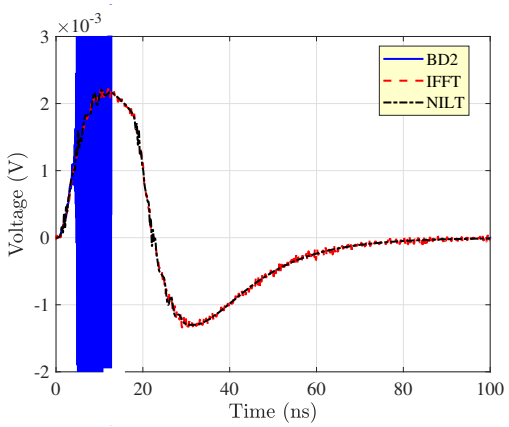

Figure 2.19: Port 6 voltage - four-layer power bus.

2.3 The Modified Numerical Inversion of the Laplace Transform

The NILT technique has demonstrated to be a powerful numerical tool for transient evaluations. As shown in the final formula (2.4), its implementation is grounded in the frequency domain and it is quite easy. In paragraph 2.2.2 are reported several numerical examples highlighting the usefulness of NILT when applied to retarded PEEC models, providing always stable and aberrations-free results if compared to standard time-stepping techniques and the IFFT. However, in several cases the

transients to be evaluated might be significant for long time periods and, hence, a good accuracy in larger time windows should be needed. The most immediate solution could be to increase the number of terms in the summation (2.4) for high values of t, reaching a better accuracy at this samples. This kind of strategy is surely valid, but at the cost of increasing the computational efforts, since the PEEC system (2.12) has to be solved over an increased number of Padé poles. Another way is represented by the achievement of a modified NILT formula which, fixed the computational burden, provides an higher accuracy order or, equivalently, fixed the accuracy degree shows a reduced computational burden. This possibility has been firstly investigated in [72], where a modified NILT formula is proposed. In particular, NILT is reformulated to scale down the approximation error in (2.7) by a factor of $(n+1)^{N+M}$, where n is an integer $n \geq 1$, i.e.:

$$x(t) - x_{N,M}^{[n]}(t) = \frac{\Psi_{N,M}}{(n+1)^{N+M}} \frac{d^{N+M+1}}{dt^{N+M+1}} x(t)\bigg|_{t=0} t^{N+M+1} + \mathcal{O}(t^{N+M+2}) \tag{2.23}$$

The new formulation was conveniently termed NILTn to distinguish it from the traditional NILT, which was referred to as NILT0. The NILTn approach provided the following computational advantage over NILT0: for the roughly the same computational cost, i.e., for a given value of M, NILTn reduces the error of approximation by several orders of magnitudes. Alternatively put, for a given acceptable level of approximation accuracy, NILTn reduces the computational cost needed in using NILT0 by requiring smaller value of the order M of the Padé approximant. For the purposes of this project, the choices $n = 1$ and $n = 2$ have been found very effective to improve the accuracy of the NILT solution, hence we will focus directly on these particular choices. In particular, for the choice $n = 1$, the NILT1 formula can be obtained as [72]:

$$x_{N,M}^{[1]}(t) = -\frac{8}{t} \sum_{i=1}^{M/2} \mathrm{Re} \left(\frac{K_i^2}{t} \frac{\mathrm{d}X(s)}{\mathrm{d}s} + K_i X(s) \sum_{\substack{j=1 \\ j \neq i}}^{M} \frac{K_j}{z_i - z_j} \right) \Bigg|_{s=\frac{2z_i}{t}} \tag{2.24}$$

for the choice $n = 2$, the NILT2 formula reads [72]:

$$x^{[2]}_{N,M}(t) = -\frac{9}{t}\sum_{i=1}^{M/2}\mathrm{Re}\left(\frac{3\tilde{K}_i^3}{8t^2}\frac{\mathrm{d}^2X(s)}{\mathrm{d}s^2} + \frac{3\tilde{K}_i^2}{2t}\frac{\mathrm{d}X(s)}{\mathrm{d}s}\sum_{\substack{j=1\\ j\neq i}}^{M}\frac{K_j}{z_i - z_j} + \right. \tag{2.25}$$

$$\left. + X(s)\left(\tilde{K}_i\sum_{\substack{j=1\\ j\neq i}}^{M}\sum_{\substack{\nu=1\\ \nu\neq i}}^{M}\frac{K_jK_\nu}{(z_i - z_j)(z_i - z_\nu)} - \frac{\tilde{K}_i^2}{2}\sum_{\substack{j=1\\ j\neq i}}^{M}\frac{K_j}{(z_i - z_j)^2}\right)\right)\Bigg|_{s=\frac{3z_i}{t}}$$

being $\tilde{K}_i = 2K_i$.

With the aim of illustrating the benefits brought by NILTn in terms of accuracy we reconsider the numerical inverse transform of the same sinusoidal waveform introduced in Paragraph 2.1. The function is built starting from its known Laplace transform using NILT0, NILT1 and NILT2, using an expansion with $M = 6$. Hence, the same Padé poles and residues are used for the three methods. The results are illustrated in Fig. 2.20 where it is evident that increasing the index n the approximated inverse transforms tend to overlap with the exact function for longer times.

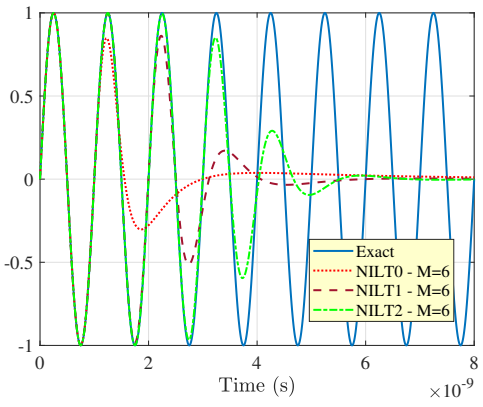

Figure 2.20: Sinusoidal waveform rebuilding varying n.

2.3.1 The Modified Numerical Inversion of the Laplace Transform applied to retarded PEEC models

The objective in this section is to show how the NILTn technique can be applied in the context of retarded PEEC circuits. We will refer to the special case of $n = 2$.

Let's consider a PEEC system expressed in the complex frequency domain in the compact form (2.11):

$$\mathbf{A}(s)\mathbf{X}(s) = \mathbf{U}(s) \tag{2.26}$$

To start the derivation process, we consider the first order derivative. This derivative can be found by differentiating both sides of (2.11) and rearranging the terms to obtain:

$$\frac{d\mathbf{X}}{ds} = \mathbf{A}^{-1}\left(\frac{d\mathbf{U}}{ds} - \frac{d\mathbf{A}}{ds}\mathbf{X}\right) \tag{2.27}$$

The computation of $d\mathbf{A}/ds$ calls for the computation of $d\mathbf{L}_p/ds$, $d\mathbf{P}^{-1}/ds$ and $d\mathbf{Z}/ds$. The first derivative of the inverse of coefficient potential matrix $\mathbf{P}^{-1}$ can be obtained from $\mathbf{P}(s)$ as:

$$\frac{d\mathbf{P}^{-1}}{ds} = -\mathbf{P}^{-1}\frac{d\mathbf{P}}{ds}\mathbf{P}^{-1} \tag{2.28}$$

Moreover, the second order derivative is necessary and can be found taking the second derivatives of both sides of (2.11) and rearranging the terms:

$$\frac{d^2\mathbf{X}}{ds^2} = \mathbf{A}^{-1}\left(\frac{d^2\mathbf{U}}{ds^2} - 2\frac{d\mathbf{A}}{ds}\frac{d\mathbf{X}}{ds} - \frac{d^2\mathbf{A}}{ds^2}\mathbf{X}\right) \tag{2.29}$$

Hence, the computation of $d^2\mathbf{L}_p/ds^2$, $d^2\mathbf{P}^{-1}/ds^2$ and $d^2\mathbf{Z}/ds^2$ is required. In particular, for the second derivative of the inverse coefficient of potential matrix, we can write:

$$\frac{d^2\mathbf{P}^{-1}}{ds^2} = -\mathbf{P}^{-1}\left(\frac{d^2\mathbf{P}}{ds^2}\mathbf{P}^{-1} + 2\frac{d\mathbf{P}}{ds}\frac{d\mathbf{P}^{-1}}{ds}\right) \tag{2.30}$$

In the following, we assume the center to center approximation. If we write (1.100), (1.124) respectively as:

$$L_{p_{i,j}}(s) = L^{qs}_{p_{i,j}} e^{-s\tau^{cc}_{i,j}} \tag{2.31}$$

$$P_{\ell,m}(s) = P^{qs}_{\ell,m} e^{-s\tau^{cc}_{\ell,m}} \tag{2.32}$$

where $L^{qs}_{p_{i,j}}$ and $P^{qs}_{\ell,m}$ are the static single partial elements, it is possible to express their first derivatives respectively as:

$$\frac{dL_{p_{i,j}}}{ds} = -\tau^{cc}_{i,j} L^{QS}_{p_{m,n}} e^{-s\tau^{cc}_{mn}} \tag{2.33a}$$

$$\frac{dP_{\ell,m}}{ds} = -\tau^{cc}_{\ell,m} P^{QS}_{\ell,m} e^{-s\tau^{cc}_{\ell,m}} \tag{2.33b}$$

and their second derivatives as:

$$\frac{d^2L_{p_{i,j}}}{ds^2} = (\tau^{cc}_{i,j})^2 L^{(qs)}_{p_{i,j}} e^{-s\tau^{cc}_{i,j}} \tag{2.34a}$$

$$\frac{d^2P_{\ell,m}}{ds^2} = (\tau^{cc}_{\ell,m})^2 P^{(qs)}_{\ell,m} e^{-s\tau^{cc}_{\ell,m}} \tag{2.34b}$$

The computation of the first and second order derivatives has to be repeated for each time sample t and for each $\frac{3z_i}{t}$. Thus, fixed M the modified algorithm requires an additional cost with respect to a standard NILT0, since are required the additional computations of $\frac{d\mathbf{X}}{ds}$, $\frac{d^2\mathbf{X}}{ds^2}$.

Hermite interpolation

The above-described NILT2, for PEEC circuits, derives its advantage from the combination of high-order approximation (order $N + M$) and the scaling down of the approximation error by the factor $1/3^{N+M}$ [72]. This advantage enables covering the interval of time-domain simulation with a large step size using a small number of sparsely-spaced points, H, requiring the computation of $\mathbf{X}(s)$ at a limited number of points for s in the complex domain.

However, from a user's standpoint, the savings in simulation time may be viewed as less advantageous if the waveforms obtained lack sufficiently dense points to offer a detailed picture of its behavior. On the other hand, trying to satisfy the requirement of densely populated waveforms using NILT2 will need more computations of $\mathbf{X}(s)$, erasing the gains in simulation time.

The core idea proposed in this regard is to reuse the points generated from the NILT2 technique to construct a polynomial interpolant that fills the gaps between those NILT2 points. This idea is principled on the following identity of the Laplace transform

$$\begin{aligned}\frac{\mathrm{d}^n\mathbf{x}(t)}{\mathrm{d}t^n} &= \mathcal{L}^{-1}\left\{s^n\mathbf{X}(s)-\sum_{\vartheta=1}^{n}\mathbf{x}\left(0\right)^{(\vartheta-1)}s^{n-\vartheta}\right\}\Big|_{t=0}\\ &= \mathcal{L}^{-1}\left\{s^n\mathbf{X}(s)-\sum_{\vartheta=1}^{n-1}\mathbf{x}\left(0\right)^{(\vartheta-1)}s^{n-\vartheta}\right\}\Big|_{t=0}\\ &- \underbrace{\mathcal{L}^{-1}\left\{\mathbf{x}(0)^{n-1}\right\}\big|_{t=0}}_{\mathbf{x}(0)^{(n-1)}\delta(t)\big|_{t=0}=0}\end{aligned} \tag{2.35}$$

where $\mathbf{x}^{(k)}(0)$ defines $\frac{\mathrm{d}^k\mathbf{x}(t)}{\mathrm{d}t^k}$ computed at $t=0$. The above identity provides the means to compute high-order derivatives at the points generated by NILT. The NILT framework is used for this purpose. For simplicity, this process is illustrated for the case of NILT0, which computes the derivatives at the points t_j generated using

$$\begin{aligned}\tilde{x}(t_j)^{(n)} &= \frac{-1}{t_j}\sum_{i=1}^{M/2}2\mathrm{Re}\left(z_i^n k_i\mathbf{X}\left(\frac{z_i}{t_j}\right)\right)\\ &+\frac{1}{t_j}\sum_{i=1}^{M/2}\sum_{\vartheta=1}^{n-1}2\mathrm{Re}\left(z_i^{n-\vartheta}\,\mathbf{x}(0)^{(\vartheta)}\right)\end{aligned} \tag{2.36}$$

(2.36) shows that computing the derivatives at the points $t=t_j$ can be achieved by reusing the values for $\mathbf{X}(s)$ computed at $s=\frac{z_i}{t_j}$. This observation confirms that computing the derivatives will not require any significant computational burdens. Beyond the computation of the time-domain derivatives at $t=0$, which can be done as shown in [73], the general implementation in the context of NILTn is provided in [74].

With those derivatives computed as shown above, a polynomial interpolant of the Hermite type can be constructed that produces the waveform in between the points t_j, $j=1,\cdots,H$. A Hermite interpolant is a polynomial that matches a given function and its higher-order derivatives at a selected set of points. The work presented in [75] shows that the coefficients of such polynomials can be explicitly expressed

in terms of the values of the functions, its derivatives, and intervals between the interpolation points. This approach [75] is then used to form the polynomial, which can be sampled at arbitrarily high density time points with negligible computational overhead.

Numerical examples

With the aim of validating the modified NILT technique, several numerical examples concerning the application of NILT2 in conjunction with the Hermite interpolation applied to PEEC retarded models are presented in this section. For comparison, the NILT2 results are presented with an emphasis on the main computational advantages brought with respect to the standard NILT0. The reference results are generated with the IFFT routine applied to the results coming from the frequency domain evaluation of the same retarded PEEC models.

Three-port microstrip power-divider

The three-port micro-strip power-divider (PWD) circuit shown in Fig. 2.21 has been modeled. In this example, we assume that the input port P_1 is excited using a 50 Ω impedance source with a trapezoidal pulse with width 2 ns, rise/fall times 0.4 ns. The other ports P_2 and P_3 are also terminated with 50 Ω. The dimensions of the circuit are [20, 20, 0.5] mm in the $[x, y, z]$ directions. The width of the micro-strips is 0.8 mm and the relative dielectric permittivity is $\varepsilon_r = 2.2$. The spectrum of the source is significant up to around 8 GHz. Hence, the PEEC model is built so to be accurate up to this frequency. At 8 GHz, the minimum free-space wavelength is $\lambda_{min} = 37.5$ mm, and the maximum dimension of the mesh elementary volumes and surfaces is set so that it does not exceed the quantity:

$$D_{MAX} = \frac{\lambda_{min}}{30} \tag{2.37}$$

Applying this constraint on the mesh, the resulting equivalent circuit consists of 3428 branches and 874 nodes.

All the NILT final port responses are built starting from the knowledge of the port ramp responses. In particular, a ramp signal source with the same slope of the

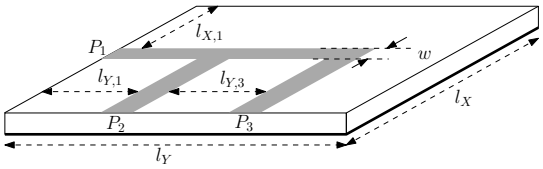

Figure 2.21: Microstrip PWD circuit.

trapezoidal rising edge is applied at the input port and the corresponding responses are observed at the output ports. Finally, each global response to the trapezoidal signal is easily obtained through the linear combination of four delayed replicas of the principal ramp response. In Fig. 2.22 it is shown the third port ramp voltage response computed through the NILT2-Hermite technique, starting from 15 NILT2 starting points (encircled in red). The interpolant is computed using the derivatives up to the fifth order (the zero one included) in the initial 15 points. More samples are required at the beginning of the response where the ramp response has its transient. In this work, the initial time samples selected for the construction of the interpolator are empirically chosen. A more in-depth study aimed at the optimal choice of temporal samples will be conducted in the near future. The final voltage signal

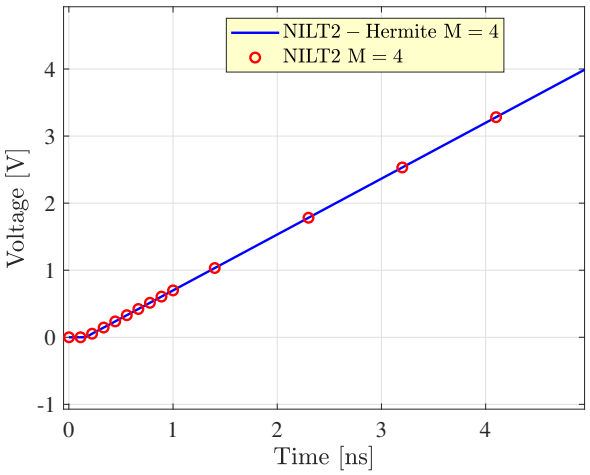

Figure 2.22: PWD port 3 voltage ramp response.

at the third output port is shown in Fig. 2.23. The NILT2 results are in a good agreement with the IFFT results. It is evident the superiority of NILT2 compared

to NILT0 where the two NILT techniques are compared by adopting order $M = 4$. It is apparent that the NILT0 results do not reproduce well the signal transitions while the NILT2 results are in a better agreement with the IFFT-based results. This numerically confirms the error factor of $(n+1)^{N+M}$ [72].

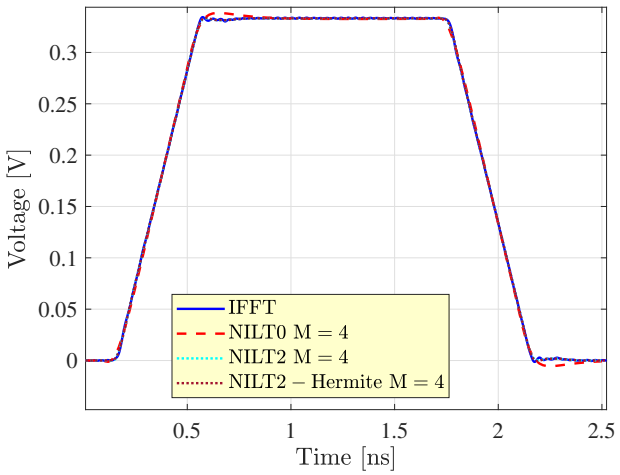

Figure 2.23: PWD port 3 voltage.

Two dipoles system

In the second example, two dipoles are considered. they are shown in Fig. 2.37. The transmitting dipole is fed at the port 1 by a trapezoidal voltage source in series with 1 kΩ resistor, while the port 2 of the receiving dipole is terminated on a load resistor of 1 kΩ. In Table 2.5 are summarized the geometric size of the dipole.

Table 2.3: Geometric features of the two dipoles system.

Data	**Length [m]**
d	0.05
l	0.05
w	0.001
t	0.001
g	0.001

The trapezoidal pulse has width 2 ns, and rise/fall times 0.4 ns. As in the previous example, the maximum significant frequency in the spectrum of the source is around 8 GHz, corresponding to a minimum free-space wavelength of about $\lambda_{min} = 37.5$ mm. Following the criterion (2.37), the resulting equivalent circuit comprises 1264 branches and 640 nodes.

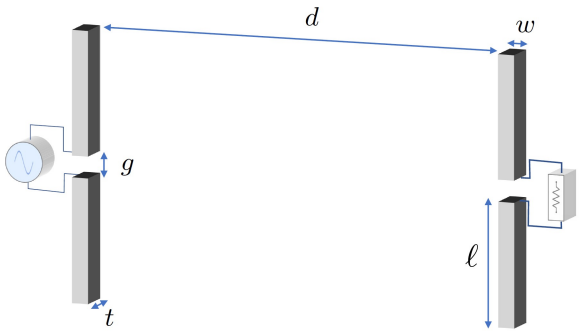

Figure 2.24: The two dipoles system.

The NILT2 voltage ramp response and its first five derivatives in 14 initial selected points, depicted in Fig. 2.25, are used for obtaining the interpolated Hermite results. It is evident from Fig. 2.25 that, in general, it is a good practice to select more initial samples where the behavior is less regular. The global Hermite interpolated voltage is obtained, as usual, by an appropriate superposition of the ramp response, properly shifted.

In Fig. 2.26 the global voltage response at the dipole receiving port is represented. The NILT-based results are compared to the IFFT reference results. All the waveforms in Fig. 2.26 are in a good agreement with the exception of the NILT0-based results, even if computed with $M = 12$. This fact is quantitatively confirmed in Fig. 2.27, where the absolute errors of NILT0 and NILT2 are sketched, assuming IFFT as a reference.

Table 2.4 compares the performance of the proposed approach in regards to the CPU computational time. The first row in the table shows the CPU time taken by the IFFT approach to produce the waveforms shown in Fig. 2.26 with 1170 time samples. The second and third rows show the total CPU time taken by the NILT approaches, using NILT0 and NILT2, respectively, supported by the Hermite

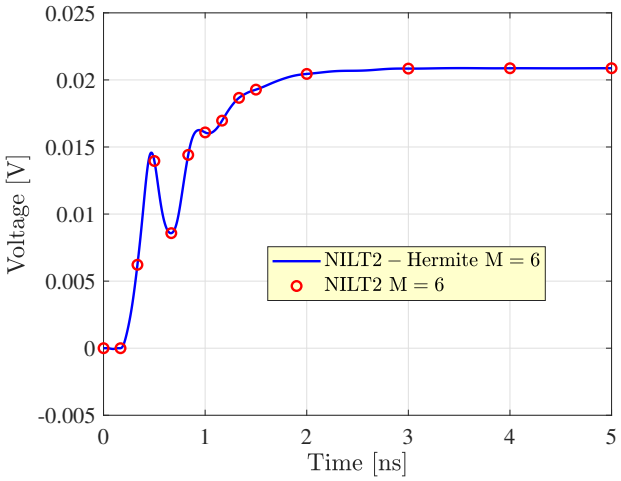

Figure 2.25: Dipoles port 2 voltage ramp response.

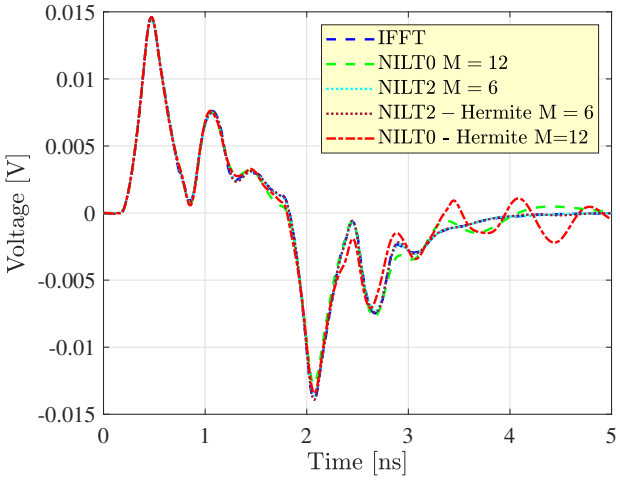

Figure 2.26: Dipoles port 2 voltage.

interpolation, to produce the waveforms at the same number of time samples. It is clear that the NILT0 - Hermite with $M = 12$ and the NILT2- Hermite with $M = 6$ require almost the same computational time, but the NILT0-based technique is affected by evident late-time inaccuracies.

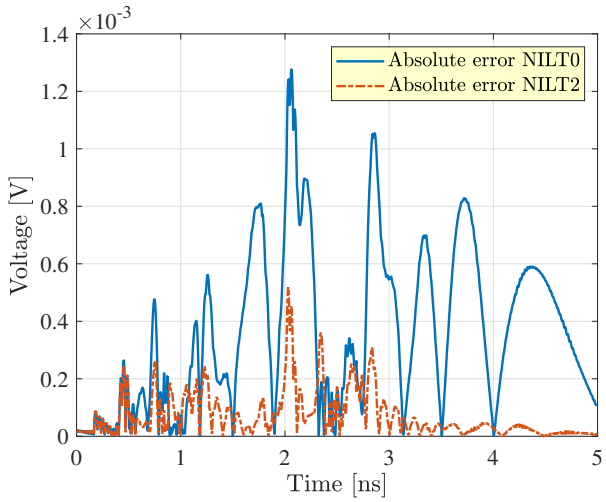

Figure 2.27: Absolute error of the NILT results assuming IFFT as a reference in the dipoles example.

Table 2.4: Computational performances for the example 2.3.1.

Technique	**CPU time** (s)
IFFT	541
NILT0 - Hermite	77.5
NILT2 - Hermite	70

Wide-band E-shaped patch antenna

In the last example, we consider the wide-band E-shaped antenna illustrated in Fig. 2.28, for wireless applications [76]. The antenna, placed 15 mm over a ground plane, is fed by a coaxial wire entering from a hole in the ground plane. Its upper end is soldered to the bottom side of the patch. While in [77] the ground plane has been considered as an infinite perfect electric conductor (PEC), in this work its finite size and finite electric conductivity have been taken into account.

The geometric sizes of the antenna are sketched in Fig. 2.29, where they are expressed in millimeters. The antenna is driven by a 50 Ω voltage source located at the base of the feeding wire, between the wire and the ground plane. The waveform of the voltage source is triangular as proposed in [77], with 500 ps rising and falling

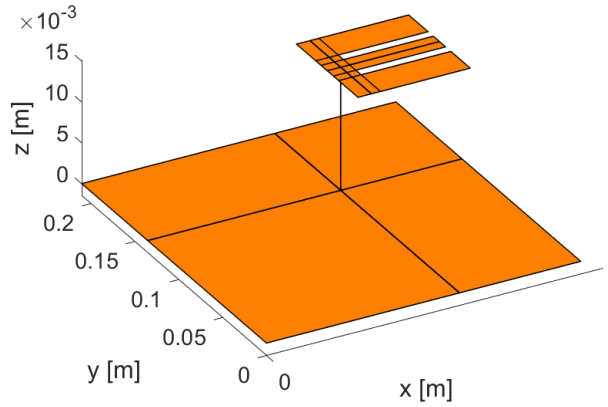

Figure 2.28: E-shaped patch antenna.

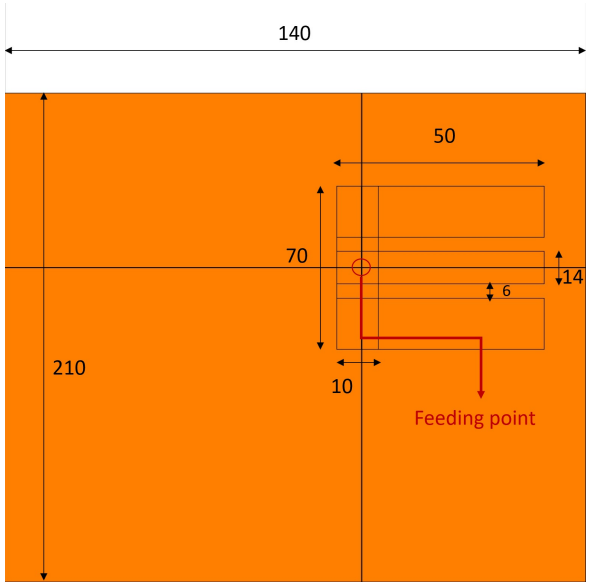

Figure 2.29: E-shaped patch antenna geometry (top view).

times. Being the source again a piecewise - linear (PWL) source, the results can be obtained also in this case by the superposition of ramp responses. For this example, the adoption of the $\lambda_{min}/30$ rule at 1 GHz results in an equivalent circuit consisting of 2540 current branches and 867 potential nodes.

In Fig. 2.30, it is shown the interpolated input ramp response voltage waveform

along with the 35 initial points encircled in red. It is interesting to observe that most of the initial NILT2 samples are placed at the beginning of the response, because it is at the early points that there is a significant variability of the derivatives and, hence, it must be properly sampled in order to build the interpolants. Finally, the port current ramp response is computed and the final NILT2 - Hermite waveform is obtained by an appropriate superposition of delayed versions of the current ramp response. The input current waveform is obtained and shown in Fig. 2.31. The NILT2 results, computed with $M = 4$, exhibit a good agreement with the MoM results presented in [77]. The NILT0, computed with $M = 6$, requires almost the same computational cost of the NILT2, but evidently shows late time inaccuracies. Hence, a larger M would be required and, consequently, the computational cost would overcome that of the NILT2.

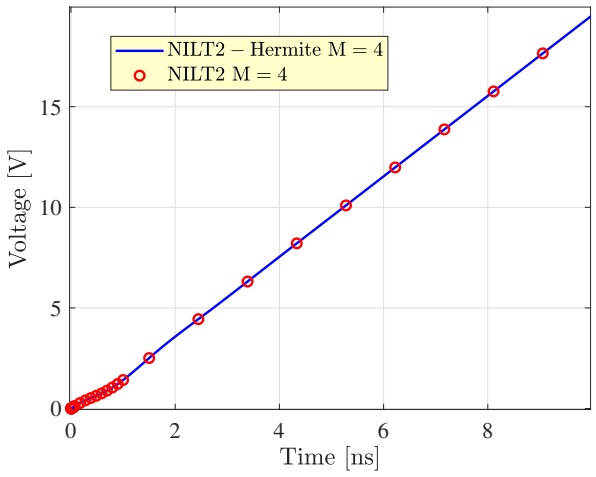

Figure 2.30: Feeding point voltage ramp response for the E-shaped patch antenna.

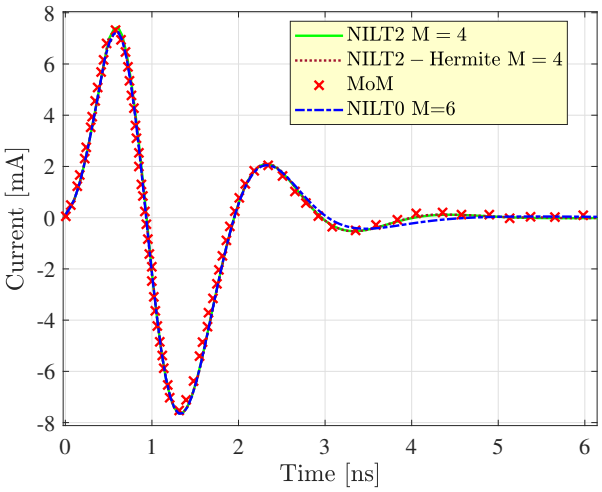

Figure 2.31: Input current for the E-shaped patch antenna.

2.4 The Fast Inversion of the Laplace Transform

Following the procedure introduced by Hosono [69], the inversion integral in (2.1) is approximated as

$$x_{ap}(t) = \frac{1}{j2\pi}\int_{\gamma-j\infty}^{\gamma+j\infty} X(s)E_{ap}(st,\alpha)ds \tag{2.38}$$

by the introduction of the approximate inversion kernel

$$E_{ap}(st,\alpha) = \frac{e^{\alpha}}{2\cosh(\alpha - st)} \tag{2.39}$$

being α a parameter that has to be properly chosen. Introducing (2.39) in (2.38), it is possible to obtain

$$x_{ap}(t) \simeq \frac{e^{\alpha}}{t}\sum_{n=1}^{K} X_n \tag{2.40}$$

where

$$X_n = (-1)^n \mathrm{Im}\left[X\left(s\right)\right]_{s=\frac{\alpha+j(n-0.5)\pi}{t}} \tag{2.41}$$

and K is the truncation number of the series.

The FILT approximation error $\epsilon_F = |x(t) - x_{ap}(t)|$ is given by:

$$\epsilon_F = |e^{-2\alpha}x(3t) - e^{-4\alpha}x(5t) + e^{-6\alpha}x(7t) - \ldots| \tag{2.42}$$

Hence, if $|x(t)| \leq Ee^{Lt}$ for $t > 0$, we have

$$\epsilon_F = \mathcal{O}(|x(t)|e^{-2(\alpha - Lt)}) \tag{2.43}$$

being L and E two finite constants [78]. In conclusion, the error is of exponential order with α. Nevertheless, the parameter α cannot be chosen arbitrarily large, because the numerical evaluation of the terms $X_n(\alpha, t)$ in (2.40) leads to overflow in finite precision. Consequentially, also in this case, the error keeps growing with time. For this reason, very often it is useful to speed up the convergence of the truncated series by applying the Euler transformation presented in [69] and [79]. This results in adding a few additional terms to the original series, for the purpose of limiting K as much as possible for the convergence. Thus, Eq. (2.40) becomes

$$x_{ap}(t) \simeq \frac{e^{\alpha}}{t}\left(\sum_{n=1}^{K} X_n + \sum_{q=1}^{p} 2^{-(p+1)} A_{p,q} X_{K+q}\right) \tag{2.44}$$

where p is the number of terms of the Euler transformation and

$$A_{p,p} = 1, A_{p,q-1} = A_{p,q} + \frac{(p+1)!}{q!(p+1-q)!}. \tag{2.45}$$

It is clear from (2.41) that, in case of system's evaluations, the state vector variables must be sampled, for each t, on $K + q$ different points on the complex plane, which share all the same real part α/t. Fig. 2.32 shows the first 10 complex points per time sample over which the state vector has to be evaluated assuming $\alpha = 3$. The trajectory is considered in the time interval [1-5] ns for illustrative purposes.

With the aim of clarification, the example regarding the FILT computation of the sin function employed in Section 2.1 is here reconsidered. In particular, in Fig. 2.33 it is evident that contrary to NILT, employing the parameters combination: $(K = 20, \alpha = 2)$ it is possible to reproduce satisfactorily the exact sin waveform in the overall time window. Unfortunately, it is also confirmed that it is not possible to choose α arbitrarily large (here $\alpha = 5$ is chosen) to reduce the approximation error in (2.43) as much as possible.

The sin inverse transforms in Fig. 2.34 complete the comparison of the two methods. The waveform is computed utilizing 12 terms for NILT ($M = 24$) and for

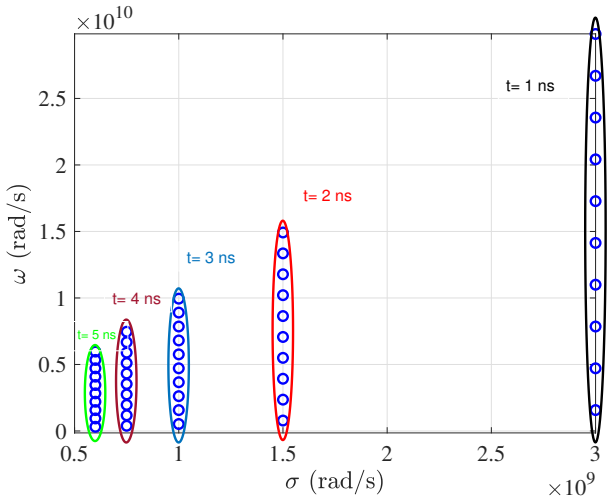

Figure 2.32: Example of complex samples pattern employed in FILT ($\alpha = 3$, $K = 10$).

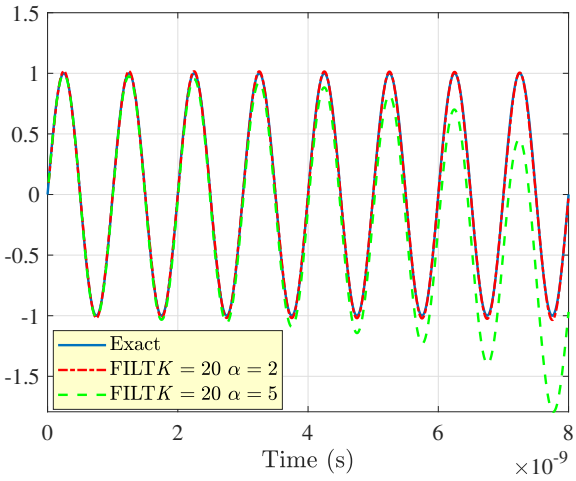

Figure 2.33: FILT-based computation of the sin function for two settings of the parameters.

FILT ($K = 12, \alpha = 2$). It is evident that by fixing the number of terms for each series, the convergence is more easily reached by NILT when treating this kind of waveform (this is true also for typical circuit waveforms).

In conclusion, if long transients have to be evaluated, the FILT technique permits

a successful evaluation in the overall time window (no matter how large it is), at the cost of an increase in the computational burden. If shorter transients are needed, employing NILT guarantees a faster convergence and, hence, a significant saving in computational costs.

It is just the case to observe that the two techniques can be combined to solve the same problem, exploiting the advantages of both of them.

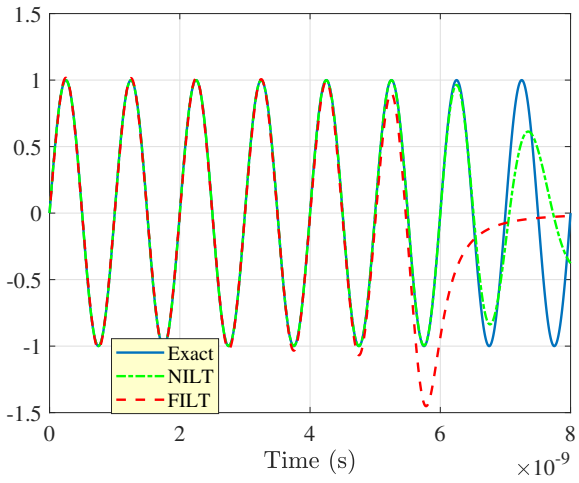

Figure 2.34: Comparison of the sin function computed using the NILT ($M = 24$) and the FILT ($K = 12, \alpha = 2$) techniques.

2.5 The Fast Inversion of the Laplace Transform applied to retarded PEEC models

The FILT is a well-established technique for the transient analysis of propagating fields of nano-antennas. In this doctoral project, FILT has been applied for the first time to retarded PEEC models, extending the applicability of CFD techniques to PEEC models of antennas. Indeed, the FILT technique offers the possibility of high-degree adjustments improving significantly the accuracy of the solution when the interacting structures are very far from each other. For this reason, in this section the attention is particularly focused on the transient modeling of interacting

separated structures. A systematic comparison with NILT is provided in various scenarios, highlighting how depending on the expected features of the transient it is possible to choose the best technique in terms of efficiency and accuracy.

2.5.1 Minimum delay extraction for the modeling of separated structures

In general, the TD response evaluated on a victim device due to a source located far away from it has to satisfy the causality principle [80] and, thus, it cannot occur before the minimum time delay t_d defined as:

$$t_d = \frac{d_{min}}{c} \tag{2.46}$$

being d_{min} the minimum distance between the interacting objects and c the phase velocity in the background medium where they are located. If t_d is too large (from tens to hundreds of ns) the approximate inverse transform solution of the far-away part of the system computed using NILT and FILT methods will be affected by a significant error unless a countermeasure is taken. To this purpose, the Bromwich integral can be recast through the introduction of the delay exponential term e^{st_d}:

$$\mathbf{x}(t) = \frac{1}{j2\pi} \int_{\gamma - j\infty}^{\gamma + j\infty} \mathbf{X}(s) e^{st_d} e^{st'} ds \tag{2.47}$$

being $\mathbf{x}(t)$ the TD vector state of a PEEC model, $\mathbf{X}(s)$ is the Laplace domain PEEC state vector, with $t' = t - t_d > 0$. It is then possible to apply the inversion techniques to the Bromwich integral considering the delayed kernel $e^{st'}$. Following this procedure, the NILT expression for the state vector becomes

$$\mathbf{x}_{N,M}(t) = -\frac{1}{t'} \sum_{i=1}^{M/2} 2\mathrm{Re}\left[K_i \mathbf{X}\left(s\right) e^{st_d} \right]_{s=\frac{z_i}{t'}} \tag{2.48}$$

while, the FILT expression for the state vector can be rewritten as

$$\mathbf{x}_{ap}(t) \simeq \frac{e^{\alpha}}{t'} \left(\sum_{n=1}^{K} \mathbf{X}'_n + \sum_{q=1}^{p} 2^{-(p+1)} A_{p,q} \mathbf{X}'_{K+q} \right) \tag{2.49}$$

where

$$\mathbf{X}'_h = (-1)^n \mathrm{Im}\left[\mathbf{X}(s)\, e^{st_d}\right]_{s=\frac{\alpha+j(h-0.5)\pi}{t'}} \tag{2.50}$$

being h a generic index representing n or q. In conclusion, the effective inversion time is $t' < t$, and the inaccuracies introduced by long simulation times are dramatically reduced.

2.5.2 Underflow issues in complex frequency domain far-field PEEC models

When the procedure already described is applied in modeling separate distant structures, it is necessary to be careful in the numerical evaluation of the delayed partial elements on the complex plane, especially if the distance between the objects is significant. Let us focus on a single generic partial element describing an interaction (magnetic/electric) between two mesh elements, each located on a different object. Their interaction assuming a center-to-center propagation delay can be generically written in the complex frequency domain as:

$$H_{m,n}(s) = H^0_{m,n} e^{-s\tau_{m,n}} \tag{2.51}$$

where $H^0_{m,n}$ describes the static interaction and:

$$\tau_{m,n} = \frac{R^{CC}_{m,n}}{c_0} \simeq \frac{d_{min}}{c_0} \tag{2.52}$$

is the propagation time delay in the background medium between the two elements, being $R^{CC}_{m,n}$ their center-to-center (CC) distance and c_0 the background medium (free-space for the standard PEEC method) phase velocity. The expression (2.51) has to be evaluated on different sets of points over the complex plane for each value of t', using both the NILT and FILT techniques. The argument of the exponential can be written as:

$$s\tau_{m,n} \simeq \frac{z}{t'}\frac{d_{min}}{c_0} \tag{2.53}$$

where z is a complex number that depends on the technique employed. For sufficiently large values of d_{min} and small values of t', it is very likely that the exponential

$e^{-s\tau_{m,n}}$ reaches an underflow condition if the absolute value of its argument exceeds a fixed value K_{max}. This value can be easily found through the knowledge of the smallest positive normalized floating-point number in IEEE double precision. Hence, in order to avoid the underflow of all the "far away" partial elements in the PEEC system, the following condition should apply:

$$\mathrm{Re}(z) < \frac{K_{max} t' c_0}{d_{min}}. \tag{2.54}$$

Obviously, the latter condition is more severe at the first computation times, if the distance d_{min} between the two elements is significant. The FILT method uses a set of poles whose real part is highly adjustable in this sense. Indeed, for each computation time t', it is sufficient to enforce the condition:

$$\alpha < \frac{K_{max} t' c_0}{d_{min}} \tag{2.55}$$

still being able to maintain a reasonable accuracy at the first computation points. On the contrary, when employing the NILT method, the only way to modify the real part of the Padé poles at the first time samples t' is to reduce the order M. Unfortunately, also using small values for M does not avoid the underflow condition if the structures are very far-apart. To better explain the underflow issues, Fig. 2.35 represents the behavior of the absolute value of the delay exponential function in (2.51) for two far-apart elementary volumes, when computed over the FILT points on the complex plane and over the Padé poles having a maximum real part, assuming $M = 20$. The exponential analysis is carried out considering the distances: $10, 20, 40$ m, and varying the quantity $t' = t - t_d$. It is clear that, for any of the three distances, the delay exponential reaches the underflow condition for a larger time interval when it is computed over the Padé poles rather than using the FILT complex points. When this case occurs, for sufficiently small values of t', the partial elements describing the mutual interactions between two or more far-away volumes or surfaces become zero, compromising the accuracy of the computation. In Fig. 2.36, it is shown that using small values of order M, e.g., $M = 4$ for the NILT technique, the time interval where condition (2.55) is not matched and the underflow occurs is reduced, but is still present for the considered distances.

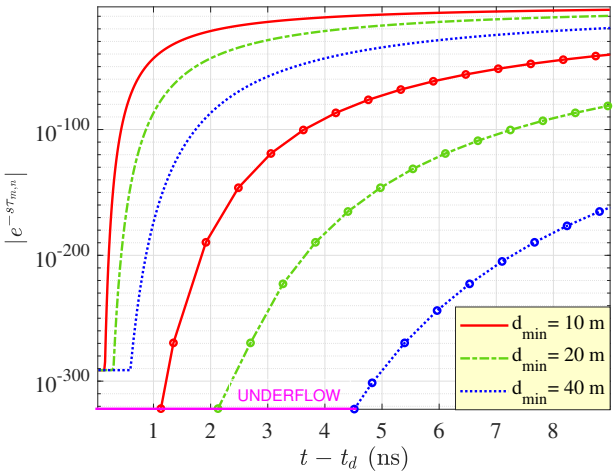

Figure 2.35: Absolute value of the complex exponential computed for different distances between two elementary volumes using NILT ($M = 20$, lines with markers) and FILT (adaptive α, lines without markers).

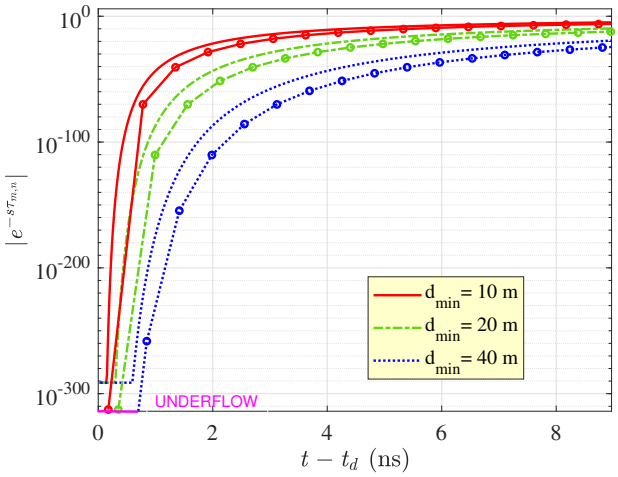

Figure 2.36: Absolute value of the complex exponential computed for different distances between two elementary volumes using NILT ($M = 4$, lines with markers) and FILT (adaptive α, lines without markers).

In this regard, despite the small values of the complex exponential in Figs. 2.35 and 2.36, it is important to point out that, in expressions (2.48) and (2.50), a

compensation factor of the same order of magnitude as the complex exponential is introduced in the final solution due to the exponential term e^{st_d}. Hence, this observation further confirms the importance to avoid the underflow condition.

Numerical results: Transmitting and Receiving Dipole Pair

To illustrate the concepts discussed in Section 2.5.2, the two dipoles sketched in Fig. 2.37 are considered, whose geometric features are described in Table 2.5. Precisely, the TD receiver voltage response is computed firstly considering the near field interaction between the dipoles, and, subsequently, the receiver dipole is moved away from the transmitting dipole, in its far field. For illustrative purposes, the transmitting dipole is driven by a voltage source in series to a resistor and we consider the receiver terminated on a load resistor. The signal source considered has a trapezoidal waveform with rising and falling times $\tau_r = 3.2$ ns and width $\tau_w = 9.5$ ns so that the spectrum is significant until $f_{max} \simeq 1$ GHz. Taking this frequency as a reference, the dipoles are half-wave long. It is known that the transition from the near field region to the far field Fraunhofer region of the transmitter occurs at distances r such that [81]:

$$r \geq R_f = \frac{2D^2}{\lambda} \tag{2.56}$$

where r is the radial distance measured from the center of the transmitting dipole, $D = 2\ell$ is its maximum physical length, and $\lambda = c_0/f_{max}$ is the wavelength in the free space at the maximum frequency of interest f_{max}.

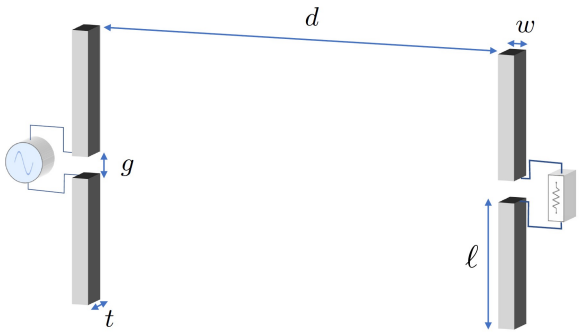

Figure 2.37: The two dipole system.

Table 2.5: Geometric features of the two dipoles system.

Data	**Length [m]**
ℓ	0.075
w	0.001
t	0.001
g	0.001

Near Field Analysis

In the near field analysis, the distance between the two dipoles d is set as $d = R_f/2$. The TD receiver voltage is computed through the inverse transform techniques and compared to the results of a time-stepping reference solver adopting the backward differentiation scheme of the second order (BD2). Fig. 2.38 shows the receiver voltage response assuming 50 Ω terminations for both ports. In this case, the transient is quite long-lasting (more than 20 ns). The FILT solution is obtained by choosing $K = 20$ and $p = 8$ in (2.49) so that it is observed a good match between the FILT solution and the reference solution throughout the time window. For the Padé expansion-based inverse transform, the modified NILT technique (NILT2) [72] has been employed, to achieve a higher degree of accuracy. It is clear from Fig. 2.38 that the maximum exploitable expansion order, in this case, is $M = 8$, while larger orders cause the result to explode because of rounding errors in the residues K_i that impact significantly the solution. In general, employing NILT2, this behavior is observed for relatively small values of M, because terms of the type: K_i^3, K_i^2 are involved in the summation. Hence, it is not possible to achieve better accuracy using more terms in the series. For this reason, in this case, the recommended method is FILT, because it allows adjusting the accuracy by choosing the optimal number of series terms. The latter becomes an important feature when dealing with long-lasting transients.

Fig. 2.39 shows the receiver voltage response assuming 1 kΩ termination for the two ports, where it is evident that the transient is more time-limited compared to the previous case. In this case, employing NILT2 with order $M = 4$ (two series terms) ensures a very good accuracy over the entire time window, while for FILT the same

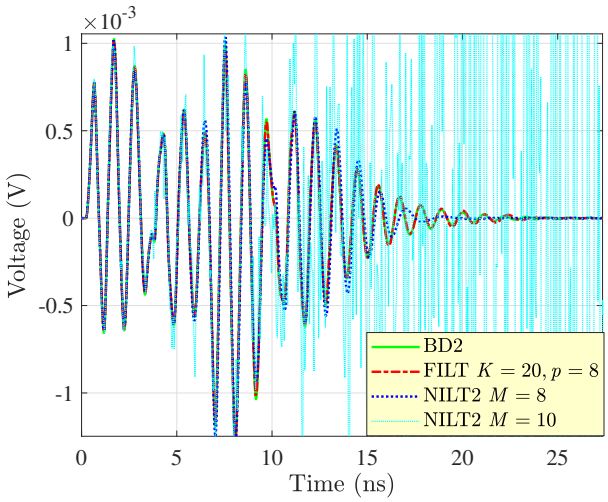

Figure 2.38: Receiver near field voltage response in the case of 50 Ω terminations.

accuracy is reached considering $K = 10$ and $p = 5$ in (2.49) for a total of 15 series terms. Hence, in this case, employing the NILT technique is more convenient in terms of computational efforts since a smaller number of system evaluations on the complex plane is sufficient to represent the response for each time sample compared to the FILT method. In particular, the cpu simulation time running NILT was 43.4 s, while it was 163.3 s for FILT, considering the same number of time computation points for the two techniques.

For completeness, the NILT2 and FILT relative errors at four different time points are compared in Table 2.6, assuming the same number of series terms ($M = 4$ for NILT2, $K = 2$ for FILT). It is seen that NILT2 outperforms FILT in terms of convergence. This confirms that employing NILT for moderately short transients offers the opportunity to minimize the computational burden.

Far Field Analysis

In the far-field analysis, the receiver dipole is moved away from the transmitter to a distance $d = 20$ m. In this configuration, the minimum propagation time delay between the two structures is $t_d = 66.67$ ns. The computation of the receiver voltage starts at a time $t_d = r/c_0$. The port terminations are assumed 50 Ω.

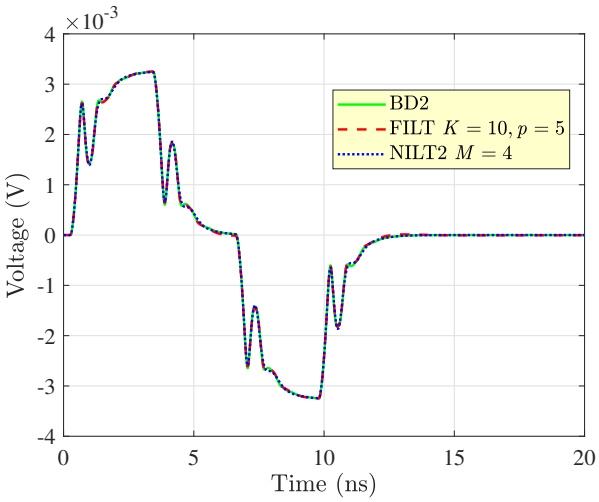

Figure 2.39: Receiver near field voltage response in the case of 1 $k\Omega$ terminations.

Table 2.6: NILT vs FILT: relative error for the near fieldshort transient example.

Time	NILT2 rel. err.	FILT rel. err.
2 ns	13×10^{-3}	0.58
4 ns	23×10^{-3}	2.12
8 ns	8.3×10^{-3}	0.30
10 ns	2.5×10^{-3}	0.66

As already explained, because of the underflow issues, the delayed PEEC model becomes inaccurate at the first computation time samples, when computed over the Padé poles using NILT. This is clear by observing a zoom of the receiver voltage response in Fig. 2.40, in which the NILT response is zero also after the propagation delay t_d between the two dipoles.

Fig. 2.41 shows the pattern of the coefficients of the potential matrix $\mathbf{P}(s)$, computed at one of the first computation instants (where the response is still wrongly zero) over the Padé poles. It is known that the coefficients of the potential matrix is full, but, when computed for small values of t', the underflow issue causes the coefficients of potential describing the mutual interactions to be zero, resulting in null off-diagonal blocks. The same behavior is observed in the partial inductances matrix $\mathbf{L}_p(s)$.

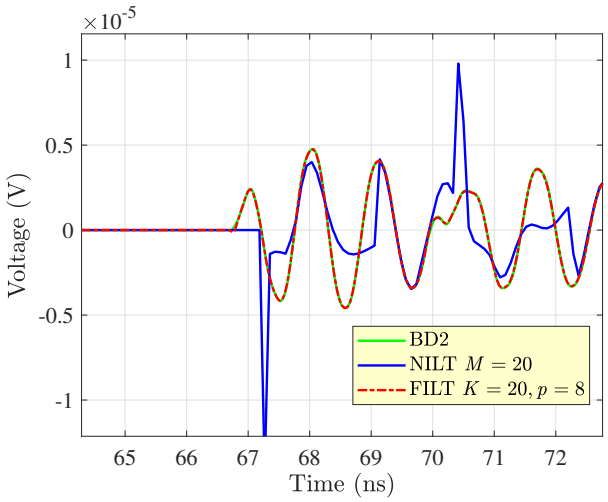

Figure 2.40: Zoom of the receiver far field voltage response at the initial instants.

In the FILT series, with reference to (2.49), the K and p parameters have been set as $K = 20$ and $p = 8$. For the choice of parameter α, the adaptive criterion (2.55) has been adopted.

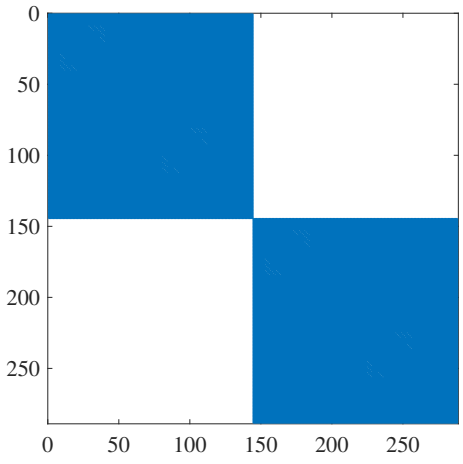

Figure 2.41: Coefficients of potential matrix pattern at the initial instants computed over the Padé poles.

Since the source is piecewise-linear (PWL), all the global responses are conveniently obtained, for each port, through the superposition of delayed versions of a

unique ramp response. When the receiver voltage is computed, the wrong null initial portion affects considerably the final result. This is evident in Fig. 2.42, where a satisfactory agreement is observed between the FILT results and the reference time-stepping solution BD2, while the NILT results, obtained with $M = 20$, are inadequate.

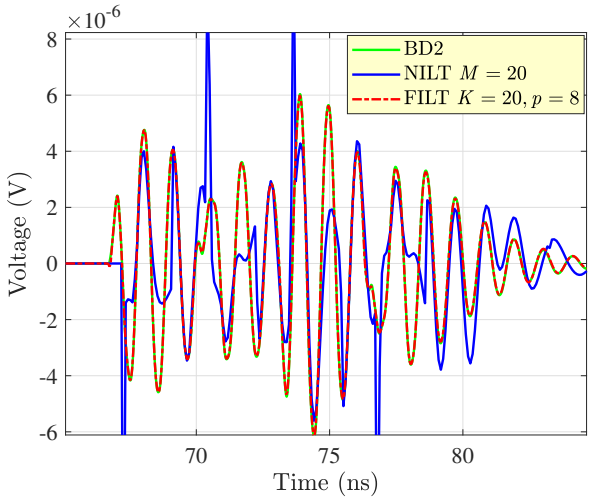

Figure 2.42: Receiver far field voltage response with 50 Ω terminations.

2.5.3 FILT-PEEC TD modeling of Reconfigurable Intelligent Surfaces

Reconfigurable Intelligent Surfaces (RISs) are an emerging technology that is gaining more and more interest, especially in the field of future 6G communications [82].

RISs offer the opportunity to alter the properties of a given transmission channel through the introduction of an array of closely spaced passive scatterers. These elements can be conveniently reconfigured in order to improve wireless communications performance and create a smart electromagnetic environment. The RISs interdistances are typically in the order of fractions of the wavelength. Hence, an electromagnetic (EM) model taking accurately into account the mutual couplings is crucial in the design stage.

RISs modeling techniques are usually based on Frequency Domain (FD) approaches [83] [84], but a Time Domain (TD) characterization of this kind of system becomes of primary importance when the RIS elements interface with reconfigurable non-linear elements. Furthermore, it becomes crucial when time-varying scenarios are considered, as in urban environments due to moving scatters, or when time-varying materials are considered in the RIS. A first approach developed entirely in the TD can be found in [85].

Since in this kind of systems the propagation delays are not negligible, their TD characterization usually requires time-stepping solvers able to handle Delayed Differential Equations (DDE). The main drawback of this approach is that the computational burden grows rapidly as the distances between the RISs and the transmitter increase. Moreover, the stability of delayed solvers is highly dependent on the spatial and temporal discretization, making almost impossible to predict it in advance.

The main observed advantage of the application of FILT in such a contest is that the solution accuracy is independent on the time-step. This attractive feature turns out to be of fundamental importance in the TD modeling of systems composed by widely spaced elements (e.g. RISs systems), permitting the optimization of the distribution of the time samples and, consequently, a reduction of the computational costs.

The purpose of this paragraph is to provide a preliminary TD analysis of a RIS-aided communication channel, starting from a Laplace domain numerical representation of the PEEC system and finally applying FILT.

The PEEC-FILT strategy for RIS modeling

Generally, a RIS aided communication system is composed by three separate antenna groups: the transmitters system (T_x), the RIS array, and the receivers system (R_x). The entire configuration can be schematized as in Fig. 2.43, where the transmitters and receivers antenna systems are embedded in two single boxes.

The EM behavior of the RIS elements plays a fundamental role in characterizing the transmission channel. In addition, the characterization of the transient response

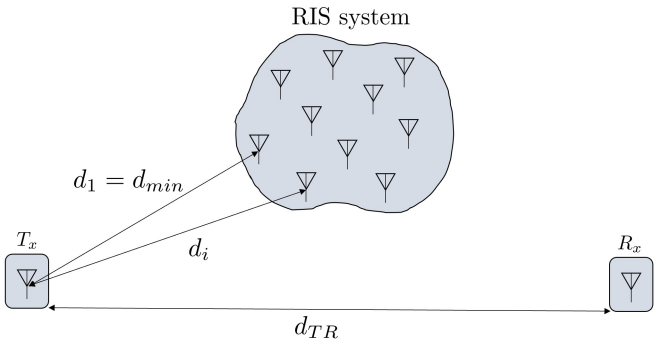

Figure 2.43: Generic RIS aided system configuration.

of such a system, given a certain excitation configuration for T_x, is of paramount importance for the derivation of an effective channel abstraction. Also in this case, the TD response evaluated over any element of the RIS group due to a source located away from it must follow the delay causality principle [80]. Rigorously, over the i-th antenna, no response should be observed earlier than the propagation delay time t_{di}, defined in the free-space as

$$t_{di} = \frac{d_i}{c_0}, \tag{2.57}$$

being c_0 the free-space propagation speed and d_i the minimum distance between T_x and the i-antenna.

Typically, the minimum distance d_{min} between T_x and the RIS can reach several tens of meters. Consequently, the transient responses require time evaluation windows in the order of hundreds of ns. For this reason, the employment of time-stepping resolution methods may lead to unacceptable computational burden and inadequate accuracy of the results. Assuming that, for a given problem, the maximum allowable time step Δt_{max} is fixed to guarantee the desired degree of accuracy, the actual time step Δt is always constrained to be less than or equal to Δt_{max}. It follows that, in the most favorable case, the necessary number of samples N_s for the computation is given by

$$N_s = \frac{t_w}{\Delta t_{max}} + 1, \tag{2.58}$$

where t_w is the length of the time window. Hence, the number of time samples and, consequently, the computational cost, scale as t_w.

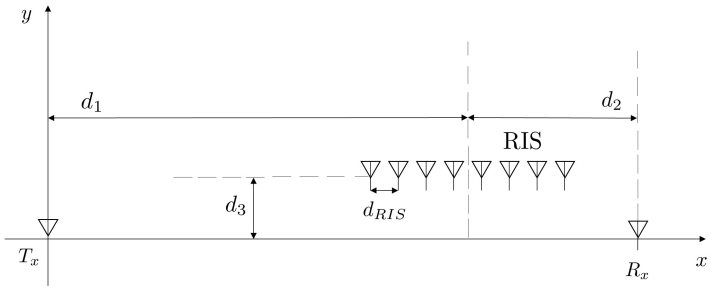

Figure 2.44: RIS aided system geometry.

Moreover, if the distances between the RIS antennas are in the order of tens of cm, FILT offers the opportunity of capturing the transient waveforms over each element of the RIS by performing only the extraction of the minimum propagation delay between T_x and the RIS array. Accordingly, the TD response evaluation of each element of the RIS begins at the time

$$t_d = \frac{d_{min}}{c_0}, \tag{2.59}$$

which means that it is not needed to compute the solution of the PEEC system before the effects have traveled the minimum propagation distance between the sources and the RIS array. This feature allows to save a significant portion of computational time if compared to standard time-stepping methods, where the response evaluation is performed starting at $t = 0$.

Numerical results

With the aim of validating the proposed formulation, the transient analysis of the eight-element RIS system depicted in Fig. 2.44 is carried out. Each RIS antenna is supposed to be a linear dipole independently loaded with a 50 Ω resistance. An in-depth analysis of a similar system considering a connected network for the RIS load configuration has been proposed in [86]. All the geometric details of the system are summarized in Table 2.7.

T_x consists of a single dipole driven by a 50 Ω voltage source applied at the gap between its arms. For exemplification purposes we assume that the voltage source

Table 2.7: Geometric features of the RIS aided system.

Description	**Data**	**Value**
distance T_x - RIS	d_1	50 m
distance RIS - R_x	d_2	2 m
RIS elements distance	d_{RIS}	10 cm
misalignment	d_3	2 m
dipoles arm length	d	5 cm

waveform is a trapezoidal pulse with rising time 1 ns and width 5 ns. R_x consists of a single dipole terminated on a 50 Ω resistance.

In Figs. 2.45 and 2.46 the voltages of the first and the last RIS dipoles are depicted, respectively. In Fig. 2.47 it is shown the voltage induced at the R_x terminals.

The results are obtained through the FILT technique by employing the delay extraction procedure, which involves only the minimum delay between T_x and the RIS array. The FILT voltages are compared with those obtained through the time-stepping solver BD2. The effective FILT TD computation begins from t_d, and the placement of the samples can be arbitrarily chosen in each interaction window. Moreover, the chosen number of computation samples does not affect in any way the accuracy of the solution, since each computed sample is independent of the others. For this example, the number of samples for the FILT method is set to 600 for each voltage response. Nevertheless, it is to be remarked that this choice is only for visualization purposes and a lower number of samples would not affect the accuracy of the proposed procedure. Furthermore, the time samples can be chosen only in the time window starting at t_d and ending at the time when the transient is expected to be reasonably extinguished.

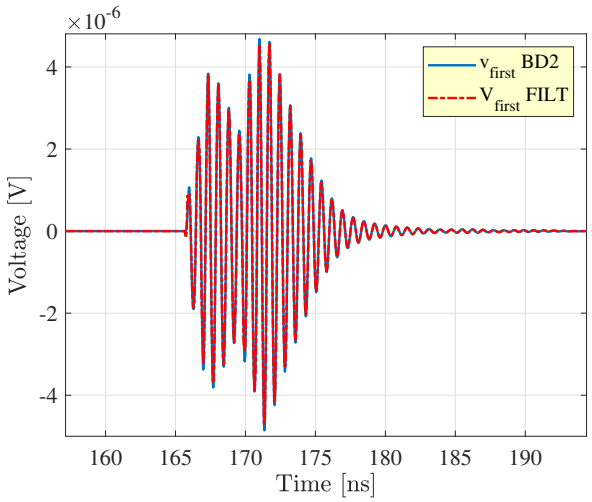

Figure 2.45: First RIS dipole port voltage.

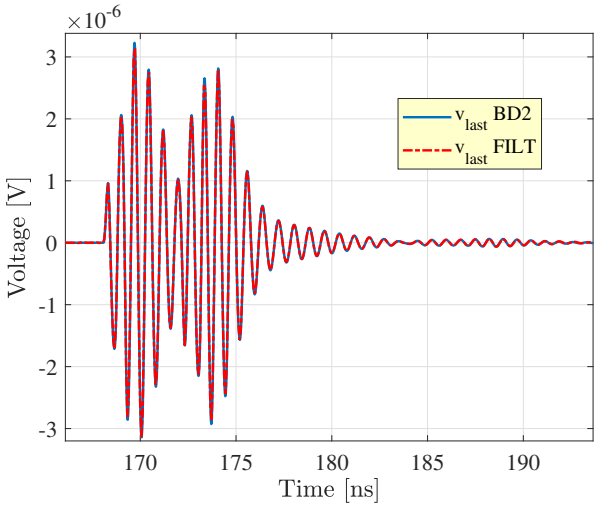

Figure 2.46: Last RIS dipole port voltage.

2.6 Complex frequency domain models for electrically long MTLs

Approximate Inverse Laplace Transform techniques have been widely used for the TD characterization of transmission line (TL) structures [87], [74].

Neglecting incident EM fields effects, the equations of multiconductor transmis-

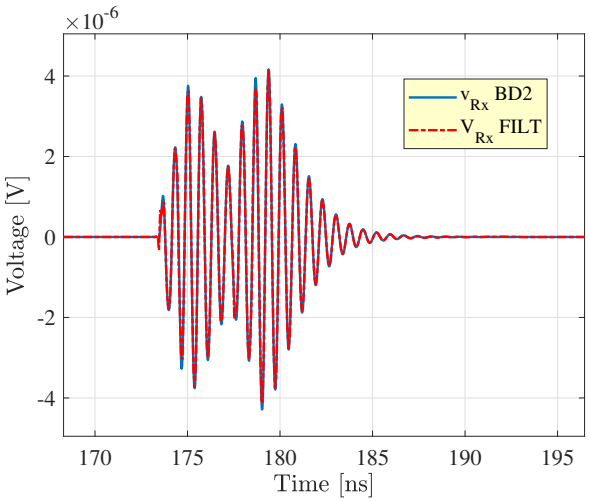

Figure 2.47: Receiver dipole port voltage.

sion lines composed by n conductors in the Laplace domain can be cast in a standard state-space form as follows [88]

$$\frac{d}{dx}\hat{\mathbf{X}}(x,s) = \hat{\mathbf{A}}(s)\hat{\mathbf{X}}(x,s) \tag{2.60}$$

where x is the line abscissa and

$$\hat{\mathbf{X}}(x,s) = \begin{bmatrix} \hat{\mathbf{V}}(x,s) \\ \hat{\mathbf{I}}(x,s) \end{bmatrix} \tag{2.61}$$

is the state vector containing the n line voltages and currents. The state matrix $\hat{\mathbf{A}}(s)$ reads

$$\hat{\mathbf{A}}(s) = \begin{bmatrix} \mathbf{0} & -\hat{\mathbf{Z}}(s) \\ -\hat{\mathbf{Y}}(s) & \mathbf{0} \end{bmatrix} \tag{2.62}$$

where $\mathbf{Z}(s) = \mathbf{R}(s) + s\mathbf{L}(s)$ and $\mathbf{Y}(s) = \mathbf{G}(s) + s\mathbf{C}(s)$. It is well known that the end voltages and currents can be related by the so-called chain parameters matrix $\hat{\mathbf{\Phi}}(\mathcal{L},s)$ as [88]

$$\begin{bmatrix} \hat{\mathbf{V}}(\mathcal{L},s) \\ \hat{\mathbf{I}}(\mathcal{L},s) \end{bmatrix} = \hat{\mathbf{\Phi}}(\mathcal{L},s) \cdot \begin{bmatrix} \hat{\mathbf{V}}(0,s) \\ \hat{\mathbf{I}}(0,s)) \end{bmatrix} \tag{2.63}$$

where the $2n \times 2n$ chain parameters matrix $\hat{\mathbf{\Phi}}(\mathcal{L}, s)$ is:

$$\hat{\mathbf{\Phi}}(\mathcal{L}, s) = \mathbf{e}^{\hat{\mathbf{A}}(s)\mathcal{L}} = \sum_{k=0}^{\infty} \frac{\mathcal{L}^k}{k!} \left[\hat{\mathbf{A}}(s)\right]^k. \tag{2.64}$$

Pertinent boundary conditions need to be enforced at the line ends $x = 0, \mathcal{L}$. Assuming linear time-invariant terminations, they read

$$\begin{bmatrix} \hat{\mathbf{V}}(0,s) \\ \hat{\mathbf{V}}(\mathcal{L},s) \end{bmatrix} = \begin{bmatrix} \hat{\mathbf{V}}_{s0}(s) \\ \hat{\mathbf{V}}_{sL}(s) \end{bmatrix} - \begin{bmatrix} \hat{\mathbf{Z}}_0 & 0 \\ 0 & \hat{\mathbf{Z}}_L \end{bmatrix} \begin{bmatrix} \hat{\mathbf{I}}(0,s) \\ \hat{\mathbf{I}}(\mathcal{L},s) \end{bmatrix} \tag{2.65}$$

where $\hat{\mathbf{V}}_{s0}(s)$, $\hat{\mathbf{V}}_{sL}(s)$, $\hat{\mathbf{Z}}_0$ and $\hat{\mathbf{Z}}_L$ are the multiport Thevenin sources and impedances of the circuits connected to the MTL at $x = 0$ and $x = \mathcal{L}$, respectively. The resulting problem described by equations (2.63) and (2.65) is well-posed for the end voltages and currents $\hat{\mathbf{V}}(0,s), \hat{\mathbf{I}}(0,s)), \hat{\mathbf{V}}(\mathcal{L},s), \hat{\mathbf{I}}(\mathcal{L},s)$.

The transient port voltages and currents can be obtained through the application of inverse Laplace transform techniques to equations (2.63) and (2.65), upon the evaluation of the chain parameters matrix over appropriate points of the complex plane, depending on the chosen inverse transform technique.

In order to better illustrate the problems that may arise in computing (2.64) in (2.63), we consider, without loss of generality, the case of perfect conductors ($\mathbf{R} = \mathbf{0}$) in a homogeneous lossy dielectric medium. The chain parameters submatrices can then be expressed in a closed form as [88]:

$$\hat{\mathbf{\Phi}}_{11} = \cosh\left[\hat{\gamma}(s)\mathcal{L}\right]\mathbf{I}_n \tag{2.66a}$$

$$\hat{\mathbf{\Phi}}_{12} = -\sinh\left[\hat{\gamma}(s)\mathcal{L}\right]\hat{\mathbf{Z}}_c \tag{2.66b}$$

$$\hat{\mathbf{\Phi}}_{21} = -\sinh\left[\hat{\gamma}(s)\mathcal{L}\right]\left[\hat{\mathbf{Z}}_c\right]^{-1} \tag{2.66c}$$

$$\hat{\mathbf{\Phi}}_{22} = \cosh\left[\hat{\gamma}(s)\mathcal{L}\right]\mathbf{I}_n \tag{2.66d}$$

where $\mathbf{I}_n$ is the $n \times n$ identity matrix and $\hat{\mathbf{Z}}_c$ is the characteristic impedance matrix defined as:

$$\hat{\mathbf{Z}}_c = \frac{s}{\hat{\gamma}(s)}\mathbf{L} \tag{2.67}$$

$$\left[\hat{\mathbf{Z}}_c\right]^{-1} = \frac{\hat{\gamma}(s)}{s\mu\varepsilon}\mathbf{C}. \tag{2.68}$$

The coefficient $\hat{\gamma}(s) = \sqrt{s\mu\sigma + s^2\mu\varepsilon}$ is the propagation constant in the Laplace domain assuming known the electrical conductivity σ, the magnetic permeability μ, and the dielectric permittivity ε of the surrounding medium.

When the physical length of the lines is large ($\mathcal{L} > 10$ m), the TD computation of the electric quantities in $z = 0$ can be very challenging. Indeed, the behavior of the complex hyperbolic functions in (2.66a) evaluated on the complex plane plays a crucial role. To explain this, we consider the generic complex point $s = z/t$, where t is the time evaluation value and z is a complex point that depends on the technique adopted to perform the inverse Laplace transform. In the limit of vanishing losses, the propagation constant can be written as $\gamma(z/t) \simeq \frac{z}{t}\sqrt{\mu\varepsilon}$ and, hence, the hyperbolic cosine function becomes:

$$f_c\left(\frac{z}{t}\right) = \frac{1}{2}\left(e^{\frac{z\mathcal{L}}{ct}} + e^{-\frac{z\mathcal{L}}{ct}}\right) \tag{2.69}$$

being $c = 1/\sqrt{\mu\varepsilon}$ the propagation speed in the homogeneous dielectric medium. The function $f_c(s)$ reaches an underflow or an overflow condition if the absolute value of the exponential arguments exceeds the value K^- or K^+ respectively. This value can be found from the knowledge of the smallest and largest positive normalized floating-point number in IEEE double precision. Hence, to avoid a data loss, it is necessary that the following inequality is satisfied for each value of t:

$$\mathrm{Re}(z) < \min\left[\frac{K^+tc}{\mathcal{L}}, \frac{K^-tc}{\mathcal{L}}\right]. \tag{2.70}$$

The condition (2.70) becomes more severe as t and c approach smaller values if the line length $\mathcal{L}$ is significant. The FILT method is more flexible in this sense since it is easy to enforce the condition:

$$\alpha < \min\left[\frac{K^+tc}{\mathcal{L}}, \frac{K^-tc}{\mathcal{L}}\right] \tag{2.71}$$

providing an accurate TD solution at the initial computational points t. The same holds for the hyperbolic sinusoidal function.

Employing the NILT technique, the only way to try to satisfy the inequality (2.70) is to reduce as much as possible the Padé expansion number M, but unfortunately, also with very small values of M it is not possible to match (2.70) when

t is small. Hence, the TD computation of the MTL transients at $z = 0$, where the port quantities are not negligible even at the first instants, becomes very difficult.

In Fig. 2.48 it is shown the trend of the absolute value of function $f_c(s)$ when evaluated over the Padé poles assuming $M = 24$ and when computed over the FILT complex points complying with (2.71). The behavior is plotted for two values of the length of the line, $\mathcal{L} = 20$ m, and $\mathcal{L} = 40$ m.

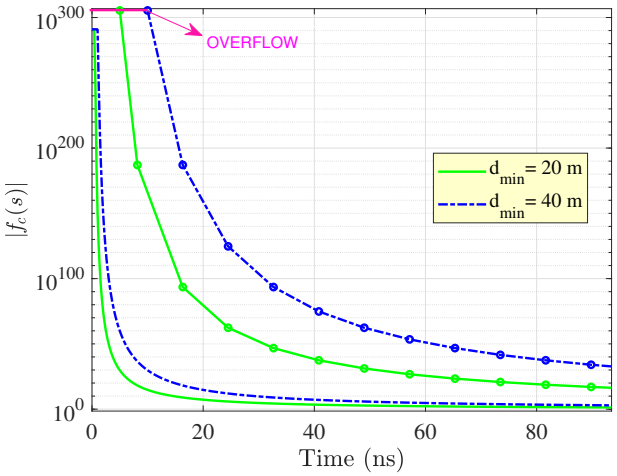

Figure 2.48: Absolute value of the complex hyperbolic cosine computed for different line lengths (lossless medium) using NILT ($M = 24$, lines with markers) and FILT (adaptive α, lines without markers).

It is evident that using the NILT method, significant portions of the time computational window are compromised, as pointed out in Fig. 2.48. As expected, the time interval where the overflow occurs increases with the length of the line. On the contrary, the adaptive choice of α in the FILT technique allows outperforming the NILT method avoiding the overflow condition also for small values of t. This guarantees an accurate computation of the port transient voltages and currents at $z = 0$, even at the beginning of the computational time window. On the other hand, if the line length is intermediate (tens of meters) and the traveling signals are smooth enough, the reconstruction of far-end signals could be more convenient using NILT for the convergence reasons.

Numerical results: Three-phase cable

In Section 2.6, it has been pointed out that the TD modeling of MTLs through inverse Laplace transform techniques is feasible and easy to implement since the formulation is closely connected to the classic frequency domain representation in terms of per-unit-length (p.u.l.) parameters. In this example, a three-phase cable is considered. Its cross-section is represented in Fig. 2.49. It is assumed that the shield is a perfectly conducting cylinder, filled with a uniform dielectric material characterized by a dielectric relative permittivity $\varepsilon_r = 3.0$. The line length is assumed as $\mathcal{L} = 10$ m, which is a standard value employed in motor drive systems applications. The cable geometrical quantities are summarized in Table 2.8.

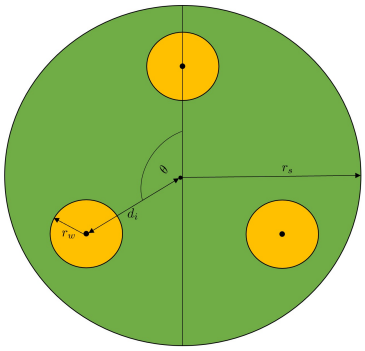

Figure 2.49: Cable cross-section geometry.

Table 2.8: Geometric features of the three wires cable.

Data	**Value**
r_w	3.3 mm
d_i	10 mm
r_s	13.4 mm
θ	120°
$\mathcal{L}$	10 m

The cable can be modeled as a six ports MTL system. The p.u.l. inductances matrix

of the MTL model is analytically known [88], exhibiting diagonal elements L_s

$$L_s = \frac{\mu_0}{2\pi} \ln\left(\frac{r_s^2 - d_i^2}{r_s r_w}\right) \tag{2.72}$$

and off-diagonal elements L_m

$$L_m = \frac{\mu_0}{2\pi} \ln\left(\frac{d_i}{r_s}\sqrt{\frac{d_i^2 + r_s^4 - 2d_i^2 r_s^2 \cos\theta}{d_i^2 + d_i^4 - 2d_i^4 \cos\theta}}\right). \tag{2.73}$$

Since the conductors are placed in a homogeneous dielectric medium, the per-unit-length capacitance matrix is easily obtained:

$$\boldsymbol{C} = \mu_0 \varepsilon \boldsymbol{L}^{-1} \tag{2.74}$$

The same holds for the per-unit-length conductance matrix

$$\boldsymbol{G} = \sigma \mu_0 \boldsymbol{L}^{-1} \tag{2.75}$$

being σ the equivalent DC conductivity of the dielectric material.
For example purposes, only one conductor is fed at one end through a 19 Ω voltage source, while the other five ports are terminated on 19 Ω passive loads. The voltage waveform is chosen as a double exponential pulse:

$$v_s = e^{-\alpha t} - e^{-\beta t} \tag{2.76}$$

with $\alpha = 20$ ps and $\beta = 33$ ps. The near-end crosstalk voltage induced in one of the victim lines is shown in Fig. 2.50. The focus should be put on the NILT solution behavior in the rising portion of the signal, shown in detail in Fig. 2.51, where it is evident that the results are unavailable for a significant part of the rising edge. The reason resides in the fact that the chain matrix reaches an overflow condition due to the very large real part of the Padé poles at the beginning of the analysis, e.g., at the first time samples. The converse is true for the FILT results, where, as described in the previous section, an adaptive choice of the real part of the FILT complex points permits an accurate representation at the early times.

For completeness, In Fig. 2.52 the far-end voltage response is sketched. In this example, $M = 24$ (12 terms in the NILT series) was found to be the minimum NILT

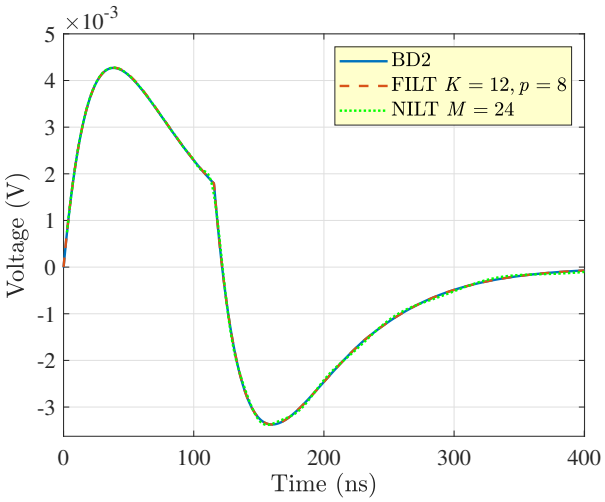

Figure 2.50: Near-end voltage response.

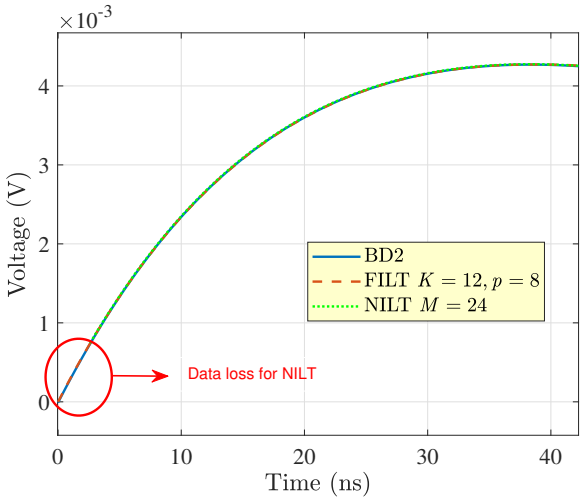

Figure 2.51: Rising front of the near-end voltage response.

expansion number that guarantees an acceptable accuracy. For the same purpose, FILT analysis is performed by adopting $K = 12$ and $p = 8$ in (2.44), for a total number of 20 evaluations per time sample of the MTL system. As a consequence of the chosen number of series terms, the simulation CPU-time for the NILT technique was 2.67 s, while for FILT was 3.78 s, suggesting that if only the far-end responses are needed the NILT technique is the most convenient since it reaches an acceptable

accuracy with a lower computational effort. On the contrary, for the computation of the near-end responses the FILT technique becomes necessary, since, due to its flexibility, it provides accurate results also at early times without losing important data. To combine the benefits offered by each technique, should not be excluded the possibility to combine the two approaches using FILT to support NILT where it is not able to provide data.

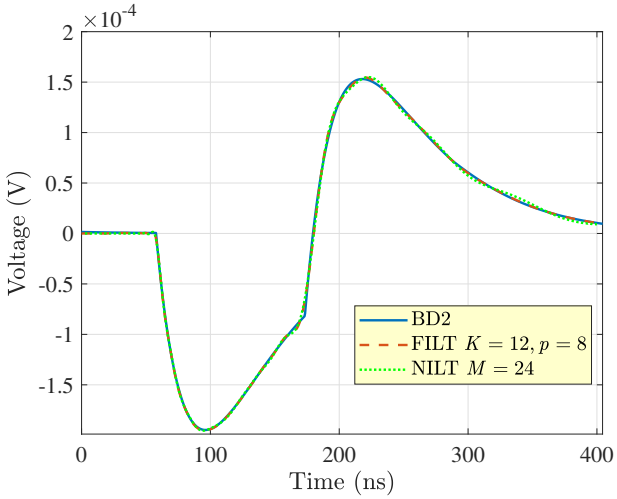

Figure 2.52: Far-end voltage response.

3

The Time Domain Representation of Partial Elements

Owing to the ever increasing interest in accurate TD simulations in the field of Electromagnetic Compatibility (EMC), full-wave TD formulations of partial elements are becoming more and more important.

When the full-wave free-space Green function is considered, the integrals are typically computed in the frequency domain (FD) by resorting to Gaussian quadrature schemes. This approach may result to be extremely time consuming because, depending on the accuracy, the order of integration can become easily very high. This is especially true for self coefficients of potential or mutual ones between close patches where the Green function becomes singular or nearly singular. In this case, the standard approach to recover the TD system response is based on the application of the IFFT technique on the FD results. Unfortunately, to obtain aberrations-free results in the TD, a pertinent number of frequency samples should be selected, performing the numerical integrations for the total number of partial elements embedded in to the system for each frequency sample, being the frequency a parameter appearing inside each interaction integral.

In this Chapter, the Cagniard-deHoop (CdH) technique [89] to calculate full-wave partial elements exactly in the TD is presented. The resulting analytical results apply to the interaction between two rectangular surfaces or two bricks (= right parallelepipeds). The CdH technique is a joint-transform method that has

been originally developed to analytically analyze the seismic-wave propagation in horizontally layered media (e.g. [90, 91]).

The analytical evaluation of TD partial elements through the CdH technique is presented in sections 3.1 and 3.2 for rectangular parallel and orthogonal patches, respectively. Subsequently, the evaluation of both rectangular and volume TD interactions through the NILT technique is explained in Sec. 3.3. In this context, such method represents a valid alternative when the integrals involved in the CdH computation become excessively expensive. In particular, such problem is found when dealing with the TD computation regarding adjacent bricks. Finally, the description and the explanation of the convolution-based PEEC solver arising from the employment of TD partial elements is presented in 3.4, where different prototype numerical example highlighting the several advantages brought by this rigorous approach over standard TD solvers often prone to stability issues.

3.1 Time-domain surface interactions of the potential type

In this paragraph the analytic derivation of the TD coefficients of potential is presented. The possible geometrical configurations involve mutually parallel and orthogonal patches. Depending on the considered configuration, a specifical derivation is used.

3.1.1 Parallel patches

In this paragraph the focus is put on the interaction between two rectangular surface elements m, n, of surfaces $\mathcal{S}_m$, $\mathcal{S}_n$, lying in two parallel planes as described in Fig. 3.1. To localize the position in the problem configuration, we employ coordinates $\{x, y, z\}$ with respect to an orthogonal Cartesian reference frame with the origin $\mathcal{O}$ and the standard basis $\{\boldsymbol{i}_x, \boldsymbol{i}_y, \boldsymbol{i}_z\}$. Consequently, the position vector is $\boldsymbol{r} = x\boldsymbol{i}_x + y\boldsymbol{i}_y + z\boldsymbol{i}_z$.

Considering the configuration in Fig. 3.1, we reconsider the retarded coefficient

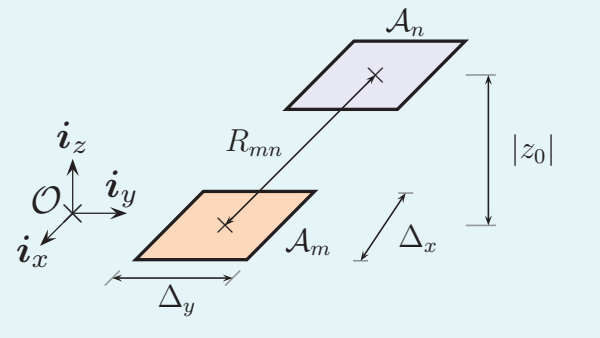

Figure 3.1: Two interacting parallel surface elements.

of potential describing the electric interaction between two rectangular surfaces expressed through a 2-D integral

$$\hat{P}_{mn}(s) = \frac{1}{\mathcal{S}_m \mathcal{S}_n} \int_{\boldsymbol{r}\in\mathcal{A}_m} dS \int_{\boldsymbol{r}'\in\mathcal{A}_n} \hat{g}(\boldsymbol{r}-\boldsymbol{r}', s) dS' \tag{3.1}$$

where $\{x_m, y_m, z_m\}$ and $\{x_n, y_n, z_n\}$ are the reference centers of the relevant surface mesh elements, $\mathcal{A}_m = \{-\Delta_x/2 < x - x_m < \Delta_x/2, -\Delta_y/2 < y - y_m < \Delta_y/2, z = z_m\}$ and $\mathcal{A}_n = \{-\Delta_x/2 < x - x_n < \Delta_x/2, -\Delta_y/2 < y - y_n < \Delta_y/2, z = z_n\}$ are the rectangular regions occupied by the interacting surfaces, where $\Delta_x > 0$ and $\Delta_y > 0$ denote the spatial discretization steps in the x- and y-direction, respectively, and $z_0 = z_m - z_n$. Consequently, the center-to-center distance between the surfaces is $R_{mn} = (r_{mn}^2 + z_0^2)^{1/2} > 0$, where $r_{mn} = [(x_m - x_n)^2 + (y_m - y_n)^2]^{1/2} > 0$ denotes their horizontal offset. Furthermore, s is the (real-valued and positive) Laplace-transform parameter, $\mathcal{S}_{m,n} = \Delta_x \Delta_y$ is the surface area of domains $\mathcal{A}_{m,n}$, respectively, and

$$\hat{g}(\boldsymbol{r}-\boldsymbol{r}', s) = \frac{e^{-s|\boldsymbol{r}-\boldsymbol{r}'|/c}}{4\pi|\boldsymbol{r}-\boldsymbol{r}'|} \tag{3.2}$$

is the free-space Green's function pertaining to a homogeneous, isotropic and loss-free medium with the EM wave speed $c > 0$.

The retarded partial coefficient as expressed through Eq. (3.1) will be next reformulated via a spatial Fourier representation. To that end, the Green's function

in the s-domain is represented via the wave slowness representation as

$$\hat{g}(\mathbf{r}-\mathbf{r}',s) = \Big(\frac{s}{2ß\pi}\Big)^2 \int_{\kappa=-ß\infty}^{ß\infty} \exp[-s\kappa(x-x')]d\kappa \int_{\sigma=-ß\infty}^{ß\infty} \frac{\exp\{-s[\sigma(y-y')+\Gamma(\kappa,\sigma)|z-z'|]\}}{2s\Gamma(\kappa,\sigma)}d\sigma \tag{3.3}$$

where

$$\Gamma(\kappa,\sigma) = (1/c^2-\kappa^2-\sigma^2)^{1/2} \text{ with } \Re(\Gamma)\geq 0 \tag{3.4}$$

has the meaning of the wave slowness normal to surfaces $\mathcal{A}_{m,n}$. Making use of the representation (3.3) in Eq. (3.1), we get

$$\begin{aligned}\hat{P}_{mn}(s) = \Big(\frac{s}{2ß\pi}\Big)^2 &\int_{\kappa=-ß\infty}^{ß\infty} \mathrm{i}_0^2(s\kappa\Delta_x/2) \\ &\times \exp[-s\kappa(x_m-x_n)]d\kappa \int_{\sigma=-ß\infty}^{ß\infty} \mathrm{i}_0^2(s\sigma\Delta_y/2) \\ &\times \frac{\exp\{-s[\sigma(y_m-y_n)+\Gamma(\kappa,\sigma)|z_0|]\}}{2s\Gamma(\kappa,\sigma)}d\sigma\end{aligned} \tag{3.5}$$

where $\mathrm{i}_0(x)$ denotes the modified spherical Bessel function of the first kind. Upon expanding the product of the modified spherical Bessel functions into their exponential factors it is found that $\hat{P}_{mn}(s)$ can be expressed in terms of a generic integral. Accordingly, we may write

$$\begin{aligned}\hat{P}_{mn}(s) = \Big[&\hat{K}(x_m-x_n+\Delta_x, y_m-y_n+\Delta_y, |z_0|, s) \\ &- 2\hat{K}(x_m-x_n+\Delta_x, y_m-y_n, |z_0|, s) \\ &+ \hat{K}(x_m-x_n+\Delta_x, y_m-y_n-\Delta_y, |z_0|, s) \\ &- 2\hat{K}(x_m-x_n, y_m-y_n+\Delta_y, |z_0|, s) \\ &+ 4\hat{K}(x_m-x_n, y_m-y_n, |z_0|, s) \\ &- 2\hat{K}(x_m-x_n, y_m-y_n-\Delta_y, |z_0|, s) \\ &+ \hat{K}(x_m-x_n-\Delta_x, y_m-y_n+\Delta_y, |z_0|, s) \\ &- 2\hat{K}(x_m-x_n-\Delta_x, y_m-y_n, |z_0|, s) \\ &+ \hat{K}(x_m-x_n-\Delta_x, y_m-y_n-\Delta_y, |z_0|, s)\Big]/\mathcal{S}_m\mathcal{S}_n\end{aligned} \tag{3.6}$$

Transforming the latter to the TD, we end up with

$$\begin{aligned} P_{mn}(t) = \Big[& K(x_m - x_n + \Delta_x, y_m - y_n + \Delta_y, |z_0|, t) \\ & - 2K(x_m - x_n + \Delta_x, y_m - y_n, |z_0|, t) \\ & + K(x_m - x_n + \Delta_x, y_m - y_n - \Delta_y, |z_0|, t) \\ & - 2K(x_m - x_n, y_m - y_n + \Delta_y, |z_0|, t) \\ & + 4K(x_m - x_n, y_m - y_n, |z_0|, t) \\ & - 2K(x_m - x_n, y_m - y_n - \Delta_y, |z_0|, t) \\ & + K(x_m - x_n - \Delta_x, y_m - y_n + \Delta_y, |z_0|, t) \\ & - 2K(x_m - x_n - \Delta_x, y_m - y_n, |z_0|, t) \\ & + K(x_m - x_n - \Delta_x, y_m - y_n - \Delta_y, |z_0|, t) \Big] / \mathcal{S}_m \mathcal{S}_n \end{aligned} \tag{3.7}$$

where the TD function $K(x, y, z, t)$ is specified by Eq. (3.13) in the next paragraph.

Computation of the integral in the TD for the parallel case

The integral representation to be transformed to TD has the following form

$$\begin{aligned} \hat{K}(x, y, z, s) = & \Big(\frac{s}{2\text{ß}\pi}\Big)^2 \int_{\kappa \in \mathbb{K}_0} \frac{\exp(s\kappa x)}{s^2\kappa^2} d\kappa \\ & \times \int_{\sigma \in \mathbb{S}_0} \frac{\exp\{-s[-\sigma y + \Gamma(\kappa, \sigma) z]\}}{s^2\sigma^2} \frac{d\sigma}{2s\Gamma(\kappa, \sigma)} \end{aligned} \tag{3.8}$$

for $x \in \mathbb{R}$, $y \in \mathbb{R}$, $\{z \in \mathbb{R}; z \geq 0\}$ and $\{s \in \mathbb{R}; s > 0\}$, where $\mathbb{K}_0$ and $\mathbb{S}_0$ are the integration paths extending along $\Re(\kappa) = 0$ and $\Re(\sigma) = 0$, respectively, that are indented to the right with semi-circular arcs with centers at the origins and vanishingly small radii (see Fig. 3.2). Recall that the vertical slowness parameter, $\Gamma(\kappa, \sigma)$, was defined in Eq. (3.4).

To transform Eq. (3.8) to TD, we shall next pursue the CdH method as described in [92]. Hence, by virtue of Jordan's lemma and Cauchy's theorem, we start by deforming $\mathbb{S}_0$ in the complex σ-plane into the CdH path that is defined via

$$-\sigma y + \Gamma(\kappa, \sigma) z = u d\Omega(\kappa) \tag{3.9}$$

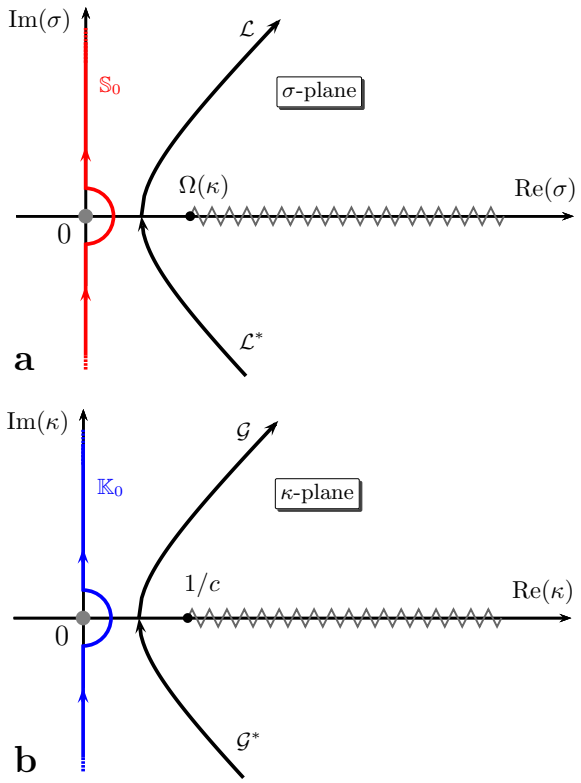

Figure 3.2: Complex slowness planes. (a) σ-plane with the CdH-path for $y < 0$; (b) κ-plane with the CdH-paths for $x < 0$.

for $\{1 \leq u < \infty\}$, where $\Omega(\kappa) = (1/c^2 - \kappa^2)^{1/2}$ with $\Re(\Omega) \geq 0$ and $d = (y^2 + z^2)^{1/2} > 0$. It is found that Eq. (3.9) is satisfied along a hyperbolic path, say $\mathcal{L} \cup \mathcal{L}^*$ (here * denotes the complex conjugate), where

$$\mathcal{L} = \big\{\sigma(u) = \big[-(y/d)u + ß(z/d)(u^2 - 1)^{1/2}\big]\Omega(\kappa)\big\} \tag{3.10}$$

for all $\{1 \leq u < \infty\}$ (see Fig. 3.2a). Further, upon introducing parameter u as the new variable of integration and accounting for the contribution of the (double) pole singularity at the origin $\sigma = 0$, the inner integral with respect to σ can be written

as

$$\begin{aligned}
&\frac{s}{2ß\pi}\int_{\sigma\in\mathbb{S}_0}\frac{\exp\{-s[-\sigma y+\Gamma(\kappa,\sigma)z]\}}{s^2\sigma^2}\frac{d\sigma}{2s\Gamma(\kappa,\sigma)}\\
&=\frac{y\mathrm{H}(y)}{2s\Omega(\kappa)}\exp[-s\Omega(\kappa)z]\\
&+\frac{d^2}{2\pi s^2\Omega^2(\kappa)}\int_{u=1}^{\infty}\exp[-sud\Omega(\kappa)]\frac{y^2u^2-z^2(u^2-1)}{[y^2u^2+z^2(u^2-1)]^2}\\
&\times\frac{du}{(u^2-1)^{1/2}}
\end{aligned}\tag{3.11}$$

Equation (3.11) is subsequently substituted in the starting Eq. (3.8), which yields

$$\hat{K}(x,y,z,s)=\hat{P}_{\|}(x,y,z,s)+\hat{Q}_{\|}(x,y,z,s)\tag{3.12}$$

where the TD counterparts of $\hat{P}_{\|}(x,y,z,s)$ and $\hat{Q}_{\|}(x,y,z,s)$ are derived in the following subsections. Relying on these results, we finally obtain

$$\begin{aligned}
K(x,y,z,t)&=\frac{c}{4\pi^2}\frac{d^2}{y^2}\int_{v=R}^{ct}(ct-v)^2\mathcal{F}_{\|}(x,y,z,v)dv\\
&+\frac{dx}{2\pi}c\left\{\left(\frac{c^2t^2}{d^2}-1\right)^{1/2}-\frac{|y|}{d}\tan^{-1}\left[\frac{d}{|y|}\left(\frac{c^2t^2}{d^2}-1\right)^{1/2}\right]\right\}\\
&\times\mathrm{H}(x)\mathrm{H}(ct-d)\\
&+\frac{\varrho y}{2\pi}c\left\{\left(\frac{c^2t^2}{\varrho^2}-1\right)^{1/2}-\frac{|x|}{\varrho}\tan^{-1}\left[\frac{\varrho}{|x|}\left(\frac{c^2t^2}{\varrho^2}-1\right)^{1/2}\right]\right\}\\
&\times\mathrm{H}(y)\mathrm{H}(ct-\varrho)+\frac{xy}{2}c\mathrm{H}(x)\mathrm{H}(y)\mathrm{H}(ct-z)
\end{aligned}\tag{3.13}$$

where $\varrho=(x^2+z^2)^{1/2}>0$, $R=(x^2+y^2+z^2)^{1/2}>0$ and $\mathcal{F}_{\|}(x,y,z,v)$ is given by Eq. (3.24). The convolution integral on the right-hand side of Eq. (3.13) can be carried out via standard integration routines or the recursive convolution technique along the lines specified in [92, Appendix H]. Expression (3.13) can be finally used in Eq. (3.7) to evaluate the desired TD coefficient.

For the sake of completeness, we shall further discuss limiting cases of Eq. (3.13) that are useful for describing the interaction of overlapping surface elements. First, it is noted that the limit $z\downarrow 0$ has been derived previously in closed form, that is, $K(x,y,0,t)=I(x,y,t)$ [93, Eq. (21)]. Consequently, it is straightforward to deduce

the following limiting cases $K(x,0,0,t) = I(x,0,t)$ with $K(0,y,0,t) = I(0,y,t)$ (see [93, Eq. (22)]) and $K(0,0,0,t) = I(0,0,t)$ (see [93, Eq. (23)]). Furthermore, for the non-zero vertical offset, we find

$$K(x,0,z,t) = \frac{|x|z}{4\pi}c\Bigg\{\frac{|x|}{2z} - \frac{z}{2|x|} - \left(\frac{c^2t^2}{z^2} - 1\right)^{1/2} + \frac{c^2t^2}{2|x|z}\Bigg\}\mathrm{H}(ct-\varrho) + \frac{zx}{2\pi}c\left(\frac{c^2t^2}{z^2} - 1\right)^{1/2}\mathrm{H}(x)\mathrm{H}(ct-z) \tag{3.14}$$

and a similar expression applies to $K(0,y,z,t)$. Finally, for the planar surfaces with the zero horizontal offset, we find

$$K(0,0,z,t) = \frac{z^2}{8\pi}c\left(\frac{c^2t^2}{z^2} - 1\right)\mathrm{H}(ct-z) \tag{3.15}$$

which completes the analysis.

Generic integral $\hat{P}_{\|}(x,y,z,s)$

The first integral to be transformed to the TD has the following form

$$\hat{P}_{\|}(x,y,z,s) = \frac{d^2}{2\pi s}\int_{u=1}^{\infty}\frac{y^2u^2 - z^2(u^2-1)}{[y^2u^2 + z^2(u^2-1)]^2}\frac{du}{(u^2-1)^{1/2}} \times \frac{1}{2\pi ß}\int_{\kappa\in\mathbb{K}_0}\frac{\exp\{-s[-\kappa x + ud\Omega(\kappa)]\}}{s^2\kappa^2}\frac{d\kappa}{\Omega^2(\kappa)} \tag{3.16}$$

To derive $P_{\|}(x,y,z,t)$, the integration contour in the complex κ-plane is deformed into the CdH path that is defined by

$$-\kappa x + ud\Omega(\kappa) = \tau \tag{3.17}$$

for $\{\tau \in \mathbb{R}; \tau > 0\}$. Solving Eq. (3.17) for κ, we obtain hyperbolic arcs, further denoted by $\mathcal{G} \cup \mathcal{G}^*$, that are described by

$$\mathcal{G} = \left\{\kappa(\tau) = -\frac{x}{R^2(u)}\tau + ß\frac{ud}{R^2(u)}\left[\tau^2 - R^2(u)/c^2\right]^{1/2}\right\} \tag{3.18}$$

for all $\tau \geq R(u)/c$, where $R(u) = (x^2 + u^2d^2)^{1/2} > 0$. Introducing next the time parameter τ as the new variable of integration and combining the contributions from

$\mathcal{G}$ and $\mathcal{G}^*$, we get

$$\begin{aligned}\hat{P}_{\parallel}(x,y,z,s) &= \hat{P}_{0,\parallel}(x,y,z,s) \\ &+ \frac{d^2}{2\pi^2 s^3}\int_{u=1}^{\infty}\frac{y^2u^2 - z^2(u^2-1)}{[y^2u^2+z^2(u^2-1)]^2}\frac{du}{(u^2-1)^{1/2}} \\ &\times \int_{\tau=R(u)/c}^{\infty}\Re\left\{\frac{1}{\kappa^2(\tau)\Omega[\kappa(\tau)]}\right\}\frac{d\tau}{[\tau^2 - R^2(u)/c^2]^{1/2}}\end{aligned} \tag{3.19}$$

where the values along $\mathcal{G}$ are taken and $\hat{P}_{0,\parallel}(x,y,s)$ denotes the contribution from the pole at $\kappa = 0$ that reads

$$\begin{aligned}\hat{P}_{0,\parallel}(x,y,z,s) = \frac{d^2 x\mathrm{H}(x)c^2}{2\pi s^2}\int_{u=1}^{\infty}\exp(-sud/c) \\ \times \frac{y^2u^2 - z^2(u^2-1)}{[y^2u^2+z^2(u^2-1)]^2}\frac{du}{(u^2-1)^{1/2}}\end{aligned} \tag{3.20}$$

In the second term of Eq. (3.19), we change the order of integration according to

$$\int_{u=1}^{\infty}du\int_{\tau=R(u)/c}^{\infty}d\tau \to \int_{\tau=R/c}^{\infty}d\tau\int_{u=1}^{U(\tau)}du \tag{3.21}$$

in which $R = R(1)$ and $U(\tau) = (c^2\tau^2 - x^2)^{1/2}/d$ and we arrive at

$$\begin{aligned}\hat{P}_{\parallel}(x,y,z,s) &= \hat{P}_{0,\parallel}(x,y,z,s) \\ &+ \frac{c^4d^2}{2\pi^2 s^3 y^2}\int_{\tau=R/c}^{\infty}\exp(-s\tau)d\tau \\ &\int_{u=1}^{U(\tau)}\frac{c\tau[3x^2c^2\tau^2 - 2x^4 - u^2d^2(c^2\tau^2 - u^2d^2 + x^2)]}{d^2U^2(\tau)(c^2\tau^2 - u^2d^2)^2} \\ &\frac{u^2 - (u^2-1)(z^2/y^2)}{[u^2+(u^2-1)(z^2/y^2)]^2}\frac{udu}{(u^2-1)^{1/2}[U^2(\tau)-u^2]^{1/2}}\end{aligned} \tag{3.22}$$

The inverse square-root singularities at the end points of the integration with respect to u can be handled via the substitution $u^2 = \cos^2(\psi) + U^2(\tau)\sin^2(\psi)$ for $\{0 \le \psi \le \pi/2\}$. Consequently, the inner integral can be carried out at once either analytically

or numerically via a standard integration routine. In this way, we end up with

$$\hat{P}_{\parallel}(x,y,z,s) = \frac{d^4x\mathrm{H}(x)}{2\pi s^2 y^2}\int_{\tau=d/c}^{\infty}\exp(-s\tau)$$
$$\times\frac{\tau^2-(\tau^2-d^2/c^2)(z^2/y^2)}{[\tau^2+(\tau^2-d^2/c^2)(z^2/y^2)]^2}\frac{d\tau}{(\tau^2-d^2/c^2)^{1/2}}$$
$$+\frac{c^4d^2}{2\pi^2 s^3 y^2}\int_{\tau=R/c}^{\infty}\exp(-s\tau)\mathcal{F}_{\parallel}(x,y,z,c\tau)d\tau \tag{3.23}$$

where the first integral represents the pole contribution (3.20), where we substituted $\tau = ud/c$ and the integrand of the second term follows from

$$\mathcal{F}_{\parallel}(x,y,z,v) = \frac{v}{d^2U^2}\Bigg\{D^2(3U^2+D^2)$$
$$\times\int_{\psi=0}^{\pi/2}\frac{\cos^2(\psi)+A^2\sin^2(\psi)}{[\cos^2(\psi)+B^2\sin^2(\psi)]^2}$$
$$\times\frac{d\psi}{[C^2\cos^2(\psi)+D^2\sin^2(\psi)]^2}$$
$$-\int_{\psi=0}^{\pi/2}\frac{\cos^2(\psi)+A^2\sin^2(\psi)}{[\cos^2(\psi)+B^2\sin^2(\psi)]^2}$$
$$\times\frac{\cos^2(\psi)+U^2\sin^2(\psi)}{C^2\cos^2(\psi)+D^2\sin^2(\psi)}d\psi$$
$$-D^2\int_{\psi=0}^{\pi/2}\frac{\cos^2(\psi)+A^2\sin^2(\psi)}{[\cos^2(\psi)+B^2\sin^2(\psi)]^2}$$
$$\times\frac{\cos^2(\psi)+U^2\sin^2(\psi)}{[C^2\cos^2(\psi)+D^2\sin^2(\psi)]^2}d\psi\Bigg\} \tag{3.24}$$

where

$$U^2 = v^2/d^2 - D^2 \tag{3.25}$$
$$A^2 = U^2 - (U^2-1)(z^2/y^2) \tag{3.26}$$
$$B^2 = U^2 + (U^2-1)(z^2/y^2) \tag{3.27}$$
$$C^2 = v^2/d^2 - 1 \tag{3.28}$$
$$D^2 = x^2/d^2 \tag{3.29}$$

With the aid of Lerch's uniqueness theorem [94, appendix], the integrals in (3.23) can be transformed to the TD and we get

$$P_{\|}(x,y,z,t) = \frac{c}{4\pi^2}\frac{d^2}{y^2}\int_{v=R}^{ct}(ct-v)^2\mathcal{F}_{\|}(x,y,z,v)dv$$
$$+\frac{dx}{2\pi}c\left\{\left(\frac{c^2t^2}{d^2}-1\right)^{1/2}-\frac{|y|}{d}\tan^{-1}\left[\frac{d}{|y|}\left(\frac{c^2t^2}{d^2}-1\right)^{1/2}\right]\right\}$$
$$\times \mathrm{H}(x)\mathrm{H}(ct-d) \tag{3.30}$$

where the second term, in fact, represents (the TD counterpart of) the pole contribution (3.20). This expression is used to derive the main result represented by Eq. (3.13).

Generic integral $\hat{Q}_{\|}(x,y,z,s)$

The second integral to be transformed to the TD has the following form

$$\hat{Q}_{\|}(x,y,z,s) = \frac{y\mathrm{H}(y)}{4ß\pi}\int_{\kappa\in\mathbb{K}_0}\frac{\exp\{-s[-\kappa x+\Omega(\kappa)z]\}}{s^2\kappa^2}\frac{d\kappa}{\Omega(\kappa)} \tag{3.31}$$

The transformation of $\hat{Q}(x,y,z,s)$ to the TD is accomplished by deforming $\mathbb{K}_0$ into the corresponding CdH path, which is permissible thanks to Jordan's lemma and Cauchy's theorem. The resulting CdH path is a hyperbolic arc, denoted by $\mathcal{G}\cup\mathcal{G}^*$, along which the following equality is satisfied

$$-\kappa x+\Omega(\kappa)z=\tau \tag{3.32}$$

where τ is the (real-valued and positive) time parameter. Solving Eq. (3.32) for κ, we then obtain

$$\mathcal{G}=\{\kappa(\tau)=-\frac{x}{\varrho^2}\tau+ß\frac{z}{\varrho^2}\big(\tau^2-\varrho^2/c^2\big)^{1/2}\} \tag{3.33}$$

for all $\tau\geq\varrho/c$ and recall that $\varrho=(x^2+z^2)^{1/2}>0$. Introducing now τ as the new variable of integration and accounting for the presence of the double pole singularity

at $\kappa = 0$, we arrive at

$$\hat{Q}_{\parallel}(x,y,z,s) = \frac{cx\mathrm{H}(x)y\mathrm{H}(y)}{2s}\exp(-sz/c) + \frac{c^2 y\mathrm{H}(y)}{2\pi s^2}\int_{\tau=\varrho/c}^{\infty}\exp(-s\tau)\frac{x^2c^2\tau^2 - z^2(c^2\tau^2-\varrho^2)}{(c^2\tau^2-z^2)^2} \times \frac{d\tau}{(\tau^2-\varrho^2/c^2)^{1/2}} \tag{3.34}$$

The transformation of the first term in Eq. (3.34) is straightforward. The integral term leads to a convolution-type integral that is amenable to analytical solution. Hence, relying on Lerch's uniqueness theorem [94, appendix], again, we after a few steps of algebra end up with

$$Q_{\parallel}(x,y,z,t) = \frac{\varrho y}{2\pi}c\Bigg\{\left(\frac{c^2t^2}{\varrho^2}-1\right)^{1/2} - \frac{|x|}{\varrho}\tan^{-1}\left[\frac{\varrho}{|x|}\left(\frac{c^2t^2}{\varrho^2}-1\right)^{1/2}\right]\Bigg\}\mathrm{H}(y)\mathrm{H}(ct-\varrho) + \frac{xy}{2}c\mathrm{H}(x)\mathrm{H}(y)\mathrm{H}(ct-z) \tag{3.35}$$

This expression is finally used to derive the main result (3.13).

3.1.2 Orthogonal patches

Now we shall assume the interaction of two rectangular surface elements lying in two mutually orthogonal planes sketched in Fig. 3.3. As before, the interacting surfaces are assumed to be located in an unbounded, linear homogeneous and isotropic medium that is characterized by constants ϵ_0 and μ_0.

In this section, we study a retarded partial coefficient expressed through a 2-D integral where now, $\mathcal{A}_n = \{-\Delta_x/2 < x - x_n < \Delta_x/2, y = y_n, -\Delta_z/2 < z - z_n < \Delta_z/2\}$ and $\mathcal{S}_m = \Delta_x\Delta_y$ and $\mathcal{S}_n = \Delta_x\Delta_z$ are the surfaces area of domain $\mathcal{A}_m$ and $\mathcal{A}_n$, respectively.

Again the free-space Green's function in the s-domain is represented via the wave slowness representation.

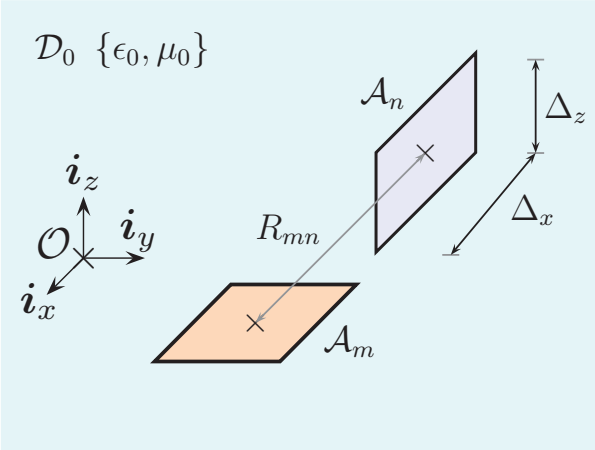

Figure 3.3: Two interacting mutually orthogonal surface elements.

Making use of the representation (3.3) in Eq. (3.1), we get

$$\begin{aligned}\hat{P}_{mn}(s) = \left(\frac{s}{2ß\pi}\right)^2 \int_{\kappa=-ß\infty}^{ß\infty} \mathrm{i}_0^2(s\kappa\Delta_x/2) \\ \times \exp[-s\kappa(x_m - x_n)]d\kappa \int_{\sigma=-ß\infty}^{ß\infty} \mathrm{i}_0(s\sigma\Delta_y/2) \\ \times \exp[-s\sigma(y_m - y_n)]\zeta(\kappa, \sigma, z_m|z_n)d\sigma\end{aligned} \tag{3.36}$$

where $\mathrm{i}_0(x)$ denotes the modified spherical Bessel function of the first kind and $\zeta = \zeta(\kappa, \sigma, z_m|z_n)$ has the following form

$$\zeta = \frac{1}{\Delta_z} \int_{z'=z_n-\Delta_z/2}^{z_n+\Delta_z/2} \frac{\exp[-s\Gamma(\kappa,\sigma)|z_m - z'|]}{2s\Gamma(\kappa,\sigma)} dz' \tag{3.37}$$

The result of integration depends on the mutual position of the interacting surfaces. Indeed, we get

$$\begin{aligned}\zeta\Delta_z = \frac{\exp[-s\Gamma(\kappa,\sigma)(z_m - z_n - \Delta_z/2)]}{2s^2\Gamma^2(\kappa,\sigma)} \\ - \frac{\exp[-s\Gamma(\kappa,\sigma)(z_m - z_n + \Delta_z/2)]}{2s^2\Gamma^2(\kappa,\sigma)}\end{aligned} \tag{3.38}$$

if $z_m > z_n + \Delta_z/2$, and

$$\zeta\Delta_z = \frac{\exp[-s\Gamma(\kappa,\sigma)(z_n - z_m - \Delta_z/2)]}{2s^2\Gamma^2(\kappa,\sigma)} - \frac{\exp[-s\Gamma(\kappa,\sigma)(z_n - z_m + \Delta_z/2)]}{2s^2\Gamma^2(\kappa,\sigma)} \tag{3.39}$$

if $z_m < z_n - \Delta_z/2$, and, finally,

$$\zeta\Delta_z = \frac{1}{s^2\Gamma^2(\kappa,\sigma)} - \frac{\exp[-s\Gamma(\kappa,\sigma)(z_m - z_n + \Delta_z/2)]}{2s^2\Gamma^2(\kappa,\sigma)} - \frac{\exp[-s\Gamma(\kappa,\sigma)(z_n - z_m + \Delta_z/2)]}{2s^2\Gamma^2(\kappa,\sigma)} \tag{3.40}$$

if $\{z_n - \Delta_z/2 < z_m < z_n + \Delta_z/2\}$. The form of constituent in Eqs. (3.38)–(3.40) suggests to define

$$\begin{aligned}\hat{\Pi}_{mn}(z,s) = \frac{1}{\Delta_z}\left(\frac{s}{2ß\pi}\right)^2 \int_{\kappa=-ß\infty}^{ß\infty} \mathrm{i}_0^2(s\kappa\Delta_x/2) \\ \times \exp[-s\kappa(x_m - x_n)]d\kappa \int_{\sigma=-ß\infty}^{ß\infty} \mathrm{i}_0(s\sigma\Delta_y/2) \\ \times \frac{\exp\{-s[\sigma(y_m - y_n) + \Gamma(\kappa,\sigma)|z|]\}}{2s^2\Gamma^2(\kappa,\sigma)}d\sigma\end{aligned} \tag{3.41}$$

Consequently, we may rewrite the coefficient as

$$\hat{P}_{mn}(s) = \hat{\Pi}_{mn}(z_m - z_n - \Delta_z/2, s) - \hat{\Pi}_{mn}(z_m - z_n + \Delta_z/2, s) \tag{3.42}$$

for $z_m > z_n + \Delta_z/2$, and

$$\hat{P}_{mn}(s) = \hat{\Pi}_{mn}(z_n - z_m - \Delta_z/2, s) - \hat{\Pi}_{mn}(z_n - z_m + \Delta_z/2, s) \tag{3.43}$$

for $z_m < z_n - \Delta_z/2$, and

$$\hat{P}_{mn}(s) = 2\,\hat{\Pi}_{mn}(0,s) - \hat{\Pi}_{mn}(z_m - z_n + \Delta_z/2, s) - \hat{\Pi}_{mn}(z_n - z_m + \Delta_z/2, s) \tag{3.44}$$

for $\{z_n - \Delta_z/2 < z_m < z_n + \Delta_z/2\}$. Upon expanding the product of the modified spherical Bessel functions into their exponential factors it is found that $\hat{\Pi}_{mn}(s,z)$ can be expressed in terms of a generic integral. Therefore, we may write

$$\begin{aligned}\hat{\Pi}_{mn}(z,s) = \Big[&\hat{\Lambda}(x_m - x_n + \Delta_x, y_m - y_n + \Delta_y/2, |z|, s)\\ &- \hat{\Lambda}(x_m - x_n + \Delta_x, y_m - y_n - \Delta_y/2, |z|, s)\\ &- 2\hat{\Lambda}(x_m - x_n, y_m - y_n + \Delta_y/2, |z|, s)\\ &+ 2\hat{\Lambda}(x_m - x_n, y_m - y_n - \Delta_y/2, |z|, s)\\ &+ \hat{\Lambda}(x_m - x_n - \Delta_x, y_m - y_n + \Delta_y/2, |z|, s)\\ &- \hat{\Lambda}(x_m - x_n - \Delta_x, y_m - y_n - \Delta_y/2, |z|, s)\Big]/\mathcal{S}_m\mathcal{S}_n\end{aligned} \tag{3.45}$$

Transforming the latter to the TD, we end up with

$$\begin{aligned}\Pi_{mn}(z,t) = \Big[&\Lambda(x_m - x_n + \Delta_x, y_m - y_n + \Delta_y/2, |z|, t)\\ &- \Lambda(x_m - x_n + \Delta_x, y_m - y_n - \Delta_y/2, |z|, t)\\ &- 2\Lambda(x_m - x_n, y_m - y_n + \Delta_y/2, |z|, t)\\ &+ 2\Lambda(x_m - x_n, y_m - y_n - \Delta_y/2, |z|, t)\\ &+ \Lambda(x_m - x_n - \Delta_x, y_m - y_n + \Delta_y/2, |z|, t)\\ &- \Lambda(x_m - x_n - \Delta_x, y_m - y_n - \Delta_y/2, |z|, t)\Big]/\mathcal{S}_m\mathcal{S}_n\end{aligned} \tag{3.46}$$

Once the TD expression for $\Pi_{mn}(z,t)$ is available, it can be used in the TD counterparts of Eqs. (3.42)–(3.44) to evaluate the desired TD coefficient $P_{mn}(t)$. The TD function $\Lambda(x,y,z,t)$ is specified by Eqs. (3.30) and (3.70) via (the TD original of) Eq. (3.12) as given in the next section.

Computation of integrals in the TD: the orthogonal Case

The integral representation to be transformed to TD has the following form

$$\begin{aligned}\hat{\Lambda}(x,y,z,s) = &\Big(\frac{s}{2ß\pi}\Big)^2 \int_{\kappa\in\mathbb{K}_0} \frac{\exp(s\kappa x)}{s^2\kappa^2} d\kappa\\ &\times \int_{\sigma\in\mathbb{S}_0} \frac{\exp\{-s[-\sigma y + \Gamma(\kappa,\sigma)z]\}}{s\sigma} \frac{d\sigma}{2s^2\Gamma^2(\kappa,\sigma)}\end{aligned} \tag{3.47}$$

for $x \in \mathbb{R}$, $y \in \mathbb{R}$, $\{z \in \mathbb{R}; z \geq 0\}$ and $\{s \in \mathbb{R}; s > 0\}$, where $\mathbb{K}_0$ and $\mathbb{S}_0$ are the integration paths extending along $\Re(\kappa) = 0$ and $\Re(\sigma) = 0$, respectively, that are indented to the right with semi-circular arcs with centers at the origins and vanishingly small radii. Recall that the vertical slowness parameter, $\Gamma(\kappa, \sigma)$, was defined in Eq. (3.4). To transform Eq. (3.47) to TD, we shall next pursue the CdH method as described in [92]. Hence, by virtue of Jordan's lemma and Cauchy's theorem, we start by deforming $\mathbb{S}_0$ in the complex σ-plane into the CdH path as defined in Eq. (3.9). It is found that Eq. (3.9) is satisfied along a hyperbolic path, say $\mathcal{L} \cup \mathcal{L}^*$ (here * denotes the complex conjugate), where

$$\mathcal{L} = \big\{\sigma(u) = \big[-(y/d)u + ß(z/d)(u^2-1)^{1/2}\big]\Omega(\kappa)\big\} \tag{3.48}$$

for all $\{1 \leq u < \infty\}$. Further, upon introducing parameter u as the new variable of integration and accounting for the contribution of the (double) pole singularity at the origin $\sigma = 0$, the inner integral with respect to σ can be written as

$$\begin{aligned}
&\frac{s}{2ß\pi}\int_{\sigma\in\mathbb{S}_0} \frac{\exp\{-s[-\sigma y + \Gamma(\kappa,\sigma)z]\}}{s\sigma}\frac{d\sigma}{2s^2\Gamma^2(\kappa,\sigma)} \\
&= \frac{\mathrm{H}(y)}{2s^2\Omega^2(\kappa)}\exp[-s\Omega(\kappa)z] \\
&- \frac{yz/d^2}{2\pi s^2\Omega^2(\kappa)}\int_{u=1}^{\infty}\exp[-sud\Omega(\kappa)] \\
&\times \frac{2u^2-1}{(u^2-y^2/d^2)(u^2-z^2/d^2)}\frac{\dot{\mathrm{u}}}{(u^2-1)^{1/2}}
\end{aligned} \tag{3.49}$$

Equation (3.49) is subsequently substituted in the starting Eq. (3.47), which yields

$$\hat{\Lambda}(x,y,z,s) = \hat{Q}_\perp(x,y,z,s) - \hat{P}_\perp(x,y,z,s) \tag{3.50}$$

where the TD counterparts of $\hat{P}_\perp(x,y,z,s)$ and $\hat{Q}_\perp(x,y,z,s)$ are derived in the following subsections.

Generic integral $\hat{P}_\perp(x,y,z,s)$

The first integral to be transformed to the TD has the following form

$$\hat{P}_\perp(x,y,z,s) = \frac{yz/d^2}{2\pi s}\int_{u=1}^{\infty}\frac{2u^2-1}{(u^2-y^2/d^2)(u^2-z^2/d^2)} \times \frac{\text{u}}{(u^2-1)^{1/2}}\frac{1}{2\pi\text{ß}}\int_{\kappa\in\mathbb{K}_0}\frac{\exp\{-s[-\kappa x+ud\Omega(\kappa)]\}}{s^2\kappa^2}\frac{d\kappa}{\Omega^2(\kappa)} \tag{3.51}$$

To derive $P_\perp(x,y,z,t)$, the integration contour in the complex κ-plane is deformed into the CdH path that is defined by

$$-\kappa x + ud\Omega(\kappa) = \tau \tag{3.52}$$

for $\{\tau\in\mathbb{R};\tau>0\}$. Solving Eq. (3.52) for κ, we obtain hyperbolic arcs, further denoted by $\mathcal{G}\cup\mathcal{G}^*$, that are described by

$$\mathcal{G} = \left\{\kappa(\tau) = -\frac{x}{R^2(u)}\tau + \text{ß}\frac{ud}{R^2(u)}\left[\tau^2 - R^2(u)/c^2\right]^{1/2}\right\} \tag{3.53}$$

for all $\tau\geq R(u)/c$, where $R(u)=(x^2+u^2d^2)^{1/2}>0$. Introducing next the time parameter τ as the new variable of integration and combining the contributions from $\mathcal{G}$ and $\mathcal{G}^*$, we get

$$\begin{aligned}\hat{P}_\perp(x,y,z,s) &= \hat{P}_{0,\perp}(x,y,z,s)\\ &+\frac{yz/d^2}{2\pi^2 s^3}\int_{u=1}^{\infty}\frac{2u^2-1}{(u^2-y^2/d^2)(u^2-z^2/d^2)}\frac{du}{(u^2-1)^{1/2}}\\ &\times\int_{\tau=R(u)/c}^{\infty}\Re\left\{\frac{1}{\kappa^2(\tau)\Omega[\kappa(\tau)]}\right\}\frac{d\tau}{[\tau^2-R^2(u)/c^2]^{1/2}}\end{aligned} \tag{3.54}$$

where the values along $\mathcal{G}$ are taken and $\hat{P}_{0,\perp}(x,y,z,s)$ denotes the contribution from the pole at $\kappa=0$ that reads

$$\begin{aligned}\hat{P}_{0,\perp}(x,y,z,s) = \frac{(xyz/d^2)\text{H}(x)c^2}{2\pi s^2}\int_{u=1}^{\infty}\exp(-sud/c)\\ \times\frac{2u^2-1}{(u^2-y^2/d^2)(u^2-z^2/d^2)}\frac{du}{(u^2-1)^{1/2}}\end{aligned} \tag{3.55}$$

In the second term of Eq. (3.54), we change the order of integration according to

$$\int_{u=1}^{\infty}du\int_{\tau=R(u)/c}^{\infty}d\tau\rightarrow\int_{\tau=R/c}^{\infty}d\tau\int_{u=1}^{U(\tau)}du \tag{3.56}$$

in which $R = R(1)$ and $U(\tau) = (c^2\tau^2 - x^2)^{1/2}/d$ and we arrive at

$$\begin{aligned}
&\hat{P}_{\perp}(x,y,z,s) = \hat{P}_{0,\perp}(x,y,z,s) \\
&+ \frac{c^4}{2\pi^2 s^3}\frac{yz}{d^2}\int_{\tau=R/c}^{\infty}\exp(-s\tau)d\tau \\
&\int_{u=1}^{U(\tau)}\frac{c\tau[3x^2c^2\tau^2 - 2x^4 - u^2d^2(c^2\tau^2 - u^2d^2 + x^2)]}{d^2U^2(\tau)(c^2\tau^2 - u^2d^2)^2} \\
&\frac{2u^2-1}{(u^2 - y^2/d^2)(u^2 - z^2/d^2)}\frac{udu}{(u^2-1)^{1/2}[U^2(\tau) - u^2]^{1/2}}
\end{aligned} \tag{3.57}$$

The inverse square-root singularities at the end points of the integration with respect to u can be handled via the substitution $u^2 = \cos^2(\psi) + U^2(\tau)\sin^2(\psi)$ for $\{0 \leq \psi \leq \pi/2\}$. Consequently, the inner integral can be carried out numerically via a standard integration routine. In this way, we end up with

$$\begin{aligned}
&\hat{P}_{\perp}(x,y,z,s) = \frac{xyz\mathrm{H}(x)}{2\pi s^2}\int_{\tau=d/c}^{\infty}\exp(-s\tau) \\
&\times \frac{2\tau^2 - d^2/c^2}{(\tau^2 - y^2/c^2)(\tau^2 - z^2/c^2)}\frac{d\tau}{(\tau^2 - d^2/c^2)^{1/2}} \\
&+ \frac{c^4}{2\pi^2 s^3}\frac{yz}{d^2}\int_{\tau=R/c}^{\infty}\exp(-s\tau)\mathcal{F}_{\perp}(x,y,z,c\tau)d\tau
\end{aligned} \tag{3.58}$$

where the first integral represents the pole contribution (3.55), where we substituted $\tau = ud/c$ and the integrand of the second term follows from

$$\begin{aligned}
\mathcal{F}_\perp(x,y,z,v) = \frac{v}{d^2U^2}\Bigg\{ & D^2(3U^2+D^2) \\
& \times \int_{\psi=0}^{\pi/2} \frac{\cos^2(\psi)+(2U^2-1)\sin^2(\psi)}{B^2\cos^2(\psi)+(U^2-A^2)\sin^2(\psi)} \\
& \times \frac{1}{A^2\cos^2(\psi)+(U^2-B^2)\sin^2(\psi)} \\
& \times \frac{d\psi}{[C^2\cos^2(\psi)+D^2\sin^2(\psi)]^2} \\
& - \int_{\psi=0}^{\pi/2} \frac{\cos^2(\psi)+(2U^2-1)\sin^2(\psi)}{B^2\cos^2(\psi)+(U^2-A^2)\sin^2(\psi)} \\
& \times \frac{1}{A^2\cos^2(\psi)+(U^2-B^2)\sin^2(\psi)} \\
& \times \frac{\cos^2(\psi)+U^2\sin^2(\psi)}{C^2\cos^2(\psi)+D^2\sin^2(\psi)}d\psi \\
& - D^2\int_{\psi=0}^{\pi/2} \frac{\cos^2(\psi)+(2U^2-1)\sin^2(\psi)}{B^2\cos^2(\psi)+(U^2-A^2)\sin^2(\psi)} \\
& \times \frac{1}{A^2\cos^2(\psi)+(U^2-B^2)\sin^2(\psi)} \\
& \times \frac{\cos^2(\psi)+U^2\sin^2(\psi)}{[C^2\cos^2(\psi)+D^2\sin^2(\psi)]^2}d\psi\Bigg\}
\end{aligned} \tag{3.59}$$

where

$$U^2 = v^2/d^2 - D^2 \tag{3.60}$$

$$A^2 = y^2/d^2 \tag{3.61}$$

$$B^2 = z^2/d^2 \tag{3.62}$$

$$C^2 = v^2/d^2 - 1 \tag{3.63}$$

$$D^2 = x^2/d^2 \tag{3.64}$$

With the aid of Lerch's uniqueness theorem [94, appendix], the integrals in (3.58) can be transformed to the TD and we get

$$\begin{aligned} P_\perp(x,y,z,t) &= \frac{c}{4\pi^2}\frac{yz}{d^2}\int_{v=R}^{ct}(ct-v)^2\mathcal{F}_\perp(x,y,z,v)dv \\ &+ \frac{c}{2\pi}x\Bigg\{ct\tan^{-1}\left[\frac{z}{c_0 t}\frac{(c^2t^2-d^2)^{1/2}}{y}\right] \\ &+ ct\tan^{-1}\left[\frac{y}{c_0 t}\frac{(c^2t^2-d^2)^{1/2}}{z}\right] \\ &- z\tan^{-1}\left[\frac{(c^2t^2-d^2)^{1/2}}{y}\right] \\ &- y\tan^{-1}\left[\frac{(c^2t^2-d^2)^{1/2}}{z}\right]\Bigg\}\mathrm{H}(x)\mathrm{H}(ct-d) \end{aligned} \tag{3.65}$$

where the second term, in fact, represents (the TD counterpart of) the pole contribution (3.55).

Generic integral $\hat{Q}_\perp(x,y,z,s)$

The second integral to be transformed to the TD has the following form

$$\hat{Q}_\perp(x,y,z,s) = \frac{\mathrm{H}(y)}{4ß\pi s}\int_{\kappa\in\mathbb{K}_0}\frac{\exp\{-s[-\kappa x+\Omega(\kappa)z]\}}{s^2\kappa^2}\frac{d\kappa}{\Omega^2(\kappa)} \tag{3.66}$$

The transformation of $\hat{Q}_\perp(x,y,z,s)$ to the TD is accomplished by deforming $\mathbb{K}_0$ into the corresponding CdH path, which is permissible thanks to Jordan's lemma and Cauchy's theorem. The resulting CdH path is a hyperbolic arc, denoted by $\mathcal{G}\cup\mathcal{G}^*$, along which the following equality is satisfied

$$-\kappa x+\Omega(\kappa)z=\tau \tag{3.67}$$

where τ is the (real-valued and positive) time parameter. Solving Eq. (3.67) for κ, we then obtain

$$\mathcal{G}=\{\kappa(\tau)=-\frac{x}{\varrho^2}\tau+ß\frac{z}{\varrho^2}\left(\tau^2-\varrho^2/c^2\right)^{1/2}\} \tag{3.68}$$

for all $\tau \geq \varrho/c$ and recall that $\varrho = (x^2 + z^2)^{1/2} > 0$. Introducing now τ as the new variable of integration and accounting for the presence of the double pole singularity at $\kappa = 0$, we arrive at

$$\begin{aligned}\hat{Q}_\perp(x,y,z,s) &= \frac{c^2 x \mathrm{H}(x)\mathrm{H}(y)}{2s^2}\exp(-sz/c) \\ &+ \frac{c^3 z \mathrm{H}(y)}{2\pi s^3}\int_{\tau=\varrho/c}^{\infty}\exp(-s\tau) \\ &\times \frac{3x^2c^2\tau^2 - z^2(c^2\tau^2 - z^2) - 2x^4 - x^2z^2}{(c^2\tau^2 - x^2)(c^2\tau^2 - z^2)^2}\frac{c\tau\, d\tau}{(\tau^2 - \varrho^2/c^2)^{1/2}}\end{aligned} \tag{3.69}$$

The transformation of the first term in Eq. (3.69) is straightforward. The integral term leads to a convolution-type integral that is amenable to analytical solution. Hence, relying on Lerch's uniqueness theorem [94, appendix], again, we after a few steps of algebra end up with

$$\begin{aligned}Q_\perp(x,y,z,t) = \frac{c}{4\pi}\Bigg\{ &(c^2t^2 + x^2)\tan^{-1}\left[\frac{(c^2t^2 - \varrho^2)^{1/2}}{z}\right] \\ &+ 2xz\tan^{-1}\left[\frac{(c^2t^2 - \varrho^2)^{1/2}}{x}\right] \\ &- 2xct\tan^{-1}\left[\frac{ct}{z}\frac{(c^2t^2 - \varrho^2)^{1/2}}{x}\right] \\ &- z(c^2t^2 - \varrho^2)^{1/2}\Bigg\}\mathrm{H}(y)\mathrm{H}(ct - \varrho) \\ &+ (c/2)x(ct - z)\mathrm{H}(x)\mathrm{H}(y)\mathrm{H}(ct - z)\end{aligned} \tag{3.70}$$

which can be used with Eq. (3.65) to evaluate $\Lambda(x,y,z,t)$ via (the TD original of) Eq. (3.50).

3.1.3 Numerical examples

To demonstrate the analytical results derived in the previous sections, we next report some numerical examples for both cases of parallel and orthogonal patches. The results obtained using the proposed approach are compared with those obtained through the NILT technique.

Parallel patches

To provide illustrative examples, the derived closed-form TD formula (3.7) has been implemented in Matlab®. For simplicity, the parallel rectangular surfaces under consideration are chosen to be unit squares of size $\Delta_x = \Delta_y = 1.0\,\text{mm}$. Their dimension is assumed to be relatively small with respect to $c_0\times$(incident wave pulse time width) or the wavelength at the frequency of analysis). With no loss of generality, the two patches are $\mathcal{A}_m = \{0 \leq |x - x_m| \leq \Delta_x/2, 0 \leq |y - y_m| \leq \Delta_y/2, z = 0\}$ and $\mathcal{A}_n = \{0 \leq |x - x_n| \leq \Delta_x/2, 0 \leq |y - y_n| \leq \Delta_y/2, z = z_n\}$ with $x_m = \Delta x/2$, $y_m = \Delta y/2$, $x_n = x_m + k\Delta x$, $y_n = y_m + k\Delta y$, $z_n = \Delta x$, and k being an integer $k \in [2-7]$. The geometrical configuration of the patches is sketched in Fig. 3.4. The results are shown in Fig. 3.5, where the proposed technique is validated through the comparison with NILT. The CdH formulation requires to carry out the convolution integral in (3.30) and, to this aim, the `quadgk` Matlab function is used. The agreement is very satisfactory. It is also worth to observe that the property of causality, ensuring the zero response before the arrival time, is accurately preserved in all cases. The arrival time can be estimated rigorously from the minimum distance between the two patches and the speed of the EM field in the background medium.

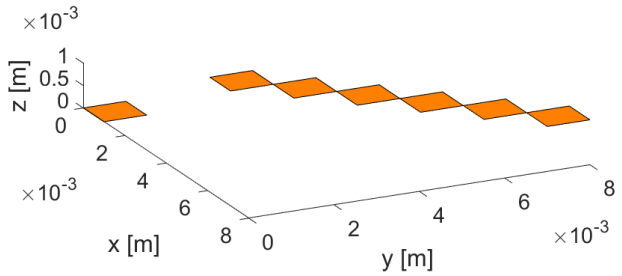

Figure 3.4: Geometrical configurations for parallel patches example: patch $\mathcal{A}_n$ in the **xy**-plane at increasing distances along the diagonal of the **xy**-plane.

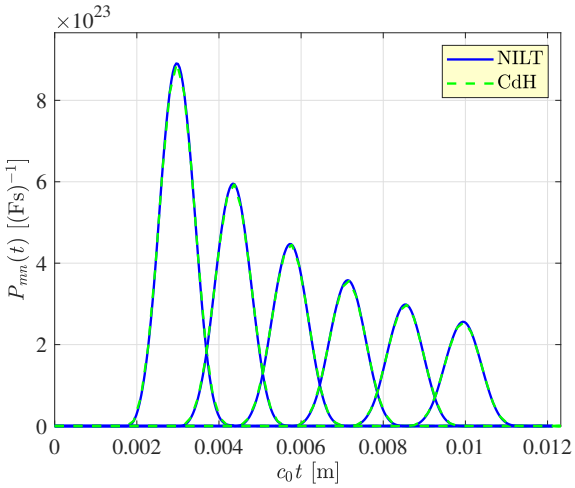

Figure 3.5: Time domain coefficients for the parallel patches example: patch $\mathcal{A}_n$ in the **xy**-plane at increasing distances along the diagonal of the **xy**-plane.

Orthogonal patches

For the case of orthogonal patches, two different geometries are considered in the following. Again, without loss of generality, the patches are characterized by a square geometry with sizes $\Delta x = \Delta y = 1.0$ mm.

Patch $\mathcal{A}_n$ in the xz-plane at increasing distances along the y-axis the two patches are $\mathcal{A}_m = \{0 \leq |x - x_m| \leq \Delta_x/2, 0 \leq |y - y_m| \leq \Delta_y/2, z = 0\}$ and $\mathcal{A}_n = \{0 \leq |x - x_n| \leq \Delta_x/2, y = y_n, 0 \leq |z - z_n| \leq \Delta_x/2\}$ where $x_m = \Delta x/2$, $y_m = \Delta y/2$, $x_n = x_m + \Delta x$, $y_n = y_m + k\Delta y$, $z_n = \Delta x/2$, k being an integer $k \in [3 - 8]$. The geometrical configuration of the patches is sketched in Fig. 3.6.

The TD coefficients have been computed with the CdH technique and compared with those obtained through the NILT method. The results are shown in Fig. 3.7, exhibiting a very good agreement. As before, the computation of the convolution integral (3.65) has been performed by using the `quadgk` Matlab function. The small oscillations in the NILT results are explained by the loss of accuracy over long times of the NILT method.

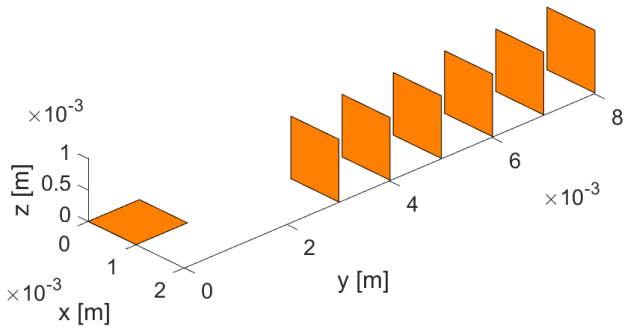

Figure 3.6: Geometrical configurations for orthogonal patches example: patch $\mathcal{A}_n$ in the **xz**-plane at increasing distances along the **y**-axis.

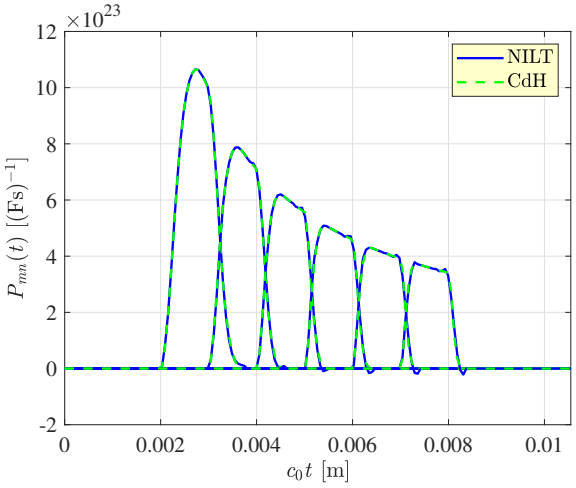

Figure 3.7: Time domain coefficients for the orthogonal patches example: patch $\mathcal{A}_n$ in the **xz**-plane at increasing distances along the **y**-axis.

Patch $\mathcal{A}_n$ in the xz-plane at increasing distances along the diagonal of xy-plane the two patches are $\mathcal{A}_m = \{0 \leq |x - x_m| \leq \Delta_x/2, 0 \leq |y - y_m| \leq \Delta_y/2, z = 0\}$ and $\mathcal{A}_n = \{0 \leq |x - x_n| \leq \Delta_x/2, y = y_n, 0 \leq |z - z_n| \leq \Delta_x/2\}$ where $x_m = \Delta x/2$, $y_m = \Delta y/2$, $x_n = x_m + k\Delta x$, $y_n = y_m + k\Delta y$, $z_n = \Delta x/2$, k being an integer $k \in [3 - 8]$. The geometrical configuration of the patches is sketched in Fig.

3.8.

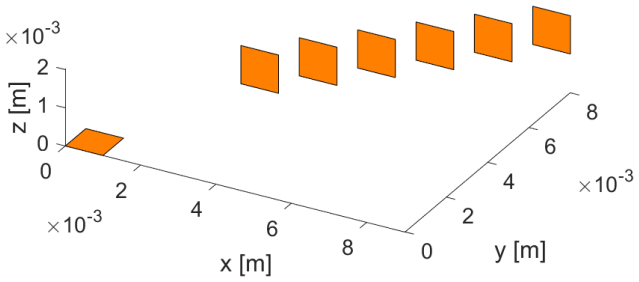

Figure 3.8: Geometrical configurations for orthogonal patches example: patch $\mathcal{A}_n$ in the **xz**-plane at increasing distances along the diagonal of the **xy**-plane.

The TD interaction integrals have been computed through the CdH technique and compared with those obtained through the NILT method. The results are shown in Fig. 3.9 exhibiting a very good agreement.

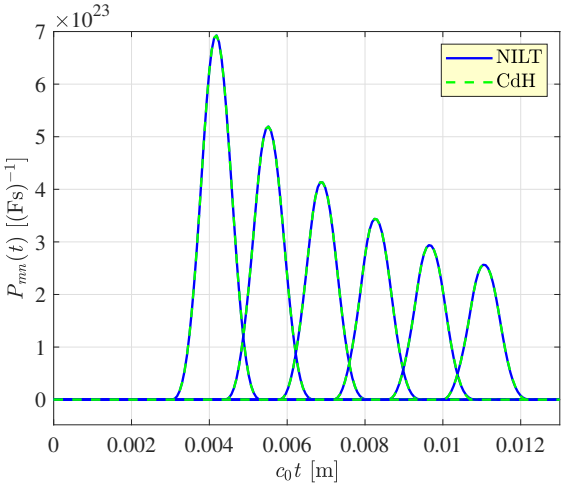

Figure 3.9: Time domain coefficients for the orthogonal patches example: patch $\mathcal{A}_n$ on the diagonal of the **xy**-plane at increasing distances.

Induced electric potential by a transient charge

Finally, as a last case of study, two orthogonal patches have been considered again. The electric potential induced on patch $\mathcal{A}_m$ by the transient charge on patch $\mathcal{A}_n$ is evaluated by convolution as:

$$v_m(t) = \int_0^t P_{mn}(t-\tau) q_n(\tau) d\tau \tag{3.71}$$

where $P_{mn}(t)$ is the transient mutual coefficient of potential and $q_n(t)$ is the charge on patch $\mathcal{A}_n$. The exciting transient charge $q_n(t)$ is taken as the time derivative of the unipolar, power-exponential (PE) pulse presented in [95, 96]:

$$\begin{aligned} q_n(t) =& Q_{peak} N(\nu) \left(1 - \frac{t}{t_{0x}}\right) \left(\frac{t}{t_{0x}}\right)^{\nu-1} \\ & \times exp\left[-\nu\left(\frac{t}{t_{0x}} - 1\right)\right] \mathrm{H}(t) \text{ for } \nu > 1 \end{aligned} \tag{3.72}$$

where Q_{peak} is the first peak magnitude in $q_n(t)$, t_{0x} is the pulse zero-crossing time (corresponding to the pulse rise time of the PE pulse), ν is the initial rise power of the PE pulse (which is related to the high-frequency asymptotic falloff in its Bode plot), and $N(\nu)$ is the normalization constant

$$N(\nu) = \nu^{\frac{1}{2}} \left(\frac{\nu^{\frac{1}{2}}}{\nu^{\frac{1}{2}} - 1}\right)^{\nu-1} exp\left(\nu^{\frac{1}{2}}\right). \tag{3.73}$$

The Laplace transform of (3.73) is:

$$Q(s) = Q_{peak} t_{0x} N(\nu) \frac{s t_{0x} \Gamma(\nu) exp(\nu)}{(s t_{0x} + \nu)^{\nu+1}} \text{ with } \mathrm{Re}(s) \ > -\nu/t_{0x} \tag{3.74}$$

where $\Gamma(\cdot)$ is the Euler gamma function. The induced electric potential has been computed by increasing the distance between the two patches, as sketched in Fig. 3.10.

The electric potential induced on patch $\mathcal{A}_m$ has been evaluated in three different ways:

- computing the convolution directly in the time domain, between the coefficient of potential $P_{mn}(t)$, evaluated by the CdH technique, and the charge $q_n(t)$ (3.72);

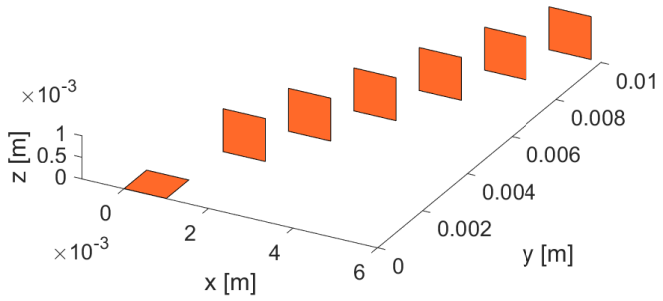

Figure 3.10: Geometrical configurations for the orthogonal patches: patch $\mathcal{A}_n$ in the **xz**-plane at increasing distances along the **xy**-plane.

- computing the convolution again in the time domain between the coefficient $P_{mn}(t)$ computed by the NILT method, and the charge $q_n(t)$ (3.72);
- computing first the convolution in the frequency domain, e.g. multiplying the fast Fourier transform of the coefficient of potential $P_{mn}(t)$, evaluated by the CdH technique, and the Fourier transform of $q_n(t)$, evaluated by using (3.74), with $s = j\omega$; then the inverse Fourier transform is adopted to recover the transient induced potential.

The results of the induced potential development are shown in Fig. 3.11 exhibiting a very good agreement among the three methods. It is also worth to observe that the property of causality, ensuring the zero response before the arrival time, is strictly preserved only using the CdH and NILT techniques.

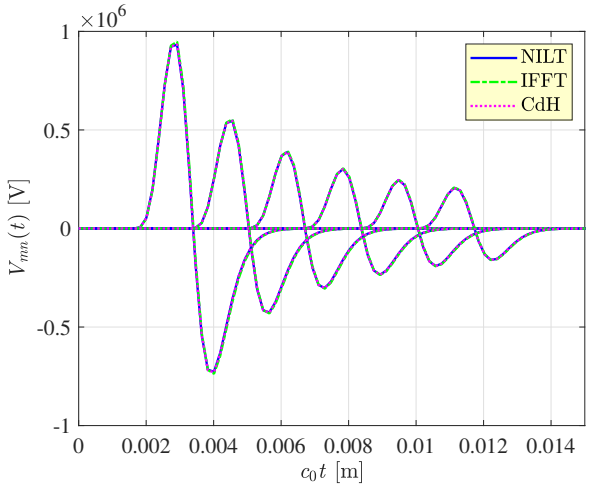

Figure 3.11: Time domain induced potential on patch $\mathcal{A}_m$ due to a charge located on patch $\mathcal{A}_n$ at increasing distances on the **xy**-plane.

3.2 Time-domain volume interactions of the inductive type

In this section we analyze the magnetic interaction between the two bricks $\mathcal{V}_m$, $\mathcal{V}_n$ depicted in Fig. 3.12. In particular, we consider study a retarded partial potential coefficient expressed through a double volume integral

$$\hat{L}_{mn}(s) = \frac{\mu_0}{\mathcal{S}_m \mathcal{S}_n} \int_{\boldsymbol{r}\in\mathcal{V}_m} dV \int_{\boldsymbol{r}'\in\mathcal{V}_n} \hat{g}(\boldsymbol{r}-\boldsymbol{r}', s) dV', \tag{3.75}$$

where $\mathcal{V}_m = \{-\Delta_x^m/2 < x - x_m < \Delta_x^m/2, -\Delta_y^m/2 < y - y_m < \Delta_y^m/2, -\Delta_z^m/2 < z - z_m < \Delta_z^m/2\}$ and $\mathcal{V}_n = \{-\Delta_x^n/2 < x - x_n < \Delta_x^n/2, -\Delta_y^n/2 < y - y_n < \Delta_y^n/2, -\Delta_z^n/2 < z - z_n < \Delta_z^n/2\}$, where $\Delta_x^{m,n} > 0$, $\Delta_y^{m,n} > 0$ and $\Delta_z^{m,n} > 0$ denote the spatial discretization steps in the x-, $y-$ and z-direction, respectively. Furthermore, s is the Laplace-transform parameter with $\Re(s) > 0$, and $\mathcal{S}_{m,n}$ are cross sections of the volumes $\mathcal{V}_{m,n}$, respectively, red that are perpendicular to the corresponding electric-current flows. Next,

$$\hat{g}(\boldsymbol{r}-\boldsymbol{r}', s) = \frac{e^{-s|\boldsymbol{r}-\boldsymbol{r}'|/c}}{4\pi|\boldsymbol{r}-\boldsymbol{r}'|} \tag{3.76}$$

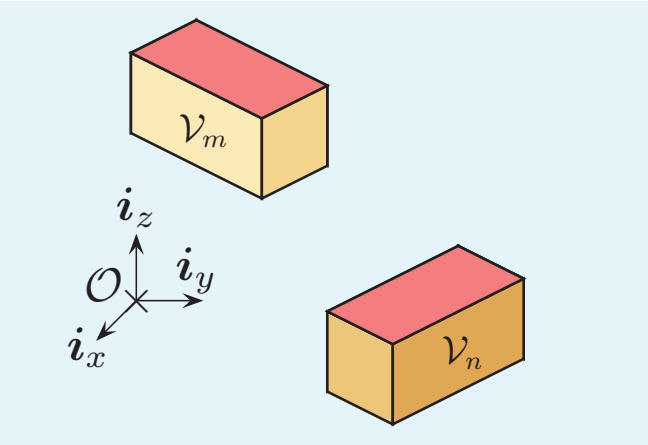

Figure 3.12: Two interacting brick elements.

is the free-space Green's function of the 3-D scalar modified Helmholtz equation and $c = (\varepsilon\mu)^{-1/2} > 0$ denotes the pertinent (real-valued and positive) EM wave speed.

3.2.1 Problem solution

The retarded partial inductance coefficient as expressed through Eq. (3.75) will be next transformed to the TD analytically with the aid of the CdH technique. Pursuing this approach and assuming that $|z_m - z_n| > (\Delta_z^m + \Delta_z^n)/2$, one may express the TD original of Eq. (3.75), further denoted by $L_{mn}(t)$ red(in henry/second = ohm), as follows:

$$\begin{aligned} L_{mn}(t) &= (\mu_0/\mathcal{S}_m\mathcal{S}_n)[J(|z_m - z_n| + \Delta_z^{mn+}, t) \\ &- J(|z_m - z_n| + \Delta_z^{mn-}, t) - J(|z_m - z_n| - \Delta_z^{mn-}, t) \\ &+ J(|z_m - z_n| - \Delta_z^{mn+}, t)], \end{aligned} \tag{3.77}$$

where

$$\begin{aligned} J(z,t) &= I(x_m - x_n + \Delta_x^{mn+}, z, t) \\ &- I(x_m - x_n + \Delta_x^{mn-}, z, t) - I(x_m - x_n - \Delta_x^{mn-}, z, t) \\ &+ I(x_m - x_n - \Delta_x^{mn+}, z, t), \end{aligned} \tag{3.78}$$

and

$$\begin{aligned} I(x,z,t) = & K(x, y_m - y_n + \Delta_y^{mn+}, z, t) \\ & - K(x, y_m - y_n + \Delta_y^{mn-}, z, t) \\ & - K(x, y_m - y_n - \Delta_y^{mn-}, z, t) \\ & + K(x, y_m - y_n - \Delta_y^{mn+}, z, t), \end{aligned} \tag{3.79}$$

where we used

$$\Delta_{x,y,z}^{mn\pm} = (\Delta_{x,y,z}^{m} \pm \Delta_{x,y,z}^{n})/2, \tag{3.80}$$

respectively. Here, $K(x, y, z, t)$ represents the TD original of the generic slowness integral, the definition and inversion of which is presented in the following paragraph. Finally, we emphasize that Eq. (3.77) applies to the configuration where $|z_m - z_n| > \Delta_z^{mn+}$. The case $|z_m - z_n| < \Delta_z^{mn+}$ must be analyzed separately.

3.2.2 The Generic Integral

The integral representation to be transformed to TD has the following form

$$\begin{aligned} \hat{K}(x,y,z,s) = & \left(\frac{s}{2\text{ß}\pi}\right)^2 \int_{\kappa\in\mathbb{K}_0} \frac{\exp(s\kappa x)}{s^2\kappa^2} d\kappa \\ & \times \int_{\sigma\in\mathbb{S}_0} \frac{\exp\{-s[-\sigma y + \Gamma(\kappa,\sigma)z]\}}{s^2\sigma^2} \frac{d\sigma}{2s^3\Gamma^3(\kappa,\sigma)} \end{aligned} \tag{3.81}$$

for $x \in \mathbb{R}$, $y \in \mathbb{R}$, $\{z \in \mathbb{R}; z \geq 0\}$ and $\{s \in \mathbb{R}; s > 0\}$, where $\mathbb{K}_0$ and $\mathbb{S}_0$ are the integration paths extending along $\Re(\kappa) = 0$ and $\Re(\sigma) = 0$, respectively, that are indented to the right with semi-circular arcs with centers at the origins and vanishingly small radii (see Fig. 3.13). Finally, $\Gamma(\kappa, \sigma)$, being the slowness parameter along the z-direction, is defined as

$$\Gamma(\kappa,\sigma) = (1/c^2 - \kappa^2 - \sigma^2)^{1/2} \text{ with } \Re(\Gamma) \geq 0. \tag{3.82}$$

The generic integral will next be transformed to the TD with the aid of the CdH technique. To that end, the integration contour in the complex σ-plane, $\mathbb{S}_0$, is

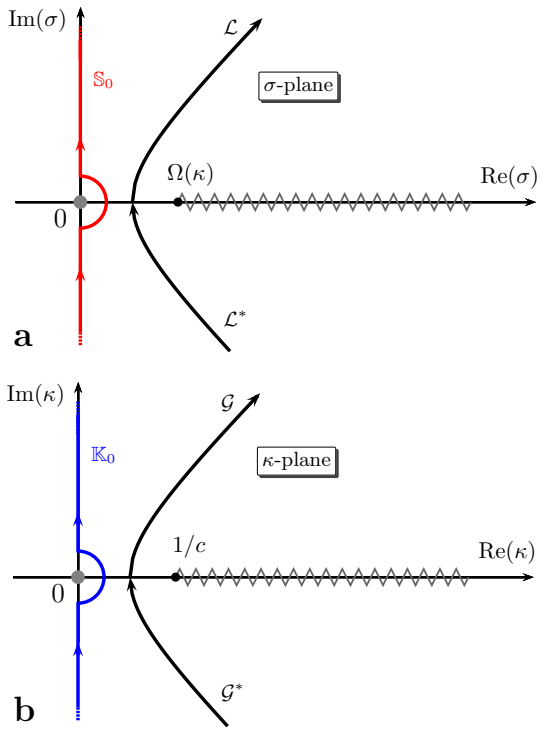

Figure 3.13: Complex slowness planes. (a) σ-plane with the CdH-path for $y < 0$; (b) κ-plane with the CdH-paths for $x < 0$.

by virtue of Jordan's lemma and Cauchy's theorem deformed into a CdH path, say $\mathcal{L} \cup \mathcal{L}^*$ (here * denotes the complex conjugate), along which $-\sigma y + \Gamma(\kappa, \sigma) z = u d\Omega(\kappa)$ for $\{1 \leq u < \infty\}$ with $d^2 = y^2 + z^2$ and $\Omega(\kappa) = (1/c^2 - \kappa^2)^{1/2}$ is satisfied (see Fig. 3.13a). Upon combining the contributions from $\mathcal{L}$ and $\mathcal{L}^*$, the inner integral with respect to σ can be cast into the integral with respect to the (real-valued and positive) parameters u. In addition, the contribution from the (double) pole singularity at $\sigma = 0$ must be for $y > 0$ accounted for. The thus expressed inner integral is subsequently substituted back in Eq. (3.81), which yields

$$\hat{K}(x, y, z, s) = \hat{M}(x, y, z, s) + \hat{N}(x, y, z, s), \tag{3.83}$$

where

$$\hat{M} = \frac{1}{2\pi ß}\frac{d^4}{2\pi s^3}\int_{u=1}^{\infty}\frac{y^2z^2 - u^2(u^2-1)(y^4-6y^2z^2+z^4)}{(u^2d^2-y^2)^2(u^2d^2-z^2)^2}$$
$$\times \frac{du}{(u^2-1)^{1/2}}\int_{\kappa\in\mathbb{K}_0}\exp\{-s[-\kappa x+\Omega(\kappa)ud]\}\frac{d\kappa}{s^2\kappa^2\Omega^4(\kappa)} \tag{3.84}$$

and

$$\hat{N} = \frac{1}{2\pi ß}\frac{y\mathrm{H}(y)}{2s^2}\int_{\kappa\in\mathbb{K}_0}\exp\{-s[-\kappa x+\Omega(\kappa)z]\}\frac{d\kappa}{s^2\kappa^2\Omega^3(\kappa)}, \tag{3.85}$$

where $\mathrm{H}(y)$ has again the meaning of the Heaviside unit-step function, i.e. $\mathrm{H}(y) = 0$ if $y < 0$, $\mathrm{H}(0) = 1/2$, $\mathrm{H}(y) = 1$ if $y > 0$.

In the first, we shall describe the transformation of $\hat{M}$ as given by Eq. (3.84). For this purpose, the integration contour in the complex κ-plane, $\mathbb{K}_0$, is deformed into a CdH path, say $\mathcal{G}\cup\mathcal{G}^*$, along which $-\kappa x+\Omega(\kappa)ud = \tau$ for $\{R(u)/c \le \tau < \infty\}$ with $R(u) = (x^2+u^2d^2)^{1/2} > 0$ is satisfied (see Fig. 3.13b). In the resulting expression, we combine the contributions from $\mathcal{G}$ and $\mathcal{G}^*$ and change the order of the integrations according to, symbolically

$$\int_{u=1}^{\infty}du\int_{\tau=R(u)/c}^{\infty}d\tau \to \int_{\tau=R(1)/c}^{\infty}d\tau\int_{u=1}^{U(c\tau)}du \tag{3.86}$$

where $U(c\tau) = (c^2\tau^2/d^2 - x^2/d^2)^{1/2}$. Upon carrying out the integration with respect to u, Eq. (3.84) can be cast into the following form

$$\hat{M} = \frac{c^6}{2\pi^2 s^5}\int_{\tau=R(1)/c}^{\infty}\exp(-s\tau)\mathcal{V}(x,y,z,c\tau)d\tau$$
$$+\hat{P}(x,y,z,s) \tag{3.87}$$

where $\hat{P}$ arises from the (double) pole singularity at $\kappa = 0$. Both terms on the right-hand side of Eq. (3.87) have the form that allows their straightforward transform to the original domain.

The transformation of $\hat{N}$ (see Eq. (3.85)) follows similar lines of reasoning. Indeed, the original integration contour, $\mathbb{K}_0$, is first replaced with a new CdH path along which $-\kappa x+\Omega(\kappa)z = \tau$ is met for all $\{\rho/c \le \tau < \infty\}$, where $\rho^2 = x^2+z^2$. Combining again the contributions from the hyperbolic arcs in the lower and upper

halves of the complex κ-plane, we end up with an integral with respect to τ that can be expressed as $\hat{P}(y,x,z,s)$ (cf. Eq. (3.87)). Representing further the contribution from the (double) pole singularity at $\kappa = 0$ by $\hat{Q}(x,y,z,s)$, we arrive at

$$\hat{N} = \hat{P}(y,x,z,s) + \hat{Q}(x,y,z,s). \tag{3.88}$$

Upon substituting Eqs. (3.87) with (3.88) in (3.83) and transform the result to the TD, we finally get

$$\begin{aligned} K(x,y,z,t) = {} & \frac{c}{48\pi^2}\int_{v=R}^{ct}(ct-v)^4\mathcal{V}(x,y,z,v)dv \\ & + P(x,y,z,t) + P(y,x,z,t) + Q(x,y,z,t). \end{aligned} \tag{3.89}$$

The function behind the integral sign is given by

$$\begin{aligned} \mathcal{V}(x,y,z,v) = {} & \int_{\psi=0}^{\pi/2} f(x,y,z,v,\psi) \\ & \times \frac{p^2 - q^2(U^2-1)\sin^2(\psi)[\cos^2(\psi) + U^2\sin^2(\psi)]}{\{(z^2/d^2)\cos^2(\psi) + [(v^2-r^2)/d^2]\sin^2(\psi)\}^2} \\ & \times \frac{d\psi}{\{(y^2/d^2)\cos^2(\psi) + [(v^2-\rho^2)/d^2]\sin^2(\psi)\}^2}, \end{aligned} \tag{3.90}$$

with $r^2 = x^2 + y^2$, $p^2 = y^2z^2/d^4$, $q^2 = y^4/d^4 - 6p^2 + z^4/d^4$, $U^2 = v^2/d^2 - x^2/d^2$ and

$$\begin{aligned} f = {} & \frac{v/d^2}{U^3\left[(x^2/d^2)\sin^2(\psi) + (v^2/d^2-1)\cos^2(\psi)\right]^2} \\ & \times \Bigg\{ \left(3\frac{x^2}{d^2} + \frac{v^2}{d^2}\right)[\cos^2(\psi) + U^2\sin^2(\psi)]^3 \\ & + \left(4\frac{x^4}{d^4} - \frac{11x^2v^2}{d^4} - \frac{v^4}{d^4}\right)[\cos^2(\psi) + U^2\sin^2(\psi)]^2 \\ & - \left(\frac{x^6}{d^6} + \frac{5x^4v^2}{d^6} - 10\frac{x^2v^4}{d^6}\right)[\cos^2(\psi) + U^2\sin^2(\psi)] \\ & - 2\frac{x^8}{d^8} + 7\frac{x^6v^2}{d^8} - 5\frac{x^4v^4}{d^8}\Bigg\}. \end{aligned} \tag{3.91}$$

The remaining terms in the final TD result (3.89) can be expressed as follows

$$
\begin{aligned}
P(x,y,z,t) = \frac{cxd^3\,\mathrm{H}(x)}{12\pi}\Bigg\{ & \frac{6|y|zct}{d^3} \\
& \times \Bigg\{ \tan^{-1}\left[\frac{|y|(c^2t^2-d^2)^{1/2}}{zct}\right] \\
& + \tan^{-1}\left[\frac{z(c^2t^2-d^2)^{1/2}}{|y|ct}\right] \Bigg\} \\
& - 3\frac{z}{d}\frac{c^2t^2+y^2}{d^2}\tan^{-1}\left[\frac{(c^2t^2-d^2)^{1/2}}{z}\right] \\
& - 3\frac{|y|}{d}\frac{c^2t^2+z^2}{d^2}\tan^{-1}\left[\frac{(c^2t^2-d^2)^{1/2}}{|y|}\right] \\
& + \left(2\frac{c^2t^2}{d^2}+1\right)\left(\frac{c^2t^2}{d^2}-1\right)^{1/2}\Bigg\},
\end{aligned}
\tag{3.92}
$$

and, finally,

$$
Q(x,y,z,t) = \frac{cxy\mathrm{H}(x)\mathrm{H}(y)}{4}(ct-z)^2\mathrm{H}(ct-z). \tag{3.93}
$$

3.2.3 Numerical Examples

In this section, numerical examples related to three different geometries are presented. For validation purposes, the results obtained through the proposed method are compared with those obtained through the NILT approach.

Two interacting cubes

As a particular application, the resulting TD expression (3.77) has been implemented in MATLAB® and applied to the case of two interacting cubes (see Fig. 3.14). The evaluations are performed in the finite time window $\{0 \leq ct/R_{mn} \leq 2\}$, where $R_{mn} = [(x_m - x_n)^2 + (y_m - y_n)^2 + (z_m - z_n)^2]^{1/2}$ represents the centre-to-centre distance between two identical cubes located at

- $(x_m, y_m, z_m) = (0, 0, 0)$,
- $(x_n, y_n, z_n) = (2\Delta_x, 2\Delta_x, 2\Delta_x)$.

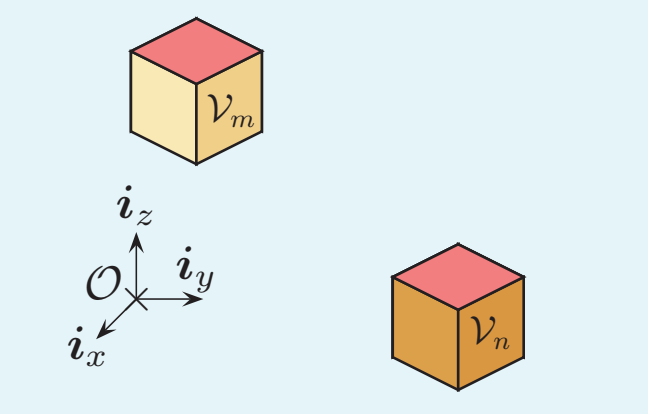

Figure 3.14: Two interacting cube elements.

In the present example we take $\Delta_x = \Delta_x^{m,n} = \Delta_y^{m,n} = \Delta_z^{m,n} = 1.0\,\text{mm}$. The resulting pulse shape of the TD coefficient is shown in Fig. 3.15. Here, for the sake of validation, the results obtained through the proposed CdH-based and the (referential) NILT technique are presented. Finally, the FD counterpart of the two TD responses is sketched in Fig. 3.16.

As can be seen, the computed results show good correspondence with dissimilarities occurring from 400 GHz up. These discrepancies are, however, virtually negligible in technical applications.

Interactions of a system of cubes

As a further example we consider the geometry depicted in Fig. 3.17, where the mutual partial inductance between the cube with the center located at the axes origin and the others are considered. All the cubes have sides $\Delta_x = \Delta_y = \Delta_z = 1.0$ mm. The cubes system is composed by 27 elements, three for each dimension. The center coordinates span a range $[2\Delta_x - 8\Delta_x]$. In Fig. 3.18 are sketched all the TD coefficients related to the system, each one computed through the proposed technique and compared to NILT results.

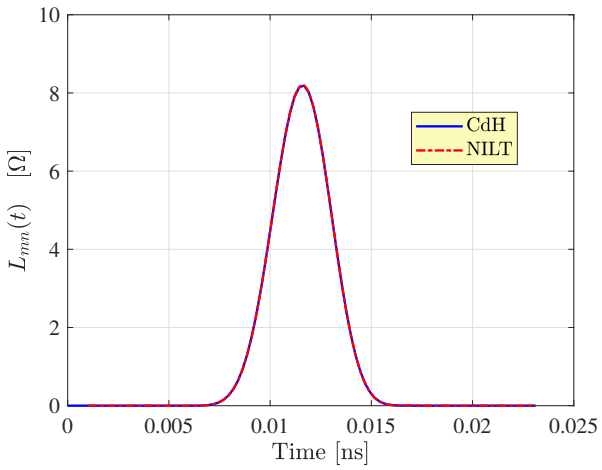

Figure 3.15: The TD coefficient for the two identical cubes: comparison between the proposed technique and the NILT technique.

Induced voltage on a cube by the currents flowing in four bricks

In Fig. 3.19 are shown four identical parallelepipeds: $1, 2, 3, 4$, with sides: $\Delta_x = 1.5$ mm, $\Delta_y = 0.5$ mm, $\Delta_z = 0.25$ mm, above a cube 0, with sides: $\Delta_x^0 = \Delta_y^0 = \Delta_z^0 = 1.0$ mm, and center located at the axes origin. The parallelepipeds are considered at the same height and are collocated unsymmetrically in the $x-y$ plane, with respect to the cube. In particular, the coordinates of the parallelepipeds are:

- $(x_1, y_1, z_1) = (-2.5 \text{ mm}, 0.5 \text{ mm}, 3\Delta_x^0)$,
- $(x_2, y_2, z_2) = (-2.5 \text{ mm}, 5 \text{ mm}, 3\Delta_x^0)$,
- $(x_3, y_3, z_3) = (11 \text{ mm}, 0.5 \text{ mm}, 3\Delta_x^0)$,
- $(x_4, y_4, z_4) = (11 \text{ mm}, 5 \text{ mm}, 3\Delta_x^0)$.

The overall induced voltage on the cube 0 by the system of parallelepipeds can be computed through a combination of four convolution integrals as:

$$v_{L_0}(t) = \sum_{n=1}^{4} \int_0^t L_{p_{0,n}}(t-\tau) \frac{di_n(\tau)}{d\tau} d\tau \tag{3.94}$$

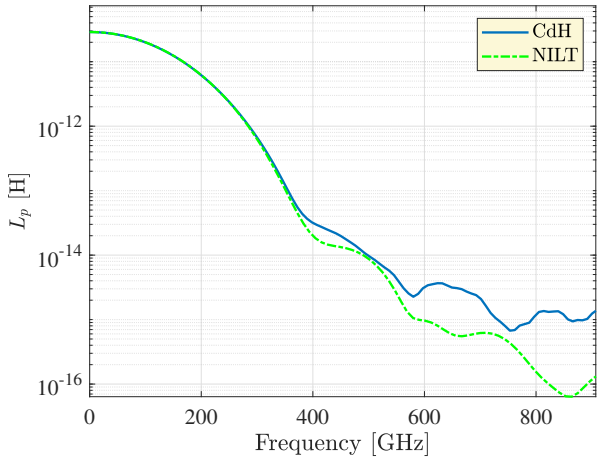

Figure 3.16: Spectrum comparison for the interaction between two identical cubes.

where $i_n(t)$ is the impressed current on each parallelepiped, $n = 1,\cdots,4$, flowing in the x direction. The impressed current $i_n(t)$, for each parallelepiped, is assumed to exhibit a windowed-power (WP) waveform [97]:

$$i_n(\tau, t) = t'^{\tau}(2 - t')^{\tau}\mathrm{H}(t')\mathrm{H}(2 - t') \tag{3.95}$$

where $\mathrm{H}(t)$ is the Heaviside unit-step function ($\mathrm{H}(t) = 0$ if $t < 0$, $\mathrm{H}(0) = 1/2$, $\mathrm{H}(t) = 1$ if $t > 0$), $t' = t/t_\mathrm{r}$, t_r being the pulse rise time. We choose $\tau = 2$ and $t_\mathrm{r} = 4.6$ ps. The induced voltage on the cube 0 is depicted in Fig. **??**, where it is observed an excellent agreement between the CdH method and the NILT-based method.

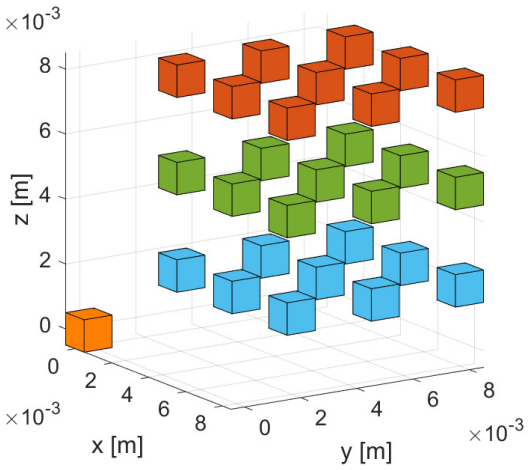

Figure 3.17: Cubes system geometry.

3.3 The computation of the TD partial inductances employing NILT-based techniques

An alternative way to perform the computation of partial elements in the TD is represented by the application of NILT to the Laplace domain integrals (3.1), (3.75). This kind of approach is based on the numerical integration of such integrals that has to be performed, for each sample t, over the points of the complex plane defined by the Padé poles. Hence, again, the computational cost is strictly related to the total number of computation points dictated by $M/2 \cdot N_t$, being M the chosen NILT order expansion and N_t the total number of the points of the time grid. On the other hand, NILT offers the advantage of the arbitrary choice of the number of the samples without loosing accuracy. Moreover, since each interaction is strictly time-limited and well-localized in the time window, the samples placement can be appropriately optimized.

In this section, the application of NILT and NILTn to inductive partial elements is discussed (the application to potential interactions is straightforward). Moreover, the Hermite interpolation technique is employed to minimize the effective computation points obtaining dense waveforms.

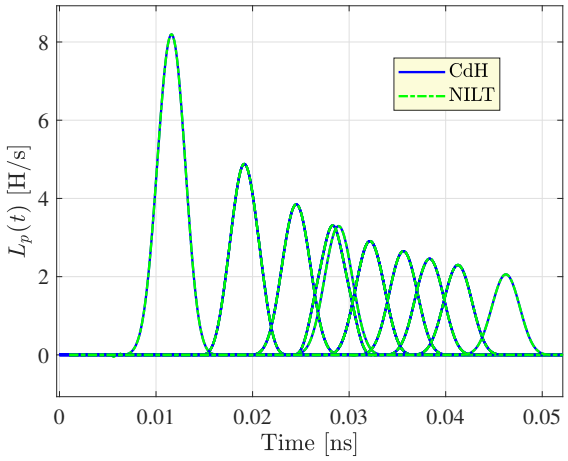

Figure 3.18: TD coefficients for the cubes system geometry.

3.3.1 The delay extraction procedure

The inaccuracies of NILT over large time intervals can be reduced by introducing a delayed version of the NILT method. We assume to know the spatial support of 2 basis functions m and n. Hence, the minimum distance R_m between the 2 spatial supports is available and the minimum propagation delay is easily computed since the propagation takes place in the background medium and the speed of propagation is rigorously known.

Writing the domains distance as $|\boldsymbol{r}-\boldsymbol{r}'| = R$ and defined the minimum distance between the two volumes R_m, we can reformulate the free-space Green's function extracting the minimum delay R_m/c_0:

$$\hat{g}(\boldsymbol{r}-\boldsymbol{r}', s) = e^{-s\frac{R_m}{c_0}} \frac{e^{-s\left(\frac{R-R_m}{c_0}\right)}}{R}. \tag{3.96}$$

which, substitued in (3.75), gives:

$$L_{mn}(t) = \frac{1}{j2\pi} \int_{\alpha-j\infty}^{\alpha+j\infty} \left(\frac{\mu_0}{4\pi} \frac{1}{\mathcal{S}_m \mathcal{S}_n} \int_{\boldsymbol{r}\in\mathcal{V}_m} \int_{\boldsymbol{r}'\in\mathcal{V}_n} \frac{e^{-s\left(\frac{R-R_m}{c_0}\right)}}{R} dV dV' \right) e^{s\left(t-\frac{R_m}{c_0}\right)} ds. \tag{3.97}$$

Thus, an auxiliary delayed time variable t' can be defined as

$$t' = t - \frac{R_m}{c_0}. \tag{3.98}$$

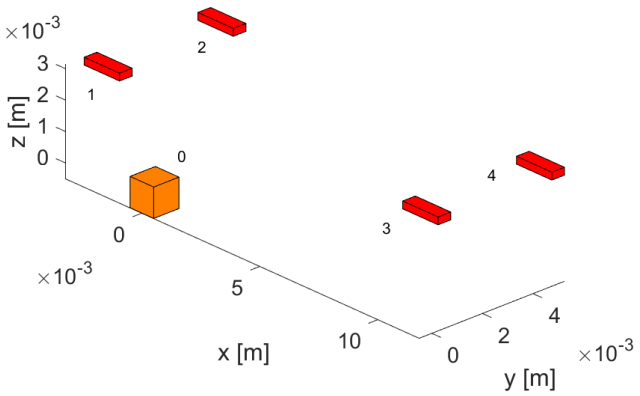

Figure 3.19: Geometry for the computation of the induced voltage on a cube by the currents flowing in the bricks system.

If the standard NILT approach is used, the NILT TD partial inductance can be then reformulated as:

$$L_{mn}(t) \approx -\frac{1}{t'}\sum_{i=1}^{W} \Re e\left\{ K_i' \frac{\mu_0}{4\pi}\frac{1}{\mathcal{S}_m\mathcal{S}_n}\int_{\boldsymbol{r}\in\mathcal{V}_m}\int_{\boldsymbol{r}'\in\mathcal{V}_n} \frac{e^{-\frac{z_i}{t'}\left(\frac{R-R_m}{c_0}\right)}}{R} dV dV' \right\} \tag{3.99}$$

The effective time of inverse transform is t' that is lower or equal than the evaluation time t. Thus, the error of the NILT approach on late times is automatically reduced. The delayed implementation of the NILT method will be referred to as dNILT in the following text. It is clear from (3.99) that the delayed version of the partial inductance in the Laplace domain is needed for the dNILT. The latter can be expressed as:

$$L_{mn}^{del}(s) = \frac{\mu_0}{4\pi}\frac{1}{\mathcal{S}_m\mathcal{S}_n}\int_{\boldsymbol{r}\in\mathcal{V}_m}\int_{\boldsymbol{r}'\in\mathcal{V}_n} \frac{e^{-s\tau'}}{R} dV dV' \tag{3.100}$$

where $\tau' = (R - R_m)/c_0$. Indeed, it is possible to notice that (3.99) is just $L_{p_{m,n}}^{del}$ in (3.100), evaluated for each time sample t over the Padé poles z_i. This procedure can be accomplished by Gaussian numerical integration schemes.

In the previous chapter it has been shown that higher degrees of accuracy with a lower order M can be reached through the adoption of the modified NILTn, being $n = 2$ an effective choice.

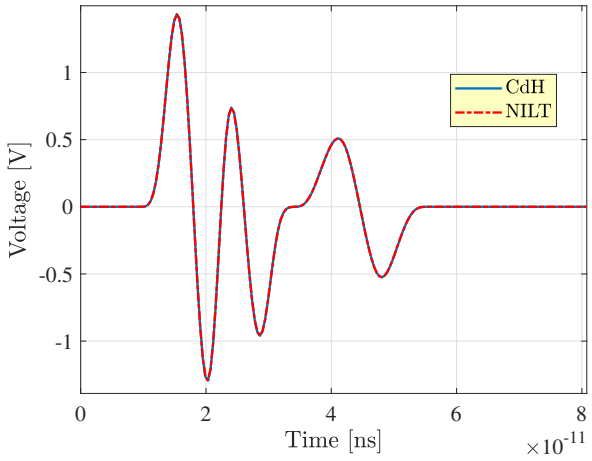

Figure 3.20: Induced voltage on the cube by the currents flowing in the system of bricks.

Further advantages can be reached combining the NILT2 and the delayed method, as long as the first 2 s-derivatives of the delayed partial inductance are known:

$$\frac{dL_{mn}^{del}}{ds} = -\frac{\mu_0}{4\pi}\frac{1}{\mathcal{S}_m\mathcal{S}_n}\int_{\boldsymbol{r}\in V_m}\int_{\boldsymbol{r}'\in V_n}\frac{\tau' e^{-s\tau'}}{R}dVdV' \tag{3.101a}$$

$$\frac{d^2L_{mn}^{del}}{ds^2} = \frac{\mu_0}{4\pi}\frac{1}{\mathcal{S}_m\mathcal{S}_n}\int_{\boldsymbol{r}\in V_m}\int_{\boldsymbol{r}'\in V_n}\frac{(\tau')^2 e^{-s\tau'}}{R}dVdV'. \tag{3.101b}$$

The combined use of dNILT and NILT2 will be referred as dNILT2 in the following sections. The mixed dNILT2 method requires the numerical computation of (3.101a) and (3.101b), in addition to (3.100), for each time sample t, over the Padé poles z_i. Using the dNILT2 approach, the computation of 3 numerical integrals instead of the only one as in dNILT0 adds computational costs to the overall procedure but the resulting interpolation greatly reduces the number of time samples and leads to a significant speed-up. Furthermore, the use of dNILT2 with a lower order M requires the numerical integrations to be performed over a smaller number of Padé poles if compared to dNILT0. This also allows to speed-up the computation.

It is clear that if a dense TD waveform is needed, then the computational complexity may overcome that of the classic inverse fast Fourier transform (IFFT). The Hermite interpolation is a useful tool to generate dense waveforms starting from a

relatively low number of samples. In order to compute the interpolant, the values of the function evaluated over a starting set of time samples and its high order derivatives at the same points (typically, up to the 5-th order is good enough) are required. This approach is particularly useful when applied to TD partial inductances. Indeed, each function $L_{mn}(t)$ is strictly time limited and the time window is known a-priori, depending on the geometry of the 2 volumes interacting. The time window is defined in the interval $[t_{min} = R_m/c_0, t_{max} = R_M/c_0]$, where R_m and R_M are, respectively, the minimum and the maximum distance between the 2 spatial supports, e.g. elementary volumes or surfaces. Hence, a few number of initial points can be strategically selected in the defined interval.

The Hermite interpolant polynomial $\Gamma(t)$ can be expressed by:

$$\Gamma(t) = \sum_{\alpha=1}^{H} \sum_{\beta=0}^{m_\alpha - 1} \frac{\theta^\beta(t_\alpha)}{\beta!} \prod_{\substack{\gamma=1 \\ \gamma \neq \alpha}}^{H} \left(\frac{t - t_\gamma}{t_\alpha - t_\gamma} \right)^{m_\gamma} \sum_{k=\beta}^{m_\alpha - 1} (t - t_\alpha)^k z_{k-\beta} \left(\sum_{\gamma \neq \alpha} \frac{m_\gamma}{(t_\gamma - t_\alpha)^r}, r \in [k - \beta] \right) \tag{3.102}$$

where:

- t_α are the initial time samples;
- H is the number of initial time samples;
- $(m_\alpha - 1)$ is the maximum order of differentiation employed for the sample evaluated in t_α;
- $z_n(x_i | i \in [n])$ are the cycle index polynomials [**?**], using the notation $z_n(x_i | i \in [n])$ to represent the multinomial $z_n(x_1, x_2, \ldots, x_n)$.

Certainly, if the function presents points where its derivatives are less regular, more initial samples have to be placed around them.

3.3.2 Numerical results

This section is dedicated to the presentation of some numerical examples. In the first example the TD partial inductance of 2 2-D patches is obtained through the

dNILT2 method and compared to the dNILT0 and analytical results. In the second example, the partial inductance of 2 volumes at increasing distances is computed by dNILT2 with and without interpolation. In the third example, the induced voltage on a (victim) cube due to 4 (source) volumes, where the current flows is obtained through the techniques here introduced. The fourth example deals with the FD computation of the total inductance of a thin loop.

In each example, also the NILT based Hermite interpolation results are shown, in order to emphasize the strength of the dNILT2 method when powered by an efficient interpolation scheme.

Two coplanar patches

The geometry under consideration is shown in Fig. 3.21. The 2 patches can be

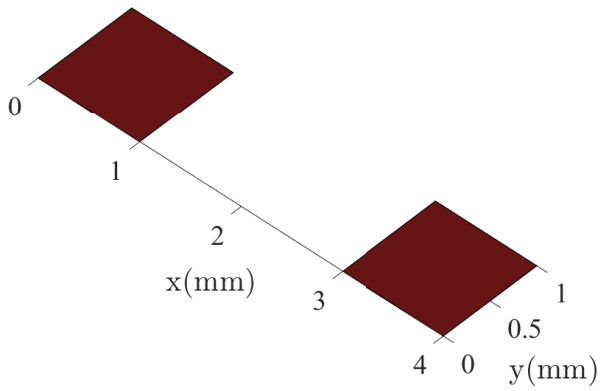

Figure 3.21: Geometrical configuration of 2 patches.

considered, in the limit, as 2 very thin volumes. Analytical results are available for coplanar patches that are based on the CdH technique yet discussed. The dNILT0 results are computed upon implementing (3.99), while the dNILT2 results are obtained by applying (2.25) to the expression (3.97) for the delayed partial inductance. The TD responses are sketched in Fig. 3.22, all showing a very good agreement. Due to the lower error of NILT2 compared to NILT0, for the same order M, dNILT0 and dNILT2 schemes are applied using $M = 12$ and $M = 4$, respectively. The rising

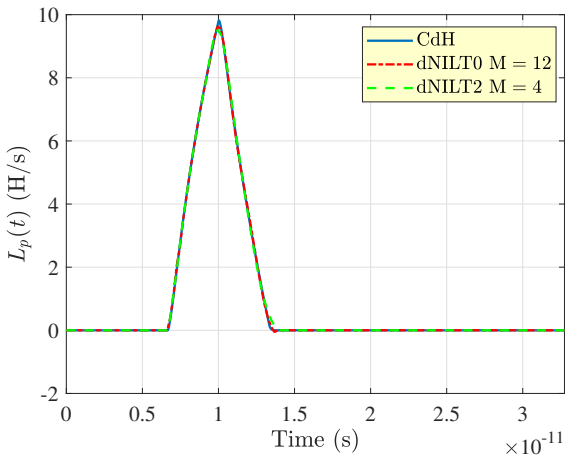

Figure 3.22: TD mutual partial inductance between 2 patches: NILT and analytical results.

edge is the most critical to reproduce. Indeed, all the NILT results are necessarily computed by numerical integration, performed over the surfaces covered by the 2 patches. At the initial points, the delayed parameter t' is very small, making the exponential in the integrals very oscillating. Hence, if the integration order is not large enough, it is likely to obtain inaccuracies at the first time samples. For the same reason, the higher the order M is, the higher the integration order required to perform the integration. Indeed, if M increases, also the number of Padé poles does, and they move in the upper part of the complex plane, as sketched in Fig. 3.23 where only the poles with positive imaginary part are shown.

Hence, choosing a higher M increases the imaginary part of the poles and makes the exponential term inside the integral more oscillating. Thus, the better error of the dNILT2 approach compared to dNILT0, allows to limit the order M making the first one less prone to numerical integration issue.

Still, the computational cost can be high if a fine set of time samples is chosen and, thus, interpolation is highly recommended. A set of 10 samples have been selected in the time window where the interaction takes place and the first 5 TD derivatives of the function are computed at the same points and used to interpolate. Then, the Hermite interpolants are built over 442 samples. The results obtained

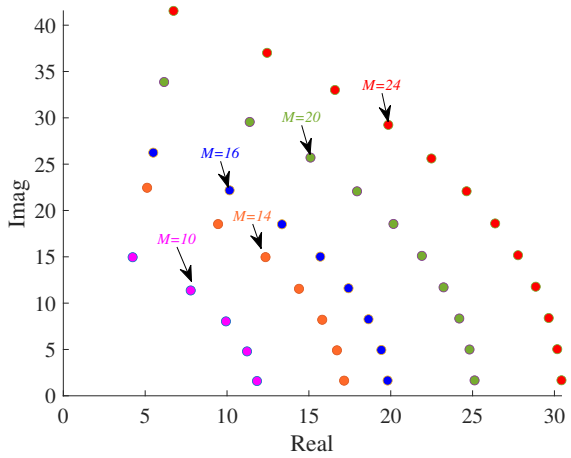

Figure 3.23: Significant poles of the Padé expansion for increasing order M.

using dNILT0 and dNILT2 are reported in Figs. 3.24 and 3.25. The red crosses

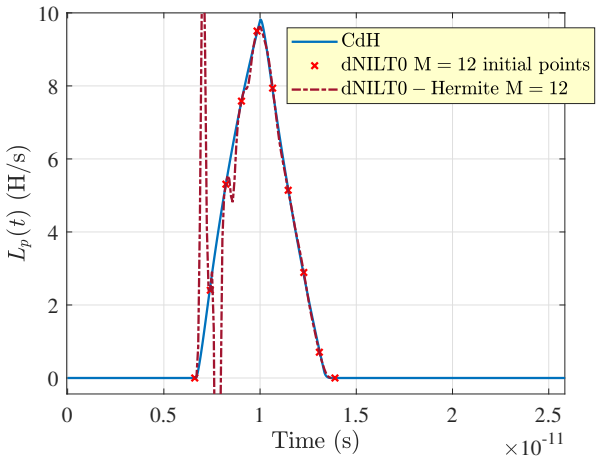

Figure 3.24: TD mutual partial inductance between 2 patches: CdH and dNILT0-Hermite interpolation based results.

indicate the starting dNILT0 and dNILT2 points computed with $M = 12$ and $M = 4$, respectively.

From Fig. 3.24, it is clearly seen that the interpolation based on the dNILT0 approach is inadequate, while the dNILT2 results shown in Fig. 3.25 are in a very good agreement with the analytical solution. Evidently, for a fixed order of integration,

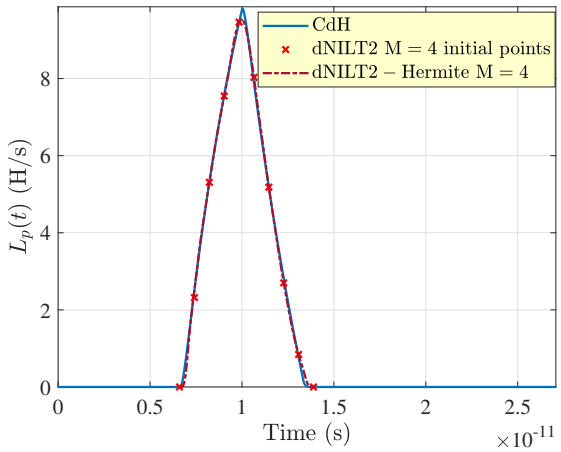

Figure 3.25: TD mutual partial inductance between 2 patches: CdH and dNILT2-Hermite interpolation based results.

the TD derivatives computed with dNILT2 are more accurate than those computed with dNILT0, making dNILT2 more suitable for the interpolation.

Coplanar cubes

The second example concerns the TD partial inductance between 2 cubes, in 3 different relative positions, as shown in Fig. 3.26.

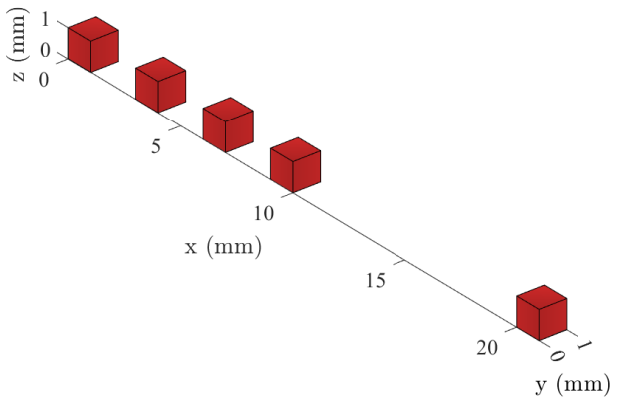

Figure 3.26: Cubes geometrical configurations.

The second cube is shifted along the x axis at increasing distances $3\Delta x, 6\Delta x, 9\Delta x, 20\Delta x$. For 3D geometries, no analytical results exist so far, but the NILT techniques provide reasonable results also in this case. For each case, the dNILT2-Hermite results are obtained starting from the knowledge of $L_{p_{m,n}}(t)$ and its first 5 derivatives on 10 points and building the interpolants over 442 samples. The initial points are chosen equidistant inside the time window of interaction that is known *a priori*. The waveforms obtained for the 4 configurations are sketched in Figs. 3.27, 3.28. It is

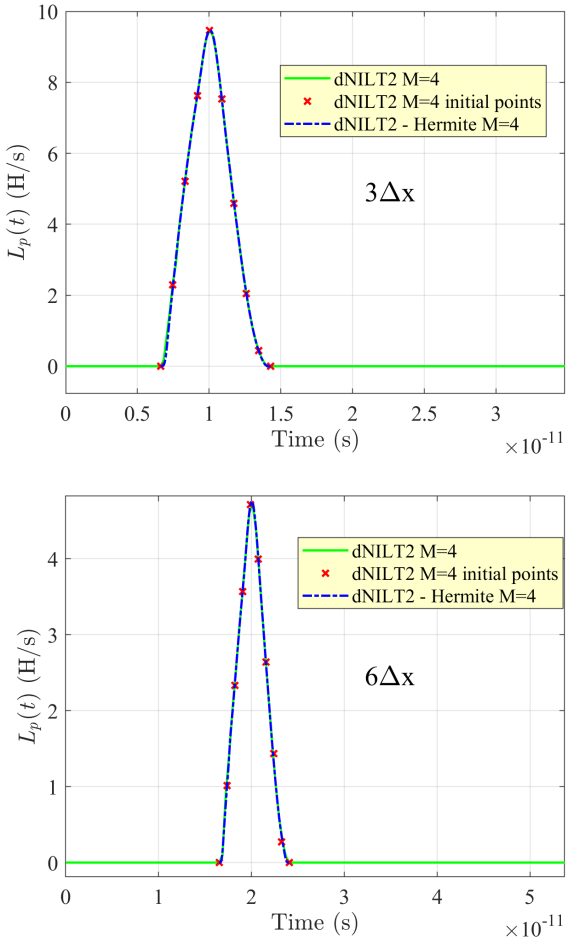

Figure 3.27: TD partial inductance $L_{p_{m,n}}(t)$ for 2 cubes at increasing distances $3\Delta x, 6\Delta x$.

to be noticed that the dNILT2-Hermite technique strictly preserves the causality of

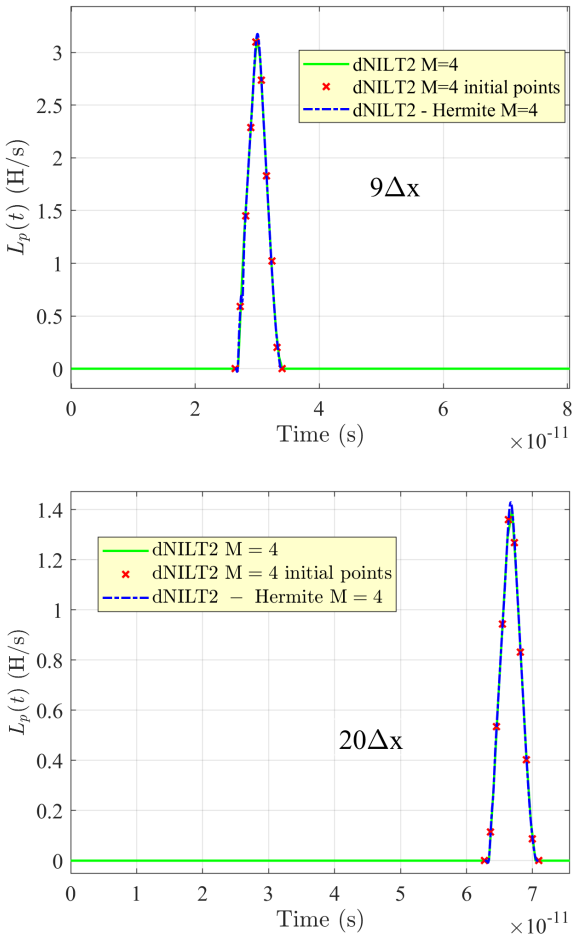

Figure 3.28: TD partial inductance $L_{p_{m,n}}(t)$ for 2 cubes at increasing distances $9\Delta x, 20\Delta x$.

the TD partial inductance $L_{p_{m,n}}(t)$, i.e. it remains zero until time $t_{min} = R_m/c_0$, R_m being the minimum distance between 2 volumes.

Induced voltage by a system of currents

Once the transient inductance $L_{p_{m,n}}(t)$ between 2 volumes m and n is computed, it can be used to compute the induced voltage (FEM) in the volume m by the current $i_n(t)$ flowing in a volume n, at the time t, through a convolution integral.

The geometry is sketched in Fig. 3.29, where the cube 0 is the "victim" volume.

Firstly, the 4 TD partial inductances $L_{p_{0,1}}(t)$, $L_{p_{0,2}}(t)$, $L_{p_{0,3}}(t)$, $L_{p_{0,4}}(t)$ are computed by the proposed dNILT2-Hermite technique. The 4 TD partial inductances are computed starting from 10 samples placed in the time window when the interaction occurs. The circles in Fig. 3.30 are the initial points employed for the interpolation, while the straight line responses are the obtained interpolants. Then, the overall

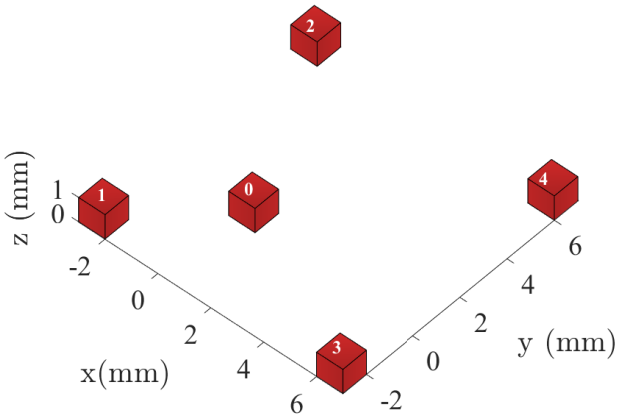

Figure 3.29: Cubes system geometry.

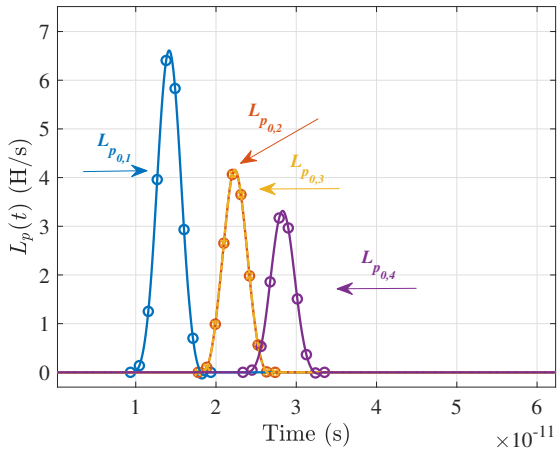

Figure 3.30: TD partial inductances between cube 0 and cubes 1-4 in Fig. 3.29 computed through the dNILT2-Hermite method.

induced voltage on the cube 0 can be computed as:

$$v_{L_0}(t) = \sum_{n=1}^{4} \int_0^t L_{p_{0,n}}(t-\tau) \frac{di_n(\tau)}{d\tau} d\tau \tag{3.103}$$

where $i_n(t)$ is assumed to be the same for each "aggressor" cube, $n = 1,\cdots,4$, and flowing in the x direction. For the impressed current $i_n(t)$, a windowed-power (WP) prototype [97] is chosen:

$$i_n(\tau, t) = t'^{\tau}(2-t')^{\tau} H(t') H(2-t') \tag{3.104}$$

where $H(\cdot)$ is the Heaviside unit step function, $t' = t/t_r$, t_r being the pulse rise time. We choose $\tau = 2$ and $t_r = 11.8$ ps. The dNILT2-Hermite based results are compared

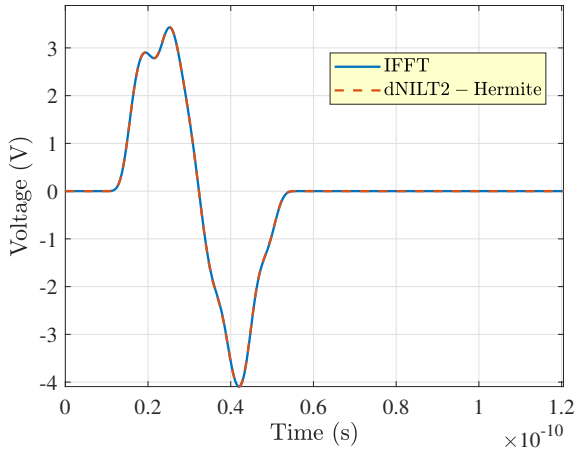

Figure 3.31: Total induced voltage on the central cube.

to the standard approach in which the partial inductances and the impressed current are firstly computed in the FD, then the overall induced voltage on the cube 0 is restored by IFFT:

$$v_{L_0}(t) = \sum_{n=1}^{4} \text{IFFT}\left(j\omega L_{p_{0,n}}(f) I_n(f)\right). \tag{3.105}$$

The induced voltage is reported in Fig. 3.31 showing a very good agreement between the 2 approaches. Hence the dNILT2-Hermite based computation of the TD partial inductances can be suitable for more general PEEC convolution-based solvers.

Total inductance of a thin loop

As a final example, the computation of the FD total inductance (internal and external) of a thin loop is proposed. The loop has a radius $r = 1$ cm, a thickness $t = 1$ μm and a width $w = 0.1$ mm. The structure comprises $N = 31$ thin volumes. The loop is discretized as shown in Fig. 3.32. It is known that, through the concept of partial inductance, it is possible to compute the total inductance of conductors within a complex geometry. In this particular case, the FD total loop inductance is:

$$L_{\ell oop}(j\omega) = \sum_{m=1}^{N} \sum_{n=1}^{N} L_{p_{m,n}}(j\omega) \tag{3.106}$$

where $L_{p_{m,n}}(j\omega)$ is the partial inductance between the volumes m and n. Each term $L_{p_{m,n}}(j\omega)$ can be computed directly in the FD resorting to Gaussian numerical integration. For the sake of comparison, firstly each TD partial inductance $L_{p_{m,n}}(t)$ is computed through the dNILT2-Hermite scheme. Then, the TD loop inductance is obtained as:

$$L_{\ell oop}(t) = \sum_{m=1}^{N} \sum_{n=1}^{N} L_{p_{m,n}}(t). \tag{3.107}$$

Finally, the FD $L_{\ell oop}(j\omega)$ is obtained via the Fourier transform (FT). All the TD mutual partial inductances are sketched in Fig. 3.33. As expected, each response is window limited and retarded of the time $R_m/c0$, where R_m is the minimum distance between the volumes m and n. Because of the symmetries of the geometry, the responses are equal in pairs (continous and dashed lines superimposed). Each mutual interaction is computed via dNILT2-Hermite from 10 starting points equally spaced and placed in the window. The self interactions $L_{p_{m,m}}(t)$ are computed using the CdH technique, since the volumes are very thin. The TD mutual partial inductances obtained by the dNILT2-Hermite approach are shown in Fig. 3.33 where the continuous line is used for the inductances $L_{p_{1,n}}(t)$ with $n = 2, \cdots, 16$ and the dashed line for the inductances $L_{p_{1,n}}(t)$ with $n = 17, \cdots, 31$. As seen, there are pairs of overlapping curves, as expected because of the geometrical symmetry. The comparison between the 2 approaches is shown in Fig. 3.34 exhibiting a very good agreement.

It is worth to remark that the proposed method presents a significant improvement in the computational complexity. Indeed, when using the dNILT2-Hermite method, most of the CPU time is spent in the computation of 10 initial samples in each window. The densely sampled final waveforms are then obtained by applying the Hermite interpolation, with a negligible additional CPU cost, no matter how many TD points are required. On the contrary, the computational cost of each partial inductance in the FD is directly related to the number of frequency points used and this is typically very large to guarantee high accuracy and avoid any aberration. In this test, the TD partial inductances in Fig. 3.33 are computed over 10.000 samples. Hence, in the direct approach, their FT counterparts are computed over 5001 samples. The performances of the 2 methods are summarized in Table 3.1, where the computational advantages of the proposed method are evident.

Table 3.1: Computational performance.

Technique	**Samples**	**CPU time** (s)	Speed-up
Standard approach	5001 (FD)	$6.1 \cdot 10^3$	1
dNILT2-Hermite	10.000 (TD)	$1.8 \cdot 10^3$	3.4

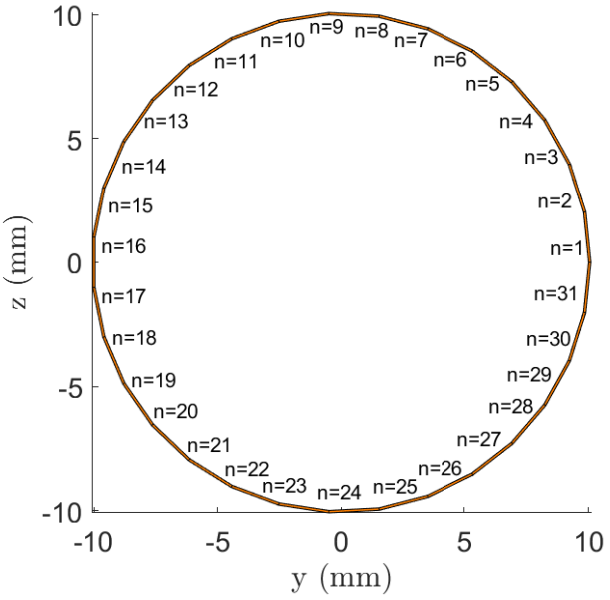

Figure 3.32: The set of thin volumes forming the closed loop geometry.

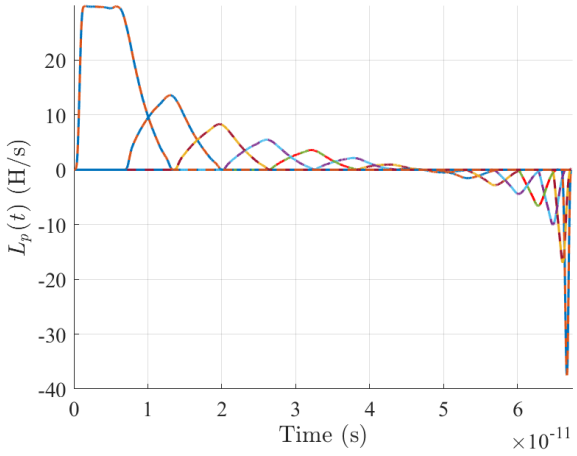

Figure 3.33: dNILT2-Hermite TD mutual partial inductances between the volumes in the loop.

3.4 Convolution-based TD PEEC solver

The rigorous full-wave representation of partial elements leads to a mathematical model which contains convolution operations between the TD partial elements and

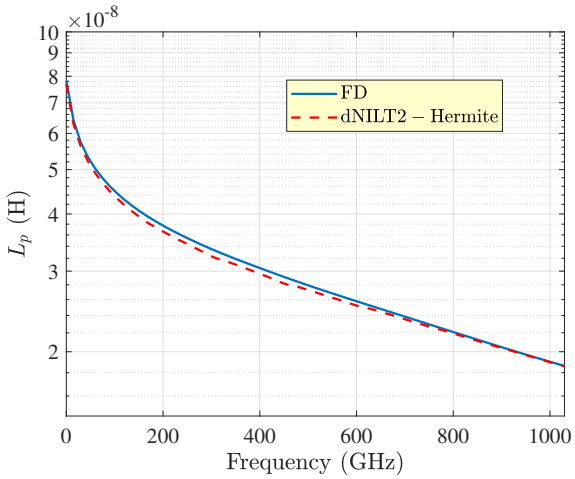

Figure 3.34: Magnitude spectrum of the total loop inductance.

the equivalent currents/potentials. The resulting system can be schematized through the usual state-space MNA form as:

$$\mathbf{C}(t)\frac{d\mathbf{x}(t)}{dt} = -\mathbf{G}(t)\mathbf{x}(t) + \mathbf{B}\mathbf{u}(t). \tag{3.108}$$

It is to be remarked that, in this case, the characteristic matrices multiplying the derivative of the state vector and the state vector itself are assumed time-dependent, since they contains the partial elements submatrices.

Referring to a PEEC formulation which avoids the inversion of the $\mathbf{P}$ submatrix, the unknowns vector $\mathbf{x}(t)$ is given as

$$\mathbf{x}(t) = \left[\mathbf{i}(t) \quad \phi_{sr}(t) \quad \phi_i(t) \quad \mathbf{v}_d(t) \quad \mathbf{q}_s(t)\right]^T, \tag{3.109}$$

where $\mathbf{i}(t)$ are the branch currents, $\phi_{sr}(t)$ are the scalar potentials for surface nodes, $\phi_i(t)$ are the scalar potentials for internal nodes, $\mathbf{v}_d(t)$ are the excess capacitance voltages for dielectric branches, and $\mathbf{q}_s(t)$ represent the surface charges. Further-

more, the state space matrices $\mathbf{C}(t)$, $\mathbf{G}(t)$ and $\mathbf{B}$ are:

$$\mathbf{C}(t) = \begin{bmatrix} \underset{n_b\times n_b}{\mathbf{L}_p(t)*} & \underset{n_b\times n_{ns}}{\mathbf{0}} & \underset{n_b\times n_{ni}}{\mathbf{0}} & \underset{n_b\times n_{bd}}{\mathbf{0}} & \underset{n_b\times n_p}{\mathbf{0}} \\ \underset{n_{ns}\times n_b}{\mathbf{0}} & \underset{n_{ns}\times n_{ns}}{\mathbf{0}} & \underset{n_{ns}\times n_{ni}}{\mathbf{0}} & \underset{n_{ns}\times n_{bd}}{\mathbf{0}} & \underset{n_{ns}\times n_p}{\mathbf{M}^T} \\ \underset{n_{ni}\times n_b}{\mathbf{0}} & \underset{n_{ni}\times n_{ns}}{\mathbf{0}} & \underset{n_{ni}\times n_{ni}}{\mathbf{0}} & \underset{n_{ni}\times n_{bd}}{\mathbf{0}} & \underset{n_{ni}\times n_p}{\mathbf{0}} \\ \underset{n_{bd}\times n_b}{\mathbf{0}} & \underset{n_{bd}\times n_{ns}}{\mathbf{0}} & \underset{n_{bd}\times n_{ni}}{\mathbf{0}} & \underset{n_{bd}\times n_{bd}}{\mathbf{C}_d} & \underset{n_{bd}\times n_p}{\mathbf{0}} \\ \underset{n_p\times n_b}{\mathbf{0}} & \underset{n_p\times n_{ns}}{\mathbf{0}} & \underset{n_p\times n_{ni}}{\mathbf{0}} & \underset{n_p\times n_{bd}}{\mathbf{0}} & \underset{n_p\times n_p}{\mathbf{0}} \end{bmatrix}, \tag{3.110}$$

$$\mathbf{G}(t) = \begin{bmatrix} \underset{n_b\times n_b}{\mathbf{R}} & \underset{n_b\times n_{ns}}{\mathbf{A}_s} & \underset{n_b\times n_{ni}}{\mathbf{A}_i} & \underset{n_b\times n_{bd}}{\mathbf{\Gamma}} & \underset{n_b\times n_p}{\mathbf{0}} \\ \underset{n_{ns}\times n_b}{-\mathbf{A}_s^T} & \underset{n_{ns}\times n_{ns}}{\mathbf{G}_{le}} & \underset{n_{ns}\times n_{ni}}{\mathbf{0}} & \underset{n_{ns}\times n_{bd}}{\mathbf{0}} & \underset{n_{ns}\times n_p}{\mathbf{0}} \\ \underset{n_{ni}\times n_b}{-\mathbf{A}_i^T} & \underset{n_{ni}\times n_{ns}}{\mathbf{0}} & \underset{n_{ni}\times n_{ni}}{\mathbf{0}} & \underset{n_{ni}\times n_{bd}}{\mathbf{0}} & \underset{n_{ni}\times n_p}{\mathbf{0}} \\ \underset{n_{bd}\times n_b}{-\mathbf{\Gamma}^T} & \underset{n_{bd}\times n_{ns}}{\mathbf{0}} & \underset{n_{bd}\times n_{ni}}{\mathbf{0}} & \underset{n_{bd}\times n_{bd}}{\mathbf{0}} & \underset{n_{bd}\times n_p}{\mathbf{0}} \\ \underset{n_p\times n_b}{\mathbf{0}} & \underset{n_p\times n_{ns}}{-\mathbf{M}} & \underset{n_p\times n_{ni}}{\mathbf{0}} & \underset{n_p\times n_{bd}}{\mathbf{0}} & \underset{n_p\times n_p}{\mathbf{P}(t)*} \end{bmatrix}, \tag{3.111}$$

$$\mathbf{B} = \begin{bmatrix} \underset{n_b\times n_b}{\mathcal{I}} & \underset{n_b\times n_{ns}}{\mathbf{0}} \\ \underset{n_{ns}\times n_b}{\mathbf{0}} & \underset{n_{ns}\times n_{ns}}{\mathcal{I}} \\ \underset{n_{ni}\times n_b}{\mathbf{0}} & \underset{n_{ni}\times n_{ns}}{\mathbf{0}} \\ \underset{n_{bd}\times n_b}{\mathbf{0}} & \underset{n_{bd}\times n_{ns}}{\mathbf{0}} \\ \underset{n_p\times n_b}{\mathbf{0}} & \underset{n_p\times n_{ns}}{\mathbf{0}} \end{bmatrix}, \tag{3.112}$$

where $*$ represents the convolution operator, and n_b, n_{ns}, n_{ni}, n_{bd} and n_p represent the cardinality of branches, surface nodes, internal nodes, dielectric cells and surface cells, respectively. Moreover, $\mathbf{C}_d$ is the excess capacitance matrix, $\mathbf{R}$ is the branches resistance matrix, $\mathbf{A}_s$ is the incidence matrix for the surface nodes, $\mathbf{A}_i$ is the incidence matrix for the internal nodes, $\mathbf{\Gamma}$ is the dielectric region selection matrix, $\mathbf{M}$ is the surface-to-node reduction matrix and $\mathbf{G}_{le}$ is the load conductance matrix.

3.4.1 Applications and preliminary results

In this section some simple 2D geometries without dielectrics are examined through the technique proposed in this chapter. Hence, focusing on thin conductors and

assuming the absence of dielectrics, the unknowns vector $\mathbf{x}(t)$ reduces to:

$$\mathbf{x}(t) = [\mathbf{i}(t) \quad \phi_s(t) \quad \mathbf{q}_s(t)]^T \tag{3.113}$$

Furthermore, the state space matrices $\mathbf{C}(t)$, $\mathbf{G}(t)$ and $\mathbf{B}$ become:

$$\mathbf{C}(t) = \begin{bmatrix} \underset{n_b \times n_b}{\mathbf{L}_p(t)*} & \underset{n_b \times n_{ns}}{\mathbf{0}} & \underset{n_b \times n_p}{\mathbf{0}} \\ \underset{n_{ns} \times n_b}{\mathbf{0}} & \underset{n_{ns} \times n_{ns}}{\mathbf{0}} & \underset{n_{ns} \times n_p}{\mathbf{M}^T} \\ \underset{n_p \times n_b}{\mathbf{0}} & \underset{n_p \times n_{ns}}{\mathbf{0}} & \underset{n_p \times n_p}{\mathbf{0}} \end{bmatrix}, \tag{3.114}$$

$$\mathbf{G}(t) = \begin{bmatrix} \underset{n_b \times n_b}{\mathbf{R}} & \underset{n_b \times n_{ns}}{\mathbf{A}_s} & \underset{n_b \times n_p}{\mathbf{0}} \\ \underset{n_{ns} \times n_b}{-\mathbf{A}_s^T} & \underset{n_{ns} \times n_{ns}}{\mathbf{G}_{le}} & \underset{n_{ns} \times n_p}{\mathbf{0}} \\ \underset{n_p \times n_b}{\mathbf{0}} & \underset{n_p \times n_{ns}}{-\mathbf{M}} & \underset{n_p \times n_p}{\mathbf{P}(t)*} \end{bmatrix}, \tag{3.115}$$

$$\mathbf{B} = \begin{bmatrix} \underset{n_b \times n_b}{\mathcal{I}} & \underset{n_b \times n_{ns}}{\mathbf{0}} \\ \underset{n_{ns} \times n_b}{\mathbf{0}} & \underset{n_{ns} \times n_{ns}}{\mathcal{I}} \\ \underset{n_p \times n_b}{\mathbf{0}} & \underset{n_p \times n_{ns}}{\mathbf{0}} \end{bmatrix}, \tag{3.116}$$

The TD partial inductance between two surfaces A_m, A_n is easily obtained from the equivalent coefficient of potential related to the two surfaces. If the direction of current flowing is supposed in the y direction, we have:

$$L_{mn}(t) = \frac{\mu_0 \epsilon_0 A_m A_n}{\Delta_{x_m} \Delta_{x_n}} P_{mn}(t) \tag{3.117}$$

where Δ_{x_m} and Δ_{x_n} are the sizes of the two rectangles in the x direction, being supposed the surface currents flowing in the y direction. If the direction of current flowing is assumed in the x direction, similar considerations apply.

Two coupled transmission lines

We consider the configuration depicted in Fig. 3.35, consisting of two nearby patch transmission lines (TL). The source TL is supposed to be fed by a Thevenin equivalent, where the generator represents a trapezoidal voltage signal characterized by a

rising time $t_r = 0.3$ ns and width $t_w = 1$ ns. The source and the load impedances are supposed to be equal and purely resistive with values $Z_s = Z_L = 50\ \Omega$. The victim TL is closed on both sides on resistive loads $Z_L = 50\ \Omega$. With reference to Fig. 3.35, the length and the width of each strip are $L = 1$ cm and $W = 1$ mm, respectively, while the distances occurring between the strips are $S_1 = S_2 = S_3 = 1.2$ mm.

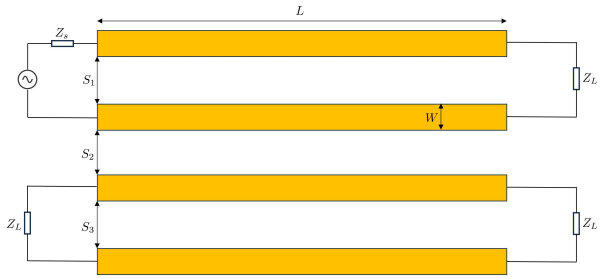

Figure 3.35: Transmission lines geometry.

The structure is discretized into elementary zero-thickness cells of size not exceeding $\lambda_{min}/20$, being λ_{min} the minimum wavelength corresponding to the maximum frequency that is significant in the spectrum of the source signal. Subsequently, TD partial elements have been computed through the CdH technique. This kind of representation of the partial elements leads to a convolution-based solver, where two groups of convolutions are performed: those between the TD partial inductances and the electric currents flowing in the branches of the inductive mesh and those between the TD coefficients of potential and the electric charges residing over the surfaces of the capacitive mesh. The load voltage of the source line and the TD far-end and near-end voltages induced over the victim line are depicted in Figs. 3.36-3.37, where the proposed CdH approach is compared to established TD techniques for the analysis of retarded PEEC systems using the backward difference scheme of the second order (BD2). It is evident that the results obtained through the CdH approach match perfectly those obtained through the application of the Inverse Fast Fourier Transform (IFFT CC) to the results obtained through the FD analysis of the model. On the other side, the TD solution using the BD2 time-stepping technique clearly exhibits an unstable behavior that is related to the approximations of the propagation delays occurring between the partial elements employed in the retarded

TD model. On the other hand, the PEEC solver using TD partial elements obtained through the CdH technique remains stable. The different behavior in terms of stability can only be related to the most accurate representation of the propagation delays and convolution integrals.

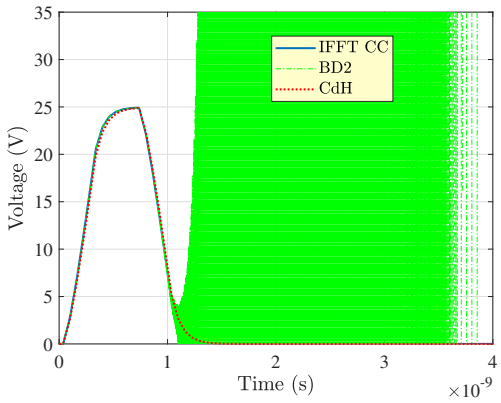

Figure 3.36: Driven line: load voltage.

Input impedance of a patch dipole

We now consider the center-fed patch dipole antenna depicted in Fig. 3.38. The two patches constituting the structure are squares with dimensions $W = L = 4.5$ mm.

Our analysis considers two different frequency ranges: the active frequency range extending up to the maximum frequency $f_{max} = 20$ GHz, and the extended frequency range up to $f_e = 200$ GHz.

The EM model of the structure is built by subdividing the geometry into surface inductive cells whose dimensions are no longer than $\lambda_{min}/60$, being λ_{min} the reference minimum wavelength at f_{max}. The dipole is characterized in the frequency domain by its input impedance. The computation is performed through a PEEC-based solver in conjunction with the TD-CdH-based representation of the partial elements, carrying out the analysis directly in the TD by resorting to the numerical evaluation of convolution integrals. In particular, the dipole is excited with an arbitrary voltage source with a series impedance $Z_s = 73\ \Omega$ and, subsequently, the TD input port voltage and current are obtained. Finally, the input impedance is obtained as the ratio of the Fourier transforms of the port quantities. The results

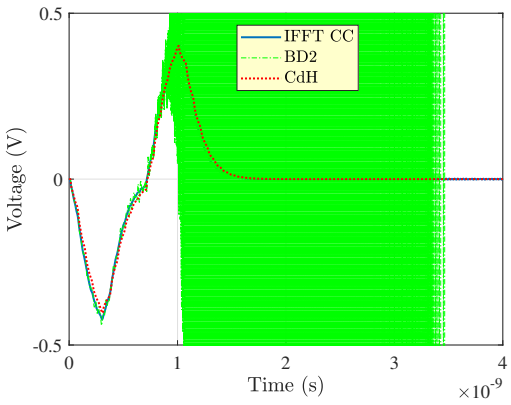

(a)

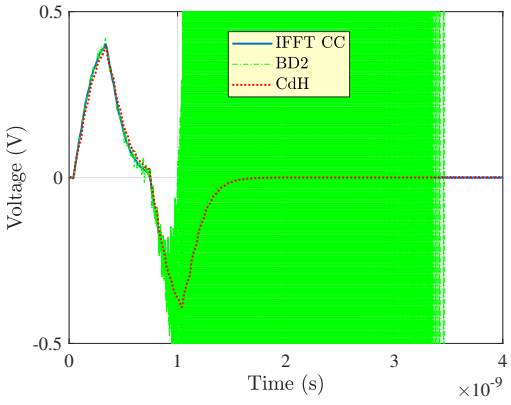

(b)

Figure 3.37: Victim line: (a) Near-end voltage, (b) Far-end voltage.

obtained through the proposed technique are compared with those achieved directly in the frequency domain by solving the FD PEEC model, expressing the partial elements through the Gaussian numerical integration along the two dimensions of each mesh patch, employing integration orders labeled as o_x and o_y for the x- and y directions, respectively. The input impedance is sketched in Fig. 3.39, in terms of input resistance (Fig. 3.39(a)) and input reactance (Fig. 3.39(b)). The results obtained by the PEEC solver using TD partial elements match very well in the active frequency range, those reported in [50], where the same geometry was considered, being the 18 GHz peak perfectly reproduced. The same holds for the reactance

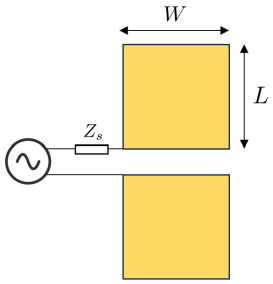

Figure 3.38: Patch dipole geometry.

behavior in the active range. Not surprisingly, the FD results show a better match with TD-CdH-based results with the increasing integration order.

Furthermore, it is worth noticing that, in the extended frequency range (i.e. 20 GHz $< f <$ 200 GHz), TD-CdH results preserve the passivity while the direct FD results do not since passivity violations are observed above 74 GHz. This aspect is crucial when dealing with TD solvers since passivity violations in the extended range (at frequencies $f > f_{max}$) cause late-time instabilities of the TD model.

Transient response of a receiver dipole placed near a transmitter dipole

We are concerned with a pair of transmitter and receiver dipoles, placed at a distance $d = 20$ cm. The geometry of each one is the same as the single dipole analyzed before. The source and the load impedance are set as $Z_s = Z_L = 73\ \Omega$. The configuration is sketched in Fig. 3.40. We are concerned with the computation of the transient response at the receiver dipole load.

The source signal driving the transmitter feeding port is a windowed-power pulse (WP) with rising time $t_r = 20$ ps and $\nu = 0.2$, which is a parameter that shapes the pulse [97]. The transient receiver voltage is computed through the CdH-based PEEC solver and is reported in Fig. 3.41. Also in this example, a comparison with the results obtained through the FD solver using partial elements computed resorting to the Gaussian integration is provided. The transient responses are obtained through the inverse Fourier transform (IFT) of the FD results. Also in this case, the transient results based on the Gaussian integration exhibit a better matching with those obtained through the TD-CdH-based method when the order of integration is

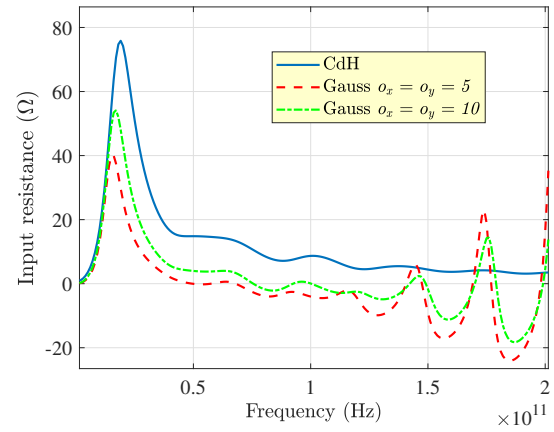

(a)

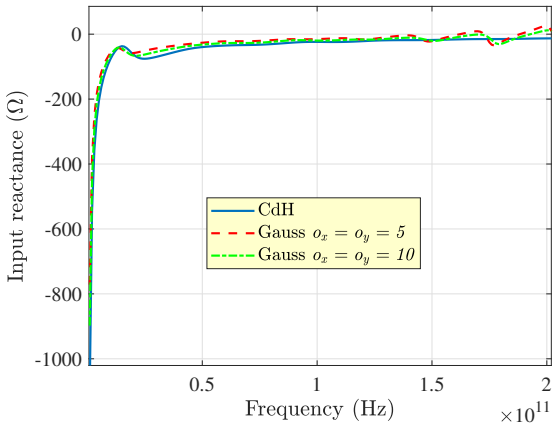

(b)

Figure 3.39: Patch dipole (a) input resistance, (b) input reactance.

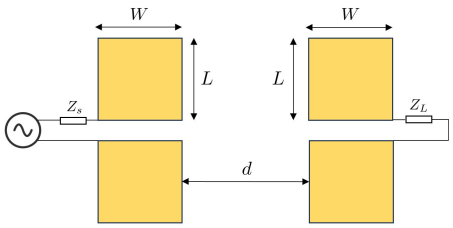

Figure 3.40: Transmitter and receiver patch dipoles configuration.

increased, confirming the results of the previous example. Further, the voltage at the receiver port is computed through a time-stepping solver that adopts a backward difference scheme of the second order (BD2). In this case, the partial elements take propagation delays into account through the widely used center-to-center (CC) approximation. It is evident that the BD2-based solver results are inaccurate if compared to the CdH-based PEEC solver. This is also highlighted by the fact that the signal propagation delay between the two dipoles is not reproduced accurately. This might happen especially when the structures are placed very close to each other, being in this case the CC approximation inadequate to correctly reproduce the propagation delay.

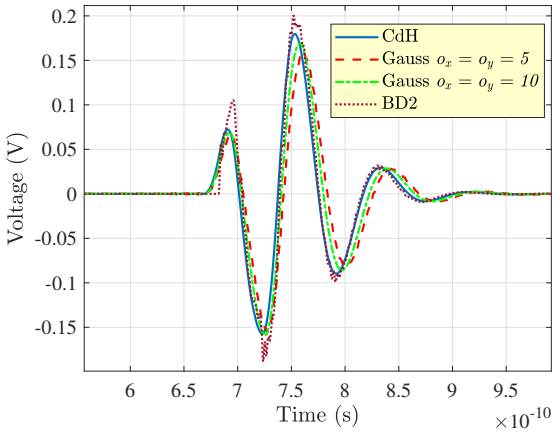

Figure 3.41: Receiver TD voltage response.

4 Publications

International peer reviewed journals

1. L. Lombardi, F. Loreto, F. Ferranti, A. E. Ruehli, M. S. Nakhla, Y. Tao, M. Parise, G. Antonini, Time-Domain Analysis of Retarded Partial Element Equivalent Circuit Models Using Numerical Inversion of Laplace Transform, *IEEE Transactions on Electromagnetic Compatibility*, Vol. 14, n. 16, pp. 870-879, 2021.

2. M. Parise, F. Loreto, D. Romano, G. Antonini, J. Ekman, Accurate Computation of Mutual Inductance of Non Coaxial Pancake Coils, *Energies*, Vol. 63, n. 3, 4907, 11 August 2021.

3. G. Antonini, G. Dattoli, F. Frezza, S. Licciardi, F. Loreto, About the Use of Generalized Forms of Derivatives in the Study of Electromagnetic Problems, *Applied sciences*, Vol. 11, n. 16, 7505, 16 August 2021.

4. F. Loreto, D. Romano, M. Stumpf, A. E. Ruehli, G. Antonini, Time Domain Computation of Full-Wave Partial Inductances Based on the Modified Numerical Inversion of Laplace Transform Method, *IEEE Transactions on Signal and Power Integrity*, Vol. 1 , pp. 32-42, 2022.

5. M. Stumpf, F. Loreto, G. Pettanice, G. Antonini, Cagniard-DeHoop technique-based computation of retarded zero-thickness partial elements, *Engineering Analysis with Boundary Elements*, Vol. 137, pp. 56-64 , April 2022.

6. F. Loreto, G. Pettanice, G. Antonini, E. Gad, M. S. Nakhla, Y. Tao, A. Ruehli, Modified Numerical Inversion of Laplace Transform Methods for the Time-Domain Analysis of Retarded Partial Elements Equivalent Circuit Models, *IEEE Transactions on Electromagnetic Compatibility*, Vol. 64, n. 6, pp. 2179-2188, 2022.

7. M. Stumpf, F. Loreto, G. Pettanice, G. Antonini, Partial-inductance retarded partial coefficients: Their exact computation based on the Cagniard-DeHoop technique, *Engineering Analysis with Boundary Elements*, Vol. 149, pp. 86-91 , April 2023.

8. M. Stumpf, F. Loreto, D. Romano, G. Antonini, J. Ekman, Pulsed Wave Propagation Along a Transmission Line With Time-Varying Wavespeed, *IEEE Antennas and Wireless Propagation Letters*, vol. 33, no. 7, pp. 963-966, July 2023.

9. F. Loreto, D. Romano, G. Pettanice, G. Antonini, A Comparative Analysis of Numerical Inverse Laplace Transform Methods for Electromagnetic Transient Analysis, *IEEE Transactions on Microwave Theory and Techniques*, Vol. 71, no. 11, pp. 4713-4724, Nov. 2023.

10. G. Antonini, A. E. Ruehli, D. Romano, F. Loreto, The Partial Elements Equivalent Circuit Method: the State-of-the-Art, *IEEE Transactions on Electromagnetic Compatibility*, vol. 65, no. 6, pp. 1695-1714, Dec. 2023.

11. G. Pettanice, R. Valentini, P. Di Marco, F. Loreto, D. Romano, F. Santucci, D. Spina, G. Antonini, Mutual Coupling Aware Time-Domain Characterization and Performance Analysis of Reconfigurable Intelligent Surfaces, *IEEE Transactions on Electromagnetic Compatibility*, vol. 65, no. 6, pp. 1606-1620, Dec. 2023.

12. M. Parise, F. Loreto, Quasi-static explicit expression for the flux linkage between non-coplanar coils in wireless power transfer systems above a lossy ground, *IEEE Transactions on Electromagnetic Compatibility*, vol. 65, no. 6, pp. 1857-1867, Dec. 2023.

International conferences

1. F. Loreto, D. Romano, G. Antonini, A. E. Ruehli, L. Lombardi, M. Parise, Taylor Series Expansion-Based PEEC Time Domain Solver for Transient Full-Wave Analysis, *2020 International Symposium on Electromagnetic Compatibility - EMC EUROPE*, Rome (Italy), September 2020.

2. F. Loreto, D. Romano, G. Antonini, M. Stumpf, A. E. Ruehli, Time Domain Computation of Full-Wave Partial Inductances Based on the Numerical Inversion of Laplace Transform Method, *2021 IEEE International Joint EMC/SI/PI and EMC Europe Symposium*, Glasgow (Scotland), August 2021.

3. F. Loreto, D. Romano, G. Antonini, M. Stumpf, I. E. Lager, G. A. E. Vandenbosch, Preserving Causality in Time Domain Integral Equation-Based Methods, *2021 51st European Microwave Conference (EuMC)*, London (England), April 2022.

4. G. Pettanice, F. Loreto, P. Di Marco, D. Romano, F. Santucci, R. Alesii, G. Antonini,Time-domain Characterization of Reconfigurable Intelligent Surfaces for Wireless Communications, *2022 International Symposium on Electromagnetic Compatibility - EMC EUROPE*, Gothenburg (Sweden), September 2022.

5. F. Loreto, G. Pettanice, D. Romano, M. Stumpf, I. E. Lager, G. Antonini, Computation of Time Domain Scattering Parameters Through the Numerical Inversion of the Laplace Transform, *2022 52nd European Microwave Conference (EuMC)*, Milan (Italy), September 2022.

6. D. Romano, F. Loreto, G. Antonini, I. Kovacevic - Badstuebner, U. Grossner, Accelerated Partial Inductance Evaluation via Cubic Spline Interpolation for the PEEC Method, *2022 52nd European Microwave Conference (EuMC)*, Milan (Italy), September 2022.

7. G. Pettanice, F. Loreto, R. Valentini, P. Di Marco, G. Antonini, Time Domain Analysis of PEEC Models Through the FFT Acceleration Technique, *2023*

17th European Conference on Antennas and Propagation (EuCAP), Florence (Italy), March 2023.

8. F. Loreto, D. Romano, G. Antonini, A. Ruehli, M. Lai, Roughness Losses Modeling Using the Partial Elements Equivalent Circuit Method, *2023 IEEE International Symposium on Electromagnetic Compatibility, Signal and Power Integrity*, Grand Rapids, Michigan (USA), August 2023.

9. F. Loreto, G. Pettanice, R. Valentini, P. Di Marco, D. Romano, M. Stumpf, F. Santucci, G. Antonini, A Time-Domain Model of Reconfigurable Intelligent Surfaces Through the Fast Inversion of the Laplace Transform, *2023 International Symposium on Electromagnetic Compatibility - EMC EUROPE*, Krakow (Poland), September 2023.

10. F. Loreto, D. Romano, G. Antonini, M. Stumpf, A. E. Ruehli and J. Ekman, "Time Domain Partial Elements: A New Paradigm for Improved PEEC Models," 2023 IEEE Electrical Design of Advanced Packaging and Systems (EDAPS), Rose-Hill, Mauritius, 2023.

11. F. Loreto, G. Pettanice, M. Stumpf, A. Ruehli, J. Ekman and G. Antonini, "Improved PEEC Modeling of Antennas Through Time-Dependent Partial Elements," 2024 18th European Conference on Antennas and Propagation (EuCAP), Glasgow, United Kingdom, 2024.

Bibliography

[1] A. E. Ruehli. Inductance calculations in a complex integrated circuit environment. *IBM Journal of Research and Development*, 16(5):470–481, Sept 1972.

[2] A. E. Ruehli and P. A. Brennan. Efficient capacitance calculations for three-dimensional multiconductor systems. *IEEE Transactions on Microwave Theory and Techniques*, 21(2):76–82, Feb 1973.

[3] A. E. Ruehli. Equivalent circuit models for three-dimensional multiconductor systems. *IEEE Transactions on Microwave Theory and Techniques*, 22(3):216–221, Mar 1974.

[4] A. E. Ruehli and H. Heeb. Circuit models for three-dimensional geometries including dielectrics. *IEEE Transactions on Microwave Theory and Techniques*, 40(7):1507–1516, Jul 1992.

[5] G. Antonini, A. E. Ruehli and C. Yang. PEEC modeling of dispersive and lossy dielectrics. *IEEE Transactions on Advanced Packaging*, 31(4):768, September 2008.

[6] D. Romano and G. Antonini. Quasi-static partial element equivalent circuit models of linear magnetic materials. *IEEE Transactions on Magnetics*, 51(7):1–15, July 2015.

[7] D. Romano and G. Antonini. Augmented quasi-static partial element equivalent circuit models for transient analysis of lossy and dispersive magnetic materials. *IEEE Transactions on Magnetics*, 52(5):1–11, May 2016.

[8] D. Romano, G. Antonini, and A. E. Ruehli. Time-domain partial element equivalent circuit solver including non-linear magnetic materials. *IEEE Transactions on Magnetics*, 52(9):1–11, September 2016.

[9] D. Romano and G. Antonini. Quasi-static partial element equivalent circuit models of magneto-dielectric materials. *IET Microwaves, Antennas Propagation*, 11(6):915–922, 2017.

[10] D. Romano, G. Antonini, and A. E. Ruehli. Time-domain partial element equivalent circuit solver including non-linear magnetic materials. In *2015 IEEE MTT-S International Conference on Numerical Electromagnetic and Multiphysics Modeling and Optimization (NEMO)*, pages 1–3, August 2015.

[11] L. Lombardi, D. Romano, and G. Antonini. Partial element equivalent circuit method modeling of silicon interconnects. *IEEE Transactions on Microwave Theory and Techniques*, 65(12):4794–4801, Dec 2017.

[12] L. Lombardi, G. Antonini, and A. E. Ruehli. Analytical evaluation of partial inductances with retardation. In *2017 IEEE 26th Conference on Electrical Performance of Electronic Packaging and Systems (EPEPS)*, pages 1–3, Oct 2017.

[13] L. Lombardi, G. Antonini, and A. E. Ruehli. Analytical evaluation of partial elements using a retarded taylor series expansion of the green's function. *IEEE Transactions on Microwave Theory and Techniques*, 66(5):2116–2127, May 2018.

[14] R. F. Harrington. *Field Computation by Moment Methods*. Macmillan, New York, 1968.

[15] C. A. Balanis. *Advanced Engineering Electromagnetics*. John Wiley and Sons, New York, 1989.

[16] L. W. Nagel. SPICE: A computer program to simulate semiconductor circuits. Electr. Res. Lab. Report ERL M520, University of California, Berkeley, May 1975.

[17] G. Antonini. The fast multipole method for PEEC circuits analysis. In *2002 IEEE International Symposium on Electromagnetic Compatibility*, volume 1, pages 446–451 vol.1, Aug 2002.

[18] M. Bebendorf. Approximation of boundary element matrices. *Numer. Math.*, 86:565–589, June 2000.

[19] G. Antonini and D. Romano. Adaptive-cross-approximation-based acceleration of transient analysis of quasi-static partial element equivalent circuits. *IET Microwaves, Antennas Propagation*, 9(7):700–709, 2015.

[20] G. Antonini and D. Romano. Multiscale decomposition based analysis of PEEC models. In *2013 International Conference on Electromagnetics in Advanced Applications (ICEAA)*, pages 1095–1098, September 2013.

[21] G. Antonini and D. Romano. Efficient frequency-domain analysis of PEEC circuits through multiscale compressed decomposition. *IEEE Transactions on Electromagnetic Compatibility*, 56(2):454–465, April 2014.

[22] G. Antonini and D. Romano. Acceleration of time-domain nodal-analysis of partial element equivalent circuits through multiscale compressed decomposition. *IEEE Transactions on Electromagnetic Compatibility*, 56(4):970–979, August 2014.

[23] G. Antonini and D. Romano. A vectorized multiscale compressed decomposition-based solver for partial element equivalent circuit method. *International Journal of Numerical Modelling: Electronic Networks, Devices and Fields*, 28(4):419–432, 2015.

[24] A. E. Ruehli, G. Antonini, J. Esch, J. Ekman, A. Mayo, and A. Orlandi. Nonorthogonal PEEC formulation for time- and frequency-domain EM and cir-

cuit modeling. *IEEE Transactions on Electromagnetic Compatibility*, 45(2):167–176, May 2003.

[25] A. Glisson and D. Wilton. Simple and efficient numerical methods for problems of electromagnetic radiation and scattering from surfaces. *IEEE Transactions on Antennas and Propagation*, 28(5):593–603, Sep 1980.

[26] S. Rao, D. Wilton, and A. Glisson. Electromagnetic scattering by surfaces of arbitrary shape. *IEEE Transactions on Antennas and Propagation*, 30(3):409–418, May 1982.

[27] S. M. Rao and D. R. Wilton. Transient scattering by conducting surfaces of arbitrary shape. *IEEE Transactions on Antennas and Propagation*, 39(1):56–61, Jan 1991.

[28] J. J. H. Wang. *Generalized Moment Method in Electromagnetics*. John Wiley and Sons, New York, 1991.

[29] B. M. Kolundzija and B. D. Popovic. Entire-domain galerkin method for analysis of metallic antennas and scatterers. *IEE Proceedings H - Microwaves, Antennas and Propagation*, 140(1):1–10, Feb 1993.

[30] Luigi Lombardi, Giulio Antonini, and Albert E. Ruehli. Analytical evaluation of partial elements using a retarded taylor series expansion of the green's function. *IEEE Transactions on Microwave Theory and Techniques*, 66(5):2116–2127, 2018.

[31] F. W. Grover. *Inductance calculations: Working formulas and tables*. Dover, 1962.

[32] P. A. Brennan, N. Raver, and A. E. Ruehli. Three-dimensional inductance computations with partial element equivalent circuits. *IBM Journal of Research and Development*, 23(6):661–668, Nov 1979.

[33] A. E. Ruehli and P. A. Brennan. Capacitance models for integrated circuit metallization wires. *IEEE Journal of Solid-State Circuits*, 10(6):530–536, Dec 1975.

[34] G. Antonini, A. Orlandi, and A. E. Ruehli. Analytical integration of quasi-static potential integrals on nonorthogonal coplanar quadrilaterals for the PEEC method. *IEEE Transactions on Electromagnetic Compatibility*, 44(2):399–403, May 2002.

[35] A. E. Ruehli and H. Heeb. Circuit models for three-dimensional geometries including dielectrics. *IEEE Transactions on Microwave Theory and Techniques*, 40(7):1507–1516, Jul 1992.

[36] G. Antonini. PEEC modelling of Debye dispersive dielectrics. In *Electrical Engineering and Electromagnetics*, pages 126–133. WIT Press, C. A. Brebbia, D. Polyak Editors, Southampton, 2003.

[37] G. Antonini, A. E. Ruehli, A. Haridass. Including dispersive dielectrics in PEEC models. In *Digest of Electr. Perf. Electronic Packaging*, pages 349 – 352, Princeton, NJ, USA, October 2003.

[38] G. Antonini, A. E. Ruehli, A. Haridass. PEEC Equivalent Circuits for Dispersive Dielectrics. In *Proceedings of Piers-Progress in Electromagnetics Research Symposium*, Pisa, Italy, March 2004.

[39] A. Ruehli, J. Garrett, and C. Paul. Circuit models for 3D structures with incident fields. In *1993 International Symposium on Electromagnetic Compatibility*, pages 28–32, Aug 1993.

[40] A. Quarteroni. *Numerical Mathematics*. Springer-Verlag, 2000.

[41] Y. Saad, M. Schultz. GMRES: A Generalized Minimal Residual Algorithm for Solving Nonsymmetric Linear Systems. *Siam J. Scientific and Statistical Computing*, 7(3):856–869, 1986.

[42] N. Engheta, W. D. Murphy, V. Rokhlin, M. S. Vassilou. The fast multipole method (FMM). In *PIERS*, July 1991.

[43] R. Coifman, V. Rokhlin, and S. Wandzura. The fast multipole method for the wave equation: a pedestrian prescription. *IEEE Antennas and Propagation Magazine*, 35(3):7–12, June 1993.

[44] J. M. Song and W. C. Chew. Multilevel fast-multipole algorithm for solving combined field integral equations of electromagnetic scattering. *Microwave and Optical Technology Letters*, 10(1):14–19, 1995.

[45] G. Antonini and A. E. Ruehli. Fast multipole and multifunction PEEC methods. *IEEE Transactions on Mobile Computing*, 2(4):288–298, Oct 2003.

[46] J. R. Phillips and J. K. White. A precorrected-FFT method for electrostatic analysis of complicated 3-D structures. *IEEE Transactions on Computer-Aided Design of Integrated Circuits and Systems*, 16(10):1059–1072, Oct 1997.

[47] Chung-Wen Ho, A. Ruehli, and P. Brennan. The modified nodal approach to network analysis. *IEEE Transactions on Circuits and Systems*, 22(6):504–509, Jun 1975.

[48] B. P. Rynne, D. A. Vechinski, and S. M. Rao. Comments on "A stable procedure to calculate the transient scattering by conducting surfaces of arbitrary shape". *IEEE Transactions on Antennas and Propagation*, 41(4):517–520, April 1993.

[49] A. E. Ruehli, U. Miekkala, and H. Heeb. Stability of discretized partial element equivalent EFIE circuit models. *IEEE Transactions on Antennas and Propagation*, 43(6):553–559, Jun 1995.

[50] J. E. Garrett, A. E. Ruehli, and C. R. Paul. Accuracy and stability improvements of integral equation models using the partial element equivalent circuit (PEEC) approach. *IEEE Transactions on Antennas and Propagation*, 46(12):1824–1832, Dec 1998.

[51] J. Pingenot, S. Chakraborty, and V. Jandhyala. Polar integration for exact space-time quadrature in time-domain integral equations. *IEEE Transactions on Antennas and Propagation*, 54(10):3037–3042, Oct 2006.

[52] J. Ekman, G. Antonini, A. Orlandi, and A. E. Ruehli. Impact of partial element accuracy on PEEC model stability. *IEEE Transactions on Electromagnetic Compatibility*, 48(1):19–32, Feb 2006.

[53] A. Ruehli, U. Miekkala, A. Bellen, and H. Heeb. Stable time domain solutions for EMC problems using PEEC circuit models. In *Proceedings of IEEE Symposium on Electromagnetic Compatibility*, pages 371–376, Aug 1994.

[54] A. Bellen, N. Guglielmi, and A. E. Ruehli. Methods for linear systems of circuit delay differential equations of neutral type. *IEEE Transactions on Circuits and Systems I: Fundamental Theory and Applications*, 46(1):212–215, Jan 1999.

[55] E. Hairer and G. Wanner. *Solving ordinary differential equations II, Stiff and differential algebraic problems*. Springer-Verlag, New York, 1991.

[56] A. Bellen, M. Zennaro. Strong contractivity properties of numerical methods for ordinary and delay differential equations. *Applied Numer. Math.*, 9:321–346, 1992.

[57] G. Antonini. Fast multipole method for time domain PEEC analysis. *IEEE Transactions on Mobile Computing*, 2(4):275–287, Oct 2003.

[58] J.C. Butcher. *Numerical Methods for Ordinary Differential Equations*. John Wiley and Sons, New York, 2010.

[59] Carmine Gianfagna, Luigi Lombardi, and Giulio Antonini. Marching-on-in-time solution of delayed peec models of conductive and dielectric objects. *IET Microwaves, Antennas & Propagation*, 13(1):42–47, 2019.

[60] Chiu-Chih Chou and Tzong-Lin Wu. Poles and stability of full-wave peec. *IEEE Transactions on Antennas and Propagation*, 69(2):950–961, 2021.

[61] A.E. Ruehli, U. Miekkala, and H. Heeb. Stability of discretized partial element equivalent efie circuit models. *IEEE Transactions on Antennas and Propagation*, 43(6):553–559, 1995.

[62] William T. Weeks. Numerical inversion of Laplace transforms using Laguerre functions. *Journal of the Association for Computing Machinery*, 13(3):419–426, 1966.

[63] H. Dubner and J. Abate. Numerical inversion of Laplace transforms by relating them to the finite Fourier cosine transform. *Computer Applications*, 15(1):115–123, 1968.

[64] Harald Stehfest. Numerical inversion of Laplace transforms. *Communications of the ACM*, 13(1):47–49, 1970.

[65] F. Durbin. Numerical inversion of Laplace transforms: an efficient improvement to Dubner and Abate's method. *The Computer Journal*, 17(4):371–376, 1974.

[66] Brian Davies and Brian Martin. Numerical inversion of the Laplace transform: a survey and comparison of methods. *Journal of Computational Physics*, 33:1–32, 1979.

[67] Alexander H-D Cheng and Younane Abousleiman. Approximate inversion of the Laplace transform. *The Mathematica Journal*, 4(2):76–82, 1994.

[68] Michel Nakhla, K. Singhal, and J. Vlach. Numerical inversion of the Laplace transform. *Electron. Letters*, 9(14):313–314, 1973.

[69] Toshio Hosono. Numerical inversion of laplace transform and some applications to wave optics. *Radio Science*, 16(6):1015–1019, 1981.

[70] G. A. Baker and P. Graves-Morris. *Encyclopedia of Mathematics*, chapter *Padé Approximants*. Cambridge Univ. Press, New York, 1995.

[71] Jiří Vlach and Kishore Singhal. *Computer Methods for Circuit Analysis and Design*. Kluwer Academic, Boston, MA, USA, second edition, 2003.

[72] Ye Tao, Emad Gad, and Michel Nakhla. Fast and stable time-domain simulation based on modified numerical inversion of the Laplace transform. *IEEE Transactions on Components, Packaging and Manufacturing Technology*, 11(5):848–858, 2021.

[73] E. Gad, M. Nakhla, R. Achar, and Y. Zhou. A-stable and L-stable high-order integration methods for solving stiff differential equations. 28(9):1359–1372, Sep. 2009.

[74] Emad Gad, Ye Tao, and Michel Nakhla. Fast and stable circuit simulation via interpolation- supported numerical inversion of the laplace transform. *IEEE Transactions on Components, Packaging and Manufacturing Technology*, 12(1):121–130, 2022.

[75] F J Hickernell and S. Yang. Explicit hermite interpolation polynomials via the cycle index with applications. *International Journal of Numerical Analysis and Modeling*, 5(3):457–465, 2008.

[76] F. Yang, Xue-Xia Zhang, Xiaoning Ye, and Y. Rahmat-Samii. Wide-band E-shaped patch antennas for wireless communications. *IEEE Transactions on Antennas and Propagation*, 49(7):1094–1100, 2001.

[77] Sergey V. Kochetov and Guenter Wollenberg. Stable and effective full-wave PEEC models by full-spectrum convolution macromodeling. *IEEE Transactions on Electromagnetic Compatibility*, 49(1):25–34, 2007.

[78] Yue-Kuen Kwok and Daniel Barthez. An algorithm for the numerical inversion of Laplace transforms. *Inverse Problems*, 5:1089–1095, 1989.

[79] Seiya Kishimoto, Tatsuichiro Okada, Shinichiro Ohnuki, Yoshito Ashizawa, and Katsuji Nakagawa. Efficient analysis of electromagnetic fields for designing nanoscale antennas by using a boundary integral equation method with fast inverse Laplace transform. *Progress In Electromagnetics Research*, 146:155–165, 2014.

[80] Mikheil Tsiklauri, Mikhail Zvonkin, Jun Fan, James Drewniak, Qinghua Bill Chen, and Alexander Razmadze. Causality and delay and physics in real systems. In *2014 IEEE International Symposium on Electromagnetic Compatibility (EMC)*, pages 961–966, 2014.

[81] C. A. Balanis. *Antenna Theory: Analysis and Design.* John Wiley and Sons, New York, 2005.

[82] Cunhua Pan, Hong Ren, Kezhi Wang, Jonas Florentin Kolb, Maged Elkashlan, Ming Chen, Marco Di Renzo, Yang Hao, Jiangzhou Wang, A. Lee Swindlehurst, Xiaohu You, and Lajos Hanzo. Reconfigurable intelligent surfaces for 6g systems: Principles, applications, and research directions. *IEEE Communications Magazine*, 59(6):14–20, 2021.

[83] Gabriele Gradoni and Marco Di Renzo. End-to-end mutual coupling aware communication model for reconfigurable intelligent surfaces: An electromagnetic-compliant approach based on mutual impedances. *IEEE Wireless Communications Letters*, 10(5):938–942, 2021.

[84] Placido Mursia, Sendy Phang, Vincenzo Sciancalepore, Gabriele Gradoni, and Marco Di Renzo. Modeling and optimization of reconfigurable intelligent surfaces in propagation environments with scattering objects, 2023.

[85] Giuseppe Pettanice, Fabrizio Loreto, Piergiuseppe Di Marco, Daniele Romano, Fortunato Santucci, Roberto Alesii, and Giulio Antonini. Time-domain characterization of reconfigurable intelligent surfaces for wireless communications. In *2022 International Symposium on Electromagnetic Compatibility EMC Europe*, pages 566–571, 2022.

[86] Shanpu Shen, Bruno Clerckx, and Ross Murch. Modeling and architecture design of reconfigurable intelligent surfaces using scattering parameter network analysis. *IEEE Transactions on Wireless Communications*, 21(2):1229–1243, 2022.

[87] L. Lu, M.S. Nakhla, and Q.-J. Zhang. A resetting algorithm for transient analysis of coupled transmission line circuits. *IEEE Transactions on Microwave Theory and Techniques*, 42(3):494–500, 1994.

[88] C. R. Paul. *Analysis of Multiconductor Transmission Lines*. John Wiley & Sons, New York, NY, second edition, 2008.

[89] A. T. De Hoop. A modification of Cagniard's method for solving seismic pulse problems. *Applied Scientific Research*, B(8):349–356, 1960.

[90] A. T. De Hoop. Large-offset approximations in the modified cagniard method for computing synthetic seismograms: a survey. *Geophys. Prosp.*, 36(5):465–477, 1988.

[91] A. T. De Hoop. Reflection and transmission of a transient, elastic, line-source excited SH wave by a planar, elastic bonding surface in a solid. *Int. J. Solids Struct.*, 39(21):5379–5391, 2002.

[92] M. Štumpf. *Time-Domain Electromagnetic Reciprocity in Antenna Modeling*. Hoboken, NJ: IEEE Press–Wiley, 2019.

[93] Martin Štumpf, Giulio Antonini, and Albert E Ruehli. Cagniard-DeHoop technique-based computation of retarded partial coefficients: the coplanar case. *IEEE Access*, 8:148989–148996, 2020.

[94] M. Štumpf. *Electromagnetic Reciprocity in Antenna Theory*. Hoboken, NJ: IEEE Press–Wiley, 2018.

[95] Ioan E. Lager, Adrianus T. de Hoop, and Takamaro Kikkawa. Model pulses for performance prediction of digital microelectronic systems. *IEEE Transactions on Components, Packaging and Manufacturing Technology*, 2(11):1859–1870, 2012.

[96] Ioan E Lager, Vincent Voogt, and Bert Jan Kooij. Pulsed EM field, close-range signal transfer in layered configurations – a time-domain analysis. 62(5):2642–2651, 2014.

[97] Ioan E. Lager and Sven L. van Berkel. Finite temporal support pulses for em excitation. *IEEE Antennas and Wireless Propagation Letters*, 16:1659–1662, 2017.